



494368

Pgs 386

UCI-ARTR-00-05

IN 107

2000 164 485

Mixing of an Airblast-Atomized Fuel Spray Injected Into a Crossflow of Air

May Y. Leong, Vincent G. McDonell, and G. Scott Samuelsen
University of California, Irvine, Irvine, California

The NASA STI Program Office . . . in Profile

Since its founding, NASA has been dedicated to the advancement of aeronautics and space science. The NASA Scientific and Technical Information (STI) Program Office plays a key part in helping NASA maintain this important role.

The NASA STI Program Office is operated by Langley Research Center, the Lead Center for NASA's scientific and technical information. The NASA STI Program Office provides access to the NASA STI Database, the largest collection of aeronautical and space science STI in the world. The Program Office is also NASA's institutional mechanism for disseminating the results of its research and development activities. These results are published by NASA in the NASA STI Report Series, which includes the following report types:

- **TECHNICAL PUBLICATION.** Reports of completed research or a major significant phase of research that present the results of NASA programs and include extensive data or theoretical analysis. Includes compilations of significant scientific and technical data and information deemed to be of continuing reference value. NASA's counterpart of peer-reviewed formal professional papers but has less stringent limitations on manuscript length and extent of graphic presentations.
- **TECHNICAL MEMORANDUM.** Scientific and technical findings that are preliminary or of specialized interest, e.g., quick release reports, working papers, and bibliographies that contain minimal annotation. Does not contain extensive analysis.
- **CONTRACTOR REPORT.** Scientific and technical findings by NASA-sponsored contractors and grantees.

- **CONFERENCE PUBLICATION.** Collected papers from scientific and technical conferences, symposia, seminars, or other meetings sponsored or cosponsored by NASA.
- **SPECIAL PUBLICATION.** Scientific, technical, or historical information from NASA programs, projects, and missions, often concerned with subjects having substantial public interest.
- **TECHNICAL TRANSLATION.** English-language translations of foreign scientific and technical material pertinent to NASA's mission.

Specialized services that complement the STI Program Office's diverse offerings include creating custom thesauri, building customized data bases, organizing and publishing research results . . . even providing videos.

For more information about the NASA STI Program Office, see the following:

- Access the NASA STI Program Home Page at <http://www.sti.nasa.gov>
- E-mail your question via the Internet to help@sti.nasa.gov
- Fax your question to the NASA Access Help Desk at (301) 621-0134
- Telephone the NASA Access Help Desk at (301) 621-0390
- Write to:
NASA Access Help Desk
NASA Center for Aerospace Information
7121 Standard Drive
Hanover, MD 21076



Mixing of an Airblast-Atomized Fuel Spray Injected Into a Crossflow of Air

May Y. Leong, Vincent G. McDonell, and G. Scott Samuelsen
University of California, Irvine, Irvine, California

Prepared under Cooperative Agreement NCC3-412

National Aeronautics and
Space Administration

Glenn Research Center

Trade names or manufacturers' names are used in this report for identification only. This usage does not constitute an official endorsement, either expressed or implied, by the National Aeronautics and Space Administration.

Available from

NASA Center for Aerospace Information
7121 Standard Drive
Hanover, MD 21076
Price Code: A17

National Technical Information Service
5285 Port Royal Road
Springfield, VA 22100
Price Code: A17

Available electronically at <http://gltrs.grc.nasa.gov/GLTRS>

TABLE OF CONTENTS

LIST OF FIGURES	vii
LIST OF TABLES.....	xiv
NOMENCLATURE.....	xv
CHAPTER 1 INTRODUCTION TO THE RESEARCH PROBLEM	1
1.1 The Conventional Gas Turbine Combustor	2
1.2 NO _x Chemistry	4
1.2.1 Role of NO _x in Tropospheric O ₃ Formation	5
1.2.2 Role of NO _x in Stratospheric O ₃ Destruction	7
1.2.3 Mechanisms of NO Formation.....	8
1.2.3a Thermal Mechanism	9
1.2.3b Prompt Mechanism	12
1.2.3c Nitrous Oxide Mechanism.....	12
1.3 Low-NO _x Combustion Concepts	14
1.3.1 Established Lean Combustion Technologies	15
1.3.2 Lean-Burn Injection	16
1.4 Statement of the Problem.....	19
1.5 Goals and Objectives	21
CHAPTER 2 BACKGROUND: ATOMIZATION AND TRANSPORT PROCESSES RELATED TO THE SPRAY JET IN CROSSFLOW	23
2.1 Basic Definitions Related to Atomization	25
2.1.1 Relevant Dimensionless Numbers	25
2.1.2 Representative Drop Diameters	29
2.2 Liquid and Spray Injection into a Quiescent Atmosphere.....	31
2.2.1 Liquid Jet Atomization	32
2.2.2 Plain-Jet Airblast Atomization	37
2.3 Liquid Jet Injection Into a Crossflow.....	49
2.3.1 Jet Penetration	51
2.3.2 Jet Deformation and Breakup	53
2.3.2a Primary Jet Breakup	56
2.3.2b Secondary Breakup.....	61
2.3.3 Mass, Droplet, and Velocity Distributions	66
2.3.4 Summary of the Liquid Jet in Crossflow Studies	72
2.4 Spray Jet Injection into a Crossflow	74
2.4.1 Droplet Transport.....	74
2.4.2 Relevant Studies	77
2.4.2a Spray Jet	77
2.4.2b Particle-Laden Jet	83
2.4.2c Airblast Spray Jet	86
2.4.3 Summary of the Spray Jet in Crossflow Studies	87
CHAPTER 3 RESEARCH GOALS AND APPROACH	88
CHAPTER 4 DESCRIPTION OF THE SPRAY EXPERIMENT	90
4.1 Hardware	90
4.1.1 Injection Panel Specifications	91
4.1.2 Crossflow Test Section	96
4.1.3 Comparison between the LBI and Single Jet Hardware	97

4.2	Non-Reacting Spray Facilities	99
4.3	Existing Diagnostic Capability	101
4.3.1	High-Speed and High-Magnification Video	101
4.3.2	Phase Doppler Interferometry	104
4.4	General Operating Conditions	108
4.4.1	Liquid Fuel Selection	108
4.4.2	Air Flows	110
4.4.3	Range of Operation	111
CHAPTER 5 DESCRIPTION AND SETUP FOR THE PLANAR IMAGING TECHNIQUES		
5.1	Principles of Light Scattering	113
5.2	Planar Mie Scattering	116
5.3	Planar Laser Induced Fluorescence	117
5.3.1	Acetone Fluorescence	118
5.3.2	Liquid Mass Fraction Imaging	120
5.4	Planar Laser Imaging Setup	123
5.4.1	Laser and Optical Train	124
5.4.2	Image Acquisition System	126
CHAPTER 6 TWIN-FLUID VISUALIZATION METHODOLOGY		
6.1	Verifying the PLLIF Mass Representation of Calibration Fluid	129
6.2	Fuel-Air Discrimination and Measurement	132
6.3	Image Processing	134
6.4	Planar D_{32} Measurement	140
6.5	Verification of the Techniques	142
6.6	Diagnostic Summary	148
CHAPTER 7 GLOBAL STRUCTURE OF THE AIRBLAST SPRAY WITHOUT CROSSFLOW		
7.1	Experimental Conditions	150
7.2	Airblast Spray Atomization Modes	152
7.3	Spray Angle	161
7.3.1	Measurement and Calculation Methods	162
7.3.2	Effect of Parametric Variation	164
7.4	Summary	172
CHAPTER 8 PLANAR CHARACTERIZATION OF THE AIRBLAST SPRAY WITHOUT CROSSFLOW		
8.1	Experimental Conditions	173
8.2	Distribution of the Liquid Component of the Spray	178
8.2.1	Comparison at the $x=10$ mm Plane	178
8.2.1a	PLLIF and Planar D_{32} Images	178
8.2.1b	Effect of the Airblast ΔP and Spray Orifice Diameter on the Airblast Velocity	188
8.2.2	Axial Evolution of the Liquid Distribution	191
8.3	Planar D_{32} Correlation and Comparison	196
8.4	Quantitative Assessment of the Spray Quality	202
8.4.1	Definitions	202
8.4.2	Application of the Defined Spray Parameters	205
8.5	Extent of the Atomizing Air in the Spray	211
8.6	Summary	216

CHAPTER 9	GLOBAL STRUCTURE OF THE AIRBLAST SPRAY JET IN A CROSSFLOW	219
9.1	Experimental Conditions	219
9.2	Two-Phase Definition of the Momentum-Flux Ratio	223
9.3	Baseline Case: Liquid Jet (Airblast $\Delta P=0\%$)	226
9.4	Effect of Airblast Air at Different Ambient Pressure Conditions	227
9.5	Development of a Spray Trajectory Equation	232
9.6	Summary	238
CHAPTER 10	PLANAR CHARACTERIZATION OF THE AIRBLAST SPRAY JET IN A CROSSFLOW	240
10.1	Spray Measurements in Transition Regime of $\Delta P=2\%$	241
10.2	Experimental Conditions for the Planar Imaging Tests	249
10.3	Distribution of the Liquid Component of the Spray Injected into a Crossflow	254
10.3.1	Effect of Injection Parameters on the Spray Jet Injected into a Crossflow at 70 m/sec	255
10.3.1a	Distributions in the $z=10$ mm plane	255
10.3.1b	Downstream Evolution of the Liquid Distributions	266
10.3.2	Effect of the Crossflow Velocity Magnitude	271
10.4	Planar D_{32} Correlation and Comparison	276
10.5	Quantitative Assessment of the Spray Quality	282
10.6	Extent of the Atomizing Air in the Spray	287
10.7	Spray Dispersion into the Crossflow of Air	292
10.7.1	Droplet Trajectory Analysis	292
10.7.2	Initial Conditions	294
10.7.3	Predicted Trajectories and Volume Distributions	299
10.8	Summary	311
CHAPTER 11	SUMMARY, CONCLUSIONS, AND RECOMMENDATIONS	317
11.1	Summary	317
11.2	Conclusions	322
11.3	Recommendations	325
CHAPTER 12	REFERENCES	327
APPENDIX A	IMAGE PROCESSING CODES	337
APPENDIX B	NONLINEAR MULTIVARIATE REGRESSION	352
APPENDIX C	ADDITIONAL SPRAY JET IN CROSSFLOW RESULTS	356
APPENDIX D	DROPLET TRAJECTORY PROGRAM FILES	362

LIST OF FIGURES

Fig. 1.1	The gas turbine (Brayton) cycle.....	2
Fig. 1.2	Schematic of a conventional annular gas turbine combustor. (Lefebvre, 1999)	3
Fig. 1.3	Relationship between the equivalence ratio and the adiabatic flame temperature and NO_x emissions (output from equilibrium code of Gordon and McBride (1976), for a condition of 478 K air preheat, 298 K jet-A temperature, at 10 atm).....	11
Fig. 1.4	Combustor utilizing the Lean Burn Injection (LBI) concept.	17
Fig. 1.5	Single spray jet in crossflow modeled after the LBI.....	20
Fig. 2.1	Decomposition of the spray jet in crossflow problem.	25
Fig. 2.2	Liquid jet breakup (without airblast air) in a quiescent environment induced by capillary instabilities that are decoupled from the surrounding gas.	32
Fig. 2.3	Different regimes of jet disintegration in a quiescent environment. (Faeth, 1990).....	33
Fig. 2.4	Liquid jet breakup regimes, mapped on (a) Oh vs. Re_L axes (Reitz, 1978), and (b) Oh vs. We_g axes (Faeth, 1990).	35
Fig. 2.5	Turbulent primary breakup at the liquid surface. (Wu et al., 1995).	36
Fig. 2.6	Atomization of a liquid jet with the aid of a co-flowing air stream.	37
Fig. 2.7	Comparison between (a) a prefilming airblast atomizer (Lefebvre, 1999), and (b) the plain-jet airblast atomizer in the LBI.....	38
Fig. 2.8	Illustration of the different breakup modes described by Farago and Chigier (1992).	39
Fig. 2.9	Mapping of the breakup regimes for a water jet with a co-flowing air stream (Farago and Chigier, 1992).....	41
Fig. 2.10	Comparison between classical and prompt breakup modes in an airblast- atomized spray.	43
Fig. 2.11	Comparison between the geometry of (a) the Nukiyama-Tanasawa (1939) plain-jet airblast injector, and (b) the fuel atomizer of the LBI Injector.....	44
Fig. 2.12	Liquid jet breakup in a crossflow of air.	50
Fig. 2.13	Jet interaction with a crossflow.	54
Fig. 2.14	Jet breakup in a crossflow (Wu et al., 1997).....	55
Fig. 2.15	A model of jet deformation and breakup (Clark, 1964).	59
Fig. 2.16	Drop deformation shapes: (a) Lenticular, (b) Cigar-shaped, (c) Bulgy (Hinze, 1955).	61
Fig. 2.17	Droplet breakup modes (Krzeczkowski, 1980).	62
Fig. 2.18	Breakup of a stream of 150-mm water droplets in atmospheric air by a 50% shock wave (Eastes and Samuelsen, 1993).	64
Fig. 2.19	Shear breakup from a drop (Wu et al., 1995).	65

Fig. 2.20	Detailed scheme of jet breakup in a supersonic crossflow. (Thomas and Schetz, 1985).	69
Fig. 2.21	The regimes of the liquid jet in crossflow assessed by the listed studies.	72
Fig. 2.22	Injection of a liquid spray into a crossflow of air.	74
Fig. 2.23	Diagram depicting the droplet path upon injection into a crossflow of air (left), and the force balance on the droplet in the present analysis (right).. . . .	75
Fig. 2.24	Zones used to analyze the trajectory of the spray jet in crossflow. (Ghosh and Hunt, 1998).	81
Fig. 4.1	Airblast spray injection panel	92
Fig. 4.2	Disks for interchanging spray orifice diameters	93
Fig. 4.3	Compact, traversable fuel tube design: (a) photograph, (b) drawing, and (c) detailed drawing of fuel tip.	95
Fig. 4.4	Hardware for the spray jet in crossflow configuration.	97
Fig. 4.5	Atmospheric test facility depicting the experiment installed in the crossflow configuration.	100
Fig. 4.6	Elevated pressure facility for non-reacting spray tests.	101
Fig. 4.7	High-speed video imaging system for bulk light scattering capture.. . . .	102
Fig. 4.8	High-magnification video system for bulk light scattering capture.. . . .	103
Fig. 4.9	PDI system (Real-time Signal Analyzer, Aerometrics) setup to measure the droplet size and velocity of the spray without crossflow in the atmospheric test facility.	106
Fig. 4.10	PDI system setup (Phase Doppler Particle Analyzer, Aerometrics) to measure the spray in the crossflow configuration in the elevated pressure facility.	107
Fig. 5.1	Light scattering of molecules by (a) Rayleigh scattering, (b) spontaneous Raman scattering via Stokes transition, (c) spontaneous Raman scattering via anti-Stokes transition. (Hecht, 1998)	115
Fig. 5.2	Acetone fluorescence emission spectra obtained upon stimulation by a 308 nm wavelength laser light source (Lozano et al., 1992).	119
Fig. 5.3	Fluorescence emission spectra of jet-A and MIL-C-7024D induced by 266 nm light excitation.. . . .	121
Fig. 5.4	UV laser imaging diagnostic, set for vertical sheet capture.. . . .	124
Fig. 5.5	Timing diagram for the UV planar imaging procedure.. . . .	127
Fig. 6.1	Absorbance of incident 266 nm light by various calibration fluid concentrations across a 1-cm sample cell width.	131
Fig. 6.2	Filter combinations for the different imaging strategies.. . . .	133
Fig. 6.3	Seeding system used to saturate the atomizing air stream with acetone vapor for acetone PLIF imaging.	134
Fig. 6.4	Image processing procedure consisting of (a) the representation of the image stack as a volume of matrices, (b) extraction of the horizontal cross-sections, and (c) application of a filter to smooth the extracted images.	135

Fig. 6.5	The temporal filtering strategy applied to the acetone PLIF images of the acetone-seeded air in the spray.	137
Fig. 6.6	Application of the temporal filter to an acetone PLIF image of the spray: (a) before (note the discrete, higher intensity droplet shapes), and (b) after... ..	137
Fig. 6.7	General image processing procedure.	138
Fig. 6.8	Sub-flow chart showing method of reconstructing horizontal images from measured vertical sheet images.	139
Fig. 6.9	Spray injection panel hardware and axis orientation for the quiescent injection setup.	142
Fig. 6.10	PLLIF image comparison with superimposed PDI-measured volume concentrations at $x=10$ mm for the 1.8 kg/h fuel flow, 3.18-mm spray orifice dia. case at a 4% airblast ΔP	144
Fig. 6.11	Mie scattering images at $x=10$ mm for the 1.8 kg/h fuel flow, 3.18-mm spray orifice dia. case at a 4% airblast ΔP	145
Fig. 6.12	Derived planar D_{32} images with overlaid PDI-measured D_{32} at $x=10$ mm for the 1.8 kg/h fuel flow, 3.18-mm spray orifice dia. case at a 4% airblast ΔP	146
Fig. 6.13	Concentration fields of the acetone-seeded atomizing air at $x=10$ mm for the 1.8 kg/h fuel flow, 3.18-mm spray orifice dia. case at a 3% and 6% airblast ΔP	147
Fig. 6.14	Acetone PLIF images of cases with and without liquid flow, at the $y=0$ mm origin plane, for the 1.8 kg/h fuel flow, 3.18-mm spray orifice dia. case at a 6% airblast ΔP	147
Fig. 7.1	Positioning of the high speed video camera relative to the spray experiment in the non-crossflow configuration.	150
Fig. 7.2	Comparison of pure liquid jet injection at different Reynolds numbers for the 0.66 mm-dia. fuel orifice.	153
Fig. 7.3	Evolution of the spray with increasing atomizing air flow for the 0.34 mm-dia. fuel orifice, 3.18 mm-dia. spray orifice case, at a fuel flow of 0.66 kg/h.	154
Fig. 7.4	Difference in geometry between the injector of Farago and Chigier (1992) and the present injector.	155
Fig. 7.5	Evolution of the spray with increasing atomizing air flow for the 0.66 mm-dia. fuel orifice, 3.18 mm-dia. spray orifice case, at a fuel flow of 5.0 kg/h.	156
Fig. 7.6	Breakup regime map from Farago and Chigier (1992) with the present range of operating conditions falling within the dashed lines.	158
Fig. 7.7	Breakup regime mapping of the airblast spray experiment with respect to Re_L and We_{airbl}	159
Fig. 7.8	Breakup regime mapping of the airblast spray experiment with respect to ALR and We_{airbl}	161
Fig. 7.9	Effect of the atomizing air pressure drop on the angle of the airblast-atomized spray for the 3.18-mm spray orifice diameter.	165
Fig. 7.10	Effect of the atomizing air pressure drop on the angle of the airblast-atomized spray for the 4.22-mm spray orifice diameter.	165

Fig. 7.11	Conception depicting the effect of the spray orifice diameter on the spread of the spray.	168
Fig. 7.12	Mean velocity and D_{32} plots across the longitudinal section ($y=0$ axis) of the airblast spray, at the $x=10$ mm plane, for the 3.18 mm-dia. spray orifice case (red), and the 4.22 mm-dia. case (black).	170
Fig. 7.13	Droplet D_{32} measured along the spray centerline parallel to the axis through the air circuits, at $y=0$ mm and $x=10$ mm, for the 1.9 kg/h fuel flow condition.	171
Fig. 8.1	Positioning of the intensified CCD camera relative to the vertical laser sheet passing through the spray experiment in the non-crossflow configuration.	174
Fig. 8.2	Sample horizontal planar section extracted from the set of vertical slices.	175
Fig. 8.3	Classification of the case conditions tested on the breakup regime map for the airblast spray.	177
Fig. 8.4	PLLIF liquid concentration images with overlaid PDI-based volume concentration distributions at the $x=10$ mm plane for the 1.8 kg/h fuel flow, 3.18-mm spray orifice dia. condition.	179
Fig. 8.5	Planar D_{32} images with overlaid PDI-measured D_{32} values at the $x=10$ mm plane for the 1.8 kg/h fuel flow, 3.18-mm spray orifice dia. condition.	180
Fig. 8.6	Comparison of PLLIF images with overlaid PDI-based volume concentration distributions at the $x=10$ mm plane for the different spray conditions.	182
Fig. 8.7	Comparison of planar D_{32} images with overlaid PDI-measured D_{32} values at the $x=10$ mm downstream plane for the different spray conditions.	185
Fig. 8.8	Force diagram on the control volume at the spray orifice.	189
Fig. 8.9	Evolution of the liquid concentration distributions for the 1.8 kg/h fuel flow, 3.18-mm spray orifice diameter case.	192
Fig. 8.10	Evolution of the liquid concentration distributions for the 1.8 kg/h fuel flow, 4.22-mm spray orifice diameter case.	193
Fig. 8.11	Evolution of the liquid concentration distributions for the 3.7 kg/h fuel flow, 3.18-mm spray orifice diameter case.	194
Fig. 8.12	Evolution of the liquid concentration distributions for the 3.7 kg/h fuel flow, 4.22-mm spray orifice diameter case.	195
Fig. 8.13	Correlation between the planar mean D_{32} intensity ratio and the corresponding point-based PDI measurement for the airblast spray.	197
Fig. 8.14	Comparison of the planar mean D_{32} for the different cases at various downstream x-positions for the 1.8 kg/h case.	199
Fig. 8.15	Comparison of the planar mean D_{32} for the different cases at various downstream x-positions for the 3.7 kg/h case.	199
Fig. 8.16	Comparison between the values of $D_{32,avg}/d_f$ predicted by Eq. 8.3 and the measured values.	202
Fig. 8.17	Comparison of the spray extent of area for the different cases at various downstream x-positions for the 1.8 kg/h case.	206

Fig. 8.18	Comparison of the spray extent of area for the different cases at various downstream x-positions for the 3.7 kg/h case.	206
Fig. 8.19	Comparison of the spatial unmixedness in the horizontal planar sections of the spray at different downstream x-positions for the 1.8 kg/h case.	208
Fig. 8.20	Comparison of the spatial unmixedness in the horizontal planar sections of the spray at different downstream x-positions for the 3.7 kg/h case.	208
Fig. 8.21	Comparison of the spray quality in the horizontal planar sections of the spray at different downstream x-positions for the 1.8 kg/h case.	210
Fig. 8.22	Comparison of the spray quality in the horizontal planar sections of the spray at different downstream x-positions for the 3.7 kg/h case.	210
Fig. 8.23	Comparison between the distributions of air and liquid, with and without the presence of liquid, for the 1.8 kg/h fuel flow, 3.18-mm spray orifice diameter case, at the y=0 mm plane.	213
Fig. 8.24	Comparison between the distributions of air and liquid, with and without the presence of liquid, for the 1.8 kg/h fuel flow, 4.22-mm spray orifice diameter case, at the y=0 mm plane.	215
Fig. 9.1	Orientation of the test section in the crossflow configuration.	220
Fig. 9.2	Image obtained from the high magnification video system.	221
Fig. 9.3	Schematic of the control volume encompassing the spray orifice.	225
Fig. 9.4	Pure liquid jet injection with 0% airblast ΔP and ALR=0.	227
Fig. 9.5	Effect of atomizing air pressure drop on spray structure for various ambient pressures.	229
Fig. 9.6	Plots of the Re_L to We_{airbl} for the elevated pressure tests, relative to the breakup regime maps obtained in Chapter 7.	231
Fig. 9.7	Comparison between the spray surface trajectories and the outer and inner spray surface curve fit from Eq. 9.3 for selected cases.	234
Fig. 9.8	Comparison between the spray surface trajectories and the modified curve fit from Eq. 9.4 for selected cases.	237
Fig. 10.1	Contour plots of normalized volume flux at various downstream z-planes.	242
Fig. 10.2	Contour plots of D_{32} at various downstream z-planes.	245
Fig. 10.3	Contour plots of the transverse velocity component (parallel to the x-axis) at various downstream z-planes.	246
Fig. 10.4	Contour plots of the axial velocity component (parallel to the z-axis) at various downstream z-planes.	247
Fig. 10.5	Picture and schematic depicting the orientation of the UV laser sheet and camera with respect to the spray jet in crossflow experiment.	251
Fig. 10.6	Sample horizontal planar section extracted from the set of vertical slices.	252
Fig. 10.7	Schematic depicting the orientation of the two-lobed spray structure prior to introducing the crossflow.	254

Fig. 10.8	PLLIF images depicting volume concentration distributions at the $z=10$ mm plane for the twelve spray conditions, after injection into a crossflow of 70 m/sec.	256
Fig. 10.9	Planar D_{32} images at the $z=10$ mm plane depicting D_{32} distributions of the twelve spray conditions, after injection into a crossflow of 70 m/sec..	260
Fig. 10.10	Droplet D_{32} distributions at the $z=10$ mm plane for the twelve spray conditions at the 70 m/sec crossflow velocity case.	262
Fig. 10.11	Evolution of the liquid concentration distributions for the 3.7 kg/h fuel flow, 3.18-mm spray orifice diameter case at a crossflow velocity of 70 m/sec.	267
Fig. 10.12	Evolution of the liquid concentration distributions for the 3.7 kg/h fuel flow, 4.22-mm spray orifice diameter case at a crossflow velocity of 70 m/sec.	269
Fig. 10.13	Liquid concentration and planar D_{32} distributions at the $z=10$ mm plane for the 3.7 kg/h fuel flow, 4% and 6% airblast ΔP sprays injected into a crossflow at 70 m/sec.	272
Fig. 10.14	Liquid concentration and planar D_{32} distributions at the $z=10$ mm plane for the 3.7 kg/h fuel flow, 4% and 6% airblast ΔP sprays injected into a crossflow at 78 m/sec.	274
Fig. 10.15	Liquid concentration and planar D_{32} distributions at the $z=10$ mm plane for the 3.7 kg/h fuel flow, 4% and 6% airblast ΔP sprays injected into a crossflow at 87 m/sec.	275
Fig. 10.16	Correlation between the planar mean D_{32} intensity ratio and the corresponding point-based PDI measurement for the airblast spray injected into a crossflow of 70 m/sec.	277
Fig. 10.17	Comparison of the planar mean D_{32} for the different cases at various downstream z -positions for the 1.8 kg/h case.	278
Fig. 10.18	Comparison of the planar mean D_{32} for the different cases at various downstream z -positions for the 3.7 kg/h case.	278
Fig. 10.19	Comparison between the predicted and actual values of plane-averaged D_{32} in a crossflow of 70 m/sec for (a) the basic correlating Eq. 10.2 and (b) the basic correlation with an additional We_{cross} factor (Eq. 10.3).	282
Fig. 10.20	Comparison of the spray quality in the horizontal planar sections of the spray at different downstream z -positions for the 1.8 kg/h case at 70 m/sec.	284
Fig. 10.21	Comparison of the spray quality in the horizontal planar sections of the spray at different downstream z -positions for the 3.7 kg/h case at 70 m/sec.	284
Fig. 10.22	Comparison of the spray quality in the horizontal planar sections of the spray at different downstream z positions for the 3.7 kg/h case at 70 m/sec.	285
Fig. 10.23	Comparison of the spray quality in the horizontal planar sections of the spray at different downstream z -positions for the 3.7 kg/h case at 78 m/sec.	285
Fig. 10.24	Comparison of the spray quality in the horizontal planar sections of the spray at different downstream z -positions for the 3.7 kg/h case at 87 m/sec.	286
Fig. 10.25	Distributions of the atomizing air without and with the liquid phase (top and middle rows), at the $y=0$ mm centerplane for the 3.7 kg/h fuel flow, 3.18 mm-dia. orifice, 70 m/sec crossflow. For comparison, the liquid volume distribution is also presented (bottom row).	288

Fig. 10.26	Distributions of the atomizing air without and with the liquid phase (top and middle rows), at the $y=0$ mm centerplane for the 3.7 kg/h fuel flow, 4.22 mm-dia. orifice, 70 m/sec crossflow. For comparison, the liquid volume distribution is also presented (bottom row).	291
Fig. 10.27	Initial mean velocities and D_{32} obtained at the $y=0$ mm centerplane for the 3.7 kg/h fuel flow sprays before introducing the crossflow.	295
Fig. 10.28	Initial velocities and data rates obtained at the $y=0$ mm centerplane for the 3.7 kg/h fuel flow, 3.18 mm-dia. spray orifice case without crossflow. . . .	297
Fig. 10.29	Initial velocities and data rates obtained at the $y=0$ mm centerplane for the 3.7 kg/h fuel flow, 4.22 mm-dia. spray orifice case without crossflow. . . .	298
Fig. 10.30	Trajectories of three droplet size classes in a 70 m/sec crossflow, obtained using the initial conditions measured in the 3.7 kg/h fuel, 3.18 mm-dia. sprays without crossflow.	300
Fig. 10.31	Trajectories of three droplet size classes in a 70 m/sec crossflow, obtained using the initial conditions measured in the 3.7 kg/h fuel, 4.22 mm-dia. sprays without crossflow.	302
Fig. 10.32	Breakdown of volume distribution at the $z=15$ mm plane of predicted liquid volume distributions, compared to the liquid concentration distributions from PLLIF imaging for the 3.7 kg/h, 2% airblast ΔP , 3.18 mm-dia., 70 m/sec crossflow case.	306
Fig. 10.33	Comparison of predicted liquid volume distributions to the liquid concentration distributions from PLLIF imaging for the 3.7 kg/h, 3.18 mm-dia., 70 m/sec crossflow cases.	307
Fig. 10.34	Comparison of predicted liquid volume distributions to the liquid concentration distributions from PLLIF imaging for the 3.7 kg/h, 4.22 mm-dia., 70 m/sec crossflow cases.	309
Fig. 10.35	Proposed model of the dispersion of the spray jet into the crossflow.	315
Fig. C.1	Evolution of the liquid concentration distributions for the 1.8 kg/h fuel flow, 3.18-mm spray orifice diameter case at a crossflow velocity of 70 m/sec. . . .	358
Fig. C.2	Evolution of the liquid concentration distributions for the 1.8 kg/h fuel flow, 4.22-mm spray orifice diameter case at a crossflow velocity of 70 m/sec. . . .	359
Fig. C.3	Comparison of predicted liquid volume distributions to the liquid concentration distributions from PLLIF imaging for the 1.8 kg/h, 3.18 mm-dia., 70 m/sec crossflow cases.	360
Fig. C.4	Comparison of predicted liquid volume distributions to the liquid concentration distributions from PLLIF imaging for the 1.8 kg/h, 4.22 mm-dia., 70 m/sec crossflow cases.	361

LIST OF TABLES

Table 2.1	Comparison between plain-jet airblast atomizer experiments.	48
Table 4.1	Comparison between the LBI and the single spray jet injector geometries. . .	98
Table 4.2	Properties of jet-A and calibration fluids MIL-C-7024D and MIL-PRF-7024E. .	109
Table 4.3	Overall range of operating conditions tested.	112
Table 6.1	Summary of primary spray diagnostics used in the experiment.	149
Table 7.1	Operating and geometric conditions for the global visualization of the airblast spray experiment in the non-crossflow configuration.	151
Table 8.1	Operating and geometric conditions for the planar imaging of the airblast spray experiment in the non-crossflow configuration.	176
Table 9.1	Operating and geometric conditions for the global visualization of the airblast spray experiment in the crossflow configuration.	222
Table 9.2	Coefficients for the outer and inner spray surface trajectory fits.	236
Table 10.1	Operating and geometric conditions for the planar imaging of the airblast spray experiment in the crossflow configuration.	253
Table 10.2	Summary of the effects of varying the spray injection parameters on the liquid distributions before and after introducing the crossflow of air.	265
Table 10.3	Curve fit coefficients for the plane-averaged D_{32} for the non-crossflow and crossflow cases.	281

NOMENCLATURE

Primary Variables

a	acceleration
A	absorbance of light energy
A_d	projected area of droplet
C_d	discharge coefficient of orifice
C_D	drag coefficient
d	diameter
D_{ab}	representative droplet diameter, $[(\sum n_i d_i^a)/(\sum n_i d_i^b)]^{1/(a-b)}$
F	force
g	gravitational acceleration
$[i,j,k]$	index notation in matrices
I	intensity of light
L	path length of light transmission
m	slope of line
$[m,n,p]$	notation representing the number of rows, columns, and elemental depth in a matrix
M	percent concentration of solute in solvent (Chapter 6), matrix of elements (Chapter 7)
P	pressure
T	temperature
u	velocity component aligned with the jet (transverse component in the crossflow configuration)

U	velocity, $u\hat{i} + v\hat{j} + w\hat{k}$
U_R	relative velocity
v	velocity component parallel to the wall, and perpendicular to the velocity component, w
V	volume
w	velocity component normal to the jet and aligned with the crossflow
x	component along jet axis
y	component orthogonal to the jet and crossflow axes, and perpendicular to the axis through the injector airblast circuits
z	component aligned with the crossflow, and parallel to the axis through the injector airblast circuits

Greek Symbols

ε	molar extinction coefficient
ϕ	fuel-air equivalence ratio
μ	absolute viscosity
ρ	density
σ	surface tension
τ	characteristic time

Subscripts

c	characteristic property, as in τ_c
d	droplet
f	fuel
g	gaseous phase
j	jet
L	liquid phase
p	particle

Dimensionless Quantities

ALR	atomizing air to liquid mass flow rate ratio
Eu	Eötvös number, $(\rho_L D_{32}^2 g) / \sigma$
l/d	length to diameter ratio of orifice
Oh	Ohnesorge number, $(\sqrt{We}) / (Re) = \mu_L / (\sqrt{\rho_L \sigma d_0})$
q, q_1	single-phase jet to crossflow momentum-flux ratio, or dynamic pressure ratio, $(\rho U^2)_f / (\rho U^2)_g$
q_2	two-phase jet to crossflow momentum-flux ratio, $[(\rho U^2 A _{liquid} + \rho U^2 A _{airblast}) / A_{spray}] / (\rho U^2 _{crossflow})$
Re	Reynolds number, $\rho U_R d / \mu$
St	Stokes number, τ_p / τ_c
We	Weber number, $\rho U_R^2 d / \sigma$

CHAPTER 1

INTRODUCTION TO THE RESEARCH PROBLEM

The goal of the next generation of gas turbine combustors is to reduce NO_x emissions to meet regulatory levels that cannot be attained with conventional combustors. The control of NO_x emissions to the atmosphere is important because of the deleterious effects of NO_x in creating photochemical oxidant in the urban environment, introducing acid rain in the troposphere, and destroying the ozone layer in the stratosphere. In gas turbine combustors, the preparation of a fuel-air mixture has evolved as a major parameter that affects combustion, and subsequently, the levels of NO_x formed. This has led to a focused attention to the processes of liquid injection and mixing in general, and the degree to which these processes can be promoted and accelerated prior to the reaction of the fuel vapor/air mixture.

The radial injection of the liquid into a high velocity cross-stream provides a means for accomplishing this goal in the retrofit of conventional as well as in the design of the next generation of gas turbine engines. This dissertation addresses the characterization of the radial injection of a liquid jet in a high velocity crossflow of air. To appreciate the significance of this research, this chapter presents an introduction to the gas turbine combustor, the relevant NO_x reactions, and the gas turbine combustor designs for low- NO_x combustion. The introduction concludes with a statement of the problem and the goals and objectives of the dissertation.

1.1 The Conventional Gas Turbine Combustor

Gas turbine engines are used in a variety of applications such as aircraft propulsion and industrial power generation. The combustor is the driving source of energy that is used to power the engine. The main function of the combustor is to rapidly expand the compressed air from the compressor stage and transform the chemical energy resident in the fuel to thermal energy. The hot gaseous products of combustion are then sent through the turbine, where the passage of the gases across the blades causes the turbine to spin and power the compressor. The residual enthalpy is available to produce thrust in a propulsion application, or to generate electric power in a stationary application. The gas turbine engine cycle in Fig. 1.1 depicts these basic features in schematic form.

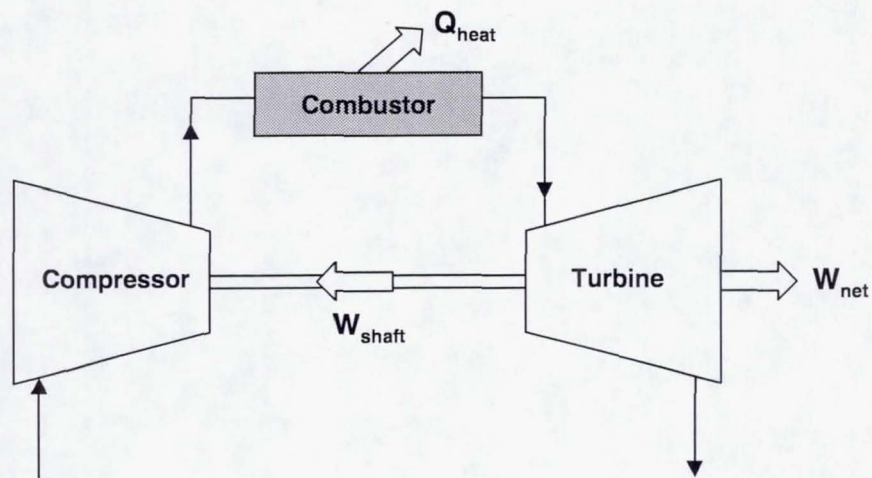


Fig. 1.1 The gas turbine (Brayton) cycle.

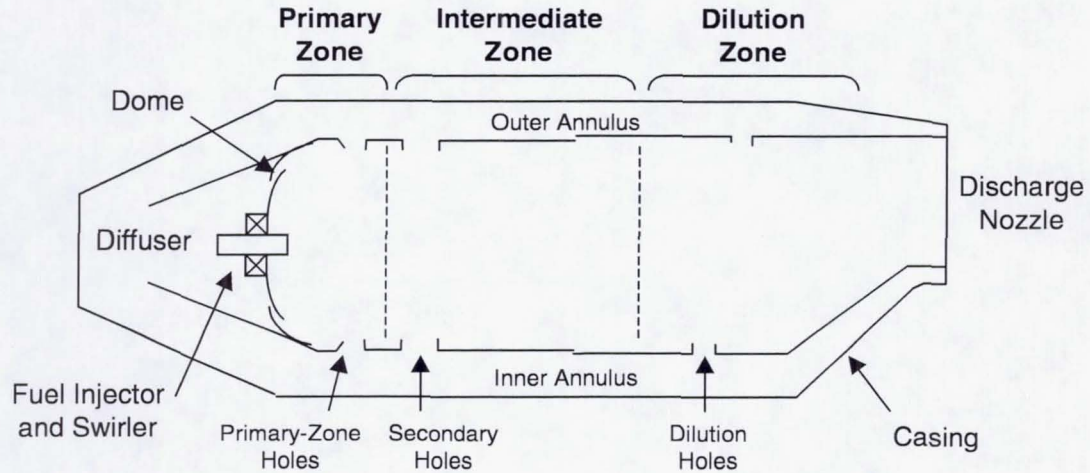


Fig. 1.2 Schematic of a conventional annular gas turbine combustor. (Lefebvre, 1999)

The conventional gas turbine combustor used in most present-day applications (Fig. 1.2) can be divided into the primary, intermediate, and dilution zones. The primary zone contains the dome region into which a fuel and air mixture is injected. According to Lefebvre (1999), the primary zone operates at an air to fuel ratio of around 18. For jet-A fuel, this corresponds to a fuel-air equivalence ratio ϕ of 0.82, where ϕ is defined as

$$\phi = \frac{\left. \frac{\text{fuel}}{\text{air}} \right|_{\text{actual}}}{\left. \frac{\text{fuel}}{\text{air}} \right|_{\text{stoichiometric}}} . \quad (1.1)$$

The overall fuel-air equivalence ratios across typical combustors range from 0.37-0.49 (based on the air/fuel values of 30-40 from Lefebvre (1999)). These lean ϕ are achieved by introducing air through the ports in the intermediate and dilution zones.

Air injected into the intermediate zone completes the reaction of any partially or unreacted gases, while the dilution zone air cools the hot products to temperatures that the turbine blades can tolerate. Despite operating at an overall lean ϕ , the attainment of near-stoichiometric equivalence ratios in the primary zone can produce the high temperatures that lead to high NO_x production via the thermal NO_x mechanism. One combustion concept based on avoiding these high temperatures involves operating the primary dome of the combustor under fuel-lean conditions, which may prevent thermal NO_x formation, but which may also increase NO_x formation via the nitrous oxide mechanism. The next section on NO_x chemistry describes these NO_x formation mechanisms, after first discussing the deleterious effects of NO_x reactions in the troposphere and stratosphere.

1.2 NO_x Chemistry

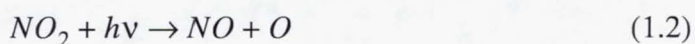
Nitric oxide (NO) and nitrogen dioxide (NO_2) are the major constituents of NO_x . NO_x reacts in the troposphere (from ground level to an altitude of 10-15 km) and in the stratosphere (from the troposphere to an altitude of 45-55 km), and detrimentally affects the environment and the general health of the public. In the troposphere, NO_2 reacts with the OH radical (Seinfeld and Pandis, 1998) to produce nitric acid (HNO_3), one of the constituents of acid rain. At the ground level, NO_x contributes to the production of ozone, a precursor to photochemical oxidant which induces respiratory and eye irritation. NO_x emitted directly into the stratosphere by the direct exhaust of supersonic aircraft engines, or by the diffusion of NO_x emissions from subsonic aircraft engines in the upper troposphere, reacts with the ozone molecules in the stratospheric

ozone layer. The ensuing destruction of the Earth's protective ozone layer leads to an increased exposure of all life forms to ultraviolet light such as UV-B (290 to 320 nm), which can increase the incidence of skin cancer (Seinfeld and Pandis, 1998).

To gain an understanding of the chemical role that NO_x plays in the environment, Sections 1.2.1 and 1.2.2 present the reactions which show how NO_x can produce ozone in the troposphere while at the same time, consume ozone in the stratosphere. In order to determine the means of controlling NO_x formation in combustion, Section 1.2.3 gives an overview of the different mechanisms involved in NO_x (specifically NO) formation.

1.2.1 Role of NO_x in Tropospheric O_3 Formation

In the troposphere, the set of reactions leading to the production of ozone (O_3) is



The photolysis of NO_2 by the sun, represented by the energy quantity $h\nu$ in Reaction 1.2, initiates the set of reactions. In Reaction 1.3, the freed O atom reacts with O_2 in the air and with the presence of a chemically inert, energy-absorbing third-party molecule M , to produce O_3 . The NO formed in Reaction 1.2 reacts with the O_3 formed in Reaction 1.3 to reverse the formation of the net reaction products, as shown by Reaction 1.4:



At steady-state conditions, the reaction rates of Reactions 1.2 to 1.4 are assumed equal, and the equilibrium concentration of O_3 ($=[hv][NO_2] / [NO]k_{1.4}$) becomes dependent on the intensity of the sunlight. The equilibrium O_3 concentration relationship is not as sensitive to the ratio of NO_2 to NO because the net formation of NO and NO_2 is zero (deNevers, 1995; Seinfeld and Pandis, 1998).

The net formation of O_3 occurs when pathways other than Reaction 1.4 become available to convert the NO to NO_2 . Volatile organic compound emissions (VOC) provide this alternate pathway by reacting with NO to form NO_2 . The result is an increase in O_3 because less O_3 is consumed via Reaction 1.4, while more O_3 is produced because the NO that is emitted by combustion sources produces more NO_2 for the O_3 -producing cycle. The termination of the cycle of NO_2 - NO - O_3 reactions can occur when NO_2 reacts with the OH radical to form HNO_3 , which itself can also reduce O_3 formation (deNevers, 1995; Seinfeld and Pandis, 1998).

This interplay between NO_x , VOC, and OH in affecting O_3 production highlights the complexity of the tropospheric O_3 chemistry. However, the main purpose of presenting these reactions is to show the primary role that NO_x plays in producing tropospheric O_3 .

1.2.2 Role of NO_x in Stratospheric O₃ Destruction

The reactions that destroy the ozone layer are represented by the following set of reactions between NO_x, O₃, and the O radical (formed by the natural photolysis of ozone O₃ in the stratosphere):



which results in the net O₃-destroying reaction



Reactions 1.5 to 1.7 account for up to 70 percent of the destruction of stratospheric ozone, and continue until NO₂ is removed by the reaction with OH that forms the nitric acid molecule HNO₃ (Seinfeld, 1986).

There are two other NO_x cycles that Seinfeld and Pandis (1998) describe which also break up the O₃ molecules in the stratosphere. One cycle, which is more likely to occur in the lower stratosphere where O₃ is more abundant, begins with Reaction 1.5 but follows with the reactions



to yield the net O₃-destroying reaction



The “null cycle” follows Reaction 1.5 with the step



to yield the net reaction



The NO_2 participating in the first two of the three cycles presented here, and the NO_2 molecules in the “null cycle” are from different molecular populations. Hence, the “null cycle” must also be considered when analyzing the effect of NO_x on stratospheric O_3 (Seinfeld and Pandis, 1998).

1.2.3 Mechanisms of NO Formation

Combustion-related activity contributes to a large percentage of NO_x emissions. To meet the increasingly stringent emissions regulations that are designed to protect our health and environment, the combustion strategy can be altered to reduce NO_x emissions. The control of combustion-related NO_x begins with understanding the mechanisms involved in its formation. Because NO is the primary component of NO_x that is emitted during combustion, this section concentrates only on the NO formation mechanisms.

NO is formed via various pathways which include the fuel, thermal, prompt, and nitrous oxide mechanisms. The fuel-NO mechanism is associated with nitrogen-

bound fuels such as coal. Light distillates such as aviation and diesel fuels, with a nitrogen constituency of up to 0.06% (Lefebvre, 1999), can be assumed to contribute negligible levels of fuel NO in a gas turbine engine.

While fuel NO can be largely neglected for aviation gas turbines, the thermal, prompt, and nitrous oxide mechanisms are important in NO formation. The extent that the different mechanisms contribute to the overall NO formation can be gauged by a table presented by Bowman (1992) which summarizes the NO values obtained from various references. The table helps to show the conditions which favor a particular mechanism (e.g., the thermal mechanism dominating at conditions near $\phi=1$, the prompt mechanism occurring under fuel-rich conditions, the N_2O mechanism occurring under fuel-lean conditions). The following Sections 1.2.3a through 1.2.3c discuss these NO mechanisms in more detail.

1.2.3a Thermal Mechanism

The thermal-NO mechanism becomes predominant in reactions that attain temperatures around and above 1800 K (deNevers, 1995). Thermal NO contributes to a large portion of the overall NO levels in most conventional gas turbine combustors, where temperatures greater than 1800 K are likely to occur. The following reactions comprise the thermal-NO mechanism of Zeldovich (1946):



The extended Zeldovich mechanism includes the additional reaction



which becomes important in fuel-rich mixtures when O and O₂ concentrations are low. The first reaction in the extended Zeldovich mechanism (Eq. 1.13) is the rate-limiting step. In this step, a high activation energy is required to break the triple bond in the N₂ molecule.

The rate of formation of NO via the Zeldovich mechanism can be obtained using chemical kinetics, combined with steady state assumptions for the N-atom concentration and a partial equilibrium assumption for the O-atom concentration. The resultant equation for the rate of NO formation shows an exponential dependence on the combustion gas temperature, as well as a weak dependence on the ambient pressure and on the concentration of O₂ in the reacting flow (Bowman, 1992).

For conventional gas turbine combustors operating with a primary zone ϕ near 0.8, the thermal mechanism dominates NO formation. This is illustrated for a representative reacting condition in Fig. 1.3, where the left plot depicting the effect of ϕ on the adiabatic flame temperature shows temperatures greater than 1800 K occurring at values of ϕ near 0.8. The corresponding plot of the NO concentration formed under the same conditions (Fig. 1.3, right plot) follows the same general trend. The lower NO concentrations occur at fuel-lean ($\phi < \sim 0.6$) and fuel-rich (typically $\phi > \sim 1.7$, but occurs for $\phi > \sim 1.2$ in Fig. 1.3) conditions. Note that the peak temperature occurs near the stoichiometric $\phi=1$ condition while the peak NO concentration is shifted left of the stoichiometric condition, toward the fuel-lean side. The presence of superequilibrium

O and OH concentrations in flames at lean and near-stoichiometric conditions leads to the increased levels of NO formation that are observed here (Bowman, 1976).

Fig. 1.3 suggests that the combustor should be operated at very fuel-lean and/or very fuel-rich conditions to avoid high thermal NO production rates. Note that the combustion of fuel-air mixtures at these conditions does not necessarily produce lower NO levels, as any spatial or temporal unmixedness leading to the formation of stoichiometric fuel packets increases NO production. Hence, the goal of thermal NO control heavily depends on ensuring a fuel-air mixture that is entirely uniform in fuel-rich and/or fuel-lean composition.

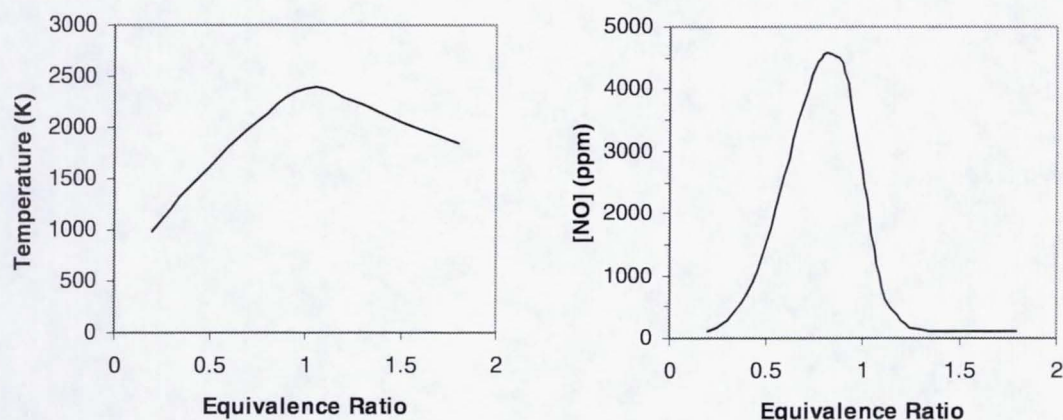


Fig. 1.3 Relationship between the equivalence ratio and the adiabatic flame temperature and NO_x emissions (output from equilibrium code of Gordon and McBride (1976), for a condition of 478 K air preheat, 298 K jet-A temperature, at 10 atm).

1.2.3b Prompt Mechanism

The prompt mechanism typically refers to the Fenimore (1971) mechanism, although references such as Bowman (1992) use the “prompt” classification to refer to NO formed at rates that are faster than that achieved for the thermal mechanism. According to the classical prompt mechanism of Fenimore (1971), NO is formed during the initial stages of combustion when hydrocarbon radicals or fuel fragments attack nitrogen molecules N_2 in the atmosphere. The following set of reactions describe the Fenimore prompt mechanism:



The N that is freed in reaction 1.16 participates in NO formation via reactions 1.14 and 1.15 from the Zeldovich thermal mechanism. In addition, NO is also produced by the reaction of O and O_2 with the CN molecule formed in reaction 1.17. Although the Fenimore prompt mechanism primarily dominates NO production under fuel-rich conditions, this mechanism cannot be neglected in lean premixed combustion (Nicol et al., 1995).

1.2.3c Nitrous Oxide Mechanism

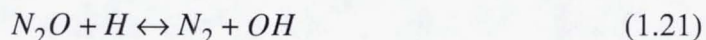
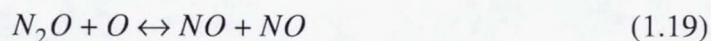
The contribution of the thermal NO mechanism to the overall NO production diminishes as lower temperatures are attained in lean-premixed combustion. At the same time, the decrease in reaction temperature, coupled with a low overall NO

formation rate, increases the importance of NO formation via the N_2O pathway in lean-premixed systems (Nicol et al., 1995).

For reaction temperatures less than 1500 K, Malte and Pratt (1974) proposed that the nitrous oxide (N_2O) pathway primarily contributes to the production of NO. N_2O that is formed by the reaction



subsequently participates in the following set of reactions that, in part, produces NO:



Nicol et al. (1995) compared the contribution of the thermal, prompt, and nitrous oxide pathways to the production of NO_x in lean-premixed combustion at gas turbine conditions. The study showed that each pathway could not be dismissed when assessing their contribution to the overall NO_x production levels. The nitrous oxide pathway, in particular, contributed to as much as 40-45% of the overall NO_x emissions at a pressure of 30 atm, and between 20-35% of the NO_x levels at a pressure of 10 atm. The nitrous oxide pathway was also responsible for producing up to 100% of the NO_x formed for concentration levels below 10 ppmv (parts per million by volume, on a dry, 15% O_2 basis). In relation to the fluid mechanics of the lean premixed combustion process, Nicol et al. (1995) recommended that the combustion flame zone be

minimized in order to decrease the exposure to the free radical concentration pools that lead to NO_x production.

1.3 Low- NO_x Combustion Concepts

Combustors utilizing low- NO_x emissions concepts operate at the low- NO_x producing lean or rich equivalence ratios, as shown in Fig. 1.3. The Rich-burn/Quick-mix/Lean-burn (RQL) concept initiates the combustion process under fuel-rich conditions, and upon the injection of air jets in a quick-mixing zone, transitions to complete the reactions in a fuel-lean stage. The fuel-rich combustion stage makes the RQL combustion concept inherently stable. However, such factors as the complexities associated with designing the quick-mix transition to prevent the formation of stoichiometric fuel-air packets, in addition to the long combustor length required to accommodate the quick-mixing section, have led to the trend of primarily running the combustors at lean equivalence ratios.

Combustors that solely burn fuel-lean provide low NO_x emissions, but are not without problems. For example, operating near the lean flammability limit runs the risk of combustor blow-out or combustor instability. In addition, the levels of carbon monoxide (CO), unburned hydrocarbons (UHC), and air toxics such as aldehydes and polyaromatic hydrocarbons (PAH) may increase to unacceptable levels. The ultra-lean-burning combustion method must overcome these challenges in order to become a viable technology.

The trend in low- NO_x combustion research has focused more on lean-burning technologies, which is evidenced by the large number of references associated with

lean-burning combustion, as compared to the RQL method. The methods associated with lean, low- NO_x combustion are first presented and are followed by a description of the fuel injector that serves as the basis for this dissertation.

1.3.1 Established Lean Combustion Technologies

The attainment of a lower level of NO_x production by lean-burning, stationary and aeroengine gas turbine combustors primarily depends on the preparation of the fuel-air mixture by fuel injectors. Fuel preparation is especially important for liquid fuels, which must be atomized in order to vaporize the fuel efficiently. The resultant mixture of fuel and air must be uniformly mixed, as NO_x production increases with fuel-air unmixedness in both spatial (Lyons, 1982; Zelina and Ballal, 1997) and temporal domains (Fric, 1993). Although the fuel-air mixture may be lean overall, a wide distribution of local equivalence ratios that bracket the stoichiometric condition will encourage thermal NO_x production.

Among the concepts being utilized and tested for lean-fired, low- NO_x combustors are the lean-premixed-prevaporized and the lean direct injection methods of fuel-air preparation. The lean-premixed-prevaporized (LPP) concept introduces a uniformly-lean mixture of fuel vapor and air into the dome region of a combustor, while lean direct injection (LDI) introduces the fuel directly into the primary combustion zone.

In the LPP combustor, low NO_x levels can be achieved by burning the fuel in its vapor phase rather than as droplets (Lefebvre, 1999). LPP combustion studies have utilized gaseous fuels (e.g., Nicol et al., 1995; Shih et al., 1996; Dutta et al., 1997) as

well as liquid fuels (Cowell and Smith, 1993) to successfully produce low NO_x levels. However, the premixed state of the fuel and air makes LPP combustion prone to autoignition and flashback. The stability limits of the LPP combustor also tend to fall in a narrow range. Noise levels increase with combustion instability if the level of fuel-air unmixedness is increased (Shih et al., 1996). The length required to fully vaporize and mix the fuel with the combustion air also lengthens the LPP combustor, which potentially makes the hardware challenging to retrofit.

The LDI combustion method has not been studied as extensively as the LPP application. In the limited tests that were reviewed by Tacina (1990), low NO_x levels as well as wider stability limits were observed with this system, but only for gaseous fuels. The LDI combustion concept has yet to be successfully proven with liquid-fired reacting tests.

1.3.2 Lean-Burn Injection

Another lean-injection strategy which combines elements from both the LPP and LDI concepts is the lean-burn injector. Developed and patented by Samuelsen et al. (1995), the lean-burn injector (LBI) consists primarily of a fuel-tube centerbody, a swirler, and a venturi mixing section that is also referred to as a "quarl." Jets of fuel spray are injected radially from the centerbody, and transversely into a swirling crossflow of air (see Fig. 1.4). The fuel sprays mix with the swirling air in a mixing chamber formed by the contracting venturi section. The partially- or fully-vaporized fuel-air mixture is subsequently ejected out of the venturi section and into the primary dome of the combustor. The swirling component in the fuel-air mixture induces the

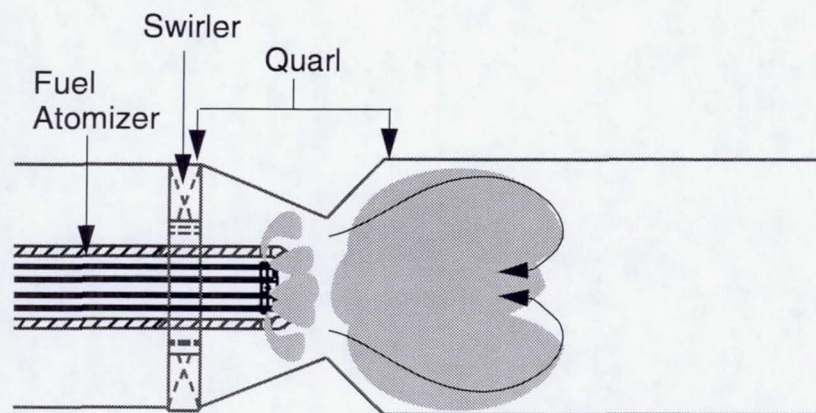


Fig. 1.4 Combustor utilizing the Lean Burn Injection (LBI) concept.

recirculation zone that anchors the combustion process, which is maintained as long as a flammable mixture of fuel and air is supplied. As noted by Shaffar (1993), combustion stabilizes downstream of the venturi throat, which is incorporated in the design to prevent flashback.

The overall product of the LBI is the direct injection into the reaction zone (as in the LDI concept) of a partially- or fully-vaporized fuel-air mixture (as in the LPP concept). The concept has been proven to achieve low NO_x production at an elevated pressure and temperature condition (Shaffar and Samuelsen, 1998). The success of the LBI injector depends on the atomization and dispersion of the jet of liquid fuel into the swirling crossflow of air. Though the mixture may be overall lean, a wide distribution of local equivalence ratios in the volume will encourage thermal NO_x production. Thus, the final dispersion of the droplets is important, as the subsequent vaporization of the fuel and its mixing with the air will affect the combustion performance.

Twin-fluid atomization—more specifically, airblast atomization—produces the initial spray in the LBI, while the dynamics of the liquid jet injection into a crossflow either produces additional atomization, affects droplet penetration, or contributes to both. The choice of the airblast atomization method becomes inherent after considering other types of atomizers such as those that employ liquid pressure-based and high air pressure-assisted methods.

Pressure atomizers, such as a swirling simplex atomizer or a plain orifice, are simple to operate because the only flow parameter that is adjusted is the flow rate of fuel through the atomizer. Atomization is governed by the pressure drop of the fuel across the injector, which is proportional to the square of the fuel velocity. This very same feature exposes the main drawback of pressure atomizers: an increase in fuel flow rate by some factor requires a (factor)² increase in the fuel pressure drop (Lefebvre, 1999). A high fuel pressure drop is undesirable because of the complication and expense associated with using pumps to achieve the supply pressure.

Atomizers that use a second fluid to perform a bulk of the atomization process can attain a higher turndown ratio of maximum to minimum fuel flow rates. Twin-fluid atomizers such as the air-assist and airblast methods also do not require a highly-pressurized fuel supply. As their names imply, air-assist and airblast atomizers utilize a flowing stream of air to generate the shear force that initiates atomization. The difference in the two methods lies in the means by which the air is supplied to the atomizer. Air-assist atomizers utilize low flow rates of highly-pressurized air to induce atomization, while airblast atomizers require high flow rates of air at a lower pressure. In aircraft engine applications, airblast atomizers become the more practical choice

because the low air supply pressures needed by the atomizers fit the operating conditions of the aircraft engine, which typically can only supply air at pressure drops ranging between 4% and 7% (Lefebvre, 1999).

Airblast atomization can be applied to either a liquid sheet or jet. During the development of the LBI, Shaffar (1993) tested the performance of fuel injectors that implemented airblast atomization of either a liquid sheet or of liquid jets in a radially-injecting centerbody. Although the intent behind the liquid sheet injector was to enhance atomization by increasing the surface area of liquid available for perturbation by the atomizing air, its atomization performance in the radial injection design was poorer than that obtained from the discrete jet injector. In addition, the lower atomizing air pressure drops, as well as a simpler design that was conducive to low-cost manufacture, led Shaffar (1993) to favor the radial-jet fuel injector that incorporated a plain-jet airblast atomizer design similar to that used by Nukiyama and Tanasawa (1939).

1.4 Statement of the Problem

Fuel preparation by the injector affects the combustion performance of the gas turbine combustor. Hence, an understanding of the combustion performance of the LBI begins with an investigation of the spray behavior under operating conditions representative of practical systems. To fulfill this goal, the present research focuses on investigating the dispersion characteristics of the single spray jet in the LBI (see Fig. 1.5) so that the important geometric and flow parameters are isolated.

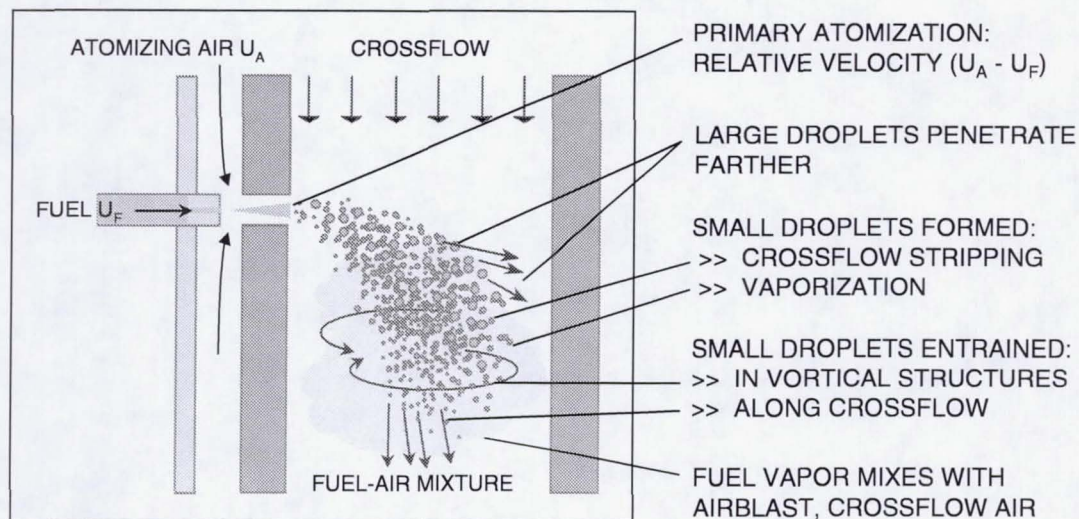


Fig. 1.5 Single spray jet in crossflow modeled after the LBI.

A single spray jet of the LBI is modeled as the injection of a fuel spray into a crossflow of air. The fuel spray is produced by airblast atomization, which involves the use of co-flowing air to induce liquid jet atomization. Rapid mixing is achieved by injecting the fuel transversely into, as opposed to coaxially with, the mainstream of air. In addition, injecting the fuel as a spray rather than as a discrete jet reduces the mixing length otherwise needed to break up a pure liquid jet. The momentum from the atomizing air aids in the penetration of the spray into the crossflow.

The spray jet in crossflow involves an interaction between the atomizing air and liquid fuel to create the spray, as well as an interaction between the droplets, atomizing air, and crossflow air that results in spray dispersion and additional atomization by the crossflow. The dynamics and interaction between the spray jet and crossflow offer the potential of adjusting jet penetration and droplet dispersion to provide optimal

performance across the entire duty cycle of the engine. An investigation determining how the spray jet interacts with the crossflow as well as how the different flow and geometric parameters affect this interaction will help in developing relationships that can be correlated with combustion behavior and used to help design future injectors.

1.5 Goals and Objectives

The primary goals of this dissertation are (1) to characterize the atomization and transport processes that determine the dispersion of an airblast-atomized spray jet into a subsonic, high velocity crossflow of air, and (2) to gain an understanding of these processes and their effect on the penetration and dispersion of the airblast-atomized spray jet in a crossflow of air.

The objectives that were established to meet the goals of the research problem include:

- A literature review related to the atomization and transport of the spray jet dispersion into a crossflow (Chapter 2).
- Modifications made to the experimental hardware to facilitate its installation and to enable additional optical access for planar characterization studies (Chapter 4).
- The development of a planar imaging diagnostic to capture the distributions and extent of the liquid and atomizing air components in the airblast-atomized spray (Chapters 5 and 6).
- The characterization of the airblast spray without a crossflow of air (Chapters 7 and 8).
- The characterization of the airblast spray into the crossflow (Chapters 9 and 10).

- The development of analyses to assess the effect of different spray parameters on the dispersion of the spray (Chapters 7 and 8), as well as models to predict the trajectory, dispersion, and atomization quality of the spray in the crossflow (Chapters 9 and 10).

The structure of the rest of the dissertation closely follows this outline of the objectives.

CHAPTER 2

BACKGROUND: ATOMIZATION AND TRANSPORT PROCESSES RELATED TO THE SPRAY JET IN CROSSFLOW

The jet in crossflow problem has been studied by researchers because of its wide application in such systems involving and including pollutant dispersion, jet mixing in the dilution zone of combustors, and fuel-injection strategies. Gaseous jet mixing in a crossflow has been extensively studied, as noted in the number of papers summarized by Holdeman (1993), in addition to recent studies by Zaman and Foss (1997), Smith and Mungal (1998), and Yuan and Street (1998). The injection of a liquid jet into a crossflow has also been widely studied because of its application as a fuel injection strategy in rocket, ramjet, scramjet (supersonic combustion ramjet), and gas turbine combustors. These applications have served as the impetus for studies on the breakup and dispersion of the liquid jet in supersonic crossflows (e.g., Schetz et al., 1980; Heister et al., 1989; Li and Karagozian, 1992) as well as in subsonic crossflows (e.g., Schetz and Padhye, 1977; Wu et al., 1997, 1998). The injection of a liquid jet into a crossflow is similar to the gaseous jet problem, but with the added complications associated with liquid breakup processes.

The research problem that is the focus of this dissertation involves the investigation of the dispersion of an airblast-atomized *spray jet* into a crossflow. The spray jet differs from the pure gas or the pure liquid jet in that it is composed of atomized liquid particles in the form of ligaments and droplets that are carried along in

a gaseous stream of co-flowing air. The air in the spray jet is either entrained from the surroundings by the moving droplets (Ghosh and Hunt, 1994), or is directly used to atomize the spray, as in the airblast atomization process that is the subject of this work.

A literature search yielded several studies that investigated the dispersion of sprays injected into a crossflow (e.g., Chin et al., 1986; Ghosh and Hunt, 1998). However, these studies did not consider sprays formed with the assistance of air. Studies related to the particle-laden gaseous jet can also provide insight into the dispersion of the spray injected into a crossflow. Still, studies such as those performed by Edelman et al. (1971), Salzman and Schwartz (1978), and Han and Chung (1992), characterized the dispersion of uniformly-sized particles, and the results do not truly represent the multi-sized droplet distributions typically found in sprays.

Despite the lack of literature specifically associated with the injection of a spray formed by twin-fluid atomization into a crossflow of air, an introduction to the formation and dispersion processes involved in the system can also be obtained by reviewing literature related to (1) plain-jet airblast atomization, and (2) liquid jet injection into a crossflow, since the airblast-atomized spray jet in crossflow system is envisioned as a combination of both systems (see Figure 2.1).

The first section of this chapter briefs the reader with spray-related terminology used in literature as well as in this dissertation. A review of the literature associated with the atomization of the plain liquid jet, with and without the assistance of air, and injected into either a quiescent atmosphere or into a crossflow, subsequently follows. The chapter then concludes with a review of literature associated with spray and particle-laden jets in a crossflow.

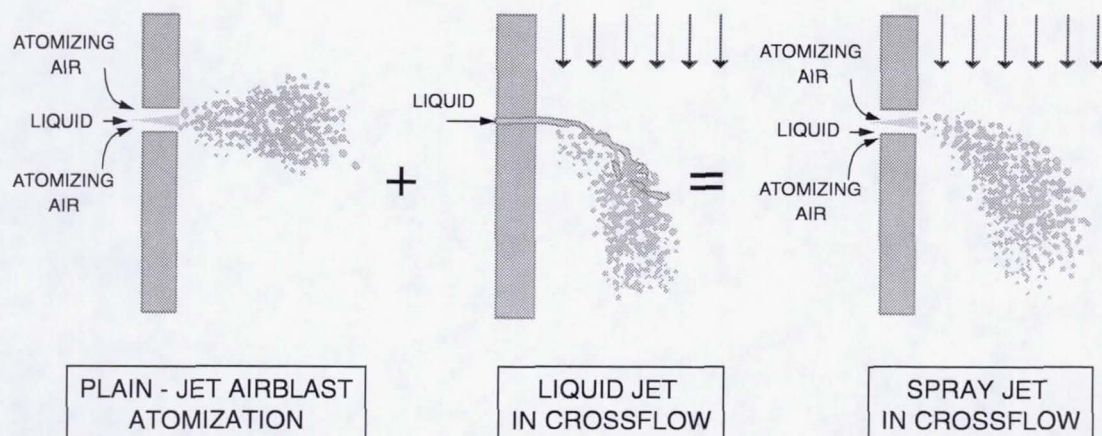


Fig. 2.1 Decomposition of the spray jet in crossflow problem.

2.1 Basic Definitions Related to Atomization

The purpose of this section is to provide the reader with several definitions that are used to characterize the spray in terms of (1) the tendency to break up and follow the surrounding flow, based on dimensionless numbers, and (2) representative droplet size (using the D_{ab} -defined values). These terms will be referred to throughout the course of the dissertation.

2.1.1 Relevant Dimensionless Numbers

A liquid can be atomized through various means, but the common denominator in all atomization processes is the need for a disturbance which induces the instabilities in the liquid that lead to breakup. A twin-fluid atomizer such as the LBI employs a high velocity airblast stream to create instabilities in the co-flowing fuel stream. In addition, the liquid and ambient air properties also dictate liquid atomization. The

viscosity, μ_L , causes the liquid to resist the development of instabilities, while the surface tension, σ , causes the liquid to resist changes that increase its surface area. The surface tension can act to either stabilize a two-dimensional sheet by retarding distortions, or can cause a liquid jet to pinch off into a spherical form, which is a shape that requires the least amount of energy to sustain (Lefebvre, 1989). Atomization also depends on the pressure and temperature of the ambient air into which the fuel is injected, because of their effect on the aerodynamic force imparted on the liquid.

For liquids of low viscosity, such as fuels used in aeroengine applications, the main factors affecting liquid breakup in an airstream are the surface tension and the aerodynamic force. Tying these two forces together into a dimensionless number yields the Weber number

$$We = \frac{\rho_A U_R^2 d_0}{\sigma} \quad (2.1)$$

which is a ratio of the force related to the dynamic pressure $(\rho_A U_R^2)/2$, and the surface-tension force related to σ/d_0 . The dynamic pressure is derived from the density of the air ρ_A and the relative velocity U_R between the atomizing air and fuel streams. The characteristic dimension d_0 can refer to either the droplet diameter or the exit diameter of a plain-jet fuel injector.

The Weber number describes the tendency of a liquid or droplet to break up. High We values indicate a high likelihood of liquid breakup occurring. A critical We , attained when the aerodynamic drag force imparted by the ambient environment on the liquid equals the forces related to the surface tension of the liquid, can be determined for different systems. The critical We for a droplet can be derived, as shown by

Lefebvre (1989), by first equating the aerodynamic drag to the surface tension force such that

$$\frac{1}{2}\rho_A U_R^2 A_d C_D = \sigma s \quad (2.2)$$

where A_d , the projected area of the spherical droplet, is equal to $(\pi d_0^2)/4$, C_D is the droplet drag coefficient, and s , the circumference through which the surface tension force acts to keep the droplet intact, is equal to πd_0 . Upon the rearrangement of terms and a substitution of the definition of the Weber number from Eq. 2.1, Eq. 2.2 becomes

$$We_{critical} = 8/C_D \quad (2.3)$$

The maximum stable drop size d_{max} and the critical relative velocity $U_{R,critical}$ leading to droplet breakup are then derived as follows:

$$d_{max} = \frac{8\sigma}{C_D \rho_A U_R^2} \quad (2.4)$$

$$U_{R,critical} = \sqrt{\frac{8\sigma}{C_D \rho_A d_0}} \quad (2.5)$$

While the Weber number takes into account the forces related to the liquid surface tension, the Ohnesorge number Oh gauges the effect of the liquid viscosity in opposing atomization. The Ohnesorge number represents a ratio of the viscous to surface-tension forces in the liquid, and is defined as

$$Oh = \frac{\sqrt{We}}{Re_L} = \frac{\mu_L}{\sqrt{\rho_L \sigma d_0}} \quad (2.6)$$

where Re_L , the Reynolds number, is

$$Re_L = \frac{\rho_L U_R d_0}{\mu_L} \quad (2.7)$$

for a liquid jet injected into an air flow.

These dimensionless numbers can be used to map the different breakup regimes of the liquid jet. For instance, Reitz (1978) classifies the liquid jet breakup modes on a chart of Oh versus Re_L (with subscript “L” referring to the liquid properties), while Faeth (1990) depicts the breakup regimes on a chart with axes of Oh versus We_g (with subscript “g” referring to the ambient gas properties). Maps of the breakup regimes for the liquid jet, using these parameters, are presented later in Section 2.2.1.

The motion of the droplets in the sprays is governed by the momentum of the droplets as well as of the surrounding flow. The Stokes number, St , determines the tendency of a particle to be affected by the flow by comparing the time scales between the particle response time, τ_p , and the characteristic time scale, τ_c , of the surrounding flow. In general form, the Stokes number is expressed as

$$St = \frac{\tau_p}{\tau_c} \quad (2.8)$$

For $St \ll 1$, the time that the particle takes to respond to the flow is much less than the characteristic time of the flow, and the particle will tend to follow the flow.

The particle response time is obtained by determining the relaxation time of the particle, which is the time that the velocity of a particle decreases by a factor of $(1/e)$.

The particle response time is derived and given by

$$\tau_p = \frac{4d_p \rho_p}{3C_D \rho_g U_R} \quad (2.9)$$

(Bachalo, 1994) where the subscript p refers to the properties of the particle, and where the other variables are previously defined. The drag coefficient C_D is obtained by using the applicable equations for the particle Reynolds number Re_p . For example, for $Re_p \ll 1$, the Stokes drag law of $C_D = 24/Re_p$ can be substituted into Eq. 2.9 to yield

$$\tau_p = \frac{d_p^2 \rho_p}{18\mu_g} \quad (2.10)$$

which shows that at low Reynolds numbers the response time of the particle is directly proportional to the square of the particle diameter.

The characteristic time is defined by the flow scale of interest. For a flow with a characteristic fluid velocity U and a characteristic length scale L , the characteristic time scale is $\tau_c = L/U$, and the Stokes number becomes (Seinfeld and Pandis, 1998):

$$St = \tau_p \cdot \frac{U}{L} = \frac{d_p^2 \rho_p U}{18\mu_g L} \quad (2.11)$$

2.1.2 Representative Drop Diameters

The atomization quality of a spray can often be conveniently characterized by representative drop diameters. In a generalized case, the definitions of representative diameters, developed by Mugele and Evans (1951), can be obtained from the following expression

$$D_{ab} = \left[\frac{\sum n_i d_i^a}{\sum n_i d_i^b} \right]^{\frac{1}{(a-b)}} \quad (2.12)$$

where d_i refers to the droplet size bin label in a histogram with i number of bins, and n_i refers to the number of droplets in the size class. The indices a and b in the subscript notation D_{ab} correspond to the power to which d_i is raised in the numerator and denominator, respectively. The $1/(a-b)$ power on the right hand side of the definition forces the expression to conform to the dimensionally correct unit of length.

The arithmetic mean droplet size, D_{10} , which simply divides the sum of all droplet sizes by the total number of drops, offers one measure of the average droplet size. However, other representative droplet size definitions often provide more useful information. The oft-utilized definitions include D_{20} , the “surface area mean diameter;” D_{30} , the “volume mean diameter;” and D_{32} , which is also referred to as the Sauter Mean Diameter (*SMD*).

In spray combustion, the mass transfer of fuel from liquid to vaporized state is of primary interest. The surface area of a spray is an important parameter to consider in this case, as droplet vaporization increases exponentially with a decrease in droplet size, in accordance with the D^2 law for droplet vaporization. D_{20} and D_{32} , which are both functions of the droplet surface area (D^2), are relevant values in combustion. However, the question as to which droplet definition— D_{20} or D_{32} —is most relevant in evaporating fuel sprays, was answered in an analysis performed by Sowa (1992), which referred to the statistical bases behind the descriptions for D_{20} as well as D_{30} .

By correlating distribution moments to the D_{ab} definitions that were applied to spray data, Sowa (1992) found that D_{20} represented the second moment—an indicator of spread about the mean—of a number-weighted diameter distribution. Likewise, D_{30} represented the third moment, or the skewness, in the diameter distribution. In addition, Sowa (1992) verified that D_{32} best represented the surface area mean diameter in both a statistical sense and in data which showed the D_{32} corresponding to the centroid of a surface-area weighted diameter distribution. Because fuel spray applications have traditionally reported mean droplet sizes as D_{32} , this dissertation follows the same convention in reporting the results.

Because droplet size distributions can be measured at different points in space, an individual D_{32} value can be determined at each point. If data are taken along an axis of the spray, a line-averaged D_{32} can be calculated. Similarly, a plane-averaged D_{32} can be obtained across a grid of data.

2.2 Liquid and Spray Injection into a Quiescent Atmosphere

The atomization of a liquid jet occurs when the relative velocity between the injected liquid and the surrounding gas medium induces instabilities that lead to breakup. The liquid jet can be injected into a gaseous medium that is either quiescent, co-flowing, or cross-flowing with respect to the jet.

The LBI injector incorporates co-flowing air and fuel at the injector tube to induce liquid atomization, and subsequently injects the liquid-air spray mixture into cross-flowing air to additionally atomize the spray (given conditions conducive to breakup), and to rapidly mix the spray with the air flow. Hence, the LBI injection

scheme combines two problems, as illustrated in Fig. 2.1: (1) spray formation from a round liquid jet and (2) jet injection into a crossflow. The rest of this section addresses the first problem—the formation of the spray jet—with a review of research performed on the atomization of liquid jets injected with and without the assistance of a co-flow of air.

2.2.1 Liquid Jet Atomization

When a round liquid jet enters a still gaseous environment (see Fig. 2.2), the coherency of the jet mainly depends on the balance between the surface tension and inertia of the liquid. At low jet velocities in which the surface-tension force is dominant, capillary waves which result from this force and which are decoupled from the surrounding gas induce instabilities that cause the jet to break up. A subsequent transition in breakup modes (depicted in Fig. 2.3) occurs when the influence of the dynamic pressure of the ambient gas is increased with an increase in the jet velocity.

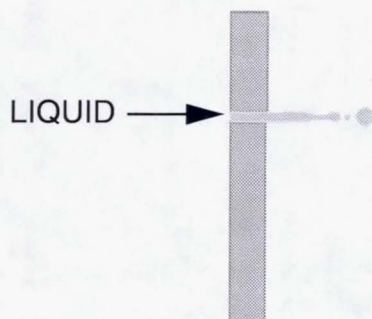


Fig. 2.2 Liquid jet breakup (without airblast air) in a quiescent environment induced by capillary instabilities that are decoupled from the surrounding gas.

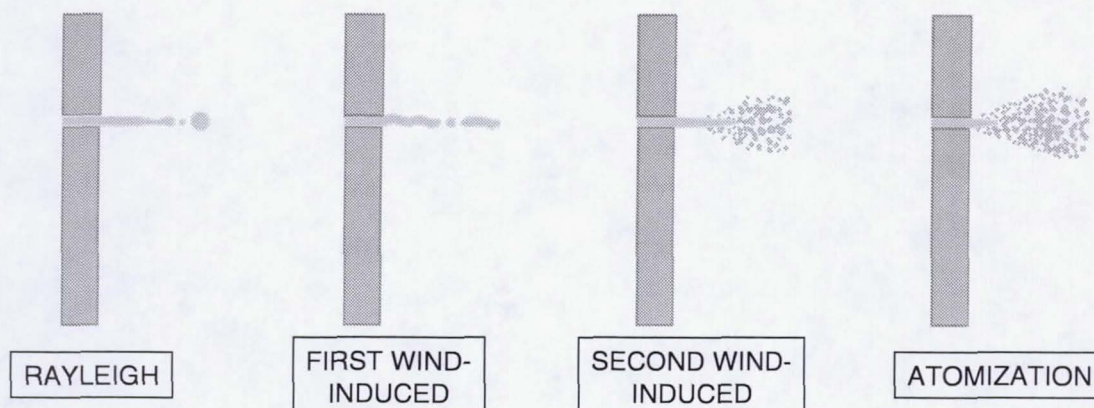


Fig. 2.3 Different regimes of jet disintegration in a quiescent environment. (Faeth, 1990).

The first stage of jet breakup, attributed to the *Rayleigh instability mode*, is caused by an axisymmetric disturbance related to the surface-tension force that leads to the growth of the capillary wavelengths in the jet. When the wavelength grows larger than the jet diameter, the fluid breaks off. In this regime, the droplets that are formed are nearly twice the diameter of the jet.

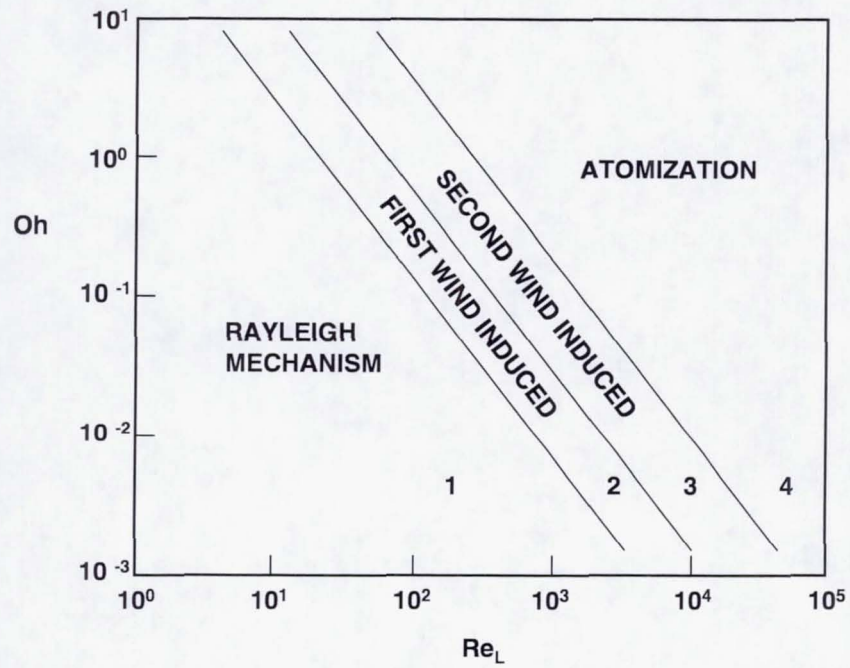
An increase in jet velocity leads to the *first wind-induced regime*. In this regime, frictional and pressure forces between the jet surface and the surrounding gas cause oscillations which produce a gross twisting effect on the liquid column that later leads to the formation of droplets with sizes on the order of the jet orifice diameter. The distance from the orifice to the initial breakup point is less than that produced by the Rayleigh mode. A further increase in jet velocity leads to the *second wind-induced regime*, which forms a wide droplet distribution ranging from small droplets obtained

from surface breakup to large droplets approaching the size of the jet diameter. The distance to the onset of liquid breakup continues to decrease as jet velocity increases. When the onset of liquid breakup begins to occur at the jet exit, the *atomization regime* is attained. The atomization regime consists of fine droplet sizes, most of which are produced by surface breakup rather than jet fracture.

The occurrence of these four modes are shown in breakup regime maps such as those presented in Fig. 2.4. In general, an increase in Re_L and We_g leads to transitions tending toward the more dynamic breakup regimes. For a constant Re_L , an increase in Oh causes the jet to transition to higher-order breakup mechanisms (Fig. 2.4a). For a constant We_g , the jet does not tend to undergo changes in mechanisms with respect to Oh (Fig. 2.4b).

Reitz and Bracco (1982) reviewed five mechanisms which researchers have attributed to jet breakup in the atomization regime (the fourth regime). The most widely-known and developed mechanism is the liquid-gas interaction which causes wave instability on the jet surface. The equation resulting from the wave stability analysis on the surface of an infinitely long cylinder describes the relationship between the growth rate of the wave and its wavelength. The Rayleigh condition describing the liquid breakup for low-velocity, inviscid jets is one limiting case of this equation, if the gas density, liquid viscosity, and initial jet velocity are set to zero. The other limiting case, which is in the atomization regime, involves droplet sizes that are considerably smaller than the jet diameter. The Taylor solution for the wave growth on the surface of an infinitely deep viscous fluid applies to this scenario.

(a)



(b)

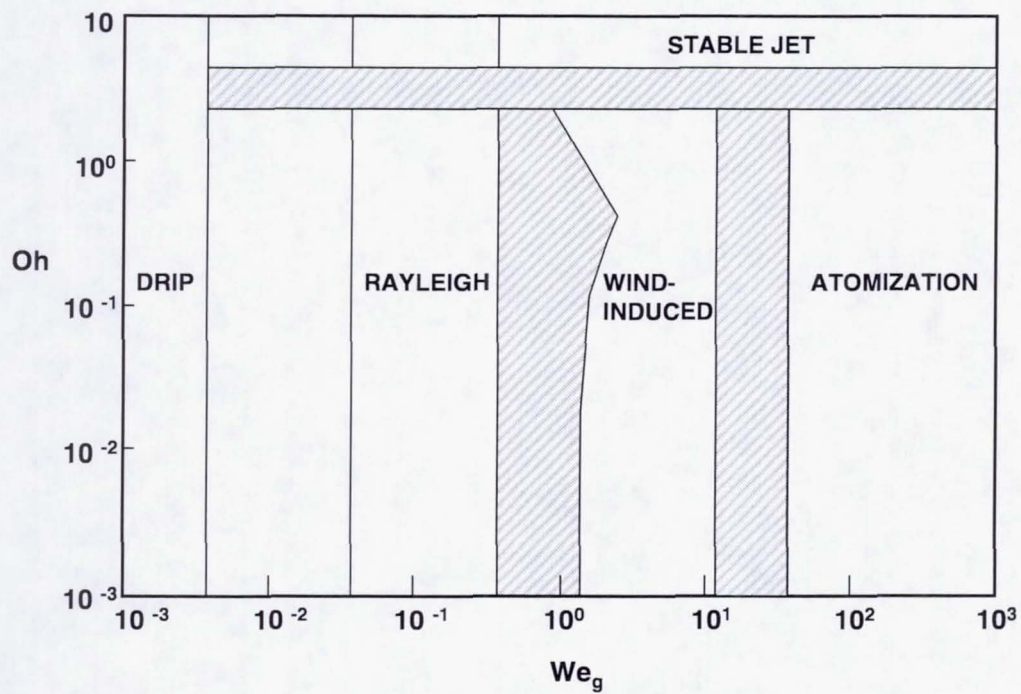


Fig. 2.4 Liquid jet breakup regimes, mapped on (a) Oh vs. Re_L axes (Reitz, 1978), and (b) Oh vs. We_g axes (Faeth, 1990).

The other breakup mechanisms for liquid jet atomization that were covered by Reitz and Bracco (1982) included such effects as the turbulence of the liquid, the change in the jet velocity profile as the jet exits the injector, cavitation, and the unsteadiness in the liquid supply pressure. Though not as extensively studied, these suggested mechanisms are plausible, depending on the injector design and flow rates. In their study, Reitz and Bracco (1982) tested fourteen different nozzles of different geometrical inlets and l/d ratios, at varying liquid viscosities, liquid injection pressures, and ambient gas densities. The results of their study, when compared with the different proposed atomization mechanisms, indicated that no single mechanism could solely account for the atomization trends that were observed in the tests. Rather, Reitz and Bracco (1982) found that a combination of the aerodynamic interaction with the other mechanisms should sufficiently fit their results.

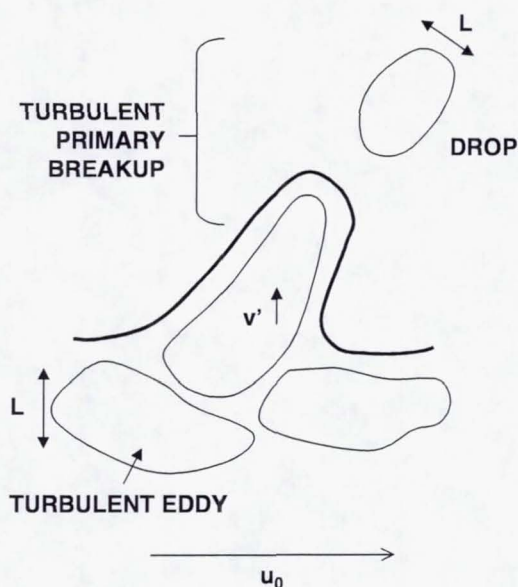


Fig. 2.5 Turbulent primary breakup at the liquid surface. (Wu et al., 1995)

The mechanism behind the surface breakup of a jet in quiescent gas has also been modeled by Wu et al. (1995) in order to obtain an expression for the D_{32} distribution. Droplets are formed from turbulent eddies generated by the relative gas-liquid velocity at the interface (see Fig. 2.5). The sheared droplet moves with a velocity equal to the relative cross stream to liquid velocity and has a size on the same order as the length scale of the turbulent eddies.

2.2.2 Plain-Jet Airblast Atomization

The process of airblast atomization involves the use of two fluids (Fig. 2.6). The liquid jet is forced to break up because of the shear forces caused by a high velocity stream of co-flowing air. The advantages of airblast atomization in gas turbine applications include such factors as requiring lower pressures to deliver the fuel, and accomplishing partial premixing of the air and liquid fuel prior to mixing with the bulk air flow for combustion (Lefebvre, 1989).

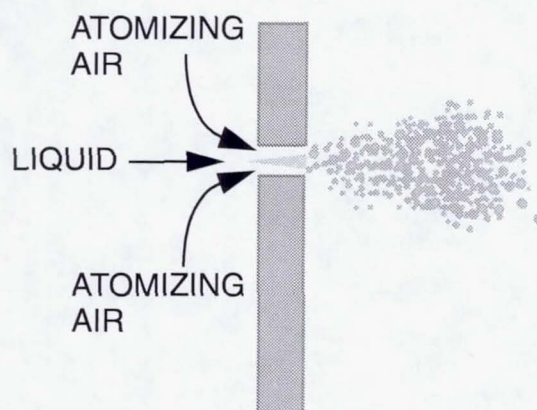


Fig. 2.6 Atomization of a liquid jet with the aid of a co-flowing air stream.

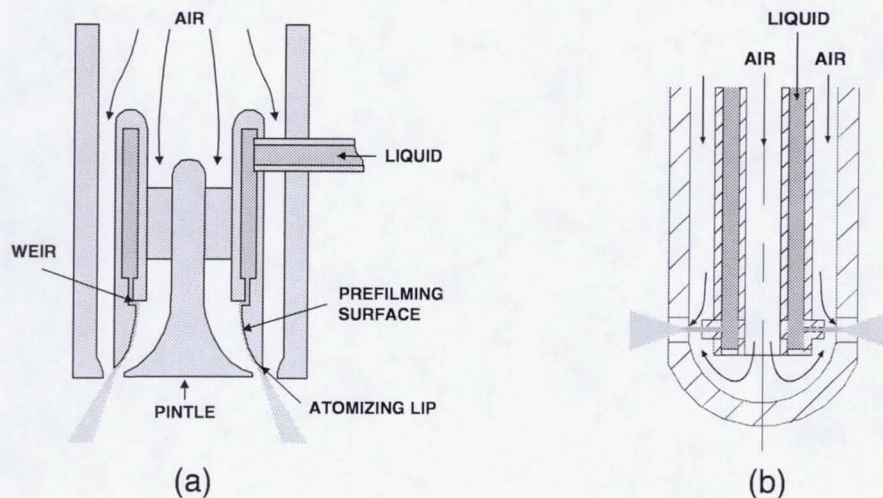


Fig. 2.7 Comparison between (a) a prefilming airblast atomizer (Lefebvre, 1999), and (b) the plain-jet airblast atomizer in the LBI.

Airblast atomizer designs fall into two categories: those that spread the liquid into a thin sheet, and those that inject the liquid as a discrete jet. In both cases, the atomizing air is introduced such that the air flows over the exposed sides of the liquid stream. Thin-sheet airblast atomizers involve a complicated design to ensure that the delivered air flows over both sides of the sheet. On the other hand, the plain-jet airblast atomizer is easier to fabricate because of its simpler design. Figure 2.7 depicts representative schematics of both types of atomizers for comparison.

The introduction of a co-flowing stream of air with the liquid jet induces additional atomization regimes, as documented by Chigier and Reitz (1996). The moving air stream imparts momentum onto the surface of the liquid jet. The large-scale eddy structures formed by the air stream cause the jet to distort and destabilize,

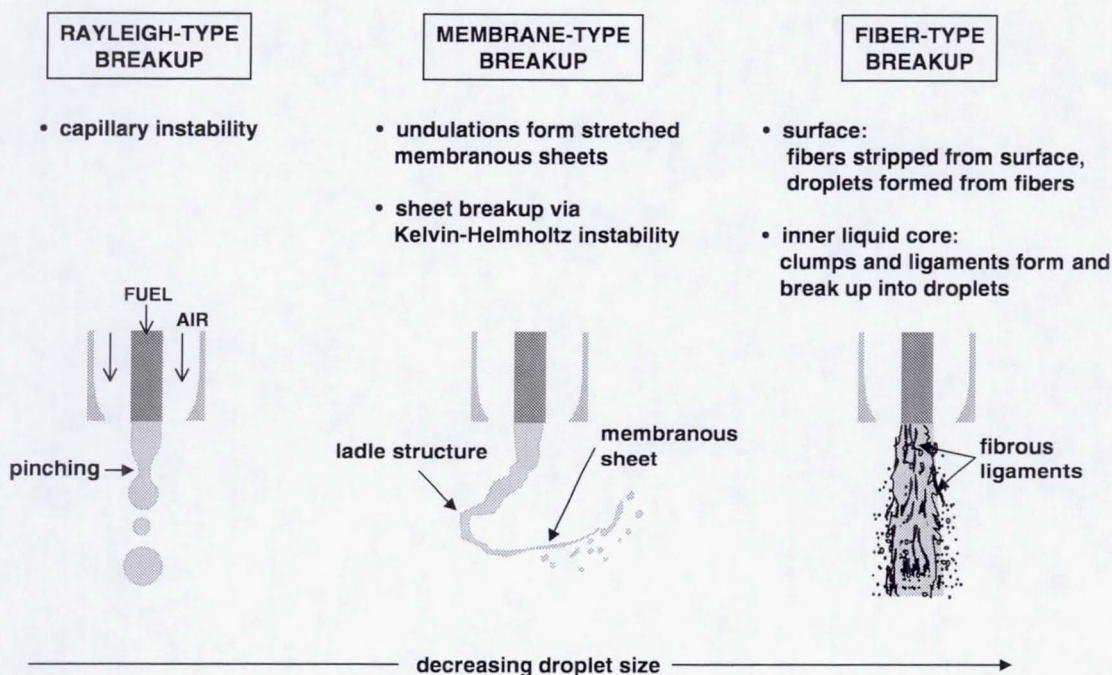


Fig. 2.8 Illustration of the different breakup modes described by Farago and Chigier (1992).

resulting in an undulating motion of the jet during breakup. From a compilation of spark photographs, Farago and Chigier (1992) formed three main categories and several subcategories to classify atomization of a water jet by a co-flowing air stream. The three main categories (pictured in Fig. 2.8), along with the Weber number range that characterizes each mode, are: (1) Rayleigh breakup, which is further subdivided into an axisymmetric mode ($We_g < 15$) and nonaxisymmetric mode ($15 < We_g < 25$), (2) atomization formed from membrane-type ligaments ($25 < We_g < 70$), and (3) atomization from fiber-type ligaments ($100 < We_g < 500$). The Rayleigh breakup mechanism was discussed in Section 2.2.1. In the second category of liquid jet breakup

in co-flowing air, the membrane-type ligaments form when the jet stretches into a thin sheet. The membranous sheet subsequently breaks up due to the Kelvin-Helmholtz instability. This instability occurs at the interface of two co-flowing fluids of different densities and velocities (Kundu, 1990). In the third mode, thin, thread-like fibers are formed as they are shed from the jet surface, which subsequently break up via the Rayleigh mechanism. Because the fiber structures are smaller than the membrane-like ligaments, the secondary breakup of the fibers result in smaller drops that are analogous to the size of the drops formed via the second-wind induced and atomization mechanisms for the plain liquid jet in quiescent air. While the fiber-type ligaments are shed from the jet surface, the liquid core accelerates and fragments into large ligaments that in turn, break down further via either of the three breakup mechanisms outlined in Fig. 2.8.

Over the ranges of Reynolds and Weber numbers tested, Farago and Chigier (1992) formed a regime map of Re_L vs. We_g plot which indicated the regions for which the different atomization modes occurred. The chart in Fig. 2.9 shows the three main regimes of Rayleigh, membrane-type, and fiber-type breakup, as well as a superpulsating submode. This submode which is induced when either the liquid Reynolds number is decreased, the aerodynamic Weber number is increased, or a combination of both events occur, as in the instance when the liquid flows with an atomizing air flow rate that is high enough to trigger the event.

The breakup process of the liquid jet injected with a coaxial flow of air has been modeled empirically by Yatsuyanagi et al. (1998). The authors developed a one-dimensional model that accounted for the primary and secondary breakup of the liquid

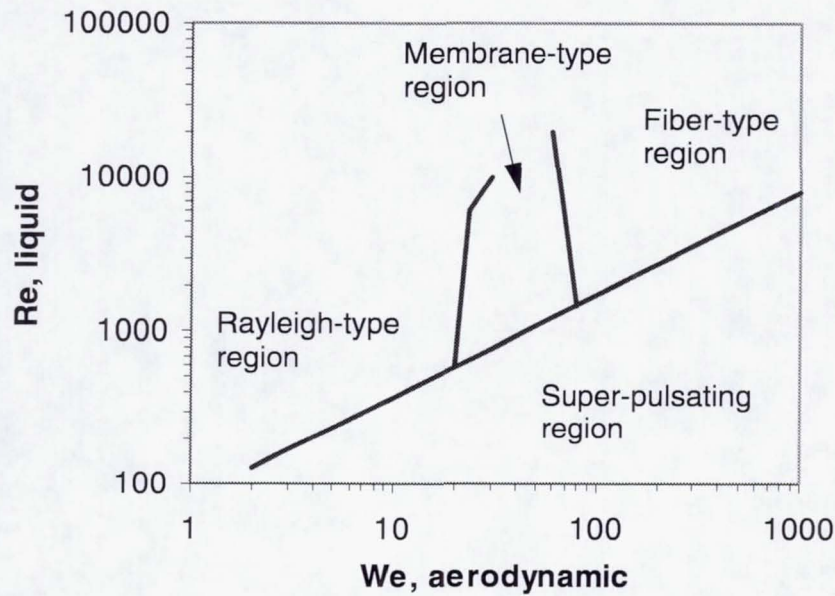


Fig. 2.9 Mapping of the breakup regimes for a water jet with a co-flowing air stream (Farago and Chigier, 1992).

jet. Droplets formed during the primary breakup of the jet originate from a disturbed layer formed by the air-liquid interaction on the jet surface, as in the fiber-type atomization mode described by Farago and Chigier (1992). The secondary breakup of the droplets produced in the primary breakup stage is determined by the critical Eötvös number

$$Eo = \frac{a}{g} \cdot \rho_L \cdot \frac{D_{32}^2}{\sigma} \quad (2.13)$$

which dictates the droplet size in relation to the droplet acceleration a , the gravitational acceleration g , the liquid density ρ_L and surface tension σ , and the spray D_{32} . The critical Eötvös number supplied from the researchers' previous experiment was used to

calculate the droplet size during its acceleration. The net result of modeling both breakup processes was a droplet size distribution that was satisfactorily compared with experimental data.

In a summary of twin-fluid atomization, Lefebvre (1992a) detailed the effects of various liquid and air properties on this type of atomization process. Although most of the discussion was derived from results obtained for thin-sheet airblast atomizers, the basic premises also hold for plain-jet airblast atomizers.

Lefebvre (1992a) reiterated the notion that the predominant factor affecting airblast atomization is the relative velocity of the air to fuel streams, U_R . This difference in velocity accounts for the forces at the liquid and air interface which lead to liquid breakup. The magnitude and component of the air stream dictates the method of atomization: liquid breakup can occur through either the classical wave instability mechanism or through prompt atomization. When the air travels in the same direction as the liquid (i.e., when the fuel and air streams are co-flowing), or when the time scale of the breakup process is relatively long (e.g., when the atomizing air velocity is low), the liquid breaks up by the classical method because there is enough time for wave instabilities to develop. For instances in which the time scale is too short for the classical breakup mechanism to develop, such as when the injector geometry induces air impingement on the liquid stream, or when the relative velocity of atomizing air to liquid is high enough, the "prompt" atomization mechanism dominates.

Depending on the regime of operation, Lefebvre (1992a) mentioned that it is possible to have both mechanisms occurring. For example, during the initial start-up period, a high, negative relative velocity resulting from liquid velocities that are higher

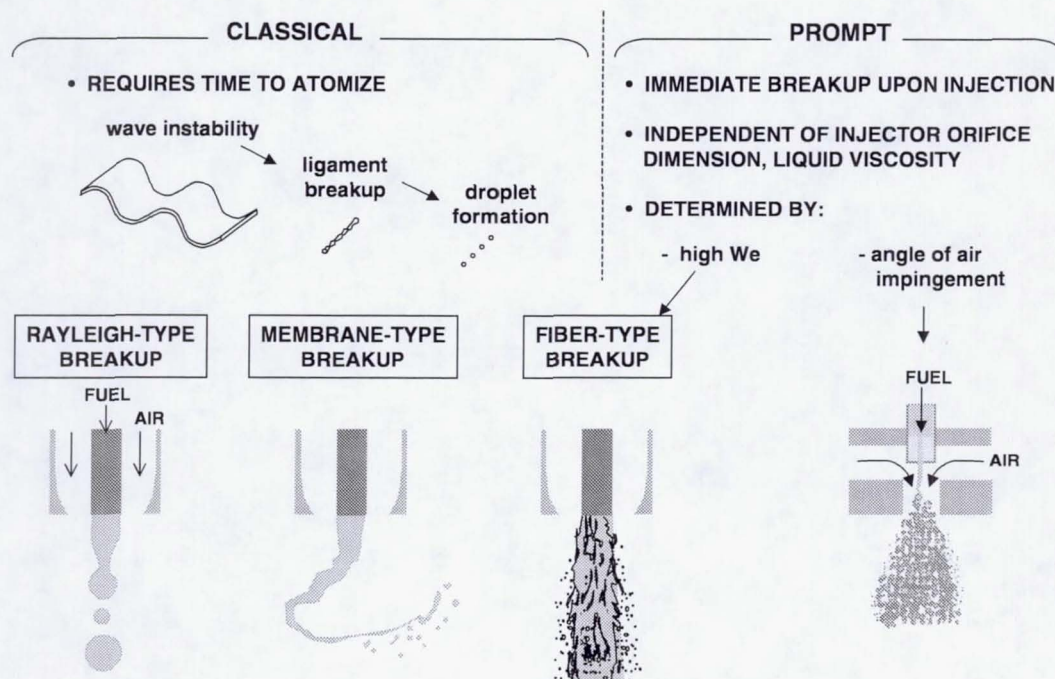


Fig. 2.10 Comparison between classical and prompt breakup modes in an airblast-atomized spray.

than the atomizing air velocities consequently causes the wave instability mechanism to ensue. An increase in the atomizing air flow increases the degree of jet disintegration, as seen in the different modes of breakup described by Farago and Chigier (1992) (refer to the three sketches of the breakup modes in Fig. 2.10). These disintegration modes are of the “classical” type because the breakup mechanism is produced by wave instabilities that arise from the generation of capillary and surface waves. The fiber-type disintegration mode can also be classified under the “prompt” heading, given a relative air-fuel velocity that is high enough to achieve the airblast Weber numbers that produce immediate breakup upon injection.

The angle at which the air impinges on the liquid jet also determines whether prompt atomization occurs. The fourth sketch in Fig. 2.10 shows an example of an injection scheme in which the atomizing air nearly impinges perpendicularly on the liquid jet to produce a spray of ligaments and droplets at the injection orifice exit plane. In another example, the injector by Nukiyama and Tanasawa (1939) (Fig. 2.11a) shows that the internal flow path guides the air to impinge on the liquid jet at a 90° angle before exiting the injector. At such an extreme angle, the prompt atomization mode dominates because there is no time for the wave instability mechanism to develop.

Unless the LBI injector is operated at an air to liquid mass flow ratio (ALR) that is low enough to prevent rapid atomization, the LBI injector operates under a prompt mode. This classification is largely based on the geometry of the injector, which shares the same scheme of a perpendicular air impingement onto the fuel jet as the Nukiyama-Tanasawa (1939) injector (see Fig. 2.11).

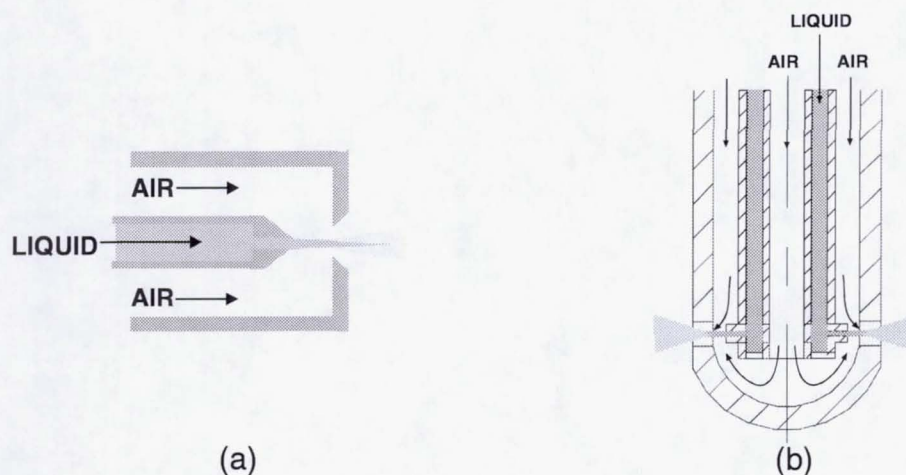


Fig. 2.11 Comparison between the geometry of (a) the Nukiyama-Tanasawa (1939) plain-jet airblast injector, and (b) the fuel atomizer of the LBI Injector.

In prompt atomization, the atomization process occurs rapidly, thereby causing such flow parameters as the liquid viscosity and air density to have no effect on the mean drop size in the spray. The liquid jet orifice diameter also does not play a large role in affecting the atomization quality of the spray. In contrast to these observations, the atomization of the liquid jet by the classical wavy-sheet instability mechanism greatly depends on the liquid viscosity, air density, and initial jet diameter (Lefebvre, 1992a).

The three main factors that are important in affecting prompt atomization, according to Lefebvre (1992a), are the relative liquid-air velocity U_R , the ratio of atomizing air to liquid mass flow rates (ALR), and the liquid surface tension σ . The atomization regimes associated with prompt airblast atomization are related to the ALR . Good atomization, as represented by low D_{32} values, occurs at an ALR of 3. For ALR s less than 3, spray atomization quality is poor, and the average droplet sizes are larger. Increasing the airblast air flow to yield ALR values greater than 3 results in a diminishing return; the degree of atomization does not increase as appreciably for comparable increases in ALR beyond this value.

In one of first studies conducted on an airblast-atomized liquid jet atomizer, Nukiyama and Tanasawa (1939) varied liquid properties of surface tension, viscosity, and density to yield a correlation for the spray droplet size parameter D_{32} . Lorenzetto and Lefebvre (1977) also derived an expression for D_{32} based on tests on their plain jet airblast atomizer by varying the liquid and air flows. Unlike the Nukiyama-Tanasawa injector, the Lorenzetto-Lefebvre injector routes the air to produce a coaxial flow of air

with the liquid. Likewise, the airblast injectors used by Rizk and Lefebvre (1983) and Eroglu and Chigier (1991) in their studies were also of a coaxial type.

The studies of Rizk and Lefebvre (1983) and Lorenzetto and Lefebvre (1977) differ in their observation of the drop size dependence on the fuel orifice diameter. The study of Rizk and Lefebvre (1983) showed a dependence of D_{32} on the square root of the fuel-orifice diameter. On the other hand, Lorenzetto and Lefebvre (1977) found that, for low viscosity fluids, the orifice size did not affect the D_{32} , which is a result similar to that found by Nukiyama and Tanasawa (1939).

The differing observations in the dependence of D_{32} on the initial jet diameter is discussed by Beck et al. (1991). Although the Beck et al. (1991) study was performed on a liquid sheet atomizer, the discussions related to the atomization process are germane to the plain-jet airblast atomizer. In their study, Beck et al. (1991) also observed that the D_{32} was independent of the initial sheet thickness, which was contrary to the result from a similar airblast sheet atomization study by Rizk and Lefebvre (1984) in which the D_{32} was found to be a function of the initial sheet thickness, raised to a power of 0.4. Upon closer inspection of their atomizer and the Rizk and Lefebvre (1984) atomizer, Beck et al. (1991) determined that the geometry of the injector affects the dependency of D_{32} on the initial liquid sheet thickness. Whereas the geometry in the Rizk and Lefebvre (1984) injector forced the air to flow parallel to the liquid sheet, the Beck et al. (1991) injector forced the air to impinge on the sheet at a 30° angle. The impinging action of the air streams was described as an “extruding” process which caused the sheet thickness to vary, and resulted in an

independent relationship between the initial sheet thickness and the droplet size. This process is essentially described by Lefebvre (1992a, 1992b) as “prompt” atomization.

The role of the injector geometry in affecting atomization in the spray can thus be used to explain the different results obtained in the Lorenzetto and Lefebvre (1977) and Rizk and Lefebvre (1983) studies on the plain-jet airblast atomizer. Because the injector used by Lorenzetto and Lefebvre (1977) forced the atomizing air to impinge on the liquid jet at a more appreciable angle than did the coaxial, co-flowing injector of Rizk and Lefebvre (1983), the droplet size in the Lorenzetto and Lefebvre injector was not as strongly dependent on the initial jet diameter.

The airblast injector of Harari and Sher (1997, 1998) differs from the Nukiyama-Tanasawa and the coaxial airblast atomizers in that the impingement of the air on the liquid occurs at a point external to the injector. Another plain-jet airblast injection scheme that differs from the coaxial, co-flowing atomizer implements a radial injection of liquid jets from the centerbody (Jasuja, 1979). The jets are atomized by the crossflow of swirling airblast air, a concept that is similar in fashion to the LBI spray injection method.

The plain-jet airblast injector geometries and a description of the study and major results associated with the injectors are summarized chronologically in Table 2.1. Note that these studies mainly characterized the droplet D_{32} distributions, but not the planar fuel mass distributions of the sprays produced by the injectors.

Table 2.1 Comparison between plain-jet airblast atomizer experiments.

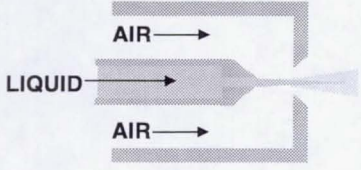
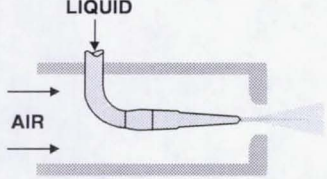
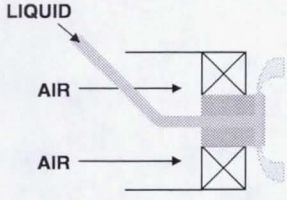
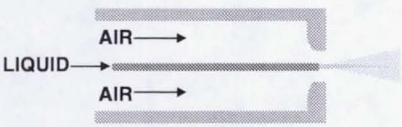
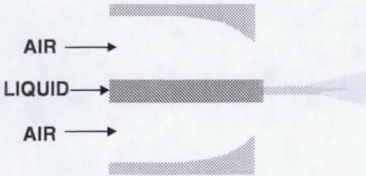

Experiment	Description and Major Findings: <ol style="list-style-type: none"> Objective Air flow pathway Parameters varied Measurements Primary Results
<p>Nukiyama and Tanasawa (1939)</p> 	<ol style="list-style-type: none"> To produce a D_{32} correlation for the atomizer. Air impinges on liquid jet at 90° angle near exit. Liquid properties (μ_L, σ, ρ_L), air to liquid flow rate ratio Droplet size measured from spray deposited on oil-coated slides. Derived a D_{32} correlation based on variables tested. No effect of atomizer orifice dia. on D_{32}.
<p>Lorenzetto and Lefebvre (1977)</p> 	<ol style="list-style-type: none"> To perform a more detailed study on the plain-jet airblast atomizer, varying more parameters to assess spray quality. Co-axial flow of air and liquid. Liquid properties (μ_L, σ, ρ_L), air velocity, fuel hole dia., ALR Droplet size measured by light-scattering technique. Derived a D_{32} correlation based on variables tested. Little effect of fuel orifice dia. on D_{32} for low viscosity fluids. Good atomization for $ALR > 3$.
<p>Jasuja (1979)</p> 	<ol style="list-style-type: none"> To study the effect of fuel properties on the D_{32}. Liquid jets injected into a swirling crossflow of air. Liquid (kerosine, gas, residual oil), airblast ΔP, air and fuel flows Droplet size measured by light-scattering technique. Comparable in performance to prefilming airblast injection for low viscosity fuel (kerosine), at airblast $\Delta P > 4\%$.
<p>Rizk and Lefebvre (1983)</p> 	<ol style="list-style-type: none"> To determine effect of linear scaling of the atomizer on atomization performance. Co-axial flow of air and liquid. Liquid (kerosine, water), air velocity, ambient air pressure, atomizer hole dia. Droplet size measured by light-scattering technique. D_{32} proportional to (hole dia.)^{0.5}; suggested that co-flowing, coaxial airflow achieves better atomization by allowing natural jet instabilities more time to fully develop.

Table 2.1 Comparison between plain-jet airblast atomizer experiments.
(Continued)

Experiment	Description and Major Findings: <ol style="list-style-type: none"> 1. Objective 2. Air flow pathway 3. Parameters varied 4. Measurements 5. Primary Results
<p>Eroglu and Chigier (1991)</p> 	<ol style="list-style-type: none"> 1. To characterize droplet D_{32}, velocity distributions after liquid jet breakup. 2. Co-axial flow of air and liquid. 3. Liquid (water) and air flow rates, exit velocities. 4. PDPA-measured D_{32}, velocity distributions. 5. Compared distributions to photographs. Bimodal drop size distribution (peaks at center and at spray boundary) corresponds to ladle-shaped structures formed by jet instability. Mean droplet velocities: minimum at center, maximum near spray boundary.
<p>Harari and Sher (1997, 1998)</p> 	<ol style="list-style-type: none"> 1. To optimize the injector geometry to produce sprays with the lowest D_{32} distribution (1997); to investigate the bimodal drop size distribution produced by the injector (1998). 2. External air impingement on liquid. 3. Injector geometry (1997), air and liquid (water) flows (1997, 1998) 4. Malvern-measured line-averaged D_{32}. 5. Found that the 45° angle worked best in producing a low D_{32} distribution (1997 study). Attributed a bimodal drop size distribution to a flow recirculation characteristic of the injector.

2.3 Liquid Jet Injection Into a Crossflow

Section 2.2 covered the spray aspect of the spray jet in crossflow with a discussion that primarily focused on its formation by airblast atomization. This section reviews the second component of the problem by presenting a background on the work related to the injection of a liquid jet into a crossflow (Fig. 2.12).

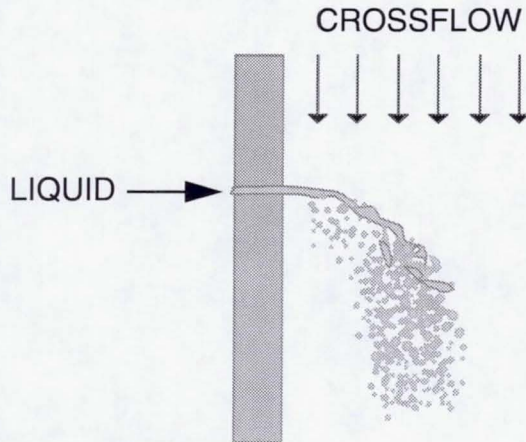


Fig. 2.12 Liquid jet breakup in a crossflow of air.

Liquid jet injection into a gaseous crossflow has mainly been studied for its application to such technologies as aircraft engine afterburner sections, rocket propulsion, and ramjet, scramjet (supersonic combustion ramjet), and gas turbine combustors. For applications which utilize high subsonic and supersonic crossflows, transverse jet injection from a wall offers an attractive alternative to coaxial jet injection. The latter method requires fuel injection from an obstruction in the flow, which causes flow losses and introduces material problems due to high stagnation temperatures. In addition, the aerodynamics associated with transverse jet injection appears to enhance droplet mixing with a crossflow of oxidizing agents (Forde et al., 1966). Slurry fuel mixtures can also be injected using the transverse jet injector because the simplistic design will not tend to clog as much as injectors that are more complicated and intricately designed (Kihm et al., 1995).

In the surveyed literature of liquid jet injection into a crossflow, studies were performed for both supersonic and subsonic crossflows, and in the compressible and incompressible regimes. Whereas subsonic crossflows occur in many applications—in the form of wind that affects pesticide spray drift or in the form of a swirling inlet air flow that mixes with spray jets—supersonic crossflows are primarily encountered in combustion applications such as rocket engines and scramjets. The difference between subsonic and supersonic crossflows in affecting jet breakup lies in the difference in breakup intensity. The flow velocities for the supersonic case yield a more violent and turbulent breakup and shearing of the jet (Schetz and Padhye, 1977).

Given the advantages of jet injection into a crossflow for fuel combustion, numerous studies have been performed to assess the structure and breakup mechanisms associated with this injection method. Sections 2.3.1 through 2.3.3 present discussions on the liquid jet into the crossflow regarding its penetration, deformation, and breakup, as well as the distributions of spray mass, droplet size, and velocities that result from these processes.

2.3.1 Jet Penetration

An important parameter to consider in jet-crossflow mixing is the jet-to-crossflow momentum-flux ratio q , also known as the dynamic pressure ratio, which is expressed as

$$q = \frac{\rho U^2|_{jet}}{\rho U^2|_{crossflow}} \quad (2.14)$$

The momentum-flux ratio takes into account the density (ρ) and velocity (U) of the liquid jet and gaseous crossflow. It is a determining factor in the penetration height of the jet. If q is high, the jet will penetrate farther into the crossflow. For a low q , the jet and its atomized drops will not have the momentum to penetrate as far into the flow, and will wet the injector wall.

Phenomenological analyses have used the definition of q to describe the maximum penetration of the spray (Schetz and Padhye, 1977), as well as the penetration of the liquid column as a function of downstream distance (Wu et al., 1997). Schetz and Padhye (1977) applied a control volume that encompassed the liquid column and spray, up to the point where the spray achieves its maximum penetration and the droplets in the spray attain the velocity of the crossflow. The equation that resulted from that analysis is of the following form

$$\left(\frac{x}{d_f}\right)_{max} = C \sqrt{q} C_d \left(\frac{d_{eq}}{d_f}\right) \quad (2.15)$$

where $(x/d_f)_{max}$ represents the maximum penetration distance x normalized by the fuel orifice diameter d_f , C is a constant that incorporates the drag coefficient C_D , C_d is the discharge coefficient of the fuel orifice, and (d_{eq}/d_f) is the equivalent injector diameter that is normalized by the fuel orifice diameter, and is equal to one for a circular injector.

While Eq. 2.15 provides only the maximum penetration distance as a function of the injection parameters, Wu et al. (1997) developed an equation to describe the trajectory of the jet column penetration. By considering the drag force along the direction of the crossflow as being the primary force that affects the bending of the

liquid column, their phenomenological analysis yielded the following equation that describes the jet penetration x/d_f :

$$\frac{x}{d_f} = \sqrt{\frac{\pi}{C_D} \cdot \frac{z}{d_f} \cdot q} \quad (2.16)$$

In Eq. 2.16, C_D is the average drag coefficient that incorporates the effects of processes such as column deformation and the stripping of droplets from the column surface. The form of this equation is similar to equations that describe the trajectories of gaseous jets in a crossflow.

2.3.2 Jet Deformation and Breakup

When a cross stream of air is introduced to the liquid jet system (see Fig. 2.13), pressure and shear forces deform the jet and induce entrainment. The crossflow forces the jet to bend toward a direction parallel to the freestream, and produces vortex shedding behind the cylindrical jet column. The counter-rotating vortex pair (CVP) that is generated within the jet produces a kidney-shaped cross-section. These vortices may account for the stripping of drops from the lee side of the jet, as well as for the entrainment of crossflow air into the atomized jet.

To describe the liquid jet behavior, researchers such as Clark (1964) and Adelberg (1967, 1968) have modeled the intact column of the jet as a circular cylinder. However, other researchers such as Heister et al. (1989), Li and Karagozian (1992), Nguyen and Karagozian (1992), and Inamura (2000) have modeled the jet cross-section as an ellipse with the major axis perpendicular to the crossflow in order to better simulate the crossflow-induced deformation of the jet. Assuming an elliptical

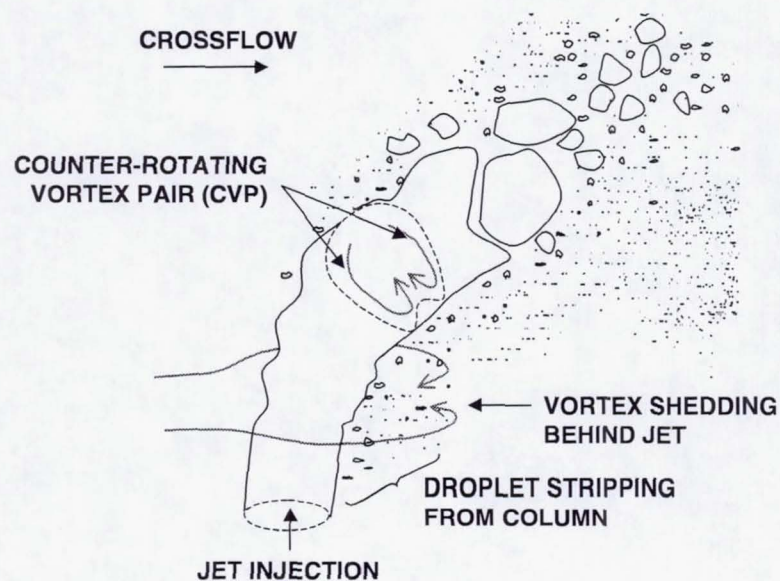


Fig. 2.13 Jet interaction with a crossflow.

shape for the cross-section of the transversely-injected jet is reasonable, as Heister et al. (1989) found that using the elliptical cross-section in their analytical model produced favorable jet trajectory predictions. Inamura (2000) also was able to closely predict measured jet trajectories, though only prior to its disintegration, with a model that balanced the momentum of the viscous, surface tension, and crossflow-induced dynamic pressure forces. In the analysis, Inamura (2000) applied a droplet breakup model to simulate the deformation of the liquid column. The application of droplet breakup models in the analysis of liquid column breakup has been performed by other researchers, as it will be seen in Section 2.3.2a.

Experimental observations by researchers have led to a general understanding of the breakup process as illustrated in Fig. 2.14. The jet exits the orifice as a column

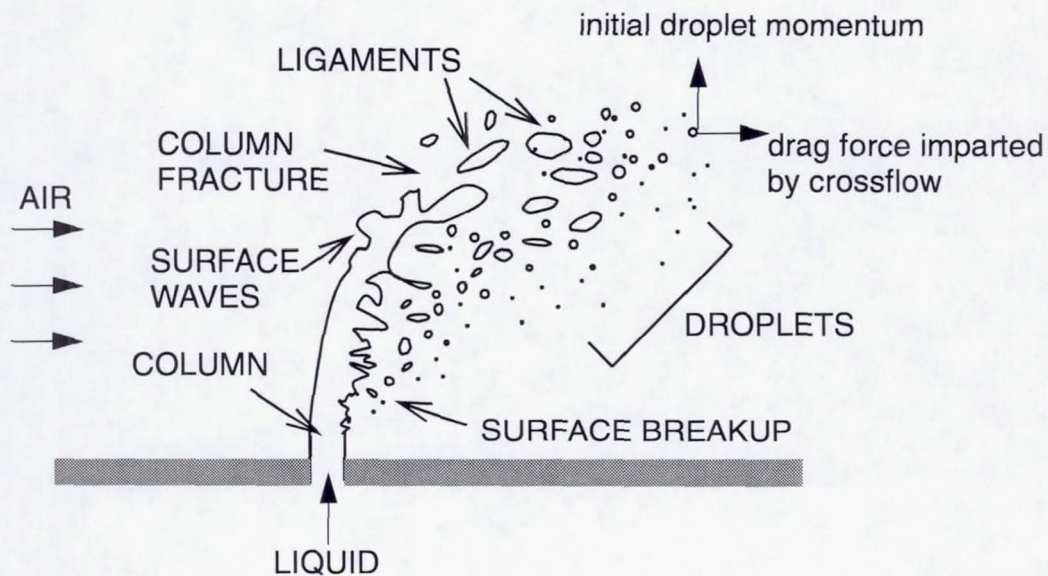


Fig. 2.14 Jet breakup in a crossflow (Wu et al., 1997).

with an initially round cylindrical cross-section. The dynamic force of the crossflow then causes the jet to bend in the flow direction and to deform in its cross-section. Waves begin to propagate on the windward surface of the jet, and their growth is magnified until jet fracture occurs. The clumps and ligaments that are formed undergo secondary atomization until the droplets attain a size that is limited by the critical Weber number. Liquid stripping from the lee side of the jet may also occur before the point of column fracture. For a jet injected into a supersonic crossflow, the structure is the same, with the addition a bow shock upstream of the jet structure.

The disintegration of the liquid jet occurs in two stages. The first stage involves the primary breakup of the jet through the fracture and/or surface stripping of the jet column. The residual ligaments and drops produced by primary atomization then

undergo a secondary breakup process. Both atomization processes are described in the following Sections 2.3.2a and 2.3.2b.

2.3.2a Primary Jet Breakup

Less and Schetz (1986) studied the transient behavior of liquid jets to observe the effect of periodic, turbulent oscillations on spray formation and atomization. These transients were attributed to vortices shed from the column and to an axial wave propagation in the jets. Waves seen on the jet column initially traveled at the same velocity of the liquid jet, but later increased in velocity because of the acceleration caused by air impingement on the column. Column fracture occurred at the trough of these column waves. Time-dependent variations in the droplet distribution corresponded to the intermittent fracture of various-sized fluid clumps from the jet.

Inamura et al. (1993) investigated the structure of the disintegrating liquid jet in a crossflow. Qualitative observations of the jet disintegration process showed a major fracture occurring at a wave trough on the windward surface, as Less and Schetz (1986) had observed. Large clumps that break off from the column disintegrated further because of secondary atomization. Small droplets resulting from the shearing force of the crossflow on the jet surface were also observed before the bending of the jet occurred.

A recent study by Wu et al. (1997) delved further into the breakup processes of the liquid jet in subsonic crossflow. Shadowgraphs were obtained to determine the liquid jet trajectory, column fracture, and surface breakup. Surface waves were observed on both the windward and leeward sides of the jet. The leeward waves, if

they developed, appeared first. The leeward wave amplitude increased as the jet velocity increased, until surface breakup, or droplet stripping from the lee side of the jet, occurred. The acceleration forces imposed by the crossflow bent the jet and produced windward waves which, when increased in amplitude, led to the breakup of the jet column into globules and ligaments. As for the effect of q on the point of major column fracture, Wu et al. found that the transverse height to the point of column fracture depended on $q^{0.5}$, while the downstream distance to the point of column fracture was independent of q .

The size of the drops resulting from surface breakup were also found by Wu et al. (1997) to be smaller than those formed from the secondary atomization of the fractured jet. The onset of surface breakup could be determined by q , an increase of which causes surface breakup to occur before jet column fracture. Insight into the surface breakup can be gained from Wu et al. (1995) in their study of the primary breakup mechanism of droplets sheared from the surface of a jet injected into a still fluid (see Fig. 2.5).

As the jet enters a crossflow, it is exposed to external forces such as pressure drag induced by the crossflow and viscous drag at the liquid-crossflow interface, as well as internal forces attributed to surface tension and viscous shear within the liquid jet (Adelberg, 1967). To model the breakup rate and the extent of penetration of a liquid jet, Adelberg (1967) extended the analysis initiated by Mayer (1961), who studied the atomization of an infinite sheet of liquid with capillary waves. As in Mayer's analysis, Adelberg (1967) utilized the energy balance on a wave surface as proposed by Jeffreys (1925) in his analysis of sheltered wave growth. The derived

equations that describe the breakup rate and penetration of the liquid jet were based on jet instabilities arising from the presence of either capillary or acceleration waves.

Waves on the surface of the jet can originate as small capillary waves triggered by pressure fluctuations or disturbances in either the crossflow or jet flow. When the wave velocity increases due to an imbalance in pressure forces caused, for instance, by an increase in the crossflow velocity, the waves transform into acceleration waves.

Acceleration waves are essentially gravity waves, which occur at the interface between two fluids of differing densities and which have as their restoring force, the earth's gravitational field. The premise behind calling these waves acceleration rather than gravity waves was to distinguish the aerodynamically-induced origin of these waves from any contribution by the earth's gravity.

A primary jet breakup model by Clark (1964) takes into account all of the internal and external forces acting on the liquid. The normal component of the aerodynamic forces produced by the crossflow push against the liquid and cause the jet to turn. The surface of the jet is affected by the shear component of the dynamic pressure force acting on the liquid surface to strip away droplets, and by the formation of waves resulting from vortex shedding in the wake. The breakup rate is defined by the rate of deformation of the liquid column. The aerodynamic force of the gaseous crossflow applied to the liquid jet surface causes a pressure distribution that flattens the liquid into a shape that is similar to a transverse ellipse (Fig. 2.15). After further deformation, ligaments are torn off the edges of the cross-section by the combination of the surface-tension force acting with the surface tangential shear. A distortion length

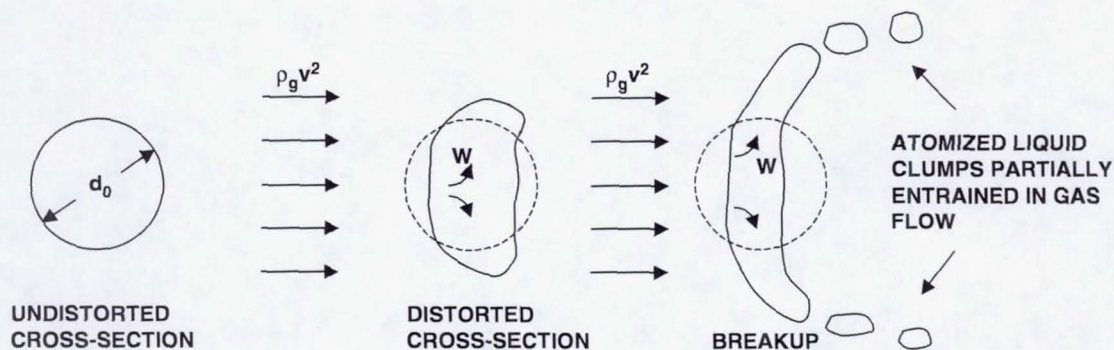


Fig. 2.15 A model of jet deformation and breakup (Clark, 1964).

parameter defined by Clark was used to denote the onset of the breakup mechanism and subsequently the occurrence of mass loss.

Kitamura and Takahashi (1976) performed an experiment and modeled the breakup process of the liquid jet in an incompressible crossflow. The model did not take the aerodynamic effect of the crossflow into consideration as a major factor in jet breakup. Rather, breakup was attributed to symmetric disturbances within the liquid jet. Their numerical results agreed with experimental results at the lower range of air velocities tested, but not with those at the higher air velocities. Injecting the jet into a low crossflow velocity produced results that approximately conformed to the assumption of a symmetric jet disturbance that was employed in their model. The higher crossflow velocity, however, resulted in a more pronounced aerodynamic effect that bent the jet, producing asymmetries along with a surface wave disturbance, and rendering invalid the main assumption in the model.

In regard to the jet breakup length, Kitamura and Takahashi (1976) showed that an increase in the crossflow velocity led to a decrease in the intact length of the jet, to the point of major fracture. In other words, a decrease in the jet to crossflow momentum-flux ratio caused a decrease in breakup length. An equivalent observation was made by Schetz and Padhye (1977) in their study of a liquid jet injected into a high subsonic crossflow.

Wu et al. (1997) formulated a model for trajectory and distance to column breakup point based on phenomenological considerations. The trajectory prediction resulted from a balance between the liquid acceleration and aerodynamic drag forces applied to the jet in the direction of the crossflow. The model for primary breakup treated the liquid jet disintegration with the same criteria as secondary drop breakup, under the premise that in both cases aerodynamic forces dominated the breakup process. For example, the time scale for breakup obtained from the study of Ranger and Nicholls (1969) was used to represent the time for the liquid column to fracture in the crossflow. An empirical correlation for the column fracture point was then derived using the momentum-flux ratio as a parameter.

A detailed classification of the primary breakup regimes of a nonturbulent liquid jet in a crossflow was performed by Mazallon et al. (1999). From shadowgraphs obtained in the near-field of the jet upon its injection, four modes of breakup were observed, including the general fracture of the liquid column, and the occurrence of the bag breakup, bag/shear breakup, and shear breakup modes at the column surface. These regimes are listed in order of an increasing degree of atomization, which correlates to an increase in crossflow velocity for a set jet velocity. The latter three

breakup regimes that Mazallon et al. (1999) used to classify the liquid column breakup of the nonturbulent jet closely parallel the secondary droplet breakup modes presented by Hsiang and Faeth (1992) as well as by Krzeczkowski (1980), whose classifications are presented in Section 2.3.2b.

2.3.2b Secondary Breakup

After clumps of fluid are torn off from the main jet column, the fluid globules continue to undergo additional breakup processes until a critical Weber number is reached. This process of breaking down atomized droplets further is generally referred to as secondary atomization.

Classifications have been made by various authors to describe the different modes of droplet breakup. Hinze (1955) described three different deformed shapes for which drops exposed to a convective air stream can exhibit. A droplet that experiences “lenticular” deformation is shaped in the form of a flattened ellipsoid (Fig. 2.16a).

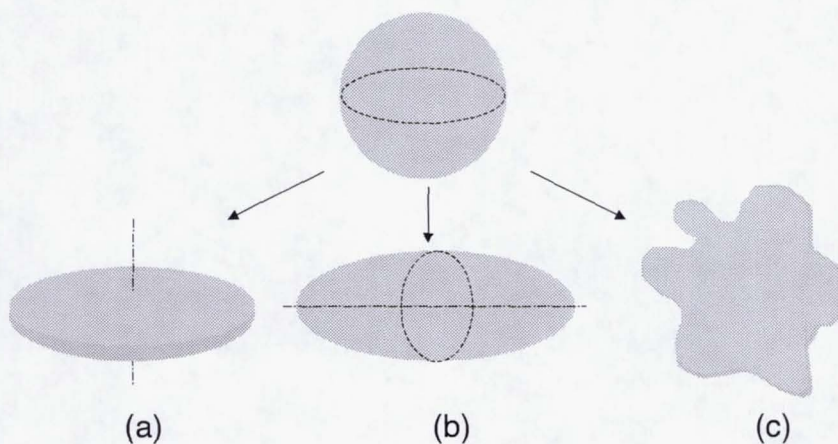


Fig. 2.16 Drop deformation shapes: (a) Lenticular, (b) Cigar-shaped, (c) Bulgy (Hinze, 1955).

Disintegration occurs when the drop in this form is stretched into a toroidal shape by a parallel or rotating flow, which causes the thinning membranes to burst. For a “cigar-shaped” droplet (Fig. 2.16b), applying either an impinging or shear flow will stretch the ellipsoidal drop into a long thin ligament that subsequently breaks up. Finally, a droplet in an amorphous “bulgy” form possesses protruding fingers of liquid from which droplets can be formed (Fig. 2.16c).

Krzeczkowski (1980) observed 4 types of deformation modes corresponding to different stages of increasing Weber number (see Fig. 2.17). In each case, the droplet deforms to a flat disk before the onset of breakup. The first mode is the bag mechanism whereby a hollow sphere is formed which subsequently breaks up into a line of drops. The next stage is the bag-jet regime in which a jet ligament occurs along with the hollow sphere. The third and fourth modes of transition and shear deformation appear chaotic and asymmetric. Shear breakup occurs when the relative air flow to drop

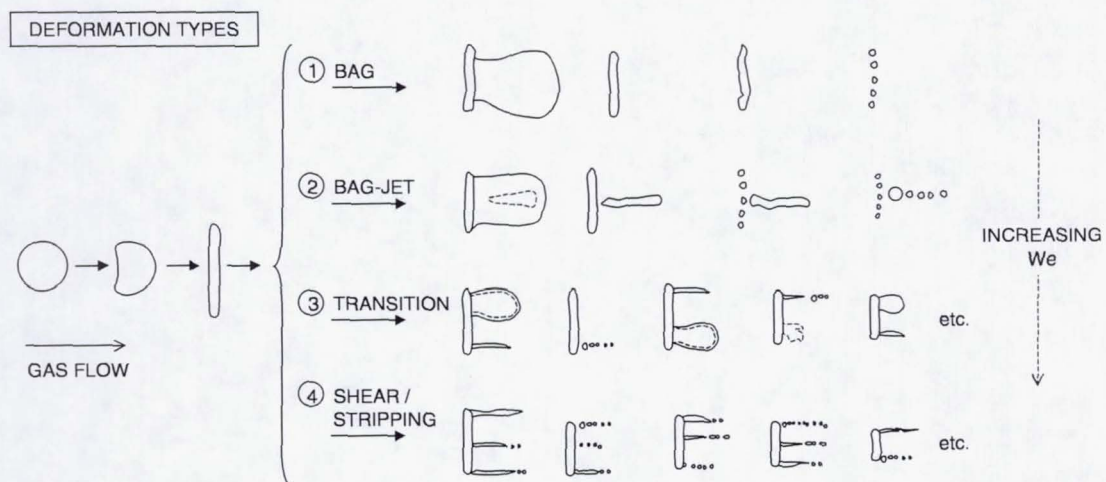


Fig. 2.17 Droplet breakup modes (Krzeczkowski, 1980).

velocity is high enough to shear off drops quickly. The droplet sizes produced are smaller than those from the bag mode, but the final product also includes ligaments.

Shadowgraphs of the breakup of a monodisperse stream of droplets in a shock tube were captured by Eastes and Samuelsen (1992, 1993) with the use of a pulsed laser light source. The different breakup modes observed by Krzeczkowski (1980) are also seen in the series of instantaneous snapshots from Eastes and Samuelsen (1993) that are presented in Fig. 2.18. Frame 1, located in the top left position in Fig. 2.18, depicts the stream of spherical water droplets prior to introducing the shock wave. Upon impact of the shock wave, the droplets progress from being flattened by the initial impact (frames 2 and 3), to breaking up via the bag mode (e.g., frame 4), and finally to breaking up via the shear mode (e.g., frames 7-8).

In combustion applications, the fragments resulting from jet injection into a crossflow most likely experience crossflow velocities that are high enough such that the shear mechanism becomes the dominant mode in secondary drop breakup. The study of Ranger and Nicholls (1969), which involved droplet shattering in a high speed convective air stream at supersonic speeds, supports this view. Their study found that the main mode of droplet disintegration was attributed to the stripping of the boundary layer by the shear forces produced by the convective air stream.

A theory of the shear breakup process as explained in Wu et al. (1995) is illustrated in Fig. 2.19. Only half of the drop of initial diameter d is shown. The liquid drop is not spherical, but instead, is deformed into a flattened globule. The crossflow travels with velocity U_o from left to right. At the drop surface, the flow splits around the drop. Shear forces induced by the air flow on the surface distort the drop and cause

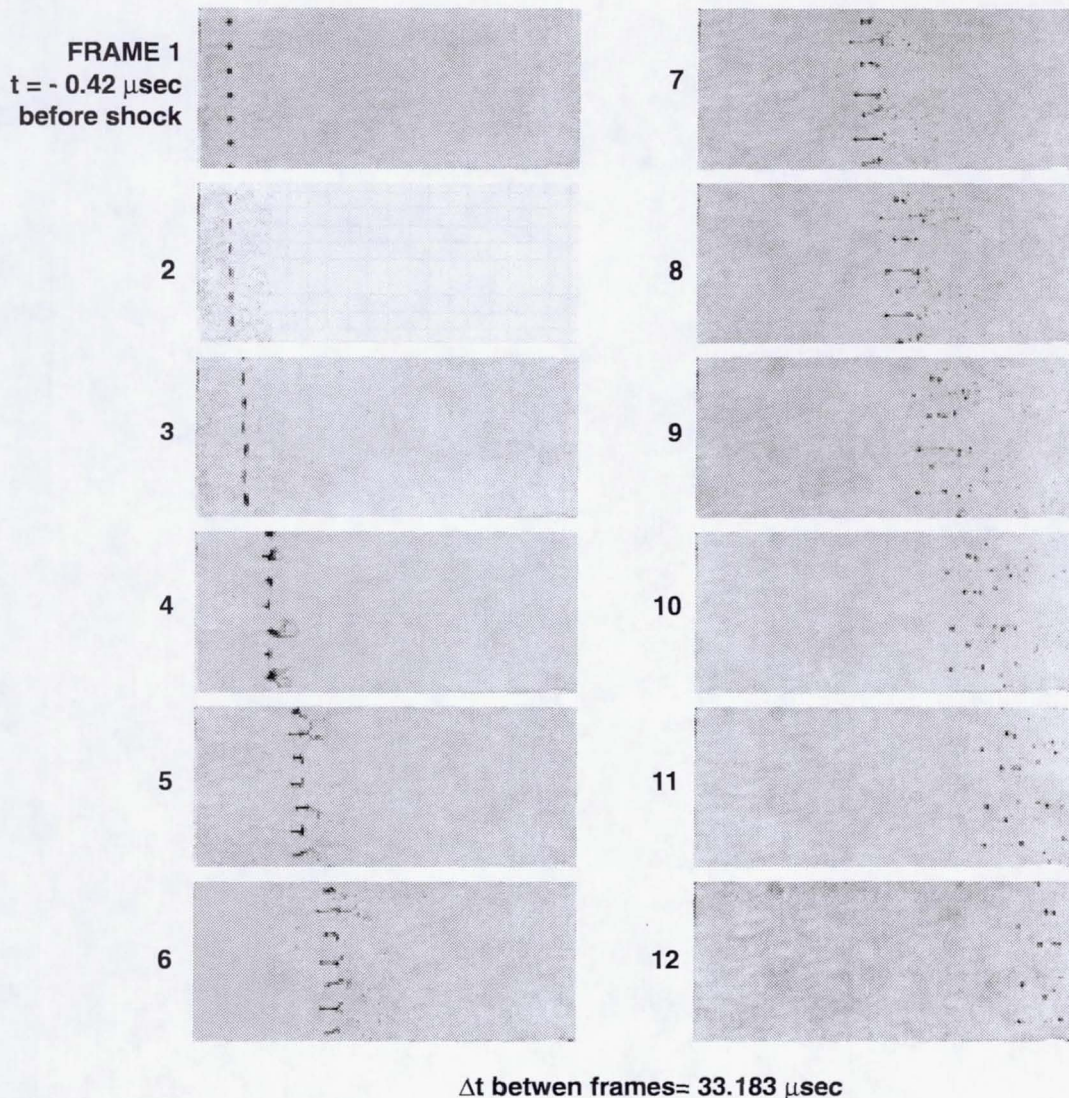


Fig. 2.18 Breakup of a stream of 150-mm water droplets in atmospheric air by a 50% shock wave (Eastes and Samuelsen, 1993).

a projection of liquid with a size on the order of the boundary layer thickness δ to appear along the outer edges. Secondary atomization is achieved when the finger of liquid on the drop ultimately breaks off and becomes a satellite droplet of the same size as δ . The end of the droplet stripping process occurs when the Eötvös number, which

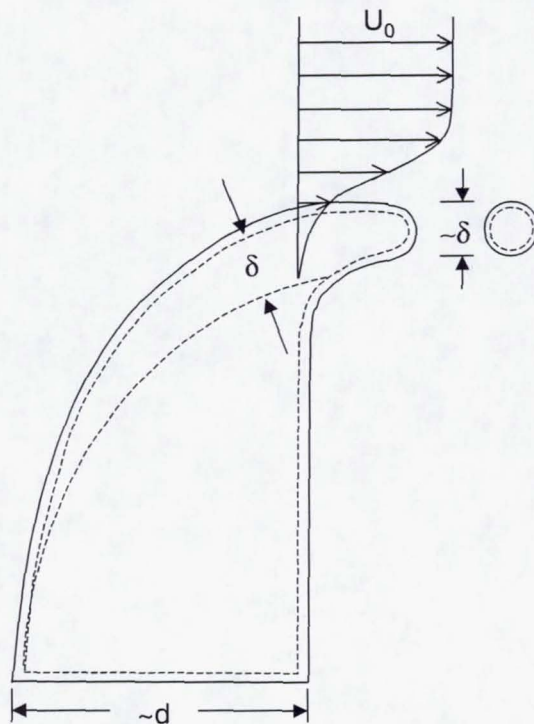


Fig. 2.19 Shear breakup from a drop (Wu et al., 1995).

relates deformation to the size of a moving drop undergoing acceleration, reaches a critical value, which was determined to be 16. After secondary breakup, the liquid drop velocity along the stream can drop by as much as 30-70% because of increased drag coefficients resulting from drop deformation, and a reduced relaxation time for the smaller drops.

Interestingly, the picture of the shear breakup of the satellite from the parent drop is similar to the model of primary column breakup by Clark (1964) (recall Fig. 2.15). The similarity between the secondary breakup model by Wu et al. (1995) and the primary breakup model by Clark (1964) validates the rationale Wu et al. (1997)

employed in applying the secondary droplet breakup analysis of Ranger and Nicholls (1969) to their primary jet breakup analysis.

Oda et al. (1994) attempted to produce a model that did not include the primary breakup of the jet column. Their numerical prediction of jet atomization and dispersion only considered the secondary droplet breakup of a Chi-square volumetric droplet distribution injected with an average initial jet velocity. Secondary droplet breakup was modeled using a Rayleigh-Taylor instability in which the wave amplitude on the droplet surface increased until the droplet disintegrated. This breakup process was repeated until the critical Weber number of 10 was attained. A comparison of the experimental and numerical results of spray penetration, spray D_{32} , and local liquid mass flow rate showed a non-conformity near the injection port which probably occurred because of the absence of primary jet column disintegration in the model.

2.3.3 Mass, Droplet, and Velocity Distributions

The spray quality produced from jet atomization by a crossflow can be characterized by liquid mass and droplet distributions of the spray. Mass distributions of the spray give an indication of the dispersement and the spatial extent of the liquid in the flow. Knowledge of the droplet velocity profiles aids in assessing fuel droplet and air mixing, which is coupled to evaporation and combustion processes.

Oda et al. (1994) presented mass-flow distributions across the cross-section of the disintegrating jet. The horizontal cross-sectional plane parallel to the injector wall showed a mass flux with a Gaussian profile that was symmetric across the spray centerplane. The mass-flow profile was sharply peaked near the injection point, with

the peak decreasing in size with downstream distance because of the expansion of the jet. The vertical cross-section through the jet centerline, and perpendicular to the injector wall, showed a skewed Gaussian profile distribution with the maximum mass flow rate occurring at a location beyond the centerline of the jet plume.

Empirical relationships between the mass-flux distribution of the liquid as a function of q and the downstream distance were obtained by Inamura and Nagai (1997). Equations describing the mass-flux distribution, which as with Oda et al. (1994), was assumed to be a standard normal function, were obtained by applying a least squares curve fit to droplet mass-flux measurements obtained with an isokinetic sample probe. As q is increased, the empirical relationship predicts that the droplets tend to disperse farther into the crossflow in the upper region, rather than disperse across the lower region of the jet. Along the width of the jet, the empirical relationship suggests an increased dispersion with an increased q . The fitted results also showed that the exit diameter of the liquid injector did not greatly affect the distribution of the mass flux along the width of the spray.

In the study of Wu et al. (1997), the upper trajectory of sprays elicited from shadowgraphs were correlated for sprays formed under different q . The values of q were varied by changing the liquid velocity, liquid type, injector hole diameter, and crossflow velocity. This work was extended by Wu et al. (1998) in the investigation of the cross-sectional spray structure for a single injector geometry and for a single liquid injectant. In that investigation, the liquid velocity and the crossflow velocity were varied to affect the q -values. The spatial distributions of the mean droplet size and axial velocity, and of the spray volume flux, were presented. Correlations relating the

area, width, and penetration of the spray based on the maximum spray height and mass-flux values were obtained with q and the downstream distance serving as the dependent variables. The resulting correlations showed that these properties of the spray were directly proportional to q and the downstream distance. However, one interesting observation drawn from the set of correlations showed that the penetration of the maximum mass flux increased at a faster rate with respect to q than did the penetration of the upper surface boundary of the spray. The data reflected this trend by showing the peak mass flux shifting toward the top of the spray as q was increased.

Measurements obtained by Thomas and Schetz (1985) for a liquid jet injected into a supersonic crossflow yielded mass-flux distributions of the liquid jet. The distributions outlined the remnant of the main structure of the kidney-shaped core. From pressure distribution measurements, Thomas and Schetz (1985) also calculated the air Mach numbers at each individual point in the domain, and noted the presence of a subsonic core region and a supersonic outer region. Based on the results of their experiment, Thomas and Schetz (1985) presented their conception of the breakup of a liquid jet as depicted in Fig. 2.20. The dashed contour line of the kidney-shaped cross-section is shown, as well as the designation of the outer supersonic and the subsonic core and jet wake regions. The primary breakup of fluid clumps detaching from the jet column and the breakup of droplets shearing from the column are shown, as is a depiction of the secondary breakup of droplets from the clumps around the circumference of the jet plume.

Investigations have obtained the droplet size distributions by measuring average D_{32} values at certain positions across the spray. Schetz and Padhye (1977)

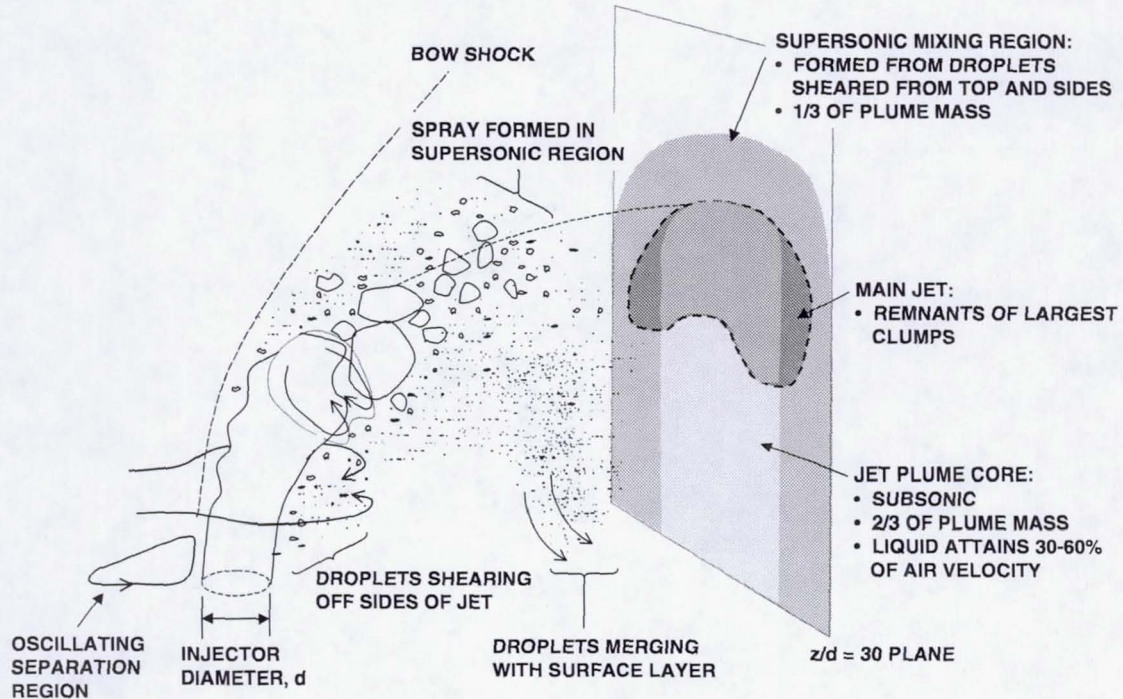


Fig. 2.20 Detailed scheme of jet breakup in a supersonic crossflow. (Thomas and Schetz, 1985).

found that droplet measurements could not be made near the injector port because of the dense spray structure. In general, they found that an increase in the crossflow Mach number, which essentially decreases q , leads to a decrease in drop sizes. Decreasing the injector diameter also led to a decrease in drop sizes.

Experimental investigations yielding drop size distributions performed by Ingebo and Foster (1957), Weiss and Worsham (1959), and Kihm et al. (1995) arrived at empirically-derived expressions for the size distribution. Both Kihm et al. (1995) and Oda et al. (1994) measured the droplet size distribution (measured as D_{32}) across the spray and found larger droplets existing or penetrating farther into the flow under

subsonic conditions. Larger droplets are expected to penetrate farther into the flow because of their higher initial momentum.

In an experiment of jet injection into supersonic crossflows, Nejad and Schetz (1983) also demonstrated the same trend of increasing D_{32} with jet penetration distance for various cases. However, some of the cases also produced droplet distributions that increased to a maximum and then decreased across the axial length. In a case performed at the same q but with a larger orifice size, larger D_{32} occurred in the core region while smaller droplets occurred along the outer edge of the spray. The change in injector orifice size apparently changed the Re and We numbers, which affected the atomization processes.

An analytical model for the mean droplet size was developed by Adelberg (1968), and was used, in part, to study the effect of the jet orifice size on the droplet size. Extending the analysis of Mayer (1961) for flat sheet atomization by a capillary wave mechanism, Adelberg (1968) derived expressions for the mean drop size obtained from a jet undergoing capillary and acceleration wave instability. The analysis showed that the mean droplet size produced by a jet in the acceleration wave regime does not depend on the injector diameter while the jet in the capillary wave regime does depend on the orifice diameter.

While droplet size distributions have been used by various researchers to characterize sprays, droplet velocity profiles have not been measured as extensively. Inamura et al. (1993) did measure droplet velocity profiles in the plane of the spray axis at various downstream positions. At the first measurement location, the droplet velocity was close to zero near the wall because of the jet wake region, and increased

with distance away from the wall up to the calculated penetration point. The jet penetration was obtained using an equation derived from earlier data which measured the distance from the wall to the outer surface of the jet. At the next downstream station, the velocity profile showed a distinct minimum at the center. The droplet velocities also increased because of droplet entrainment by the crossflow. Droplet velocities decreased in the core region because the fluid there is shielded from crossflow entrainment. Subsequent downstream locations revealed a general increase in the magnitude of the droplet velocities and a flattening of the profile as the jet diffuses, while the core region dissipates and the droplets are entrained by the crossflow air.

Inamura and Nagai (1997) also measured droplet size and velocities in addition to the liquid mass fluxes in the spray. The data revealed a differing dependence of the droplet size and velocity distributions on the crossflow velocity. At lower crossflow velocities, larger droplets penetrated farthest, but at higher crossflow velocities, the mean droplet size distribution peaked in the core region. However, the highest droplet velocities parallel to the crossflow direction tended to peak along the outer edge of the spray, despite the different crossflow velocities that were tested.

Drop size and velocity distributions affect vaporization and ignition, which in turn affect the combustion process. An advantage of liquid jet injection into a crossflow that benefits a combustion system is the opportunity to tailor droplet sizes in the spray. Larger drops possessing higher momenta penetrate farther into the crossflow than do smaller drops, thus producing an increasing size distribution of drops outward from the wall. This droplet size distribution has its merit in cases such as a turbojet

combustor where the igniter is positioned to ignite the smaller drops near the wall (Lefebvre, 1989).

2.3.4 Summary of the Liquid Jet in Crossflow Studies

In the interest of improving fuel injector designs for propulsion applications, researchers have studied the breakup mechanisms of a liquid jet injected into a crossflow and its resulting spray quality. A visual summary of the papers reviewed for the liquid jet in crossflow case is shown in Fig. 2.21. Primary breakup of the column

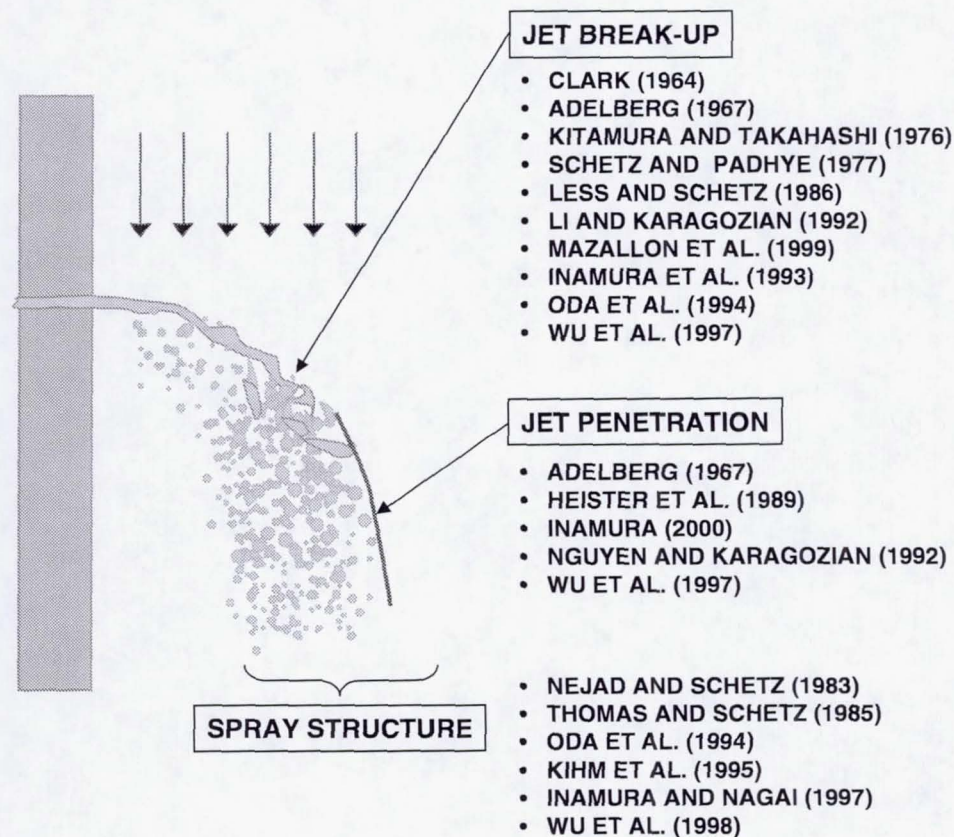


Fig. 2.21 The regimes of the liquid jet in crossflow assessed by the listed studies.

occurs because of the presence of a large surface wave instability generated by the aerodynamic force on the jet column. The jet fractures into clumps within a few troughs from the emanation point of the surface wave at the upper surface of the jet. Before the onset of the major fracture point, finer drops may also be formed—depending on the crossflow velocity magnitude—from the leeward side of the jet because of the aerodynamic shear forces induced across the column surface. The breakup mechanisms employed in primary breakup are similar to those that occur in the secondary atomization of droplets.

Investigation into the disintegration of a jet injected into a crossflow have yielded visual observations of the different breakup regimes. Empirical and analytical models describing the jet trajectory and average drop size distributions have also been developed. Mass-flow distributions obtained in the spray plume generally indicated the presence of a kidney-shaped cross-section typically observed in gaseous jets injected into a crossflow.

Droplet size distributions have been measured at various points in these flows, although the complexities of the primary and secondary atomization processes have so far precluded experimental and analytical investigations that describe the droplet distribution across the entire spray. Larger droplets are found in the spray core, with a decreasing droplet distribution toward the wall that is expected because the higher momentum resulting from the mass of the larger droplets enable them to penetrate farther into the crossflow. Smaller droplets may also be found above the spray core region if sufficient secondary atomization occurs.

2.4 Spray Jet Injection into a Crossflow

2.4.1 Droplet Transport

In the transverse injection of a spray into a high velocity air flow (Fig. 2.22), the droplets are subjected to forces that affect their motion in the flow field. The trajectories of the spray droplets can be tracked by applying a Lagrangian-based analysis to the droplets. The momentum equations for a droplet are obtained by equating the droplet motion with the viscosity- and pressure-related drag forces, the pressure gradient and viscous forces related to the fluid surrounding the droplet, the inertia of the virtual mass that occurs when the particle acceleration affects the fluid mass acceleration, and the Basset force, which takes into account the acceleration history of the droplet.

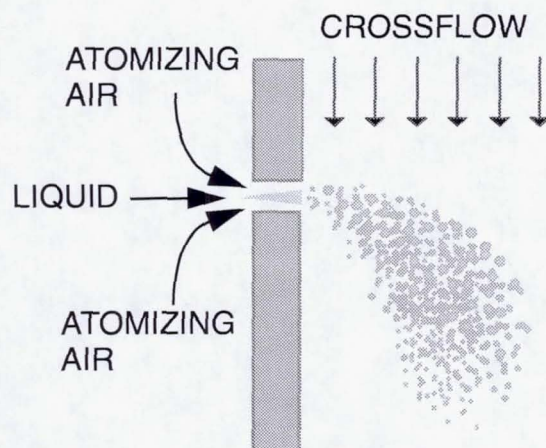


Fig. 2.22 Injection of a liquid spray into a crossflow of air.

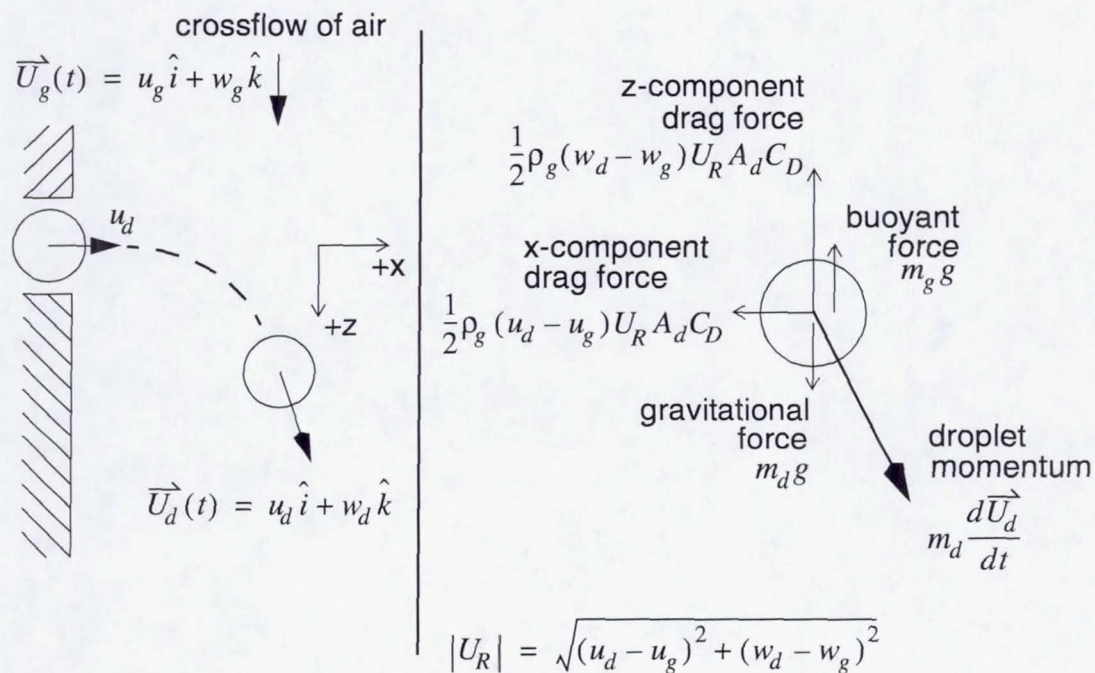


Fig. 2.23 Diagram depicting the droplet path upon injection into a crossflow of air (left), and the force balance on the droplet in the present analysis (right).

An analysis of the droplet motion in a spray that is injected into a crossflow can be used to obtain the droplet position and velocity with respect to time. The given set of assumptions are:

1. The droplets are spherical.
2. No additional droplet breakup occurs.
3. Vaporization is negligible.
4. Lift, virtual mass, and Basset forces are neglected.

These assumptions reduce the droplet momentum equations to include only the drag and body forces. The general momentum equation for a single droplet injected along

the positive x -direction, transversely into a downward-flowing air stream in the positive z -direction as shown in Fig. 2.23, is described by

$$F_d = -F_{drag} + F_{body} \quad (2.17)$$

where the net force F_d that drives the droplet motion results from the drag force opposing its motion and the field forces applied on the droplet body. The aerodynamic drag force is given by

$$F_{drag} = \frac{1}{2} \cdot \rho_g U_R |U_R| A_d C_D \quad (2.18)$$

where ρ_g is the air density, and A_d and C_D are, respectively, the projected area and the drag coefficient of the droplet. The relative velocity, U_R , between the droplet and the crossflow, has a magnitude of

$$|U_R| = \sqrt{(u_d - u_g)^2 + (w_d - w_g)^2} \quad (2.19)$$

The transverse and axial velocity components are u and w , which correspond to the x - and z -directions. The subscript “ d ” refers to the droplet and the subscript “ g ” refers to the crossflow air.

The body force, which includes the gravitational force and the buoyant force, and which results from an equivalent volume of air that buoys the droplet, is given by

$$F_{body} = (\rho_d - \rho_g) V_d g \quad (2.20)$$

The body force is equal to the product of the relative droplet and air densities ($\rho_d - \rho_g$), the droplet volume V_d , and the gravitational acceleration g .

Substitution of Eqs. 2.18 and 2.20 into Eq. 2.17 yields the following x - and z -momentum equations

$$\rho_d V_d \frac{du_d}{dt} = \frac{-1}{2} \rho_g (u_d - u_g) |U_R| A_d C_D \quad (2.21)$$

$$\rho_d V_d \frac{dw_d}{dt} = \frac{-1}{2} \rho_g (w_d - w_g) |U_R| A_d C_D + (\rho_d - \rho_g) V_d g \quad (2.22)$$

The following relationships

$$\frac{dx}{dt} = u_d \quad (2.23)$$

$$\frac{dz}{dt} = w_d \quad (2.24)$$

can then be substituted into the equations of motion in order to derive the (x,z) position of the droplet with respect to time. A simple Runge-Kutta numerical routine can be implemented to solve the system of ODEs in Eqs. 2.21 through 2.24.

2.4.2 Relevant Studies

2.4.2a Spray Jet

As the trend toward reducing the size and weight of aeroengines requires a more compact combustor, increased emphasis is placed on decreasing the mixing length while attaining a well-mixed fuel and air mixture for low-pollutant emissions. The reduction of the mixing length is important especially in lean premixed prevaporized systems in which the long premixing chambers result in the combustor becoming more prone to autoignition (Chin et al., 1986). Atomizing the liquid before

its injection into a crossflow reduces the mixing length by the distance that would have been associated with the time required for liquid breakup. Injecting the spray transversely into, rather than coaxially with, a flow of air also takes advantage of the dynamic mixing induced by the jet-crossflow interaction.

Section 2.3 featured numerous studies that investigated the atomization and spray structure of a pure liquid jet injected into a crossflow. By comparison, research into the injection of spray droplets has not been as extensive. However, because the particle laden jet is similar to the spray jet, these studies are also reviewed in Section 2.4.2b.

As part of a model validation, Crowe et al. (1977) demonstrated the application of their "Particle-Source-In Cell" (PSI-CELL) model to a spray cooling system which consisted of jets of water sprays injected at an angle into a crossflow of cooling air. The name of the model, which incorporates mass, momentum, and energy transfer between the droplet and ambient gas, is based on the idea that any mass, momentum, and energy received by the gaseous medium originates from the droplets. The PSI-CELL model predicts the droplet trajectories, size, and temperatures after considering the effects of mass, momentum, and energy coupling with the velocity, pressure, and temperature field of the surrounding gas. The model predicted the trajectories of specified droplet sizes, as well as the gas flow field distributions in a spray in crossflow situation. Other than demonstrating the model on this type of flow, this study did not perform any parametric variation on the system.

Chin et al. (1986) studied the evaporation history of a spray of droplets injected into a crossflow. The authors developed a code to predict the volume fraction of

vaporized fuel as a function of downstream distance. Rosin-Rammler parameters (Rosin and Rammler, 1933) described the initial droplet size distribution of the injected spray. The D^2 -law for droplet vaporization was used with the appropriate convection coefficients that accounted for the droplet heat-up period and steady-state evaporation. The governing momentum equation equated the droplet momentum with the drag force acting upon the droplet in order to solve for the relative velocity of the droplets. The drop trajectories were computed with initial zero velocity components except for the velocity component normal to the crossflow, which was set to the initial fuel injection velocity. The effects of the ambient pressure and temperature of the air, the drop size distribution and the mean drop size, and the crossflow air and initial fuel injection velocities on the spray vaporization history were observed. The ambient temperature, mean drop size, and crossflow air velocity produced the most significant effects on droplet vaporization.

Other models that have been developed for the spray jet in crossflow are geared toward agricultural applications in order to describe the drift of a spray that is injected by a moving spray boom. The crossflow velocities affecting agricultural sprays are considered weak, as they are induced by a spray boom that is moving on the order of 10 m/sec with respect to the ground. The models are concerned with simulating spray drift, which is important in the spraying of pesticides, and which is more likely to occur under weak crossflow conditions. The analysis performed on such a system still involves the consideration of the different phenomena affecting the droplet in order to simulate spray transport. A model developed by Holterman et al. (1997), for example, accounted for the effects of gravitational and drag forces, initial velocity, and

vaporization on the droplets; the effect of air entrainment into the spray as induced by the moving droplets; and the effect of the crossflow velocity profile, which was assumed to be logarithmic for the region above a crop canopy. The model is three-dimensional near the injector exit where entrainment occurs, but essentially becomes two-dimensional in the far-field region where only the crossflow effects are felt. The governing equations for this system were primarily used to determine the effects of such parameters as the jet injection height, crossflow velocity, nozzle size, and liquid pressure supply on the sedimentation of the spray onto the ground.

A more rigorous investigation into the injection of a spray of droplets into the crossflow was pursued by Ghosh and Hunt (1998). Their study was also applied to agricultural boom spraying. Their main goal was to develop an analytical solution describing the trajectory of the various spray size classes in the z - r (axial-radial) plane with a set of differential equations that can be solved with simple numerical routines. The derivation was first made for an axisymmetric spray and later applied to flat fan sprays. The droplet equations of motion considered only the drag and gravitational forces acting upon the droplets, and resulted in equations similar to Eqs. 2.21 and 2.22. The analysis assumed that the droplets were spherical, and neglected droplet collision, secondary breakup, and vaporization effects.

To solve the droplet momentum equations, a characterization of the velocity flow field was required in order to calculate the relative velocity between the crossflow air and the droplets. Although the droplet trajectories in only the r - z plane were described, Ghosh and Hunt (1998) accounted for the three-dimensional nature of the flow field in deriving the velocity fields.

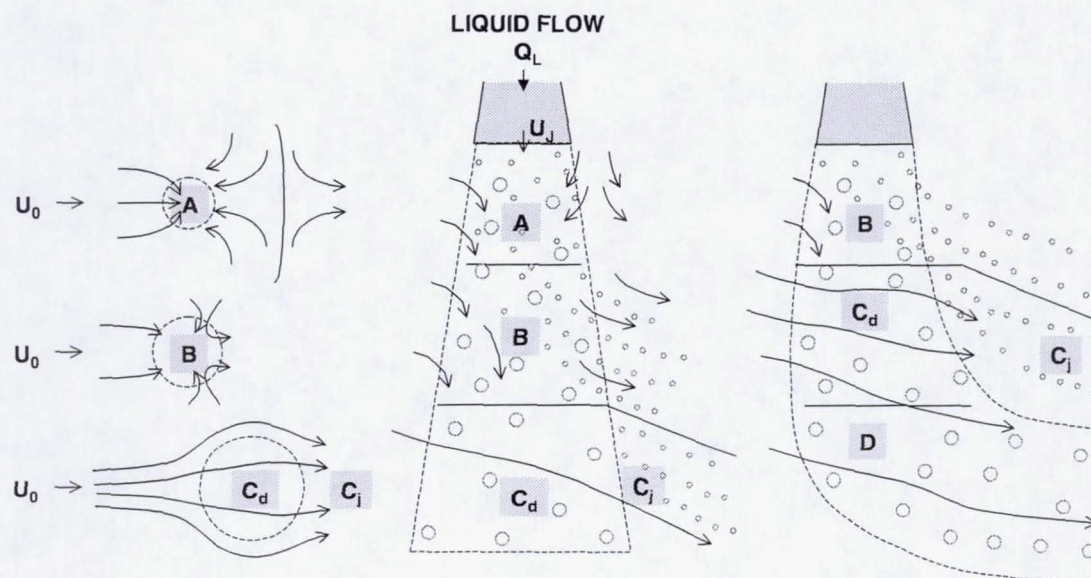


Fig. 2.24 Zones used to analyze the trajectory of the spray jet in crossflow. (Ghosh and Hunt, 1998).

The velocity fields were derived for different spray zones (Fig. 2.24).

Depending on the magnitude of the crossflow velocity, the modeled spray was comprised of a certain combination of the different zones. For example, for weak crossflow velocities ($U_{cross}/U_{jet} < 0.1$), the zones comprising the spray included: zone (A), in which the induced vertical air velocity within the spray entrains the surrounding air; zone (B), in which the surrounding air is still entrained into the jet while small droplets are being dispersed downstream of the spray; and zone (C), in which the small droplets are still being dispersed while the crossflow air passes through the spray. For moderate crossflow velocities ($U_{cross}/U_{jet} > 0.3$), the spray consists of

zones (B) and (C) as described above, as well as zone (D), in which the crossflow passes through the spray and disperses large droplets.

Due to the differences in flow fields, the velocity field analysis depended on each zone. For instance, the velocity field in zone (A) was modeled as an irrotational flow consisting of the sum of two potential fields—one which simulated a uniform flow around a bluff body, and the other which resulted from the vortex sheet formation around the jet. On the other hand, the infusion of the crossflow air into the spray jet resulted in modeling the velocity field in zone (C) as an air flow through a porous cylinder with the velocity fields based on the horizontal and vertical velocity perturbations in the spray.

The model of Ghosh and Hunt (1998) was used to obtain droplet trajectories for various size classes of droplets. The predicted droplet trajectories showed the potential of the model to provide insight into the effect of parameters such as the liquid injection rate, spray angle, and the crossflow velocity profile. Ghosh and Hunt (1998) also suggested that the analysis provided a more accurate description of the flow field than a turbulent free jet model. The spray jet velocity field is similar in structure to that of the turbulent air jet, but both differ in turbulent structure. The difference between the spray jet and the turbulent air jet is attributed to the presence of the injected droplets, which impart extra momentum on the induced air flow and in turn, lead to a decreased rate of decay in the induced air flow velocity.

The studies by Ghosh and Hunt (1998) and Holterman et al. (1997) are geared more toward agricultural applications in which the crossflow velocity, induced by the relative velocity of an atomizer to its surroundings (e.g., as in a crossflow produced by

a slow-moving pesticide-spraying truck), is weak. These studies also utilized flat fan atomizers, commonly used in agricultural applications, to produce the spray jet. Flat-fan sprays are pressure atomizers that do not use air to assist in atomization.

Flat-fan sprays were also the focus of recent experimental studies that were conducted on sprays in a crossflow (Phillips and Miller, 1999; Phillips et al., 2000). In the experimental studies, the spray field was characterized in terms of its volume flux, and its droplet size and velocity characteristics. Whereas Phillips and Miller (1999) investigated the flow field of a single flat-fan spray injected into a crossflow, Phillips et al. (2000) studied the effect of an overlapping series of flat-fan sprays on the flow of the droplets and air. In the Phillips et al. (2000) study, a bubble tracing method that was also used to visualize the crossflow interaction with the spray showed that the crossflow air could not penetrate the spray under a weak crossflow velocity of 0.75 m/sec, but did penetrate the spray at moderate crossflow velocities of 3.0 m/sec. It should be noted that the crossflow velocities encountered in gas turbine spray applications are typically one to two orders of magnitude higher than these velocities.

2.4.2b Particle-Laden Jet

Studies on particle-laden jets injected into a crossflow can also shed insight into the behavior of spray. The particle-laden jet, usually composed of a gaseous jet loaded with a uniform spherical particle distribution, does not reflect the polydispersed droplet distribution in a spray. However, the two-phase nature of the particle-laden jet still warrants its comparison to an airblast spray.

Edelman et al. (1971) conducted experiments using still photography and temperature profile measurements in which 1- to 5- μm graphite particles and 1- μm boron particles were seeded into an air jet and injected into a crossflow of air. The results showed that the particle trajectories appeared to coincide with the trajectories of the gaseous phase of the jet, which suggested that the motion of the particles were affected by the momentum of the gaseous phase. In addition, a model that combined the equations of motion of the particles with those related to the gas phase was developed to predict the trajectories of the particles in the crossflow. The Stokes drag law, though limited to creeping flows, was used in the model, and compared with the results obtained from using an empirically-derived drag law from Rudinger (1963). The comparison between the experimental and modelling results showed that the empirically-derived drag law predicted the penetration of the particles better than the Stokes drag law, because the empirical law accounted for the large changes in the acceleration of the particles, as well as for the interactions between the particles and the gaseous phase of the jet.

Salzman and Schwartz (1978) also performed an experimental study in which a gaseous jet seeded with 15- μm silicate particles were injected into a crossflow and assessed in terms of its penetration and dispersion. The particle distribution was measured across the cross-sectional plane through the center of the jet, in the direction of the crossflow. To scale the jet trajectory and dispersion equations, Salzman and Schwartz (1978) developed a characteristic momentum length, l_m . Their definition of l_m combines the jet momentum length, $d_j(U_j/U_{cross})$, used by Pratte and Baines (1967) and by Wooler (1969) in their jet-crossflow studies, with the characteristic length of a

turbulent jet, $d_j(\rho_j/\rho_{cross})^{0.5}$, developed by Ricou and Spalding (1961) for an axisymmetric free jet, to obtain

$$l_m = d_j \cdot \left(\frac{\rho_j}{\rho_{cross}} \right)^{0.5} \cdot \frac{U_j}{U_{cross}} \quad (2.25)$$

where d_j is the diameter of the jet, and (ρ_j/ρ_{cross}) and (U_j/U_{cross}) are, respectively, the jet-to-crossflow density and velocity ratios. The momentum length l_m in Eq. 2.25 is essentially the product of the jet diameter and the square root of the jet-to-crossflow momentum-flux ratio. Upon applying l_m to scale the downstream and penetration distances, the following correlations for jet trajectory (Eq. 2.26) and jet dispersion across the crossflow (Eq. 2.27) were obtained:

$$\frac{x}{l_m} = 1.92 \cdot \left(\frac{z}{l_m} \right)^{0.33} \quad (2.26)$$

$$\frac{\Delta x}{l_m} = 2.22 \cdot \left(\frac{z}{l_m} \right)^{0.14} \cdot \left(\frac{U_j}{U_{cross}} \right)^{-0.31} \quad (2.27)$$

In these equations, x denotes the penetration distance and z represents the downstream distance. Based on a comparison of the trajectories predicted by Eq. 2.26 and the trajectories predicted by single-phase penetration equations, Salzman and Schwartz (1978) suggested that the particle-laden jet can be treated as a single phase jet with an equivalent jet density that takes into account the densities of the different components of the jet.

Han and Chung (1992) developed a numerical simulation to describe the trajectory, velocity, and density of a two-phase, particle-laden jet injected into a

crossflow. The particles in the jet were assumed to be solid spheres of uniform diameter. The trajectory results depicted interesting phenomena with regard to the penetration of the particle and gaseous components of the jet. Both the particle and gaseous components of the two-phase jet achieved a significantly farther penetration into the crossflow than did the single phase gaseous jet. The particle phase exhibited a slightly higher penetration than the co-flowing gaseous component, though this difference was not as great as the difference between the trajectories of the pure gaseous jet and each individual component in the two-phase jet. The close interaction seen here between the particle and gaseous phases of the two-phase jet can be seen later in the results presented in this dissertation.

2.4.2c Airblast Spray Jet

The set of hardware that was used in this experiment was designed and first tested by Seay (1995). The hardware simulates a single spray jet of the LBI injector, which enables the study of single spray dispersion into a crossflow of air. In addition to directly scaling the experiment to the LBI injector, the hardware was designed with modularity and parametric variation in injector geometry in mind. The width of the crossflow can be varied. The fuel tube is interchangeable with other fuel tubes having a different hole size d and orifice length to diameter ratio, l/d . The adjustable fuel tube tip protrudes into or recedes from the airblast air plenum to affect the velocity of the atomizing air that passes over the fuel tube tip. The orifice diameter through which the spray is injected can also be varied.

The tests conducted by Seay (1995) mainly concentrated on idealized spray conditions. An "unconfined" large-area crossflow section was utilized. Methanol was used as the liquid fuel, partly because of its proven use in liquid mass fraction imaging (Igushi et al., 1993). In addition, all of the tests were conducted under atmospheric pressure conditions. As it can be seen, the experimental conditions tested by Seay (1995) do not correspond to realistic operating conditions in a gas turbine engine. This dissertation takes a step toward bridging the experiment with practical operating conditions by conducting the tests under elevated pressures to simulate the compressed air feed to the combustor, by using a distillate fuel as the liquid injectant, and by using a narrow crossflow width that is scaled to the gap in the LBI injector into which the fuel spray is injected.

2.4.3 Summary of the Spray Jet in Crossflow Studies

Several observations can be made from the studies on the injection of the spray/particle-laden jet into a crossflow. The main responses that were investigated included the droplet/particle trajectories, and the vaporization and sedimentation history of the spray with respect to downstream distance. The atomization of the spray is not considered in the studies; rather, the droplet or particle size distributions are presumed. Given the relatively unexplored field of airblast-atomized spray jets in crossflow as well as the need to investigate the airblast spray jet under conditions relevant to the gas turbine engine, the work presented in this dissertation is a step toward filling this void.

CHAPTER 3

RESEARCH GOALS AND APPROACH

A rapid mixing strategy for liquid fuels involves the transverse injection of a fuel spray into a high velocity air flow. This strategy offers a means of producing a well-mixed fuel and air mixture within a compact length so that the combustor can be operated under the ultra fuel-lean conditions that preclude NO_x pollutant formation. The overall goals of the research program are (1) to characterize the atomization, mixing, and transport processes that control the dispersion of an airblast-atomized spray jet that is injected into a crossflow of air, and (2) to establish an understanding of the processes that govern the penetration and dispersion of an airblast-atomized spray jet in a crossflow of air. To meet the goals of the program, this study is split into three main parts which are delineated as follows:

Part I: Development of the Spray Imaging Techniques (Chapters 5-6)

To characterize the spray field, diagnostic tools are developed to probe the airblast spray. A procedure involving UV planar imaging and processing is used to separately visualize the fuel and atomizing air components in the spray.

Part II: Characterization and Analysis of the Airblast-Atomized Spray Jet without a Crossflow (Chapters 7-8)

The objective of this part is to assess the overall and internal structure of the spray before introducing the crossflow velocity. Parametric variations of injector geometry and flow rates are performed to gauge their effect on the spray. The high-speed video

system is used to capture the overall structure of the airblast spray for a wide range of air and fuel flow conditions. The UV planar imaging protocol developed in Part I, together with phase Doppler interferometry (PDI), are applied to probe the airblast spray and provide detailed measurements. The images are analyzed in terms of such parameters as the spray angle and quality in order to identify the key conditions that affect the atomization and dispersion of the spray. The results from the non-crossflow condition also serve as a basis for comparison with the sprays injected into a crossflow.

Part III: Characterization and Analysis of the Airblast-Atomized Spray Jet in a Crossflow (Chapters 9-10)

The overall structure of the airblast spray jet in a crossflow is captured over a wide range of operating conditions using high-magnification video, the results of which are also used to derive a correlation that describes the trajectory of the jet. PDI, combined with the UV planar imaging techniques developed in Part I, are applied to yield plane-specific imaging results for various conditions. The spray quality analysis developed in Part II is used to assess the effects of the parametric variation on spray dispersion. In addition, a simplified droplet trajectory analysis utilizing the PDI-measured droplet size and velocity data obtained in Part II is developed to predict the volumetric dispersion of the liquid, and to compare the results with corresponding images of the spray in order to determine the validity of the analysis.

Before presenting and discussing the results of the different phases of the research program, a description of the hardware, facilities, and present diagnostic capability is summarized in Chapter 4.

CHAPTER 4

DESCRIPTION OF THE SPRAY EXPERIMENT

A model experiment was designed and built to simulate a single airblast-atomized spray jet from the LBI injector. The experimental hardware was designed with the following in mind: (1) relatively clean boundary conditions to facilitate modeling efforts, (2) modularity of parts which allow for a parametric study, and (3) portability, which enables the installation of the experiment into an atmospheric test stand as well as into a vessel designed for elevated pressure studies. This chapter describes the features of the hardware, as well as the facilities, operating conditions, and existing diagnostics used in the experiment.

4.1 Hardware

In the following description of the hardware dimensions, the primary units are given in SI. However, because the fabrication of the hardware utilized tools based on the English system of units, the corresponding English units are noted in parentheses. While English units are given alongside the SI units in this chapter, the English units are omitted from the text in subsequent chapters.

The modular design of the single spray jet experiment facilitates its installation into either the atmospheric or elevated pressure facilities. The single spray jet injection panel can be installed in either a downward injection orientation to issue a spray into still ambient air, or for a sideways injection into a crossflow of high velocity air. The

crossflow test section exists in two configurations—a confined test section with a cross-sectional length of 76.2 mm (3.0 in.) and transverse width of 18.0 mm (0.71 in.), and a larger test section possessing a transverse width of 101.6 mm (4.0 in.). In these tests, the smaller cross-section measuring 76.2 mm x 18.0 mm (3.0 in. x 0.71 in.) was used in order to simulate the narrow confines in the quarl of the LBI injector.

Since the inception of the basic design by Seay (1995), several hardware modifications have been made to expedite the parametric hardware changes. Among the notable have been the shortening of the fuel tube and the integration of a compact traversable fuel tube system to enable the experiment to fit into the elevated pressure vessel facility, the incorporation of an interchangeable disk design to facilitate the changing of the spray orifice diameter, and the fabrication of a back panel that allows additional optical access in the crossflow duct. The fuel hole diameter was also doubled in diameter to directly scale the single jet experiment to the LBI geometry. The fuel holes of the LBI injector had been doubled in size from the original design of Shaffar and Samuelsen (1998) after tests at high temperature conditions caused the fuel to coke and clog the fuel ports (Leong et al., 2000). The effect of enlarging the fuel hole diameter on atomization is minimal, as explained later in Section 4.1.1.

4.1.1 Injection Panel Specifications

The main hardware component is the injection panel, which is shown in Fig. 4.1. The injection panel consists of the main body which houses the atomizing air plenum, a detachable fuel injection tube, and interchangeable disks that allow for the parametric variation of spray jet hole size. Note that the injection panel contains two

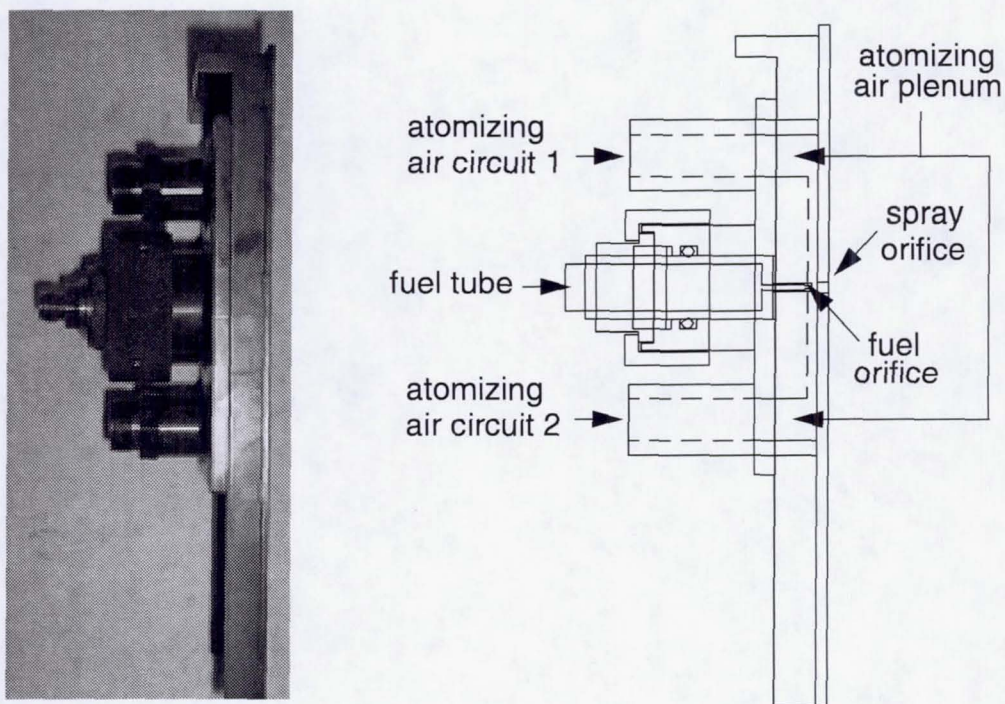


Fig. 4.1 Airblast spray injection panel

orifices—one which belongs to the fuel injection tube (referred to as the *fuel* orifice), and one through which the atomized fuel and air are injected (referred to as the *spray* orifice). The fuel jet, upon injection from the fuel orifice, is atomized by the air in the plenum. The fuel and atomizing air mixture is injected through the spray orifice and emerges as a spray jet that issues into either a quiescent environment or directly into a crossflow of high velocity air.

Two air circuits feed the atomizing air plenum on opposite sides of the fuel tube through two ports that are 12.7 mm (0.50 in.) in diameter. The placement of the air circuits opposite from each other and across the fuel injection tube is supposed to

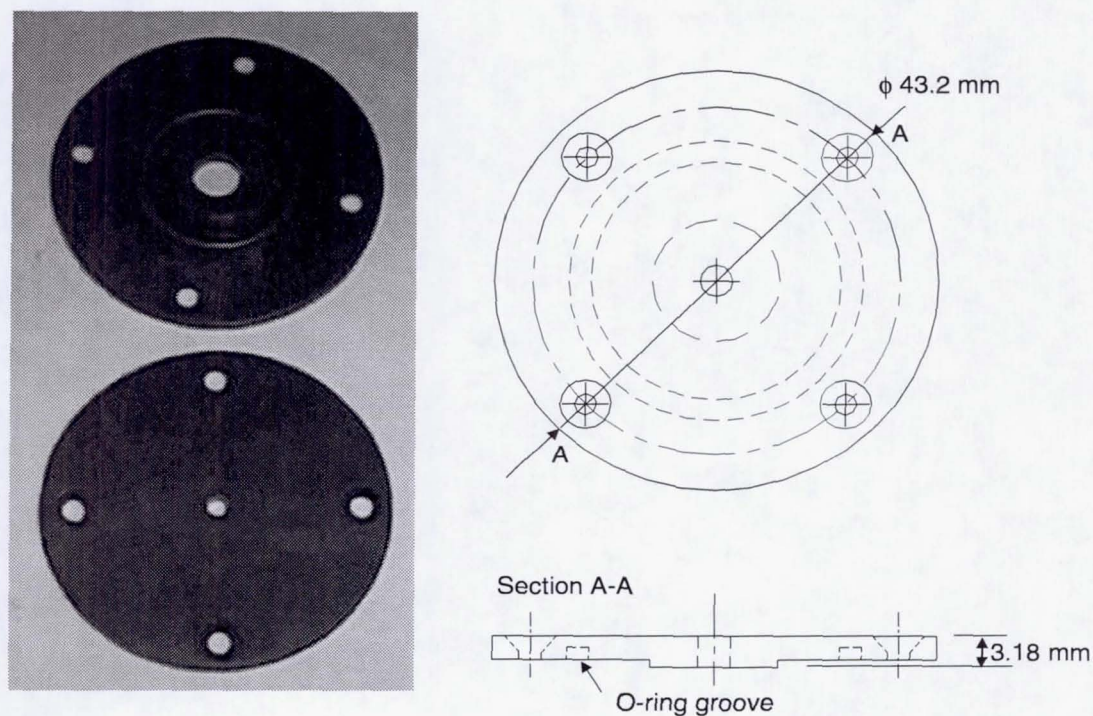


Fig. 4.2 Disks for interchanging spray orifice diameters

simulate the atomizing air flow path in the LBI injector. The plenum dimensions are 92.7 mm x 19.1 mm x 3.18 mm (3.65 in. x 0.75 in. x 0.125 in.), which respectively represent the length, width, and depth of the channel. The plenum feed is welded onto a plate that is 3.18 mm (0.125 in.)-thick. The plate contains a circular recess into which disks with varying spray orifice sizes (Fig. 4.2) are seated flush with the rest of the plate, and are secured by four flathead screws. The disks are 3.18 mm (0.125 in.)-thick at the spray orifice. Two disks with hole diameters of 3.18 mm (0.125 in.) and 4.22 mm (0.166 in.) are interchanged in the experiment. The dimensions of the spray orifices for these two disks result in length to diameter ratios (l/d) of 1 and 0.75 for the

3.18 mm (0.125 in.)- and 4.22 mm (0.166 in.)-dia. holes, respectively. The discharge coefficient of the orifices, measured in the injection panel, was 0.71.

The fuel injection tube has a body made of a round tube to which a rectangular tip is welded (Fig. 4.3). The fuel tube is interchangeable, and allows for fuel holes of various diameters and l/d to be tested. The fuel tube is also traversable, which enables the variation of fuel tip distance to the back of the injection panel. Threads soldered onto the fuel tube work in conjunction with a captive nut to traverse the tube as the nut is turned. The insertion of the fuel injection tube can be adjusted in order to set the protrusion of the injector tip into the channel of the air plenum. The fuel tube tip was adjusted such that the tip protruded halfway, or 1.59 mm (0.0625 in.) into the channel.

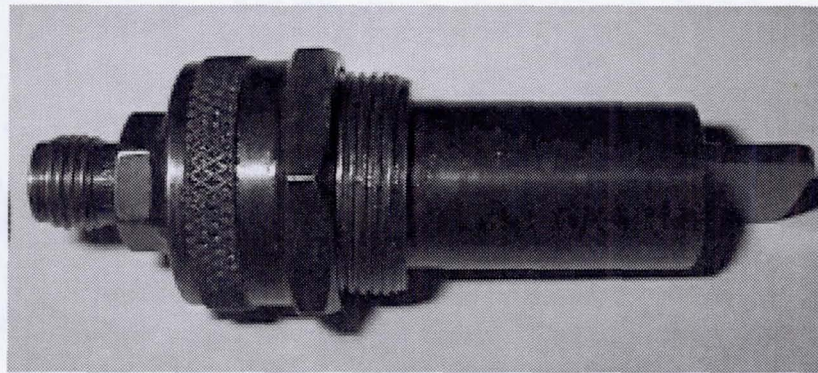
Although the fuel hole diameter in the present injector was doubled in size from the tests of Seay (1995), the effect of the fuel hole size enlargement on spray formation is minimal. For low-viscosity fluids, the orifice diameter should not affect the D_{32} of the spray if a high Re_L number is maintained. The following relationship by Lorenzetto and Lefebvre (1977), which characterizes the D_{32} of a spray formed by airblast atomization of a plain jet in terms of the liquid and air properties, also illustrates this point:

$$D_{32} = 0.95 \frac{(\sigma \dot{m}_L)^{0.33}}{\rho_L^{0.37} \rho_A^{0.30} U_R} \left(1 + \frac{\dot{m}_L}{\dot{m}_A}\right)^{1.70} + 0.13 \left(\frac{\mu_L^2 d_0}{\sigma \rho_L}\right)^{0.5} \left(1 + \frac{\dot{m}_L}{\dot{m}_A}\right)^{1.70} \quad (4.1)$$

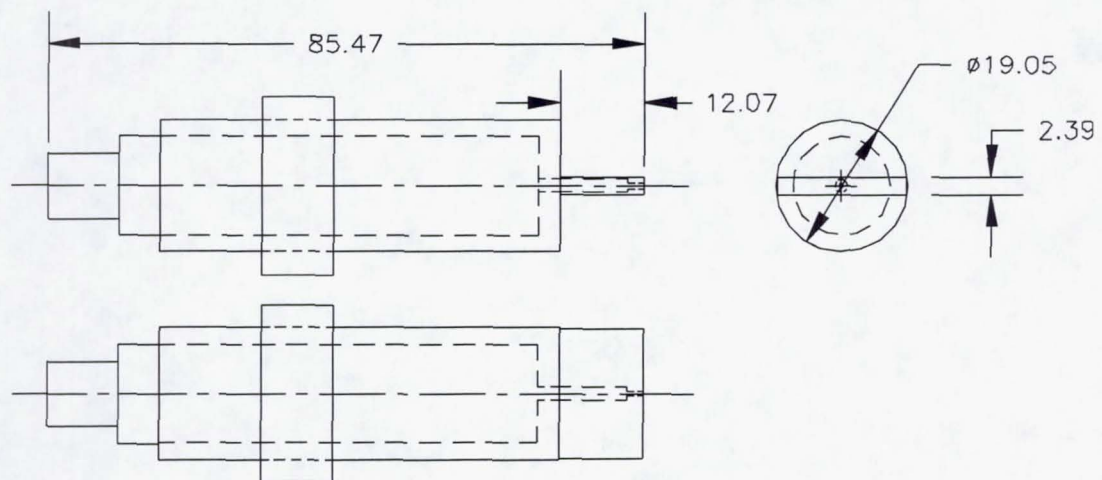
Eq. (4.1) shows that the first term is weighted more toward the liquid surface tension, σ , while the second term is weighted more toward the liquid dynamic viscosity, μ_L .

For fluids such as jet-A and calibration fluid, in which σ is relatively larger than μ_L , the

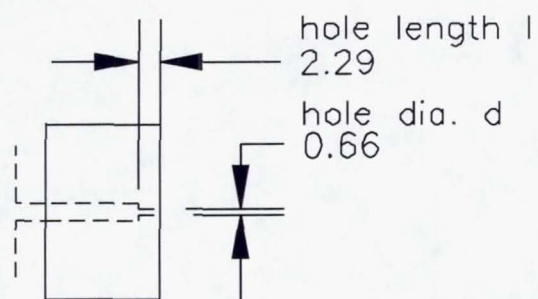
(a)



(b)



(c)



Note: All dimensions are shown in mm.

Fig. 4.3 Compact, traversable fuel tube design: (a) photograph, (b) drawing, and (c) detailed drawing of fuel tip.

first term dominates (Lefebvre, 1999). As the second term becomes negligible, the effect of the fuel hole diameter d_0 on the droplet D_{32} also diminishes. The doubling in size of the fuel hole diameter in the experiment should not affect D_{32} as much as other parameters such as σ , the fuel and atomizing air flow rates \dot{m}_L and \dot{m}_A , and the fuel-air relative velocity U_R .

4.1.2 Crossflow Test Section

The crossflow conditioning section used in the crossflow tests prepares the high velocity air flow that enters the rectangular duct. The crossflow test section was designed by Seay (1995) to transition from the entrance, which has a circular geometry of diameter 133.4 mm (5.25 in.), to the rectangular geometry of the crossflow test-section, which measures 76.2 mm x 18.0 mm (3.0 in. x 0.71 in.). Fig. 4.4 shows the transition piece installed in the experiment. The transition piece slides into a pipe with a nominal diameter of 152.4 mm (6.0 in.), and is held inside the pipe by interfacing plates to which the injection panel, back panel, and windows are installed. The discharge coefficient of the transition piece, which was designed to introduce a uniform velocity profile to the test section, is near unity.

In the crossflow configuration, the experiment is oriented vertically so that the crossflow of air flows downward in the axial z -direction. The spray is injected transversely into the flow in the x -direction. The y -axis runs parallel to the injector and back wall panel, and perpendicular to the side windows. The origin of the coordinate system is located at the center of the exit plane of the spray orifice.

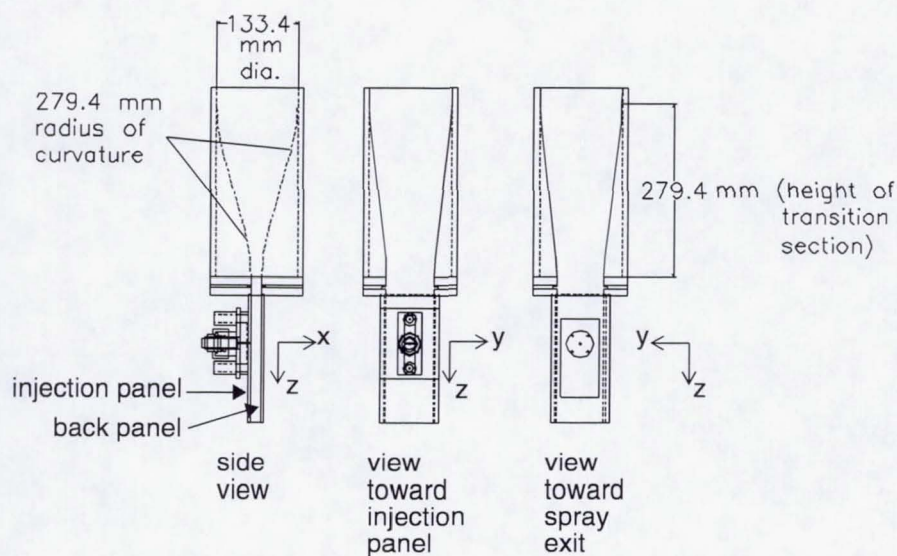
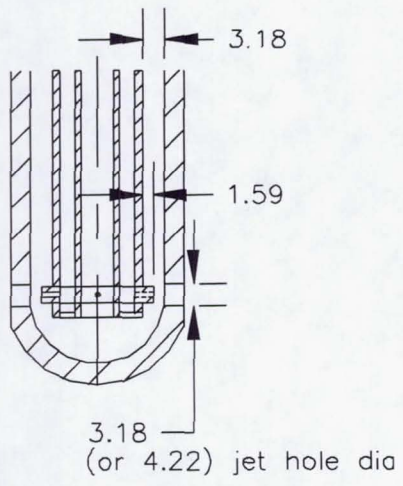
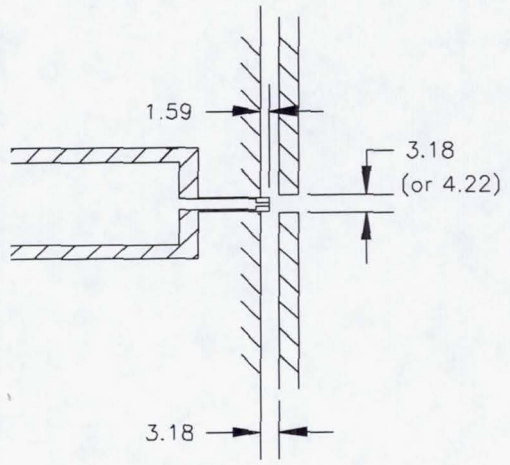
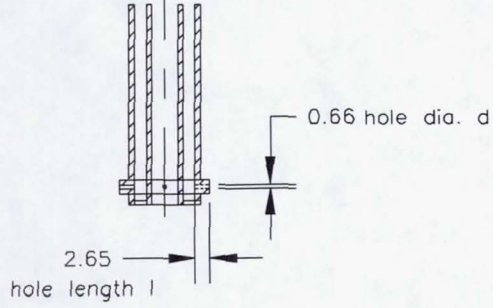
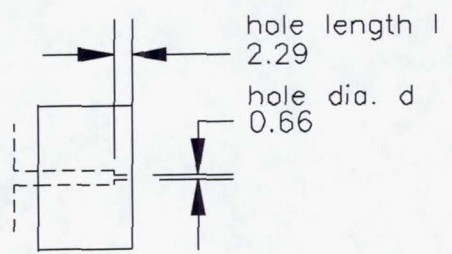
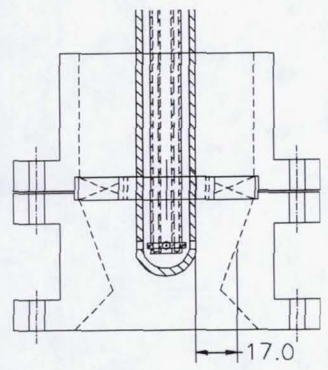
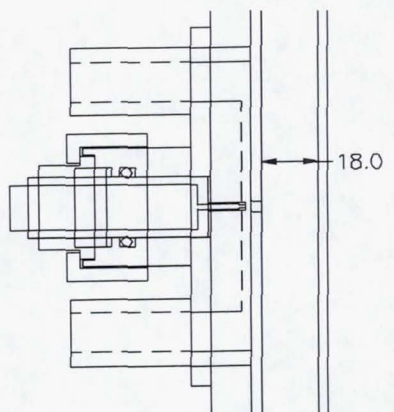


Fig. 4.4 Hardware for the spray jet in crossflow configuration.

4.1.3 Comparison between the LBI and Single Jet Hardware

The hardware used in the fundamental single jet studies is directly scaled to represent one of the eight jets from the LBI injector. Table 4.1 compares the main features of the LBI injector that were maintained in the spray jet experiment. Relevant parameters in the airblast passageway (Table 4.1, first row) that are kept in the spray jet experiment include the protrusion of the fuel tube tip halfway across the airblast channel ($1.59 \text{ mm}/3.18 \text{ mm} = 0.5$), and the l/d of the spray orifice ($l/d = 1.0$ and 0.75 for the spray orifice diameters of 3.18 mm [0.125 in.] and 4.22 mm [0.166 in.]). For the fuel tube passageway (Table 4.1, second row), the l/d of the fuel orifice is 4 for the LBI injector, and 3.5 for the spray experiment, although the fuel orifice diameter is 0.66 mm (0.026 in.) for both cases. Finally, the crossflow channel width (Table 4.1) at

Table 4.1 Comparison between the LBI and the single spray jet injector geometries.

LBI geometry	single spray jet geometry
<p>Airblast passageway</p>  <p>3.18 (or 4.22) jet hole dia</p>	 <p>3.18 (or 4.22)</p>
<p>Fuel tube passageway</p>  <p>0.66 hole dia. d</p> <p>2.65 hole length l</p>	 <p>hole length l 2.29</p> <p>hole dia. d 0.66</p>
<p>Crossflow channel width</p>  <p>17.0</p>	 <p>18.0</p>

Note: All dimensions are shown in mm.

the point of spray injection in the LBI quarl is within 94% of the channel width in the spray experiment.

Although the main features of the LBI injector are matched by the spray experiment, the reader should note that some of the flow field features produced by the injector are not accounted for in the spray tests. For example, the effect of multiple jet interactions are not considered in this experiment. The non-uniform velocity profile imparted on the main air flow by the swirler is also not studied here. However, the characterization of the dispersion of a single spray jet into a uniform crossflow is necessary in order to establish the protocol of measurement and analysis in this system, as well as to understand the basic case before introducing more complexities to the problem.

4.2 Non-Reacting Spray Facilities

The experimental hardware was designed for operation under atmospheric and elevated pressure conditions. The atmospheric test facility (Fig. 4.5) consisted of an aluminum framework on which the experiment was mounted. A metered air circuit for the atomizing air was split into two lines of equal length immediately before the two atomizing air ports in the injection panel. The liquid flow to the injector was supplied by a tank of liquid that was pressurized with gaseous N_2 and metered with a rotameter. For the spray jet in crossflow tests, the crossflow air was provided by a separately-metered circuit that supplied air to the experiment via a 50.8 mm-dia. (2.0 in.) air line. The rotameters that metered the air circuits were calibrated with a laminar flow element

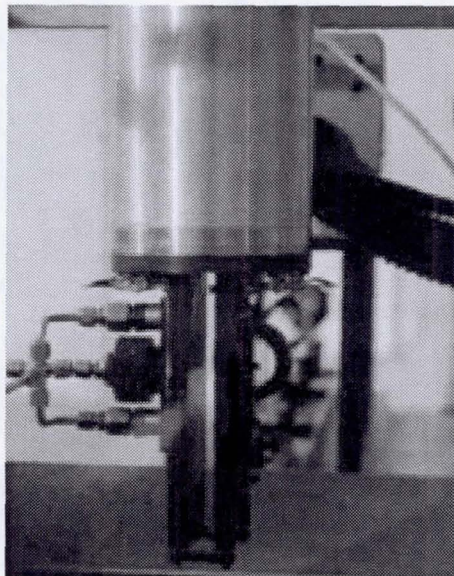


Fig. 4.5 Atmospheric test facility depicting the experiment installed in the crossflow configuration.

(Meriam) for the appropriate flow range. The fuel rotameter was calibrated by measuring the mass flow rate at different rotameter settings.

The elevated pressure facility was utilized only for the spray trajectory study reported in Chapter 9. The vessel, pictured in Fig. 4.6 with the installed hardware, contains two oblong ports set at 180° apart that allow access for laser diagnostics. A pair of oblong Pyrex windows 44.5 mm (1.75 in.)-thick are set into the ports. The facility is rated for operation of up to 15 atm, and has an air preheat capability of 922 K (1200° F). The crossflow air flow is plenum-fed by air supplied through two ports at the top of the vessel (see right picture in Fig. 4.6). The atomizing air is fed by a separately metered air line. Depending on the flow range and conditions, the air flows

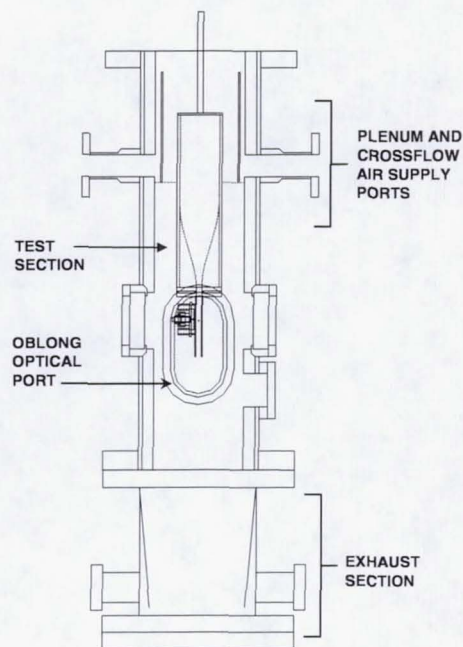
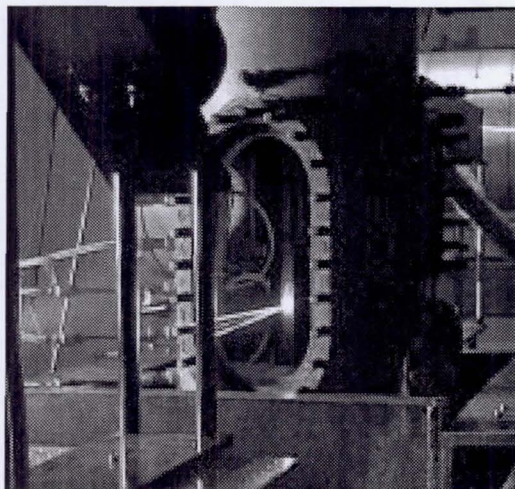


Fig. 4.6 Elevated pressure facility for non-reacting spray tests.

were metered using either orifice plates, rotameters, or mass flow controllers, while the liquid flow was metered by either a rotameter or a turbine meter.

4.3 Existing Diagnostic Capability

4.3.1 High-Speed and High-Magnification Video

Video of a spray that is back-lit with a light source provides a quick means of evaluating sprays under different geometric and operating conditions. The video images taken of the spray are not plane-specific—a compilation of these images does not yield a three-dimensional characterization of the spray. Nonetheless, the images

can be used to capture the overall structure, and the maximum and minimum extent of spray penetration with and without the crossflow of air.

Two camera systems were used in order to gain information on the structure of the spray. Both the high-magnification and the high-speed video systems can record video of the spray structure at the injection point, and can magnify the system to resolutions of at least 6 pixels/mm.

The setup for obtaining high speed video of the spray is depicted in Fig. 4.7. The system consists of a high speed video camera (Redlake Motion Scope Model PCI 2000) fitted with a macro lens (Pentax 50-mm focal length, f/2.8 lens), a light source, and a computer with a PC board that records and stores movies of the spray. The high speed video camera faces the spray while a 300 W flat-faced halogen lamp illuminates the spray from the rear. The camera system is capable of recording movie files at a rate of up to 2000 frames/sec, a rate that corresponds to a computer storage limitation of two seconds. For each run in this experiment, a 100 frame segment is saved to disk and averaged using an image processing software (Image Pro Plus 4.0,

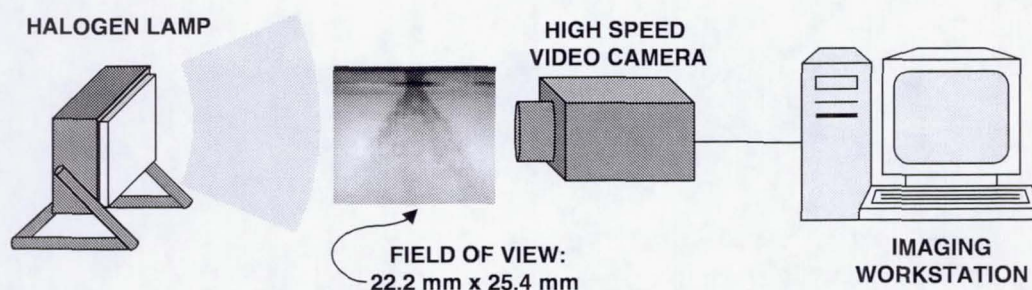


Fig. 4.7 High-speed video imaging system for bulk light scattering capture.

Media Cybernetics). The captured field of view measured 22.2 mm x 25.4 mm, and had an image resolution of 6.3 pixels/mm.

Time-averaged images of light scattering by the spray are captured using a high-magnification video camera setup. The video imaging system, consisting of a CCD (charged coupled device) camera head and control unit (Toshiba 1KM41A), is shown in Fig. 4.8. A continuous light source illuminates the spray field from the rear. The CCD video camera (Toshiba 1KM41A) and long distance microscope lens (Infinity Model KV) setup captured a field of view measuring 13.9 mm x 8.9 mm, with an image resolution of 29.6 pixels/mm. Camera shutter speeds as fast as 1/10000 sec can be set using the camera control unit. A 30-sec segment of video was recorded with a video cassette recorder (Sony SVO-2000). An imaging workstation captured and

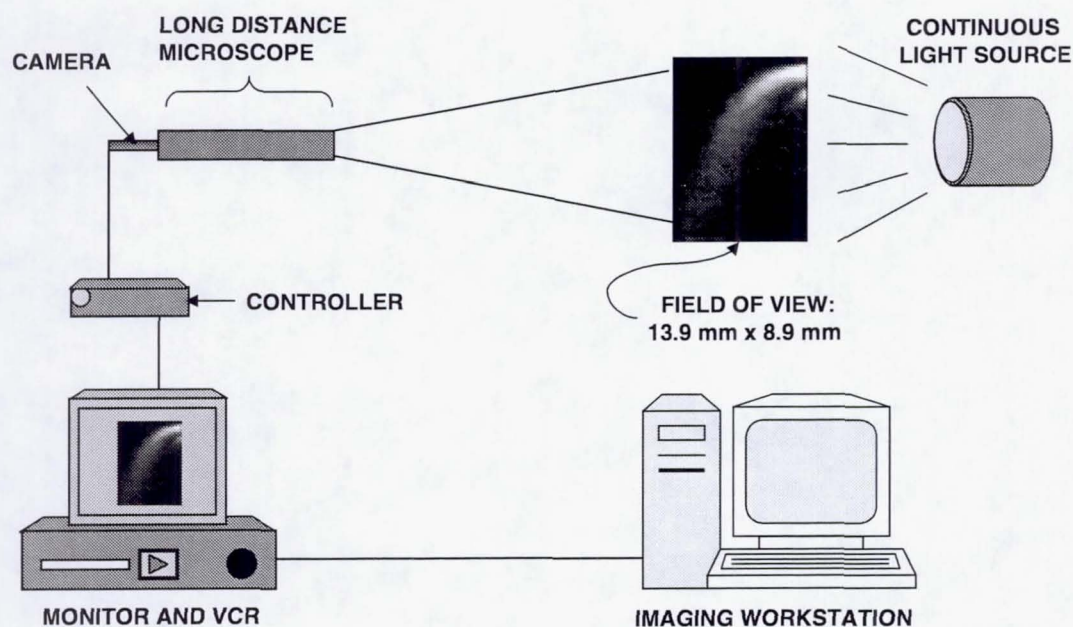


Fig. 4.8 High-magnification video system for bulk light scattering capture.

averaged 15 frames of video. The time-averaged images were processed using an image processing software package (Image Pro Plus 4.0, Media Cybernetics) to reduce background noise.

Each system offers its advantages and disadvantages. The high-speed video can capture a near-instantaneous structure of the spray by attaining shutter speeds as low as $1/20000$ sec. The motion of the drops can be tracked at this shutter speed at a maximum rate of 2000 frames/sec. However, due to disk storage and software limitations, only a few seconds of data can be stored. The high-magnification video system can continuously record a segment of spray images over a longer period of time onto a videotape. However, the image transfer rate of approximately 30-50 frames/sec does not allow for the tracking of spray breakup and droplet motion. The lighting setup for the high-magnification system is also insufficient for capturing "frozen" images of the spray. In summary, the high-magnification video is best applied to characterize the spray over a longer time period, as it has been used in the spray trajectory study presented in Chapter 9. The high-speed video system can also be used to capture the spray trajectory, though only for a period of approximately 2 sec. In this experiment, the high-speed video system was mainly used to capture the instantaneous spray structure of the non-crossflow spray cases presented in Chapter 7.

4.3.2 Phase Doppler Interferometry

Phase Doppler interferometry (PDI) is used to obtain droplet size and velocity measurements simultaneously in the spray. The basic premise behind the system involves the capture and analysis of the light scattered by droplets that pass through a

laser-generated probe volume in the flow. The implementation of PDI involves the creation of a probe volume formed by an intersecting pair of laser light beams. The probe volume, which has a size that is on the order of the laser beam diameter, consists of high- and low-intensity light fringes that result from the interference pattern produced by the intersecting beams. When a droplet passes through the probe volume, the droplet scatters the light such that the fringe spacing varies in accordance to its size. The scattered light also undergoes a Doppler shift in frequency that is related to the droplet velocity. The phase difference between the Doppler-shifted light and a reference signal is used to calculate both the droplet size and its velocity. A detailed description of the theory and implementation of the PDI system can be found in papers by Bachalo and Houser (1984), and McDonell and Samuelsen (1988).

Figures 4.9 and 4.10 depict the setup of the PDI system with respect to the experiment in the atmospheric test facility. The PDI system consists of a 1W Argon-ion laser (Lexel Model 85) that is used in conjunction with a 2-D transmitter (Aerometrics Model 1100-3S) to generate the pairs of blue (488.0 nm) and green (514.5nm) laser beams that produce the probe volume. The planes through each beam pair are oriented at right angles to one another in order to measure two orthogonal velocity components. A receiver that houses the detectors that capture the scattered light (Aerometrics Model 2100-3) is positioned 30 degrees from the axis of the transmitter. The captured light is then sent to a photodetector for processing and analysis.

The droplet sizing component of the PDI system sizes the droplets as they pass through the set of green fringes in the probe volume. This set of fringes must be

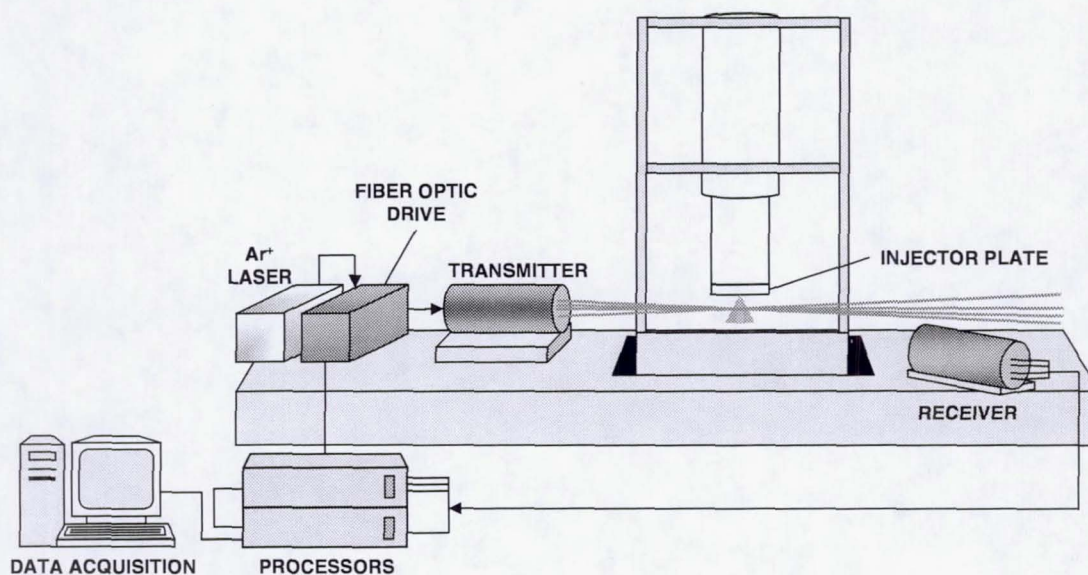


Fig. 4.9 PDI system (Real-time Signal Analyzer, Aerometrics) setup to measure the droplet size and velocity of the spray without crossflow in the atmospheric test facility.

oriented perpendicular to the main directional component of the droplets. Hence, the positioning of the transmitter and receiver depends on the direction of spray injection. In the non-crossflow case, the injection panel is installed for a downward spray injection with the plate parallel to the table, as seen in Fig. 4.9. In this configuration, the transmitter is installed with the green beams projected from the upper and lower quadrants of the transmitter lens. The receiver is positioned 30° from the axis of the transmitter, and on top of the optical bench so that the detector arrangement in the receiver detects the appropriate scattering signals.

In the crossflow configuration such as that depicted in Fig. 4.10, the spray is injected transversely into the crossflow of air, which flows downward. For this

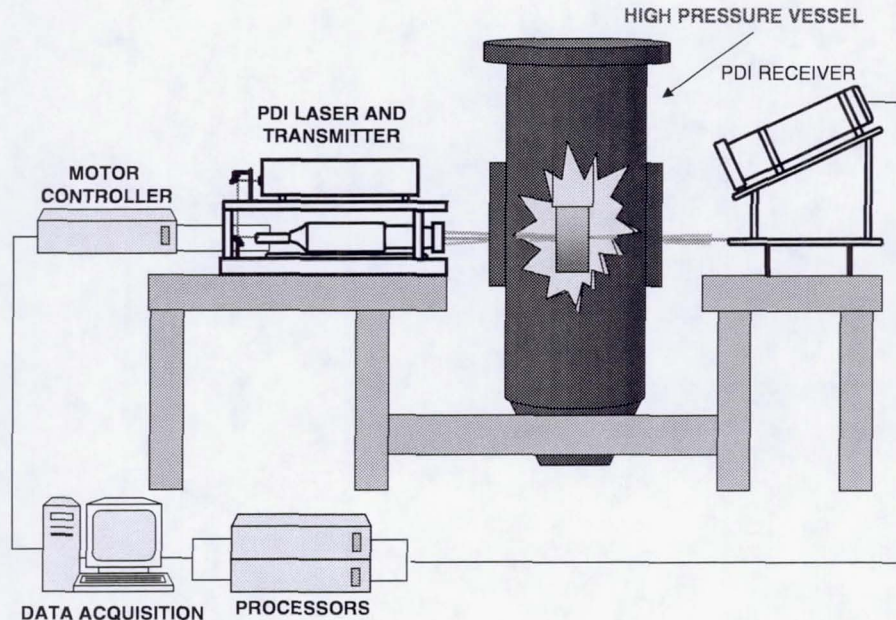


Fig. 4.10 PDI system setup (Phase Doppler Particle Analyzer, Aerometrics) to measure the spray in the crossflow configuration in the elevated pressure facility.

configuration, the spray experiment and PDI system in Fig. 4.9 are essentially rotated from the horizontal plane by 90° . The PDI system needs to be rotated in order to follow the injection direction, which originates from the side in the crossflow configuration, rather than from the top in the non-crossflow configuration. The transmitter is simply rotated about its longer axis, but the receiver must be installed atop a stand with a top plate oriented 30° from the horizontal plane.

In both the atmospheric and elevated pressure test facilities, the PDI system remained fixed to the optical table while the experiment was traversed in the x -, y -, and z -directions. Data were obtained at discrete points in grids at each measurement plane.

The extent of the grid depended on the valid count of droplets measured at each point. Only points with a droplet data rate in excess of 10 counts per second were considered.

4.4 General Operating Conditions

4.4.1 Liquid Fuel Selection

To determine the suitability of the injector for aircraft engines, the experimental test matrix is designed to fall within the range of practical operating conditions of the aircraft engine. In selecting the liquid to be used in this experiment, jet-A was targeted because of its use in aircraft engines. Jet-A (Arco) was used to visualize the global structure of the sprays issuing into a quiescent environment (Chapter 7) and into a crossflow of air (Chapter 9). However, because the existing 266 nm light source capability rendered jet-A as being unsuitable for mass fraction imaging via UV planar laser-induced fluorescence (as discussed in detail in Chapter 6), other distillates were also utilized in this study.

An alternative to jet-A is calibration fluid, which is a Stoddard solvent that commonly substitutes for practical jet fuels in spray nozzle tests. An advantage of using calibration fluid in tests is its batch consistency. Whereas the composition of jet-A may vary across different batches, the calibration fluid composition is held to a controlled standard.

Two grades of calibration fluid, MIL-C-7024D (Type II), and MIL-PRF-7024E, (Type II) (Ashland Chemical), were used. MIL-C-7024D is now obsolete, while MIL-PRF-7024E is the current formulation of the calibration fluid. Selected physical properties of the two grades of calibration fluid were measured along with the

properties of jet-A, and are presented in Table 4.2 for comparison. The density was calculated from the mass of a volume of liquid measured with a calibrated burette. The surface tension was measured with a surface tension apparatus (Q-Glass Company), while the dynamic viscosity was measured with a falling ball viscosimeter (Gilmont Instruments). The measurements, obtained to within $\pm 2\%$ accuracy, show that the fluids share surface tension values within 15% of each other. For air-assisted jet atomization, the surface tension plays a primary role in determining jet breakup, and the comparable values of σ for the calibration fluids and jet-A validate the substitution of either calibration fluid grade for jet-A in the tests.

MIL-C-7024D and MIL-PRF-7024E were found to be more conducive than jet-A to mass fraction imaging via the UV planar imaging diagnostic (for a 266 nm light source). While the UV planar fluorescence studies were conducted with only MIL-C-7024D, the spray scattering and droplet size measurements were obtained using

Table 4.2 Properties of jet-A and calibration fluids MIL-C-7024D and MIL-PRF-7024E.

Fuel	density ρ (kg/m ³)	absolute viscosity μ (kg/m-s)	surface tension σ (N/m)	molecular weight (g/mol)
jet-A	822	1.32E-03	0.0277	167 ^a
MIL-C-7024D, Type II	764	7.96E-04	0.0245	144 ^b
MIL-PRF-7024E, Type II	762	7.57E-04	0.0280	144 ^b

a. Based on the molecular formula $C_{12}H_{23}$.

b. Based on the MSDS for Stoddard solvent.

both MIL-C-7024D and MIL-PRF-7024E. Despite the switchover from MIL-C-7024D to MIL-PRF-7024E, both fluids are presumed to form sprays of similar quality because of their similar physical properties as seen in Table 4.2.

4.4.2 Air Flows

The atomizing air flow is set according to the pressure drop across the spray orifice. Because aircraft engines operate with a pressure drop of up to 7% across the combustor liner (Lefebvre, 1999), the atomizing air pressure drop was primarily limited to a reasonable range of 2-6%. Setting the atomizing air flow by varying the pressure drop is equivalent to varying the velocity, and consequently, the fuel-air relative velocity.

Another factor which affects atomization is the atomizing air to liquid mass flow rate ratio (ALR). In order to vary the ALR while maintaining a certain atomizing air pressure drop, the spray orifice size was varied. For a specified airblast pressure drop and fuel flow, an increase in the spray orifice diameter leads to an increase in air flow, and a subsequent increase in ALR.

The crossflow velocity was also varied in the experiment, since it is a parameter of the momentum-flux ratio q . The crossflow velocity magnitude was varied while maintaining a uniform velocity profile at values that fell within the range of conditions tested in LBI combustor tests (e.g., Leong et al., 2000).

4.4.3 Range of Operation

The tests were primarily conducted under atmospheric conditions. The planar imaging diagnostic is restricted to atmospheric conditions because of the difficulties associated with performing laser imaging studies under elevated pressures (e.g., beam steering and attenuation through the thick windows in the facility, pressure dependency of the fluorescence signal). The elevated pressure facility was utilized in the spray trajectory experiment and analysis presented in Chapters 9 and 10 in order to expand the range of parameters that were used to develop the correlations.

Table 4.3 lists the general operating ranges of the variables used in the tests. A detailed listing of the operating and geometric parameters is included in each chapter of results presented in Chapters 7 through 10.

Table 4.3 Overall range of operating conditions tested.

Operating Condition	Chapters 5 and 6 Planar Imaging Diagnostic Development	Chapters 7 and 8 Spray Jet without Crossflow	Chapters 9 and 10 Spray Jet with Crossflow
ambient P	1 atm	1 atm	1, 3, 5 atm
fuel type	MIL-C-7024D ^a	MIL-C-7024D ^a jet-A ^b	MIL-C-7024D ^a MIL-PRF-7024E ^a jet-A ^b
fuel mass flow	n/a	1.8-3.7 kg/h ^a 0.66-6.4 kg/h ^b	1.8-3.7 kg/h ^a 0.66 kg/h ^b
air pressure drop	n/a	2-10%	0-6% ^a 0-4.8% ^b
ALR	n/a	0.2-1.6	0-1.6 ^a 0-11 ^b
crossflow velocity	n/a	n/a	71-88 m/sec ^a 31-54 m/sec ^b

a. used with planar imaging diagnostic under atmospheric pressure

b. used with video imaging diagnostics

CHAPTER 5

DESCRIPTION AND SETUP FOR THE PLANAR IMAGING TECHNIQUES

Instantaneous plane-specific imaging provides a quick and detailed means of characterizing the distribution of the liquid and vapor phases of fuel, and in the case of twin fluid atomizers, the presence of air. These planar imaging techniques provide a quick means of depicting fuel distribution in a plane, which is useful when a large set of operating conditions is tested. Planar imaging differs from the high-speed and high-magnification video techniques, which both record the total back-scattering of light by the spray. The purpose of this chapter is to provide a background and impetus for developing the UV planar imaging diagnostic for the spray. A description of the setup of the diagnostic is also presented at the end of the chapter.

5.1 Principles of Light Scattering

Light scattering involves the absorption and re-radiation of light by particles. The particles can range between sizes on the order of the molecular level to objects that are visible to the naked eye. Different types of light scattering occur, depending on the particle size and energy state, and the state of the incident light.

When a photon with energy $h\nu$ is absorbed by a particle, the particle can radiate the same quantity of energy with its wavelength preserved. This occurrence is called elastic scattering. For particles smaller than a fifteenth of a wavelength λ , such as

atoms and common molecules whose sizes are on the order of a few angstroms (10^{-10} m), this phenomenon is known as Rayleigh scattering (Fig. 5.1a). A dimensional analysis by Lord Rayleigh in 1871 showed that the intensity of scattered light by such particles is inversely proportional to λ^4 . An analysis of spherical particle scattering by Mie in 1908 further showed that scattering is weakly dependent on wavelength, and independent of λ once the particle size is greater than λ .

If a molecule absorbs an incident photon but does not emit the same amount of energy at the same wavelength, the event is called spontaneous Raman scattering. The energy absorbed by the molecule increases its vibrational energy level, but the subsequent release of light brings the molecule to a different energy state. A Stokes transition (Fig. 5.1b) occurs when the final energy state is higher than the original state. Fluorescence emission by molecules falls under this category. Conversely, an anti-Stokes transition (Fig 5.1c) takes place when the final energy state is lower than the original state. This type of transition usually occurs when the molecules are already in an excited state before absorbing the incident light. For example, heated molecules which absorb incident light radiate the inherent thermal energy as well as the absorbed light—an event which sends the molecules to a lower energy state (Hecht, 1998).

The diagnostics used in this experiment utilize the principles of light scattering to measure the characteristics of the spray. Planar imaging techniques measure (1) Mie scattering by the spray droplets, (2) the fluorescence of the calibration fluid, and (3) the fluorescence of acetone that is seeded into the atomizing air stream. Phase Doppler Interferometry (PDI) also measures the scattering of light by particles passing through a probe volume in order to calculate their size and velocities.

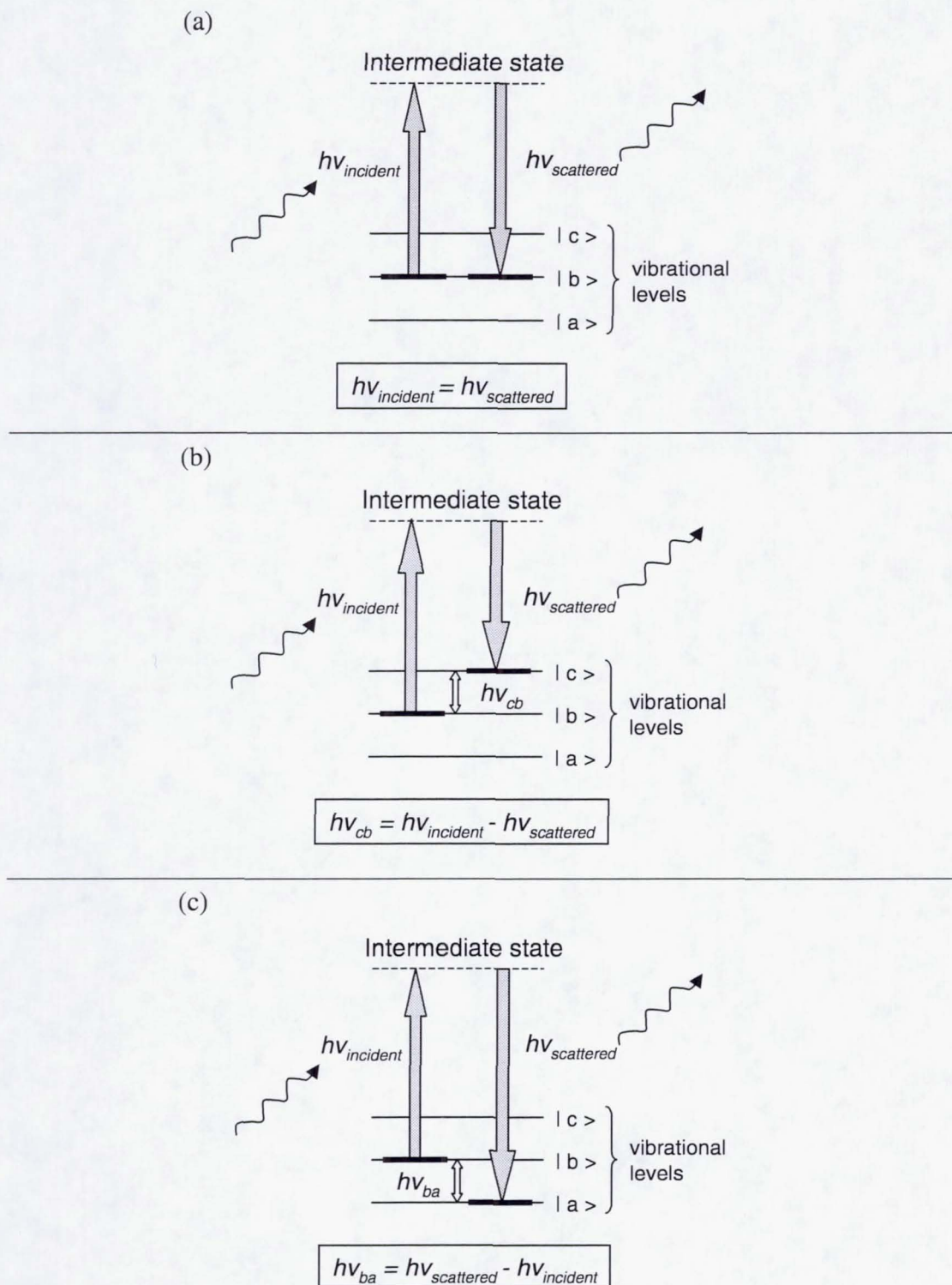


Fig. 5.1 Light scattering of molecules by (a) Rayleigh scattering, (b) spontaneous Raman scattering via Stokes transition, (c) spontaneous Raman scattering via anti-Stokes transition. (Hecht, 1998)

5.2 Planar Mie Scattering

Planar Mie scattering by the spray droplets offers a qualitative measure of the spray structure. Whereas the high speed video system captures the light scattered by the entire spray, planar Mie scattering involves the particle scattering of light from a thin laser sheet that is passed through the spray. This results in the illumination of particles present in the laser sheet, which is approximately 0.97 mm thick in this experiment. The equipment used to produce and capture planar Mie scattering is the same as that used for planar laser induced fluorescence. The basic setup for planar Mie scattering consists of a light source passing through the spray, and a camera which captures the scattered signal. The temporal resolution of the signal is defined by the light source. The use of an Nd:YAG laser emitting light with a 5-7 nsec pulse width, for example, effectively captures an instantaneous representation of the spray signal.

The intensity of the Mie scattering signal is a function of the size of the droplet and its refractive index, the wavelength and polarization of the incident light, and the scattering angle. For an absorbing droplet, the Lorenz-Mie theory shows that Mie scattering is proportional to the surface area of a droplet (Sankar et al., 1999). However, because the intensity of the scattered light can potentially correspond to different droplet diameters, it is difficult to elicit droplet size distributions from collected Mie scattering signals.

5.3 Planar Laser Induced Fluorescence

Planar Laser Induced Fluorescence (PLIF) has been used to examine mixing processes in gaseous flow fields. The main utility of PLIF is its production of instantaneous, two-dimensional spatial maps of the tracer of interest.

Hanson (1986) summarized the basic premise, setup, and examples of different types of PLIF, including the use of gaseous molecular markers such as acetone, iodine, OH, and NO, as well as the use of exciplexes to mark the presence of liquids. The basic PLIF system is comprised of a pulsed laser, optics that expand the beam into a laser sheet, a CCD (Charged Coupled Device) camera that records an intensity value per pixel in an array, a delay pulse generator to synchronize the opening and closing of the camera shutter relative to the laser pulsation, and an image processing computer with software that records the images captured by the camera. Fluorescence occurs on the order of 10^{-7} sec, several nanoseconds after the incoming light waves bombard the molecule (Hecht, 1998). Because this light emission is relatively weak, intensified CCD cameras with an adjustable gain are typically used to record fluorescence images.

Besides obtaining spatially-resolved, instantaneous images, another advantage of PLIF is its use of tracers that, in general, do not disturb the flow. Tracers can either be seeded into the flow (e.g., acetone and iodine vapor), or can already be inherent in the flow (e.g., NO₂ and OH in combusting flows). The fluorescence signal from the tracers must be proportional to their molecular concentration in order to validate the concentration-based representation of the PLIF images.

The fluorescence of the liquid phase can also serve as an indicator of liquid concentration, provided that the signal is proportional to the volume of fluoresced liquid. To differentiate the fluorescence of liquids from that of vapor, liquid PLIF is hereafter referred to as PLLIF, an acronym for Planar LIQUID Laser-Induced Fluorescence.

The purpose of applying PLIF and PLLIF to this spray jet experiment is to image the distribution of the different components of the spray at specific planes. By obtaining a series of cross-sections across the entire spray, a three-dimensional representation can be constructed and used to assess the spray mass distributions through different planes of interest. A background of the specific PLIF and PLLIF techniques that were explored for this experiment is presented in the following sections.

5.3.1 Acetone Fluorescence

Acetone vapor has been extensively used as a molecular tracer in gaseous mixing studies under both non-reacting and reacting flows. Lozano et al. (1992) pioneered the use of acetone PLIF as a measure of the concentration fields in a flow by taking advantage of its photophysical properties. Upon stimulation by a UV light source, acetone emits a strong fluorescence signal in the violet-blue-green range of the visible spectrum that lasts for approximately 3 nsec (Fig. 5.2). The high fluorescence signal intensities allow for the use of low seeding concentrations in the flow of interest. The linearity of the fluorescence signal with laser light intensity and with acetone

concentration allows one to increase the acetone PLIF signal by either increasing the intensity of the incident laser light, or by increasing the concentration of acetone seeded into the flow.

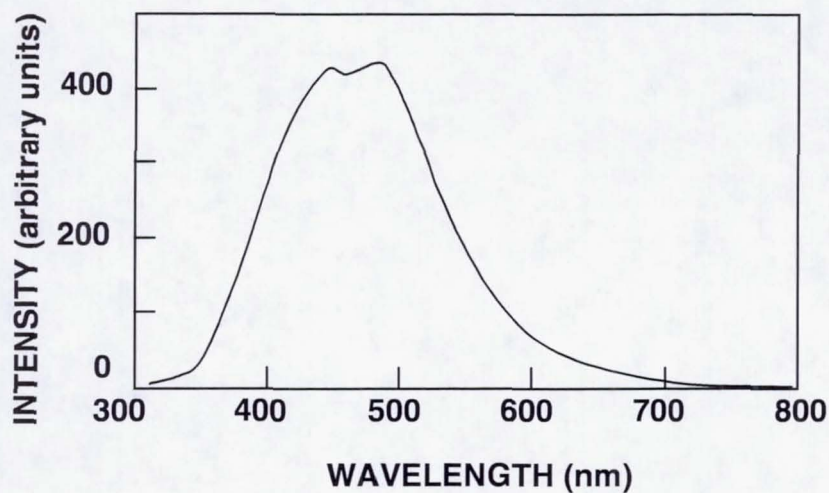


Fig. 5.2 Acetone fluorescence emission spectra obtained upon stimulation by a 308 nm wavelength laser light source (Lozano et al., 1992).

While acetone vapor has been widely used as a molecular tracer in gas mixing studies, the liquid phase of acetone is highly absorbing, which results in a non-linear relationship between the fluorescence signal and droplet volume (e.g., as Bazile and Stepowski (1995) found for a 284 nm wavelength stimulation). This non-linear relationship precludes the use of liquid acetone fluorescence as a suitable strategy for liquid volume fraction imaging.

In relation to this experiment, PLIF of the acetone vapor is applied to track the atomizing air in the airblast spray before and after the introduction of the crossflow. The use of acetone PLIF is restricted to atmospheric pressure conditions because acetone fluorescence shows a pressure dependency, which was observed for pressures ranging as low as 1 to 4 atm (Yuen et al., 1997). Although acetone PLIF has been used to investigate the mixing of the gaseous jet in crossflow on a quantitative level (Smith and Mungal, 1998), the intent here is to use acetone PLIF to qualitatively compare the atomizing air component of the airblast spray under varying parametric conditions. Of particular interest is the relationship between the extent of the atomizing air relative to the liquid phase, under both quiescent and cross-flowing air conditions.

5.3.2 Liquid Mass Fraction Imaging

Images of PLLIF and PLIF in a spray system can show the presence of the liquid or vapor phases of fuel in a spray system. Until recently, the imaging of the mass fraction of liquids has been achieved using methanol dissolved with dyes such as fluorescein (Igushi et al., 1993) or rhodamin (Bazile and Stepowski, 1994), or by inducing fluorescence in organic exciplexes (excited-state complex).

Exciplex fluorescence takes advantage of the chemical-induced fluorescence emission produced by mixing specific organic liquids. The exciplex-based fluorescence technique can discriminate between the liquid and vapor phases of an organic compound (Melton, 1993), and under a high temperature and high pressure environment (Suzuki et al., 1994). However, the quenching of the exciplexes in the presence of oxygen limits its applicability to an oxygen-deficient environment.

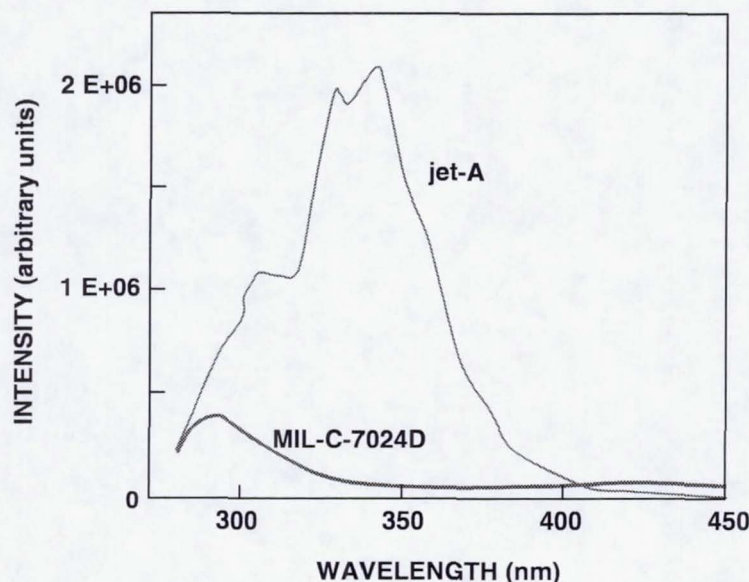


Fig. 5.3 Fluorescence emission spectra of jet-A and MIL-C-7024D induced by 266 nm light excitation.

The UV absorption and fluorescence of aromatic molecules has been documented (Berlman, 1971) and used to track spray droplets (Locke et al., 1998). Applying PLLIF to aromatic liquids eliminates the need for dyes. Aromatic hydrocarbons such as aviation fuel (jet-A) and MIL-C-7024D, a Stoddard solvent composed of aromatic and aliphatic hydrocarbons, absorb ultraviolet wavelengths of light and emit fluorescence that also peaks in the ultraviolet range (up to ~390nm). Figure 5.3 depicts such fluorescence emission spectra for both jet-A and MIL-C-1024D, which were captured by a spectrophotometer upon stimulation by light at a 266nm wavelength. For these UV-absorbing molecules, an appropriate laser choice to induce fluorescence emissions is the Nd:YAG (Neodymium-doped yttrium

aluminum garnet) laser, which is equipped with a second and fourth harmonic generator to produce a final light output that quadruples the frequency of the initial 1024nm of laser light to the desired 266nm light wavelength.

In order for the fluorescence intensity to be proportional to volume, an “optically thin” droplet must be ensured. In cases where it is convenient to control the composition of the fluorescing media, this can be assured. For example, a linearly-proportioned response for liquid volume and fluorescence can be obtained with dyed fuel mixtures such as fluorescein-doped methanol (Igushi et al., 1993) or rhodamin-doped methanol (Bazile and Stepowski, 1994). PLLIF imaging of a dyeless fuel such as kerosene has elicited fuel distributions under reacting conditions (Locke et al., 1998). Although the kerosene PLLIF images qualitatively agreed with mass-flux measurements made with phase Doppler interferometry for one case, the issues of droplet absorption and extinction of the incident lasing source were not fully addressed in Locke et al. (1998).

If a suitable volume imaging method is identified, the spray images can be used to show such characteristics as spray structure and mass dispersion. More recently, the ratio of fluorescence to scattering has been utilized to map out the relative average size in a plane (Sankar et al., 1999; Le Gal et al., 1999). The planar imaging of size distribution allows one to assess the atomization quality of the spray more quickly and efficiently than the alternate method of mapping a region with point measurements obtained by phase Doppler interferometry.

Previous studies performed on the same hardware (Seay et al., 1995; Leong et al., 1997) characterized the dispersion of the spray in the crossflow using fluorescein-doped methanol to track the mass fraction of the liquid component of the spray. These studies did not utilize a distillate fuel, nor did they examine the role of the airblast air in the dispersion process. This research program addresses these concerns by developing UV planar imaging techniques to assess the two-phase airblast spray characteristics of a distillate.

5.4 Planar Laser Imaging Setup

One objective of this research program is to visualize the respective distributions of the air and liquid components of the airblast spray system. A fortunate consequence of using acetone vapor and an aromatic liquid for this study is that UV light can be used to stimulate fluorescence emissions in both fluids. Thus, a single lasing source—the Nd:YAG laser with a quadrupled wavelength output of 266 nm—can be used to obtain either acetone PLIF or PLLIF of an aromatic compound. The Mie scattering signal can also be obtained using the same lasing system, since the signal is produced by the elastic scattering of the incident light by the droplets in the spray. In this experiment, the Mie scattering that is captured consists of the 266 nm light from the Nd:YAG laser.

5.4.1 Laser and Optical Train

The laser and camera setup for this experiment is pictured in Fig. 5.4. A two-deck platform houses the laser, which sits on the top level, and the sheet-forming optics, which sit on the bottom level. An Nd:YAG laser (Continuum Surelite III) operating at 10 Hz with a second and fourth harmonic generator produces a beam of light 9 mm in diameter. A pair of dichroic mirrors enclosed in a wavelength separation package (Continuum SSP-3) separates the 266 nm wavelength of light from the residual 532 nm and 1024 nm wavelengths.

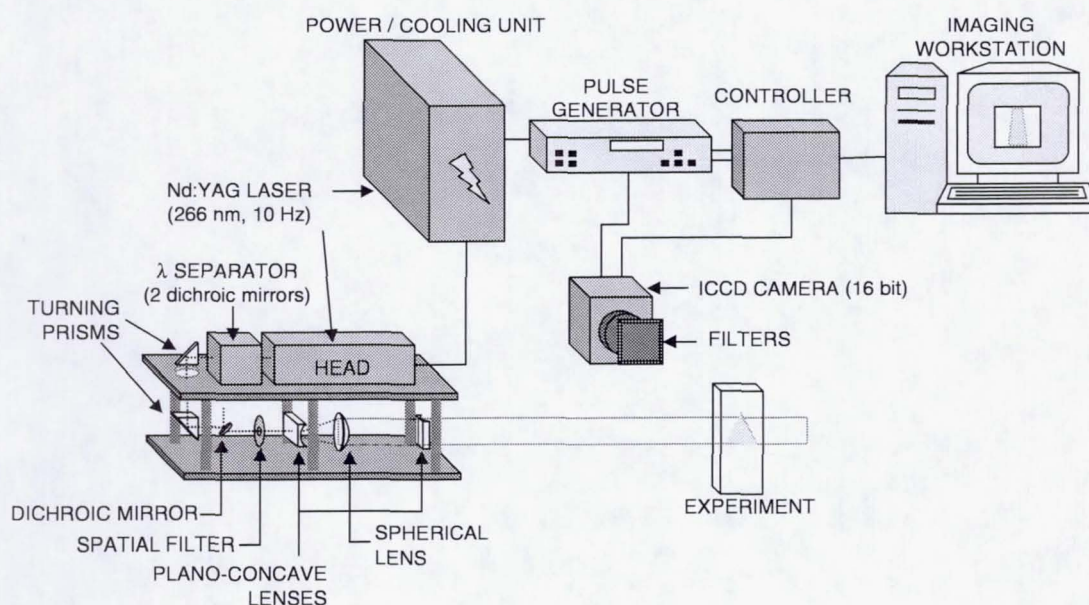


Fig. 5.4 UV laser imaging diagnostic, set for vertical sheet capture.

Right-angle fused silica prisms turn the beam for transmission along the lower level. The beam passes through a spatial filter, and then through another dichroic mirror to purify the 266 nm light further. Although the SSP-3 wavelength separation package specifications guarantee a removal of 99% of the 532 nm wavelength, the intensity of the remaining 1% of 532 nm light was still high enough to contaminate the fluorescence measurements with elastic scattering. The final dichroic mirror was used to eliminate another 99% of the 532 nm light, thus resulting in an overall 532 nm light transmittance of less than 0.01%.

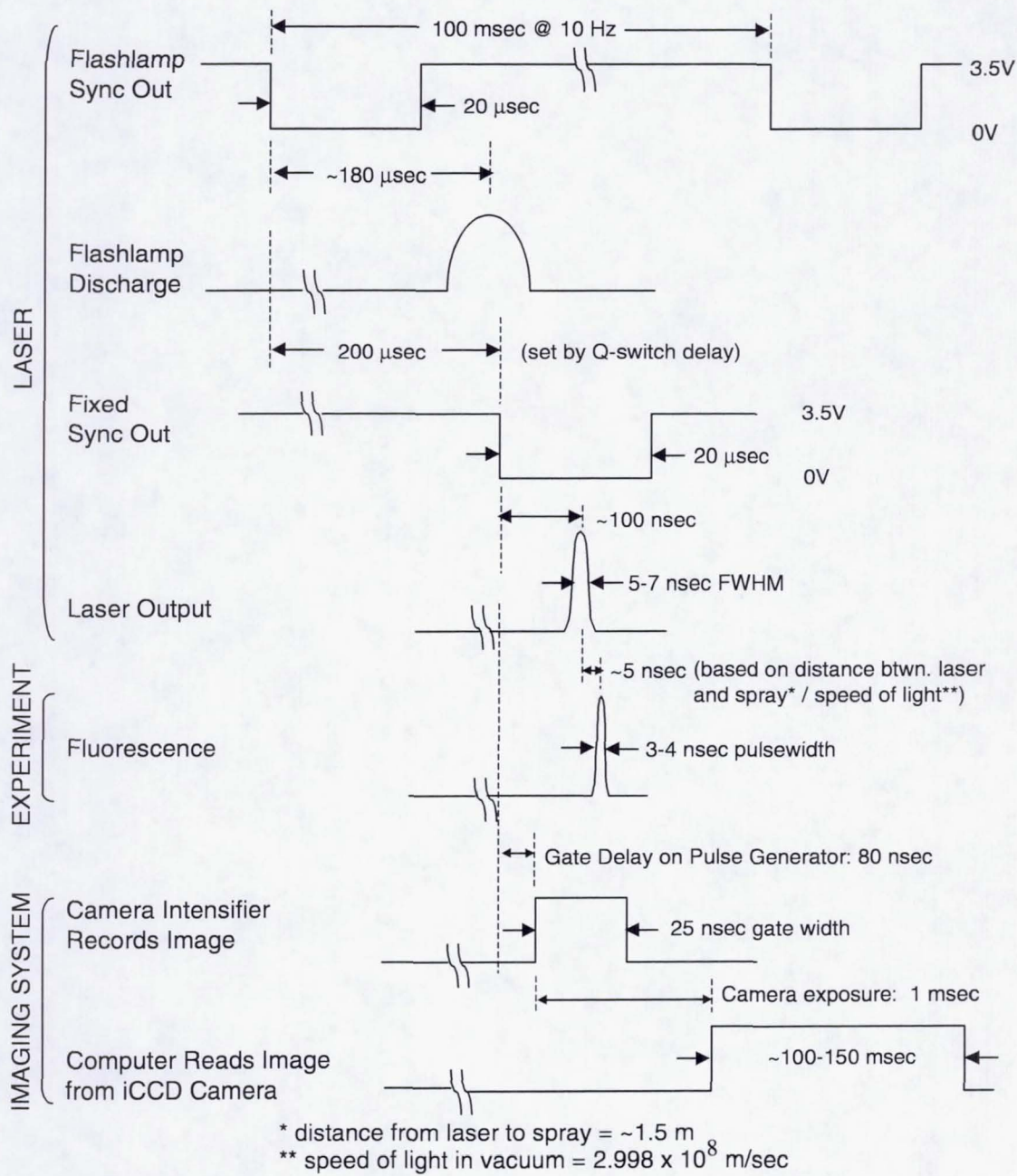
To expand the beam into a collimated sheet, a series of plano-concave cylindrical and plano-convex spherical lenses made of fused silica were used. The beam passes through the first plano-concave cylindrical lens and expands in the length-wise and width-wise directions, transverse to its axial propagation. The expanding sheet is collimated in the length-wise direction as it passes through the spherical lens, and further collimated in the width-wise direction after it passes through another cylindrical lens that is rotated 90 degrees from the first cylindrical lens. The optical train of lenses was designed to produce an emerging planar sheet with cross-sectional dimensions of 27.5 mm x 0.97 mm (1.08 in. x 0.038 in.). All of the optics (CVI Laser Corp.) are of UV-grade, and for a majority of the cases, are specially coated for optimal transmission of the 266 nm wavelength.

5.4.2 Image Acquisition System

The image acquisition system, also pictured in Fig. 5.4, consisted of a camera, controller, pulse generator, and computer. The camera used in this experiment is a 16-bit, intensified charged coupled device (iCCD) (Princeton Instruments Model ITE/CCD-576-G-RB-E) that is equipped to detect UV light. A 50.4-mm focal length, f/3.5 UV lens (Hamamatsu Model A4869) was attached to the iCCD camera. Filters installed directly in front of the camera lens transmitted the desired wavelengths of interest.

The iCCD camera operates by capturing the image onto an intensifier tube, which subsequently amplifies the signal level. This amplified output is correlated to a CCD pixel array. The use of the intensifier tube also allows for quick electronic shuttering of the camera, which can be gated to times as low as 5 nsec at FWHM (full-width, half maximum of the peak of the signal).

The electronic shutter of the camera was gated by the controller (Princeton Instruments Model ST-133). The pulse generator (Princeton Instruments Model PG-200) was used to program the delay time to gate the camera to the event. A gate pulse width of 25 nsec was used in the tests. Fig. 5.5 depicts a diagram showing the synchronization of the camera to the laser pulse. The signal, whether it is scattering or fluorescence, occurs on the order of 10 nsec after the laser sheet passes through the fluid. The exact synchronization of the camera to the signal is set by the gate delay function on the pulse generator. For the tests, a gate delay time of 80 nsec was used in conjunction with the 25 nsec gate pulse width.



NOTE: Timing diagram not drawn to scale.

Fig. 5.5 Timing diagram for the UV planar imaging procedure.

The image intensities captured on the intensifier tube are amplified and correlated to a 576 x 384 pixel array. An imaging workstation retrieved and stored the intensities at each pixel in the array. The measured grid resolution at the focusing plane of interest was 6 pixels/mm. The elapsed time from exposure to readout was approximately 2 seconds per image.

The short gating time of the camera, in addition to the glass filters that are used to transmit the wavelengths corresponding to either acetone PLIF, PLLIF, or Mie scattering, helped to minimize the background intensity levels captured by the camera. Typical maximum background intensities averaged about 150, which is only 0.2% of the maximum intensity level on a 16-bit (2^{16}) scale.

CHAPTER 6

TWIN-FLUID VISUALIZATION METHODOLOGY

The previous chapter laid out the background and principles behind PLIF for both gaseous and liquid systems. The experimental setup for the UV planar imaging diagnostic was also described in Chapter 5. The purpose of this chapter is to document the development of the UV planar imaging diagnostic, a process which encompassed the validation of calibration fluid as a mass-fraction indicator of liquid concentration, and the establishment of image processing methodologies. The techniques are subsequently demonstrated in the visualization of the liquid and air components of the airblast spray without crossflow.

6.1 Verifying the PLLIF Mass Representation of Calibration Fluid

To use MIL-C-7024D-Type II PLLIF as a measure of the volumetric distribution of liquid in the spray, the calibration fluid must not strongly absorb the operating wavelength of the laser. Absorption tests were conducted on various calibration fluid concentrations in a quartz sample cell with a 1-cm path length. Different concentrations were obtained by diluting the calibration fluid with hexane, which itself absorbs 4% of the incident 266 nm light across a 1-cm path. The absorbance A of light energy by the liquid solution is calculated by

$$A = \log\left(\frac{I_0}{I}\right) \quad (6.1)$$

where I_0/I is the ratio of the incident to the transmitted energy intensity. By measuring the power absorbed by various calibration fluid concentrations, a correlation between A and the concentration, M (in units of [moles/L]), of the liquid can be obtained. If the fluorescence yield from the excited molecules of the calibration fluid is assumed to be linearly proportional to the absorbance of light by the molecules, then the optical thickness of the liquid must be short enough to allow all molecules in the path length to be stimulated equally. A strongly absorbing liquid would quench the light at the surface, as Bazile and Stepowski (1995) showed for liquid acetone.

To ensure that the calibration fluid does not strongly absorb the 266 nm wavelength in the spray, the range of calibration fluid concentration that is linearly proportional to its absorbance first needs to be determined. From there, the optical thickness of the liquid can be calculated using the Beer-Lambert law. The Beer-Lambert law can be written as

$$\frac{I}{I_0} = 10^{-\epsilon ML} \quad (6.2)$$

(Berlman, 1971), where ϵ is the molar extinction coefficient, and L is the path length across the liquid through which the light is transmitted. Combining the absorbance relationship in Eq. 6.1 with the Beer-Lambert law in Eq. 6.2 yields

$$A = \epsilon ML \quad (6.3)$$

A plot of A obtained for various concentrations, M , of calibration fluid in hexane is presented in Fig. 6.1. Calibration fluid concentrations of up to 12% absorbed the laser sheet linearly with respect to its concentration in the 1-cm wide sample cell. For

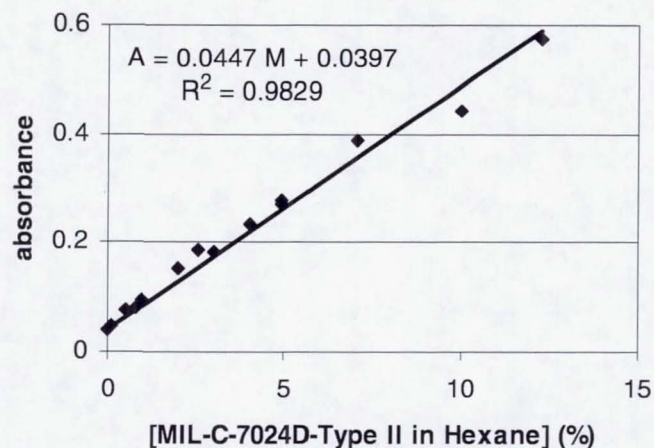


Fig. 6.1 Absorbance of incident 266 nm light by various calibration fluid concentrations across a 1-cm sample cell width.

$L=1$ cm, ϵ essentially represents the slope of the curve of A vs. M . From Fig. 6.1, the value of ϵ for MIL-C-7024D is $0.0447 \text{ (moles/L)}^{-1} \cdot \text{cm}^{-1}$.

The low value of ϵ for this range of MIL-C-7024D concentrations indicates that calibration fluid concentrations of up to 12% exhibit high transmission and low absorption of light. Based on this value of ϵ , a 200-micron drop is expected to absorb 8.9% of the incident energy under the ambient conditions of the spray experiment. From previous analysis and measurements it is known that this drop size is a conservative upper limit. Therefore it can be concluded that the calibration fluid droplets are optically thin for the conditions studied. The signals obtained in the PLLIF of calibration fluid MIL-C-7024D thus represent a volumetric, or in this case, a mass fraction distribution of liquid. For the current operating conditions (room temperature and pressure), it is also assumed that the fluorescence signal represents the liquid

component of the spray, as the amount of vapor produced during the injection process represents a negligible signal intensity compared to the liquid fluorescence.

As an additional note—the same test, when applied to jet-A, showed that a 1-cm path length of jet-A concentration as low as 0.1% still absorbed nearly all of the energy of the incident laser sheet. The extinction of the laser sheet by such a low concentration of jet-A shows that it is not a viable candidate for characterizing the volumetric distribution of the liquid spray. For jet-A, the incident light is absorbed at the droplet surface, which results in an unequal distribution of fluorescence emission as noted by Locke et al. (1998).

6.2 Fuel-Air Discrimination and Measurement

Ideally, three detectors could have been used to obtain Mie scattering, calibration fluid PLLIF, and acetone PLIF measurements simultaneously. However, with the present capability consisting only of a single detector, the spray was canvassed three times for each measurement at each condition. The filter stack and camera gain were changed according to measurement type (refer to Fig. 6.2 for the filtering strategies). The calibration fluid fluorescence was captured by using a combination of WG295 and BG1 Schott glass filters to transmit UV wavelengths above 266 nm, as well as a neutral density filter (optical density O.D.=0.2) to attenuate the signal and prevent image saturation. Mie scattering of the incident 266 nm wavelength was obtained by using an interference filter at 266 nm (with a FWHM of 10 nm and a 12% peak transmittance) and two neutral density filters (O.D.=0.2). A 500V gain was maintained for these measurements. The acetone PLIF images were obtained with a

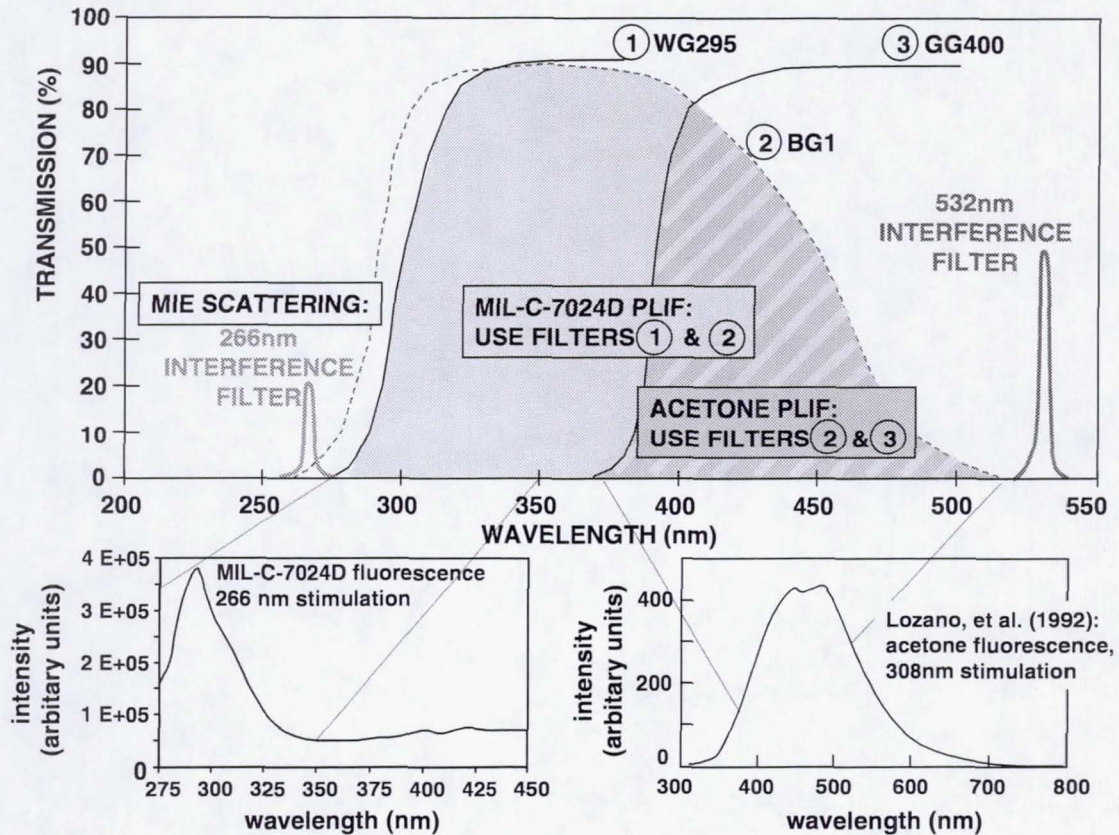


Fig. 6.2 Filter combinations for the different imaging strategies.

BG1 and GG400 Schott glass combination to transmit the violet-blue light emitted by the acetone fluorescence while attenuating the fluorescence signal from the calibration fluid. A camera gain of 600V was used to obtain the acetone PLIF images.

Acetone PLIF enabled the visualization of the seeded atomizing air in the spray. The air was seeded with the acetone seeding system pictured in Fig. 6.3. A 2.25-L stainless steel tank was filled half- to three-quarters-full of liquid acetone. Metered air was directed into the liquid in the tank to immerse the air and facilitate the vaporization

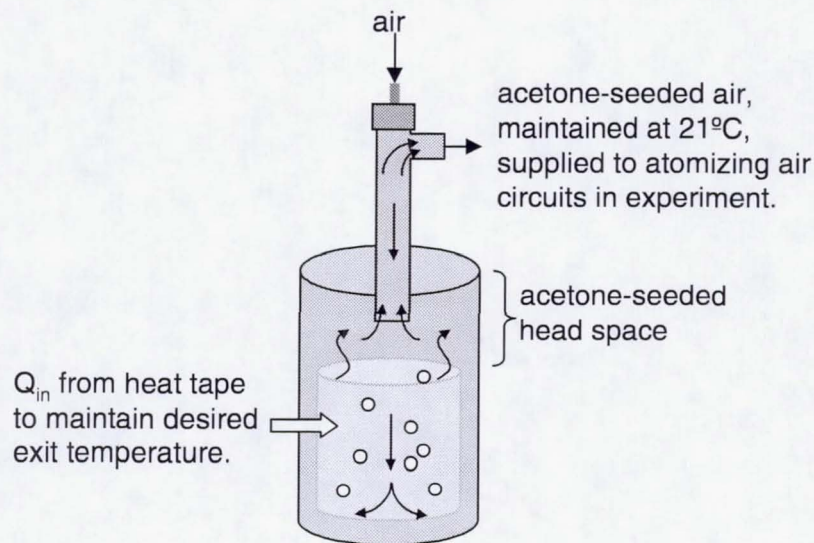


Fig. 6.3 Seeding system used to saturate the atomizing air stream with acetone vapor for acetone PLIF imaging.

of acetone. Acetone-laden air drawn from the saturated head space in the tank was sent to the injection panel. The tank was heated by an external tape that was driven by a controller in order to maintain the temperature of the acetone-seeded air at 21°C.

6.3 Image Processing

The region of interest in the spray image measured 23.5 mm x 20.2 mm. Images of the spray without crossflow were obtained at planes from $y = -10$ mm to +10 mm, at 1-mm increments. At each y -position, a time-averaged image of 25 frames was obtained. Each averaged image was corrected for laser sheet intensity variation. From the three-dimensional block of collective xz -planes (see Fig. 6.4a), horizontal cross-sections in the yz -plane were reconstructed by linearly interpolating between the

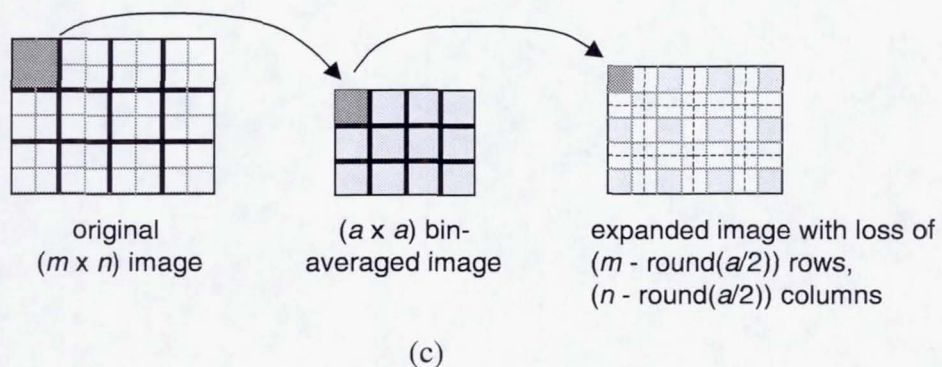
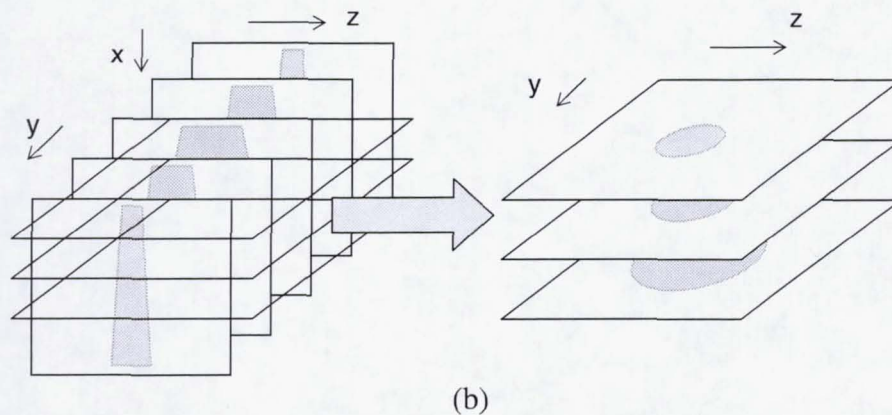
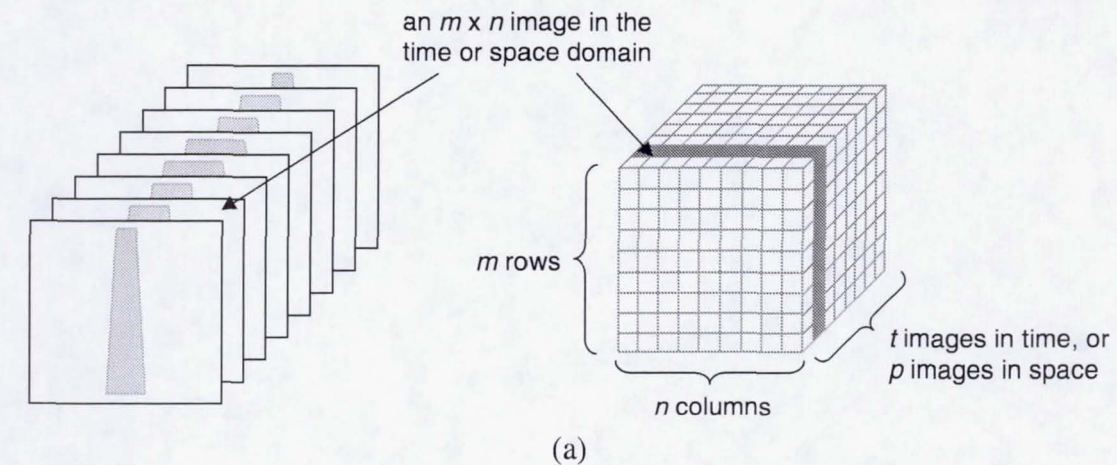
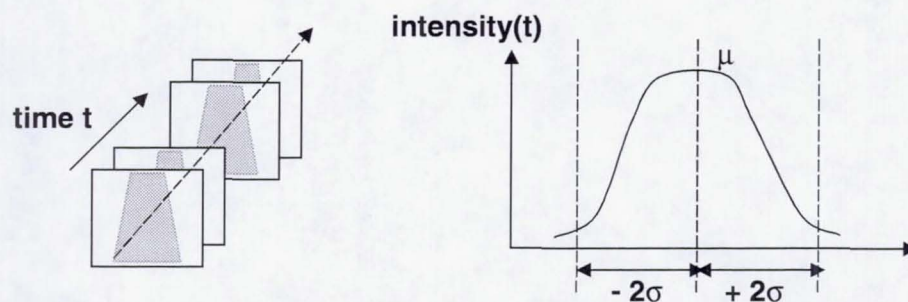


Fig. 6.4 Image processing procedure consisting of (a) the representation of the image stack as a volume of matrices, (b) extraction of the horizontal cross-sections, and (c) application of a filter to smooth the extracted images.

sheet pixels (Fig. 6.4b). To refine the cross-sectional images, a smoothing operation was applied which consisted of condensing and expanding the pixel array using a 6 x 6 bin of pixels (Fig. 6.4c). The expansion process resulted in a loss of rows and columns which decreased the yz planar dimensions to 19.2 mm x 25.2 mm and resulted in an xy-cross-section measuring 22.2 mm x 25.2 mm.

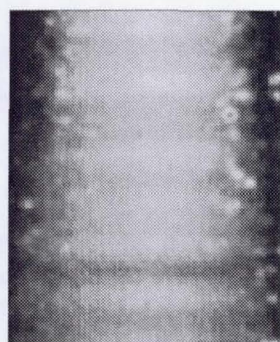
A different procedure was used to average the acetone PLIF images because of the presence of discrete drops in the images. The BG1-GG400 filter combination that was supposed to attenuate the UV signals associated with calibration fluid fluorescence and with Mie scattering worked well in blocking the signals from the spray before the air was seeded with acetone. However, it was observed that once the acetone was added to the atomizing air, faint images of isolated drops appeared. An investigation into this phenomenon using a 532 nm interference filter as well as polarization filtering showed no evidence of the scattering of any residual 532 nm light from the YAG laser. Because the droplets appear when the acetone seeding is turned on, it is possible that the droplets may be scattering light from the fluorescence of the acetone. Further work needs to be performed to investigate this phenomenon, but since the tests involved a qualitative assessment of the conditions, the acetone PLIF images were still processed and examined.

To further reduce the faint signals from the droplets present in the acetone PLIF images, a temporal filtering scheme was applied (Fig. 6.5). On a 16-bit scale, the droplet intensities are on the order of 10^4 while the acetone fluorescence is on the order of 10^3 . The probability of a droplet occupying the same space in more than one frame is low. Therefore, by taking the average μ and standard deviation σ across the 25

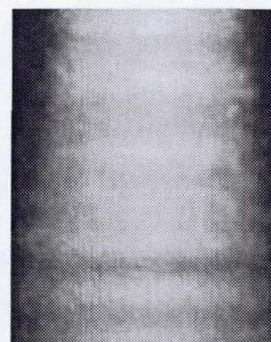


* Intensities not within \pm (*constant* * standard deviation σ) of mean μ are excluded from the time-average.

Fig. 6.5 The temporal filtering strategy applied to the acetone PLIF images of the acetone-seeded air in the spray.



(a)



(b)

Fig. 6.6 Application of the temporal filter to an acetone PLIF image of the spray: (a) before (note the discrete, higher intensity droplet shapes), and (b) after.

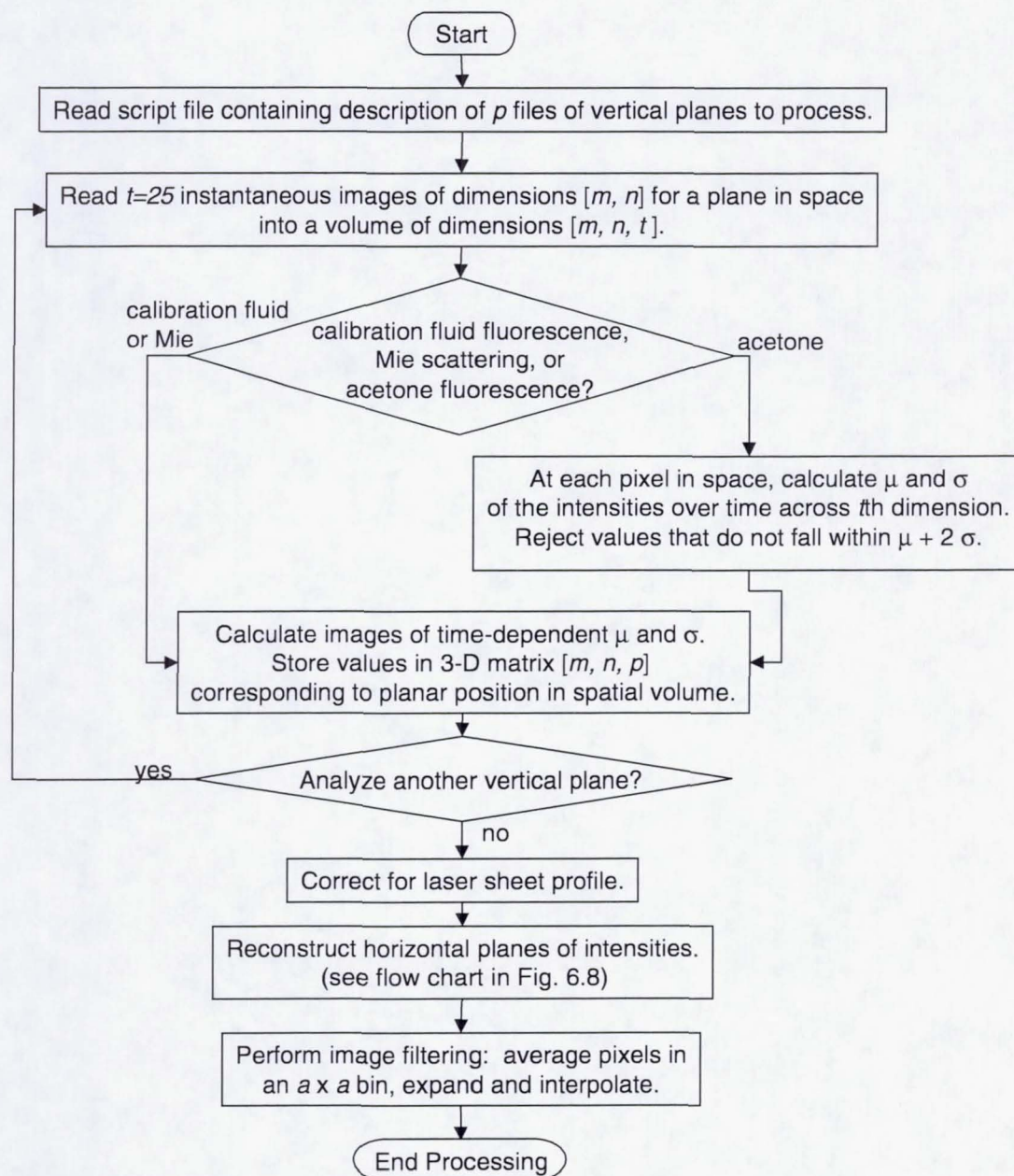


Fig. 6.7 General image processing procedure.

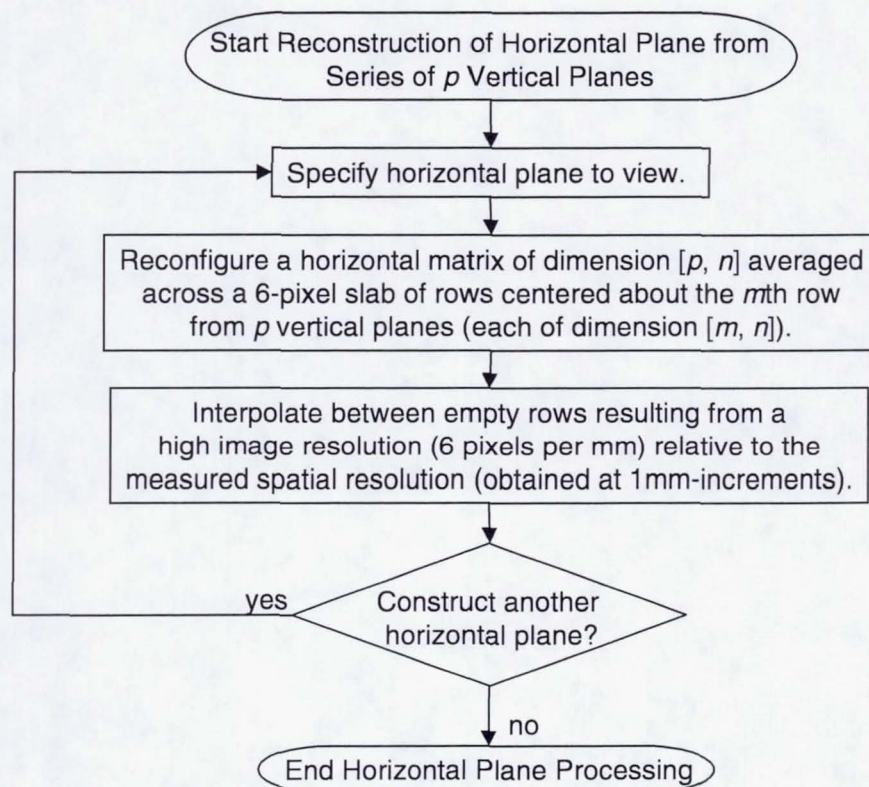


Fig. 6.8 Sub-flow chart showing method of reconstructing horizontal images from measured vertical sheet images.

frames in time at each pixel, the intensity associated with the droplet can be eliminated because the value will likely be higher than $(\mu + c\sigma)$, where c is a constant. For the acetone PLIF images, a value of $c=2$ achieved satisfactory results, as seen in Fig. 6.6.

The image processing steps outlined above are summarized as a flow diagram in Fig. 6.7. A sub-flow chart presented in Fig. 6.8 details the method of extracting horizontal planes from the block of vertical images, a process that is pictured in Fig. 6.4b. The codes for the image processing procedures discussed in this chapter are contained in Appendix A.

6.4 Planar D_{32} Measurement

The planar images of PLLIF and Mie scattering of the calibration fluid were used to calculate a planar distribution of droplet D_{32} . The principle behind the method, described by both Sankar et al. (1999) and Le Gal et al. (1999), rests with the assumptions that the liquid being imaged in the laser sheet are in the form of spherical droplets and that the droplets are “optically thin” such that light is absorbed equally throughout their volume.

The droplets must be spherical in order to simplify the result from the Lorenz-Mie theory, which is used to predict elastic light scattering by particles. The Lorenz-Mie theory states that the light scattered by absorbing droplets with diameter D greater than $1\text{ }\mu\text{m}$ is proportional to the square of the droplet diameter, as represented by the following relationship

$$I_{Mie} = C_{Mie}D^2 \quad (6.4)$$

where I_{Mie} is the intensity of elastically-scattered light by the droplet, and C_{Mie} is a constant of proportionality.

For a droplet that absorbs the incident light equally and throughout its volume, the fluorescence intensity I_{PLLIF} is proportional to the droplet volume by a constant factor C_{PLLIF} as shown by the following relationship

$$I_{PLLIF} = C_{PLLIF}D^3 \quad (6.5)$$

Note that as the liquid absorptive property increases, the droplet absorption of the incident light becomes limited to the surface, as Bazile and Stepowski (1995) showed

for liquid acetone, and as discussed in Section 6.1 for jet-A. For a highly-absorbing droplet, the relationship in Eq. 6.5 changes from a cube-power to a value between 2 and 3 (Le Gal et al., 1999).

Each (i, j) pixel in the image array captures the signals from n number of droplets of diameter D . The signal intensity at each pixel can be represented by the sum of the discretized distribution of n_k droplets per size bin D_k . Eqs. 6.4 and 6.5 can then be rewritten as

$$I_{Mie}(i, j) = C_{Mie} \sum n_k(i, j) \cdot D_k^2(i, j) \quad (6.6)$$

$$I_{PLLIF}(i, j) = C_{PLLIF} \sum n_k(i, j) \cdot D_k^3(i, j) \quad (6.7)$$

The ratio of signals from the PLLIF (Eq. 6.7) and Mie scattering (Eq. 6.6) measurements yields

$$\frac{I_{PLLIF}(i, j)}{I_{Mie}(i, j)} = \frac{C_{PLLIF} \sum n_k(i, j) \cdot D_k^3(i, j)}{C_{Mie} \sum n_k(i, j) \cdot D_k^2(i, j)} \quad (6.8)$$

Substituting the definition of D_{32} and an overall constant of proportionality K for the ratio of C_{PLLIF} to C_{Mie} , Eq. 6.8 becomes

$$\frac{I_{PLLIF}(i, j)}{I_{Mie}(i, j)} = K \cdot D_{32}(i, j) \quad (6.9)$$

The constant K can be derived from experimental results using, for example, droplet size data measured by PDI.

6.5 Verification of the Techniques

To evaluate the UV planar imaging protocol for characterizing the airblast spray, the techniques were applied to the spray injector in the non-crossflow configuration (see Fig. 6.9). A volumetric region extending from $x=9$ mm to 31 mm from the injection plate was imaged across the spray. However, only the images from the $x=10$ mm cross-section are presented in this demonstration.

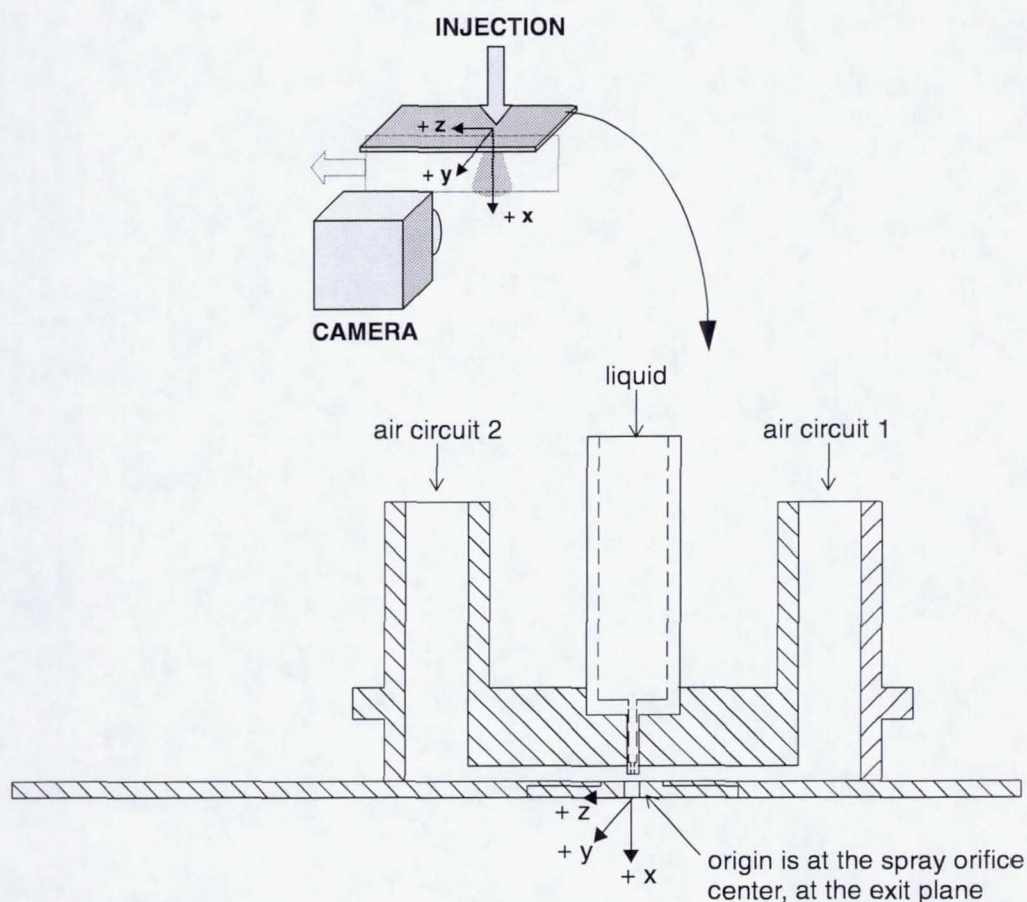


Fig. 6.9 Spray injection panel hardware and axis orientation for the quiescent injection setup.

To complement as well as to draw comparisons with the planar images, droplet size and velocities of the spray were measured with the PDI system. The PDI system remained fixed to the optical table while the experiment was traversed along the y - and z -axes at a plane of $x=10$ mm. Data were obtained along each axis in 1-mm increments until the droplet data rate dropped below 50 counts per second.

Results are shown for the case of 1.8 kg/h fuel flow and 3.18-mm hole dia. case at an airblast pressure drop of 4%. The images are presented on a red (high) to blue (low) intensity scale, normalized with respect to the maximum value in the image.

To qualitatively verify the mass fraction measurement obtained by PLLIF, the image obtained for this case is compared with PDI measurements. The PDI-based volume concentrations used to assess the PLLIF images were calculated by using the measured values of spatial-weighted, volume mean diameter D_{30} (Igushi et al., 1993). The spatially-weighted D_{30} is calculated from the corrected count of droplets that removes the bias against smaller droplets. Because of the Gaussian profile of the laser beam, droplets that pass through the tails of the profile scatter less light. For smaller droplets, the scattering intensity is such that the droplets may not be counted in the run. Bias weighting provided by the PDI instrument accounts for this undercount with factors that provide additional weighting to smaller droplets in the spray. The correction weighting, which is provided in the raw output file by the diagnostic, was thus used to compute the spatially-weighted D_{30} .

Figure 6.10 presents the sample PLLIF image overlaid with a plot of circles whose relative size represents the volume concentration of liquid at the (y, z) coordinate where the value was measured. The PLLIF image represents the

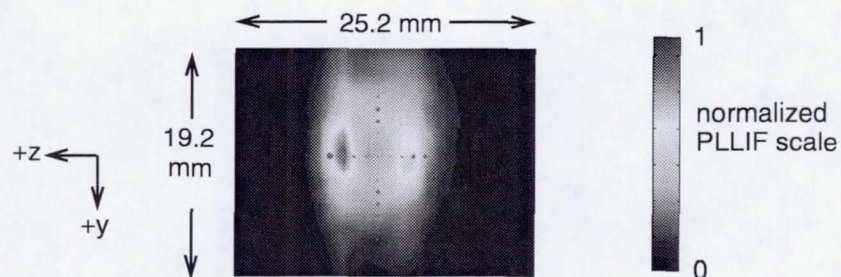


Fig. 6.10 PLLIF image comparison with superimposed PDI-measured volume concentrations at $x=10$ mm for the 1.8 kg/h fuel flow, 3.18-mm spray orifice dia. case at a 4% airblast ΔP .

concentration of liquid fluoresced by the laser sheet during the near-instantaneous time duration of the laser pulse (approximately 5 nsec). The volume concentrations correspond well with the peaks in the images, as the larger circles are coincident with the high-concentration peaks.

The demonstration of PLLIF in representing the liquid volume fraction in the spray allows us to characterize the spray structure in terms of its liquid distributions. For example, the image shown in Fig. 6.10 depicts a two-lobed structure in the spray. The presence of the lobes is not surprising, given the dual-air circuit design of the injector (refer to Fig. 6.9). The air impinges on the emerging fuel jet from the negative and positive z -directions, pushing the spray toward opposite x -directions. Despite the non-axisymmetric dispersion of the liquid, the spray does exhibit symmetry across the y - and z -axes.

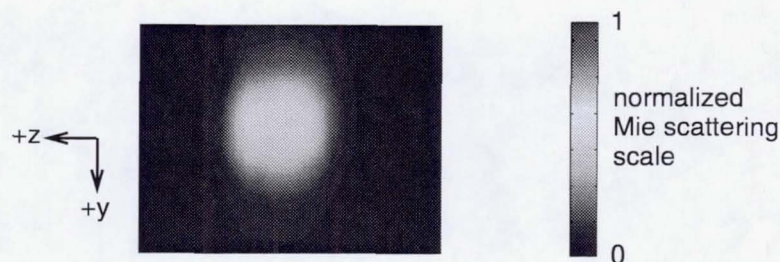


Fig. 6.11 Mie scattering images at $x=10$ mm for the 1.8 kg/h fuel flow, 3.18-mm spray orifice dia. case at a 4% airblast ΔP .

In contrast to the double-lobed structure observed in the PLLIF images, the images obtained by planar Mie scattering do not present such a structure (Fig. 6.11). The Mie scattering image of the spray is circular in shape, with the scattering intensity centered at the origin.

Because the intensity levels in the PLLIF images are proportional to the droplet volume, and because the intensities in the Mie scattering images are proportional to the droplet surface area, a ratio of these images should yield an estimate of the droplet D_{32} distribution in the plane (Sankar et al, 1999). The result of such an operation is shown in Fig. 6.12, which essentially takes the ratio of the PLLIF image in Fig. 6.10 to the Mie scattering image in Fig. 6.11. PDI-measured droplet D_{32} , whose magnitudes are denoted by the size of the circles, are also superimposed on the image for comparison. The generated images show that the intensity ratio produces a D_{32} distribution that is well-matched by the PDI data in this case.

The acetone PLIF image of the seeded atomizing air tracks the concentration of air relative to the droplets. Figure 6.13 presents the images obtained for the 3% and 6%

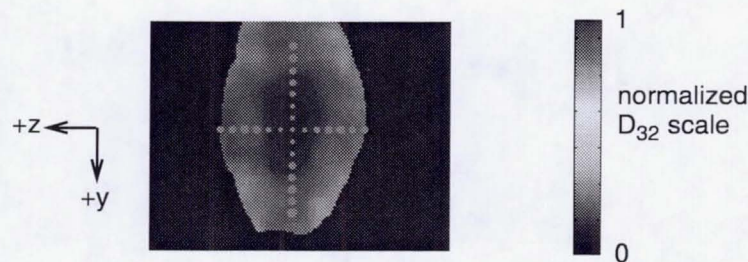


Fig. 6.12 Derived planar D_{32} images with overlaid PDI-measured D_{32} at $x=10$ mm for the 1.8 kg/h fuel flow, 3.18-mm spray orifice dia. case at a 4% airblast ΔP .

airblast ΔP conditions, which bracket the 4% airblast ΔP condition. The atomizing air distributions produced by the 3% and 6% airblast ΔP cases show similar shapes. The airblast air is concentrated in the center of the spray, with the bounding region of air decreasing and tending toward a smaller circular shape as the pressure drop is increased.

A close interaction between the dispersion of the atomizing air and the droplets is observed in Fig. 6.14, which compares the vertical acetone PLIF cross-sections of the 1.8 kg/h fuel flow, 3.18-mm spray orifice dia. case at a 6% airblast ΔP , with and without the liquid flow. The image of the seeded air with the liquid flow present contains higher overall intensities relative to the cases without liquid flow. The higher intensities suggest the scattering of acetone fluorescence by the droplets. Despite this interference, a qualitative comparison of images suggests that the atomizing air expands more rapidly when the droplets are present, as the droplets pull the atomizing air along with them during a transfer of momentum. This close interaction between the

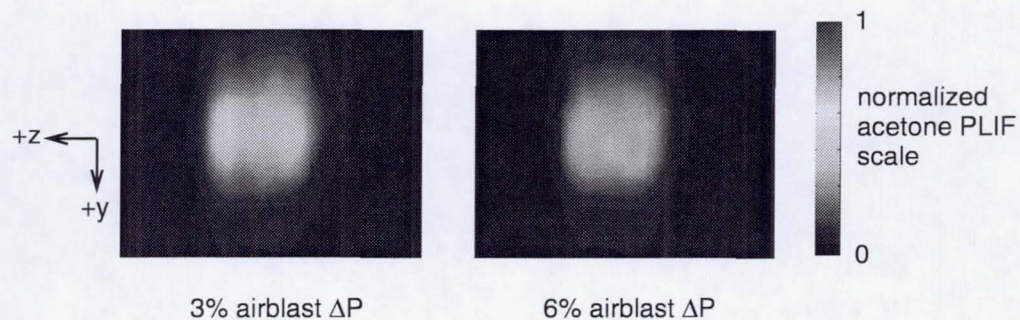


Fig. 6.13 Concentration fields of the acetone-seeded atomizing air at $x=10$ mm for the 1.8 kg/h fuel flow, 3.18-mm spray orifice dia. case at a 3% and 6% airblast ΔP .

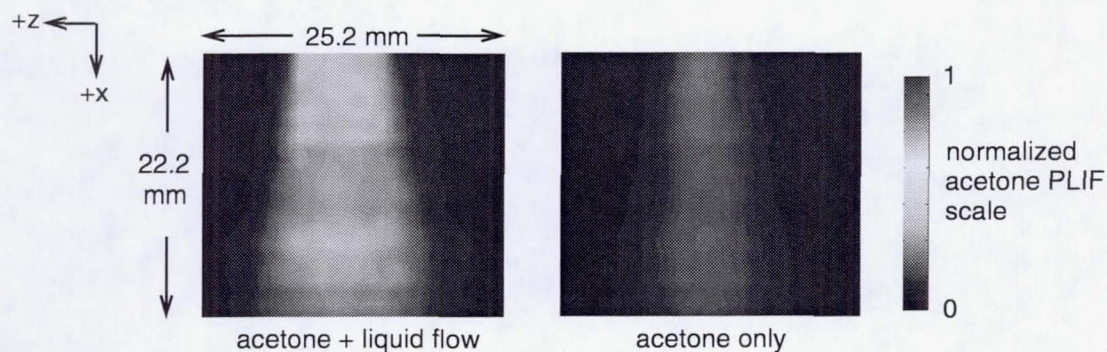


Fig. 6.14 Acetone PLIF images of cases with and without liquid flow, at the $y=0$ mm origin plane, for the 1.8 kg/h fuel flow, 3.18-mm spray orifice dia. case at a 6% airblast ΔP .

droplets and atomizing air, which is also suggested in studies by Briffa and Dombrowski (1966), Ghosh and Hunt (1994), and Han and Chung (1992), indicates a need to incorporate two-way coupling when modeling this system.

6.6 Diagnostic Summary

A procedure for the assessing the spray performance of an airblast spray injector was developed and used to evaluate the effects of parametric changes on the spray. Planar imaging of an aromatic compound (calibration fluid MIL-C-7024D, Type II) showed a distinct two-lobed structure that is produced by this injector which Mie scattering was not able to discern. A ratio of the PLLIF and Mie images yielded a means of quickly evaluating the droplet D_{32} in a plane. PDI measurements were used to qualitatively verify the magnitudes in the PLLIF and D_{32} images. Acetone PLIF images were also obtained to view the distribution of atomizing air. The results of applying these diagnostic methods to the airblast spray injector are presented in Chapters 8 and 10.

With the successful demonstration of the UV planar imaging techniques—which yield liquid volume fraction, spray D_{32} , and airblast concentration distributions—the diagnostics that are utilized in this dissertation can be summarized. Table 6.1 lists the planar imaging techniques along with the diagnostics described in Chapter 4 and includes a description of the experimental conditions for which each diagnostic is used, as well as the data type and information that each diagnostic yields.

Table 6.1 Summary of primary spray diagnostics used in the experiment.

DIAGNOSTIC	EXPERIMENT	DATA TYPE	INFORMATION YIELDED
high-speed video: high speed video camera + halogen lamp	Pressure: 1 atm quiescent injection	Video files (*.avi) of light scattering (resolution: 8-bit)	near-field jet and spray structure (instantaneous and average)
high-magnification video: CCD camera + long-distance microscope lens + lamp	Pressure: 1-5 atm crossflow injection	Time-averaged (*.tif) images from videotape (resolution: 8-bit)	jet trajectory (average)
phase Doppler interferometry: Argon-ion laser (532nm) + transmitter + receiver	Pressure: 1-5 atm quiescent and crossflow injection	Droplet size, two velocity components	Point-specific, planar grid measurements; also used to verify planar D_{32} measurement
calibration fluid PLLIF: Nd:YAG laser (266nm) + filter transmission of 295-400nm	Pressure: 1 atm quiescent and crossflow injection	Multi-frame (*.spe) image files (resolution: 16-bit)	Liquid volume fraction distribution per plane (instantaneous and average values)
Mie scattering: Nd:YAG laser (266nm) + filter transmission of 266+/- 10nm	Pressure: 1 atm quiescent and crossflow injection	Multi-frame (*.spe) image files (resolution: 16-bit)	Planar distribution of 266 nm light scattered by droplets (instantaneous and average values); used with PLLIF images to yield planar D_{32}
acetone PLIF: Nd:YAG laser (266nm) + filter transmission of 400-500 nm	Pressure: 1 atm quiescent and crossflow injection	Multi-frame (*.spe) image files (resolution: 16-bit)	Atomizing air concentration fields (instantaneous and average values)

CHAPTER 7

GLOBAL STRUCTURE OF THE AIRBLAST SPRAY WITHOUT CROSSFLOW

The objective of this chapter is to utilize high speed video to canvass a wide range of conditions in order to determine the effect of varying operational and geometric parameters on the quality of the airblast spray (without crossflow). The near-instantaneous snapshots characterize the behavior and structure of the spray, which will help to determine the important parameters that control its formation.

7.1 Experimental Conditions

The experiment was installed in the non-crossflow configuration as pictured in Fig. 7.1. The camera was situated to capture the spray from the side, in the xz -plane. The halogen lamp was placed behind the spray, thus allowing the camera to obtain

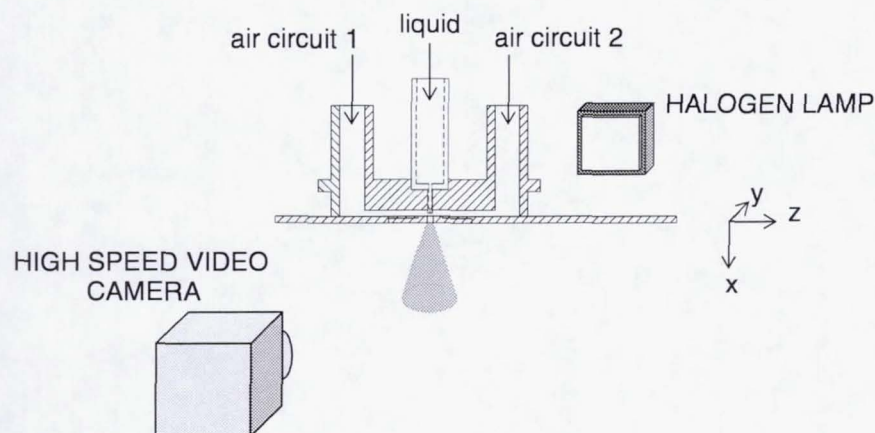


Fig. 7.1 Positioning of the high speed video camera relative to the spray experiment in the non-crossflow configuration.

Table 7.1 Operating and geometric conditions for the global visualization of the airblast spray experiment in the non-crossflow configuration.

Parameter	Range of Variation
Ambient pressure (kPa)	101.3
Fuel flow (jet-A) (kg/h)	0.66 - 6.4
Airblast pressure drop (%)	0 - 10
Airblast velocity, U_{airbl} (m/sec)	0 - 132
Airblast air to liquid mass flow ratio, ALR	0 - 2.45
$Re_L = \frac{\rho_L U_L d_f}{\mu_L}$	754 - 3400
$We_{airbl} = \frac{\rho_g (U_{airbl} - U_L)^2 d_f}{\sigma_L}$	0.09 - 478
$Re_{airbl} = \frac{\rho_g U_{airbl} d_{spray}}{\mu_g}$	0 - 4.12×10^4
Fuel orifice diameter, d_f [corresponding l/d in brackets]	0.34 mm (0.0135 in.) [$l/d = 6.7$], 0.66 mm (0.0260 in.) [$l/d = 2.5$]
Spray orifice diameter, d_{spray} [corresponding l/d in brackets]	2.26 mm (0.089 in.) [$l/d = 1.4$], 2.72 mm (0.107 in.) [$l/d = 1.2$], 3.18 mm (0.125 in.) [$l/d = 1.0$], 4.22 mm (0.166 in.) [$l/d = 0.75$], 6.35 mm (0.250 in.) [$l/d = 0.50$]

Notes:

- $\rho_L = 822 \text{ kg/m}^3$ for jet-A; $\rho_g = 1.19 \text{ kg/m}^3$ for air at room temp. and pressure
- $\mu_L = 1.32 \times 10^{-3} \text{ kg/m-sec}$ for jet-A; $\mu_g = 2.00 \times 10^{-5} \text{ kg/m-sec}$ for air at room temp. and pressure
- $\sigma_L = 0.0277 \text{ kg/sec}^2$ for jet-A
- For reference, hardware dimensions are also given in English units, which were the primary units used in the machining process.

images of back-scattered light from the spray. The 140-pixel x 160-pixel images represented a field of view measuring 22.2 mm in height x 25.4 mm in width.

Flow conditions as well as geometric conditions were varied. Among the operating conditions varied were the fuel flow and the airblast pressure drop. Jet-A was used as the fuel in these tests, since the objective of these tests was to visualize the global structure of the jet (refer to Section 4.4.1). To affect the airblast air to liquid mass flow ratio (ALR) while maintaining a constant airblast pressure drop, the spray orifice size was varied. In addition, results for two fuel orifice diameters are included. A summary of the operating and geometric conditions used in the high speed video tests is shown in Table 7.1. The tests were performed at room temperature and pressure.

7.2 Airblast Spray Atomization Modes

Before the atomizing air flow rate was applied in each test, the image of the fuel jet was captured to record its initial condition. Figure 7.2 shows selected images of the liquid jet injected from the fuel orifice diameter of 0.66 mm, with the corresponding liquid mass flow rate and Reynolds number Re_L noted for each picture. From the images, the emerging jet is approximately 5 pixels in diameter, which is close to the 4-pixel dimension that corresponds to the 0.66-mm orifice diameter of the fuel injector.

These images, as with the other video images shown in this chapter, represent a single instantaneous (~ 0.5 msec) snapshot of the spray. For Re_L of up to 1060, the jet issues out of the orifice as a laminar jet. Surface aberrations appear on the jet at a Re_L of 1460, which develop further into a corkscrew-like behavior for the Re_L of 2030 and

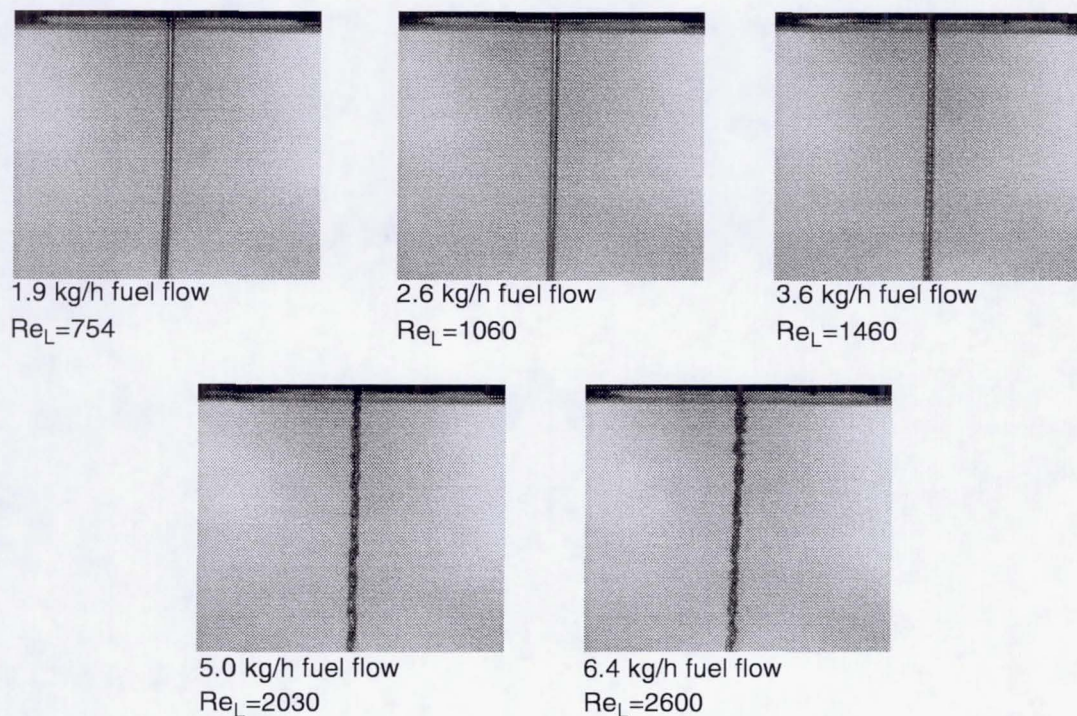


Fig. 7.2 Comparison of pure liquid jet injection at different Reynolds numbers for the 0.66 mm-dia. fuel orifice.

above. These surface markings, however, do not lead to instabilities great enough to atomize the jet at these conditions.

The addition of the atomizing air flow induces the jet instabilities that lead to the breakup of the liquid jet column. The degree of breakup as well as the breakup length of the intact jet from the lesser atomization modes both depend on the amount of airblast air applied to the system. For example, Fig. 7.3 depicts the modes of atomization that occur in the liquid jet. The left image, obtained with an atomizing air pressure drop of 1%, shows the jet breakup occurring halfway across the frame of the

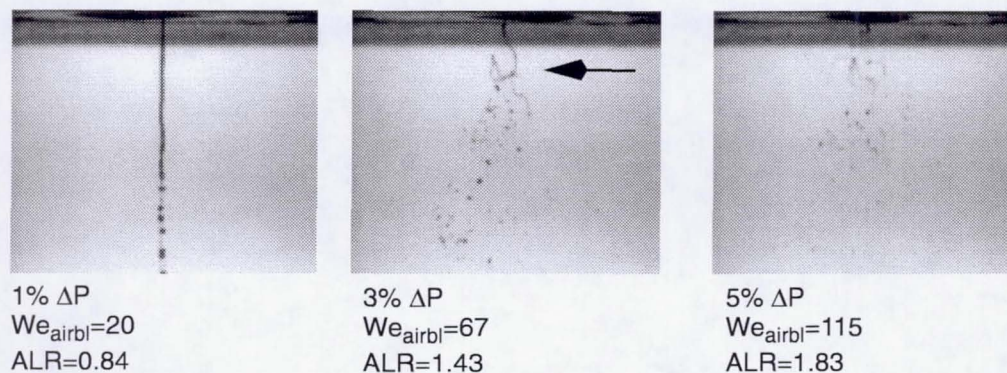


Fig. 7.3 Evolution of the spray with increasing atomizing air flow for the 0.34 mm-dia. fuel orifice, 3.18 mm-dia. spray orifice case, at a fuel flow of 0.66 kg/h.

image. Near the breakup point, the liquid jet undergoes a sinuous motion caused by the friction between the relative velocity of the air and fuel streams. The wave-like disturbance causes the jet to break off and form droplets that are on the order of the size of the liquid column. In their study of the breakup mechanisms of a liquid jet with a coaxial air stream, Farago and Chigier (1992) classified this mode of jet disintegration in the Rayleigh-type category.

With the increase in atomizing air flow rate to a 3% pressure drop, the liquid jet undergoes more oscillations due to the increased friction between the moving air and liquid streams (see center image in Fig. 7.3). The jet veers toward the left in this image as a result of the random undulations of the jet. It is this sinuous motion that also produces the thin sheets that transition into the “ladle” structure described by Farago and Chigier (1992). This curved ladle, shown by the arrow in Fig. 7.3, stretches the jet

into a thin film such that, with enough aerodynamic force, the membranous structure breaks up into smaller droplets. This mode of jet breakup falls under the “membrane”-type mode in the classification scheme of Farago and Chigier (1992).

The third main classification of Farago and Chigier (1992)—jet breakup by “fiber”-type ligaments, does not occur in this experiment. The difference in the nozzle geometry of Farago and Chigier (1992) and the geometry of this experiment explains the absence of this fiber type mechanism. Whereas the injector of Farago and Chigier directs the air to flow parallel with the liquid jet surface, the passageway for the atomizing air in the present experiment directs the air to impinge on the liquid jet almost perpendicularly (see Fig. 7.4). In the airblast experiment, the high atomizing air flows that would otherwise precipitate the fiber-type mechanism in the coaxial airblast injectors of Farago and Chigier instead forms a spray via a “prompt” atomization

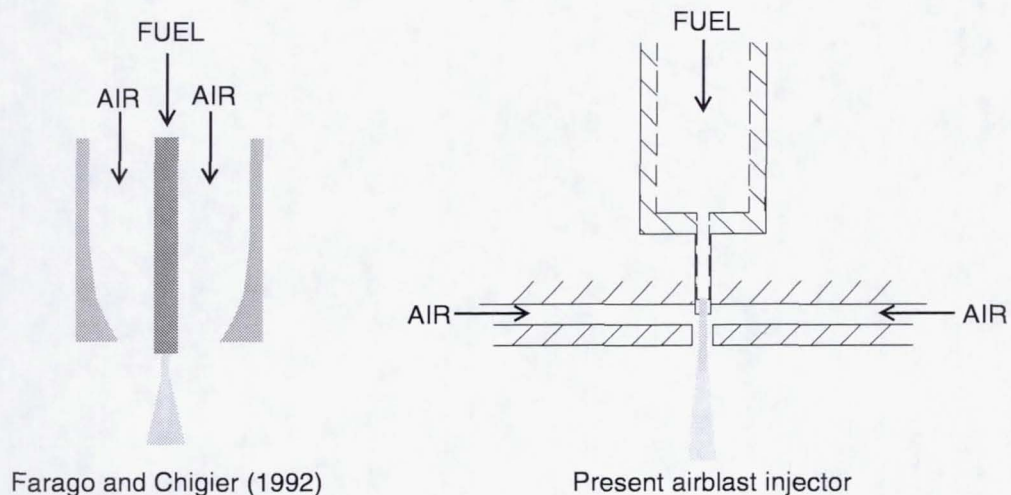


Fig. 7.4 Difference in geometry between the injector of Farago and Chigier (1992) and the present injector.

mechanism (Lefebvre, 1992a and 1992b). The liquid emerges from the orifice as a fully formed spray, as seen in the rightmost picture in Fig. 7.3, with a smaller droplet size distribution. The “prompt” name for this mode is fitting because of the “extrusion” of the emerging liquid jet by the impinging atomizing air streams, a mechanism to which Beck et al. (1991) referred in their airblast sheet injector geometry.

At a higher fuel flow rate, the same three jet breakup mechanisms are observed. Figure 7.5 depicts the sprays formed for a fuel flow rate of 5.0 kg/h for a spray orifice diameter of 3.18 mm and a fuel orifice diameter of 0.66 mm. The left image demonstrates the jet surface instabilities induced by a flow of atomizing air which produces a 0.9% pressure drop across the spray orifice. The increase in atomizing air flow to a 2% airblast ΔP causes the jet surface to expand, as evidenced by the thicker jet column exiting the spray orifice in the center image of Fig. 7.5. At the breakup

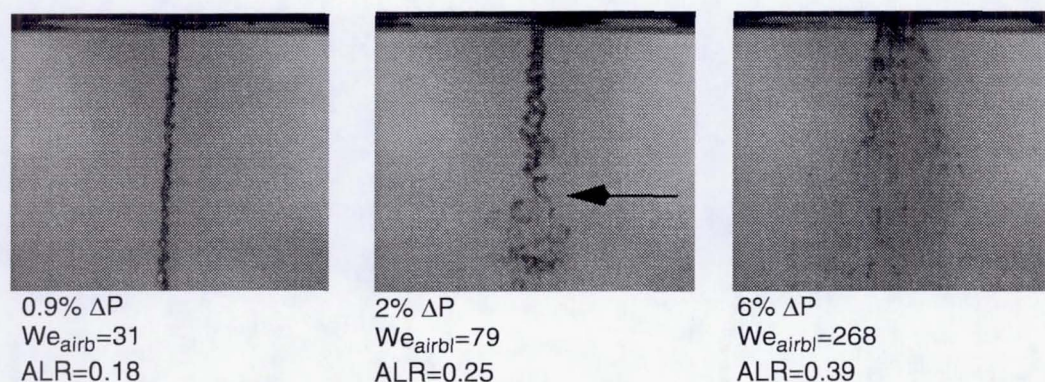


Fig. 7.5 Evolution of the spray with increasing atomizing air flow for the 0.66 mm-dia. fuel orifice, 3.18 mm-dia. spray orifice case, at a fuel flow of 5.0 kg/h.

point denoted by the arrow, the jet column disintegrates into stretched ladders from which smaller droplets are formed. The rightmost image in the figure depicts the prompt atomization mode induced in the spray as the airblast pressure drop is increased to 6%.

The spray images in Figs. 7.3 and 7.5 suggest three distinct flow regimes under which the sprays fall. The results suggest, for instance, that the Rayleigh mode occurs for the approximate ranges of $0\% < \Delta P < 1\%$ and $0 < We_{airbl} < 31$, the membrane-type mode corresponds to the approximate ranges of $1\% < \Delta P < 4\%$ and $66 < We_{airbl} < \sim 80$, and the prompt atomization mode occurs for the approximate values of $\Delta P > 4\%$ and $We_{airbl} > \sim 100$. To formally map the regimes in which these atomization modes fall, the images obtained for 130 combinations of flow conditions were viewed and classified.

Figure 7.6 presents the Re_L - We_{airbl} breakup regime mapped by Farago and Chigier (1992) for their coaxial airblast injector. This chart type takes into account, by virtue of the definitions of Re_L and We_{airbl} , the pertinent liquid properties of ρ , μ , and σ , the liquid velocity and initial jet diameter, and the air ρ and velocity. Overlaid on this graph is a box bounded by a dashed line, which represents the range limits of the present experiment. The box also corresponds to the range limits of the plot in Fig. 7.7, which presents the results obtained by classifying the images according to the mode of breakup.

Fig. 7.7 shows that the chart can generally be divided into three distinct regions that correspond to each of the breakup modes. The only deviation in the division occurs with the Rayleigh-type cases (denoted by the square markers), which shows

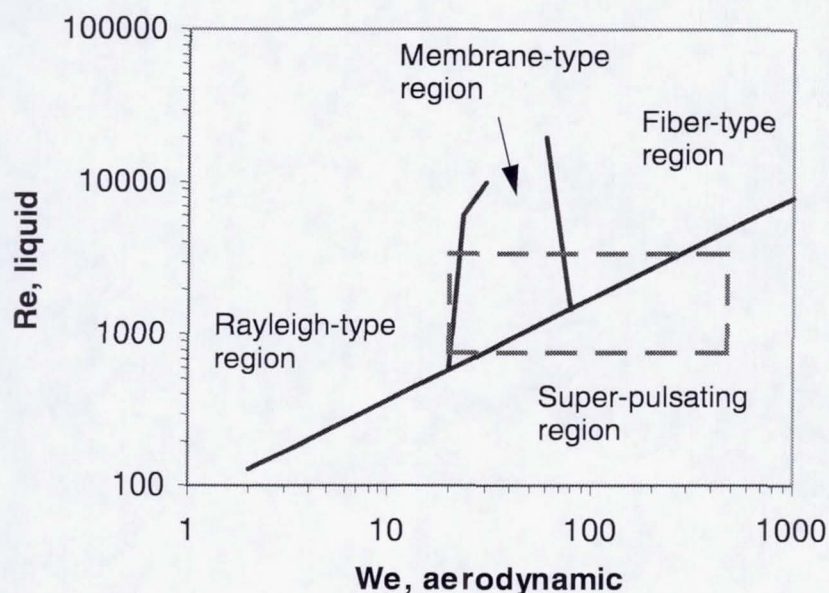


Fig. 7.6 Breakup regime map from Farago and Chigier (1992) with the present range of operating conditions falling within the dashed lines.

several of these cases occurring at a Re_L of 877 and for We_{airbl} between 43 and 162, falling in the other regimes. These cases correspond to the 6.35 mm-dia. case, which is the largest spray orifice that was tested. There apparently reaches a point in this system where any further increase in the hole diameter, which increases the mass flow of air used to atomize the jet (which also increases the We_{airbl} of the spray), does not result in a comparable increase in atomization. Because only the air in closest contact with the jet produces an effect, the rest of the air exits the spray orifice without aiding in the atomization process, as Lefebvre (1992b) has noted for other twin-fluid atomizers.

Also overlaid on Fig. 7.7 are the divisions derived by Farago and Chigier (1992) from their experiment. Although the slopes of the dividing lines from the

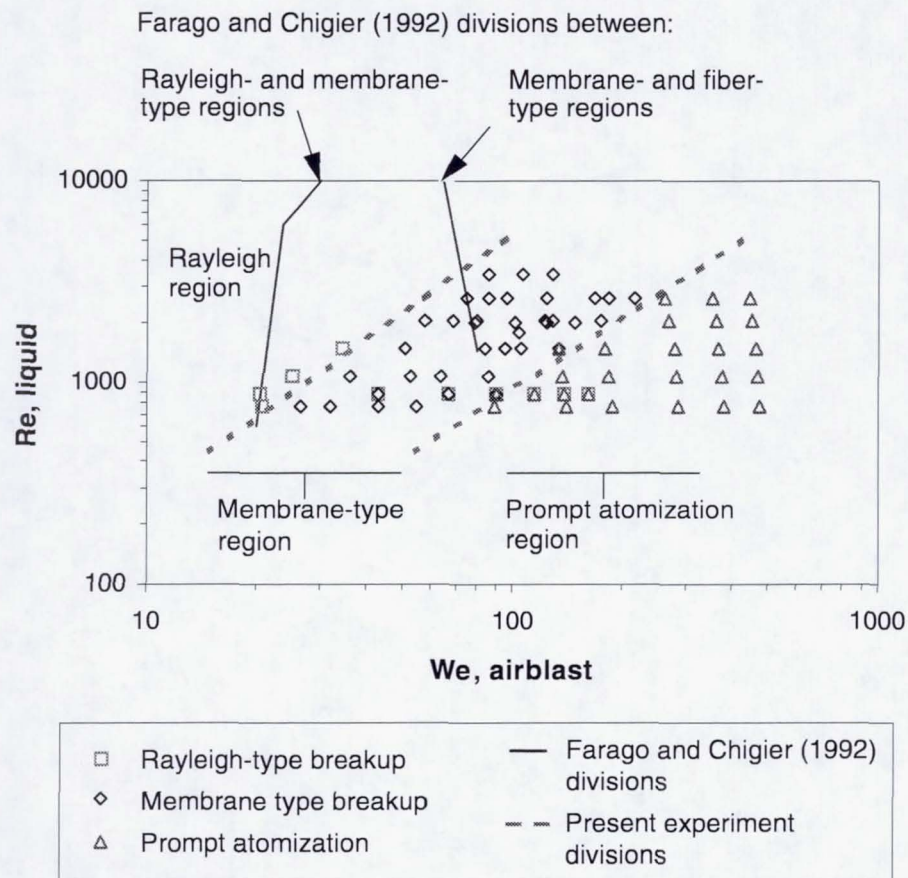


Fig. 7.7 Breakup regime mapping of the airblast spray experiment with respect to Re_L and We_{airbl} .

Farago and Chigier experiment and the present experiment do not match, the divisions occur within a range of Re_L and We_{airbl} values that are on a comparable order of magnitude. Duplication of the regime divisions is not expected because of the different means that the injectors introduce the atomizing air stream to the liquid jet. In the Farago-Chigier injector, the atomizing air stream flows co-axially with the liquid, and an increase in co-flowing air enhances breakup at the surface of the liquid jet as it

issues from the orifice and produces a fiber-type of disintegration. On the other hand, the present airblast injector induces a near-normal impingement of the atomizing air on the liquid jet, which is a factor that leads to the “prompt” atomization mode described by Lefebvre (1992a, 1992b). An increase in air flow causes the jet to break up within the injector passageway, as seen in the 6% airblast ΔP condition in Fig. 7.5.

The divisions between the Rayleigh- and membrane-type regimes and between the membrane-type and prompt atomization regimes are of a positive slope. For a set injector geometry, any increase in the liquid velocity may pull the jet back toward a less severe breakup mode (e.g., from the prompt atomization mode to the membrane-type mode) because of the increase in Re_L and decrease in We_{airbl} . To offset this action and induce the jet to undergo a higher-order mode of jet breakup, the aerodynamic force placed upon the jet must increase by increasing the relative velocity between the jet and the coflowing air stream. This step would increase We_{airbl} and result in pulling the spray back toward the more dynamic breakup regime.

The cases were also plotted on an $ALR-We_{airbl}$ chart to determine the jet breakup mode dependence on ALR , since the ALR is a parameter that is often referred to in airblast atomization. The ALR is changed at a particular pressure drop setting by changing the size of the spray orifice. Figure 7.8 shows the appearance of regions where the different breakup modes lie. Unlike the divisions in the Re_L-We_{airbl} breakup regime map, the divisions in the $ALR-We_{airbl}$ chart do not follow a linear slope. There is also a transition region in which spray conditions related to either the membrane-type or the prompt atomization modes fall. The results from the 6.35-mm spray orifice diameter case, which was shown to deviate from the regional divisions in the Re_L-

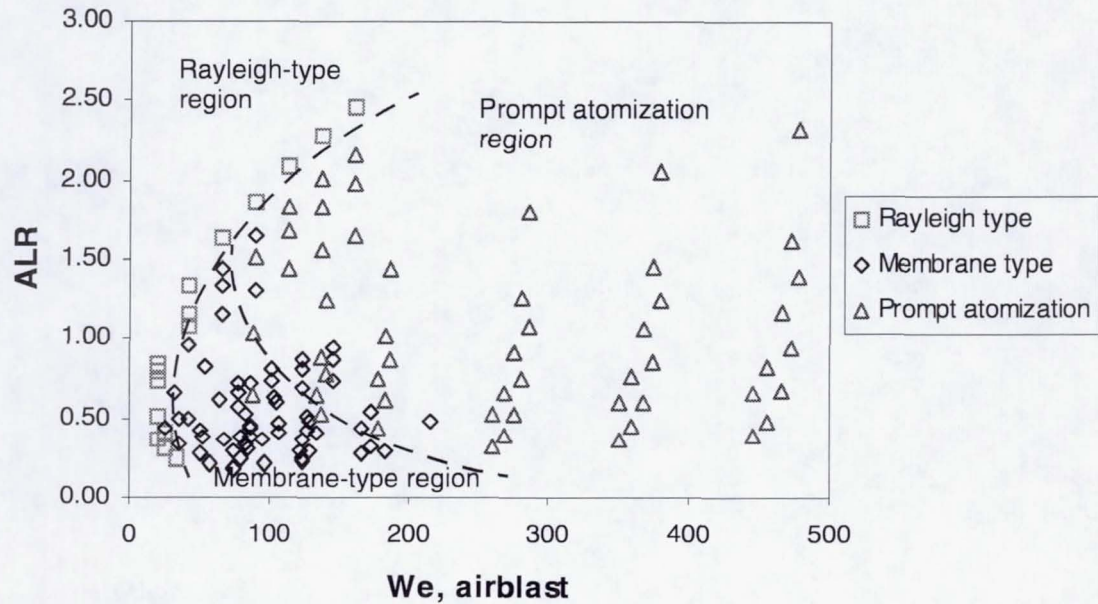


Fig. 7.8 Breakup regime mapping of the airblast spray experiment with respect to ALR and We_{airbl} .

We_{airbl} breakup regime map of Fig. 7.7, are represented on the $ALR-We_{airbl}$ by the square markers corresponding to ALR values above 1.6. This further shows that the supposed gain in atomization, obtained by increasing the ALR with the use of a larger orifice diameter (e.g., the 6.35 mm-dia. orifice) while maintaining the same airblast ΔP setting, does not guarantee the formation of a fully-atomized spray.

7.3 Spray Angle

The spray angle is another property that is often used to characterize the spray. The spray angle relates to the dispersion of the spray, as a wider spray angle distributes

the spray across a larger area for fuel-air mixing. The penetration and dispersal of the spray jet into the crossflow could also potentially depend on the spray angle.

The spray angle was measured for the set of cases with fuel flows above 1.9 kg/h, and for a fuel hole diameter of 0.66 mm because these images offered the highest contrast between the fuel spray and the background. For these conditions, only the spray orifice diameters of 3.18 mm and 4.22 mm were tested. The fuel flow was varied between 1.9 kg/h and 6.4 kg/h, and the airblast pressure drop was set at 2%, 3%, 4%, 6%, 8%, and 10%. An averaged frame was obtained from a set of 100 images that were acquired at a rate of 2000 frames/sec.

Section 7.3.1 details the methodology used to measure and calculate the spray angle, while Section 7.3.2 discusses the results obtained from the parametric variations.

7.3.1 Measurement and Calculation Methods

The spray angle was obtained from the time-averaged high speed video images. A Sobel-based edge detection method was applied to the near-field region of the jet, within 5 mm of the exit plane of the spray. Derivatives along the *i*- and *j*- dimensions of the image were obtained at each pixel value by applying the following 3 x 3 masks at each point:

$$\text{Mask}_1 = \begin{bmatrix} -1 & 0 & 1 \\ -2 & 0 & 1 \\ -1 & 0 & 1 \end{bmatrix} \quad (7.1)$$

$$\text{Mask}_2 = \begin{bmatrix} 1 & 2 & 1 \\ 0 & 0 & 0 \\ -1 & -2 & -1 \end{bmatrix} \quad (7.2)$$

At the (i, j) pixel in an $m \times n$ image, each element of the mask expressed in Eqs. 7.1 or 7.2 is multiplied to its corresponding element in a 3×3 submatrix centered at (i, j) , and the sum of the products is returned to the (i, j) pixel in the original image. Applying Mask_1 in Eq. 7.1 produces a derivative along the horizontal axis, while applying Mask_2 in Eq. 7.2 yields the derivative along the vertical axis of a planar image. The mask is swept over the image between row numbers 2 and $m-1$, and between column numbers 2 and $n-1$, resulting in a final matrix of size $(m-2, n-2)$. The loss of the top-most and bottom-most rows, and of the left-most and right-most columns do not affect the spray angle analysis.

The final step in the edge detection uses the matrices containing the horizontal and vertical gradients to calculate the sum of the squared gradients. If the image matrix of horizontal gradients is defined as $\partial M / \partial x$, and the image matrix of vertical gradients is defined as $\partial M / \partial y$, then a final squared gradient magnitude (SGM) at each pixel is calculated by

$$SGM = \left(\frac{\partial M}{\partial x} \right)^2 + \left(\frac{\partial M}{\partial y} \right)^2 \quad (7.3)$$

By applying the squaring function, the edge detection method becomes insensitive to the local orientation of the edge (Russ, 1995).

Each time-averaged image was scanned within the first 50 rows, which encompassed a distance of 5 mm within the spray exit plane. At each row, the positions of the two maxima values corresponding to the spray edges were recorded. The elicited edges were plotted atop their respective spray image to qualitatively check

the fit of the points. Points that clearly did not fall on the spray edge were neglected. Despite the loss of such points, each edge of the spray was still defined by at least ten points.

A least squares fit of the points yielded linear equations for each edge. The slopes m_1 and m_2 of the two lines were then used in the following relationship from analytic geometry to solve for the spray angle, α :

$$\tan \alpha = \left| \frac{m_1 - m_2}{1 + m_1 m_2} \right| \quad (7.4)$$

The uncertainty associated with the accuracy in pinpointing the edge resulted in a $\pm 5^\circ$ uncertainty in the spray angle measurement.

7.3.2 Effect of Parametric Variation

The results of the spray angle measurements are depicted in Fig. 7.9 for the set of sprays associated with the 3.18-mm spray orifice diameter, and in Fig. 7.10 for the cases which used the 4.22-mm spray orifice diameter. Each plot displays the effect of varying the airblast pressure drop on the spray angle. The different fuel flow cases are represented by the different symbols and colors noted on the legend.

In the smaller spray orifice (3.18-mm dia.) case in Fig. 7.9, angles of less than 35° indicate a narrow spray. The smallest spray angles (less than 5°) are basically liquid jets that are slightly expanding due to the onset of a wind-induced instability. These small spray angles occur at the lower airblast pressure drop range of 2-3% for the higher fuel flow rates of 5.0 kg/h and 6.4 kg/h. These operating conditions, which

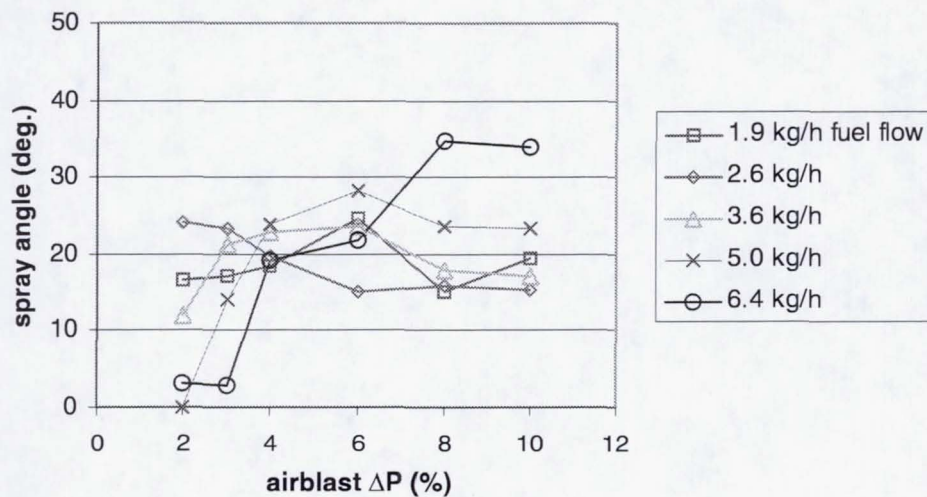


Fig. 7.9 Effect of the atomizing air pressure drop on the angle of the airblast-atomized spray for the 3.18-mm spray orifice diameter.

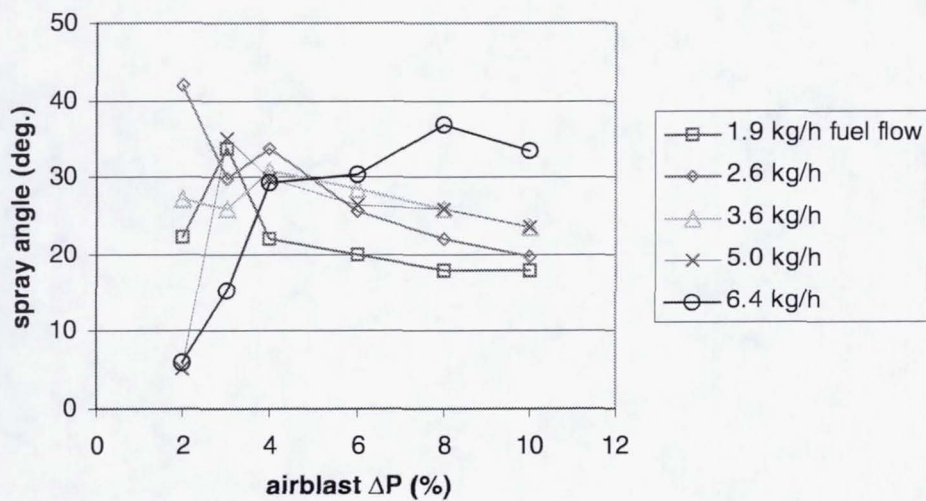


Fig. 7.10 Effect of the atomizing air pressure drop on the angle of the airblast-atomized spray for the 4.22-mm spray orifice diameter.

combine high fuel flow rates and low airblast flows, result in low We_{airbl} flows that are not conducive to full spray formation.

The 1.9 kg/h and 2.6 kg/h fuel flow rates produced spray angles at the different airblast flows that were largely invariant, as the angles for these conditions fall within the $\pm 5^\circ$ band of uncertainty. The 2% airblast ΔP —the lowest pressure drop tested—sufficiently achieves the desired spray angle for these fuel flows. As the fuel flow increases, the point at which the maximum spray angle is achieved occurs at higher airblast pressure drops. For the 3.6 kg/h fuel flow, the 3% airblast ΔP condition is the critical point. At the higher fuel flows of 5.0 kg/h and 6.4 kg/h, the critical pressure drop occurs at the 4% level. For a set airblast flow velocity, an increase in the fuel flow decreases the relative velocity between the two streams, which decreases the intensity of breakup, and in turn, the spray angle.

The results for the larger spray orifice diameter of 4.22 mm (Fig. 7.10) produced similar trends. For the lower fuel flow rates of 1.9 kg/h, 2.6 kg/h, and 3.6 kg/h, the spray is already fully formed, with angles above 20° occurring at a minimal airblast pressure drop of 2%. In the higher fuel flow cases of 5.0 kg/h and 6.4 kg/h, the onset of full spray formation shifts toward higher airblast pressure drops of 3% and 4%, respectively.

Interestingly, in the larger spray orifice case, all of the sprays except for the highest fuel flow rate show a slight decreasing trend in spray angle as the airblast flow is increased beyond 4% (see Fig. 7.10). This trend results from a two-fold effect of the increased air flow. First of all, the increased velocity of airblast air through the orifice enhances the atomization of the liquid. Secondly, the high air velocity forces the jet to

issue from the orifice as a fast-moving column of air that carries the finely-atomized spray along with it. The highest fuel flow case (6.4 kg/h) does not show this trend, because the spray was probably not well-atomized for this case. If airblast pressure drops higher than 10% were tested, then the decreasing trend in the spray angle would be induced in the 6.4 kg/h case.

The spray angles produced by the 4.22-mm spray orifice diameter are larger overall than the angles produced by the 3.18 mm-dia. orifice. The reason for this observation is related to the difference in the injector geometry (see Fig. 7.11). A smaller diameter confines the jet as it exits the spray orifice—more so than would be achieved for a larger diameter orifice with the same orifice length. As Fig. 7.11 depicts, an increase in diameter allows more air to exit the orifice at a shallower angle with respect to the injection plate.

To further illustrate this point, droplet size and velocities were measured across the z -axis of the spray. The PDI system (Phase Doppler Particle Analyzer, Aerometrics) measured the x - and z -components of droplet velocities across the $z=0$ mm axis, in 1-mm increments, at the $x=10$ mm plane. Fig. 7.12 contains plots of the mean droplet velocity vectors obtained for a 1.9 kg/h fuel flow condition at varying airblast pressure drops. The vectors associated with the 3.18 mm-dia. case are shown in red, and are overlaid on the black vectors associated with the 4.22 mm-dia. case. For reference, the corresponding mean D_{32} values are shown at each measured point as proportionally-sized circles.

The plots in Fig. 7.12 show that the velocity magnitudes of the droplets produced by the smaller hole diameter (3.18 mm) are higher than the velocity

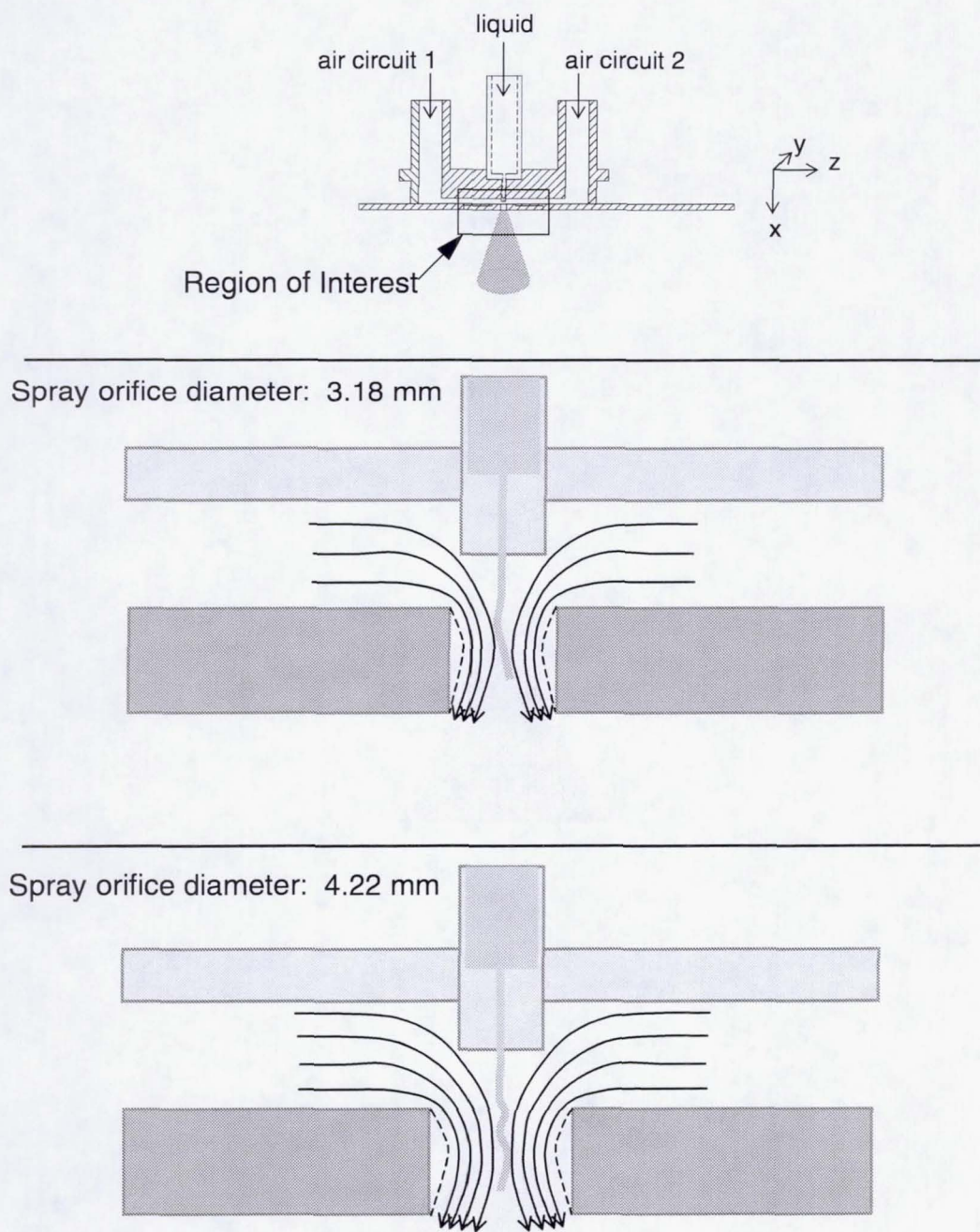


Fig. 7.11 Conception depicting the effect of the spray orifice diameter on the spread of the spray.

magnitudes at the corresponding points in the larger hole diameter (4.22 mm) case. The different airblast ΔP settings were held constant for the different hole sizes, which would imply that the bulk airblast velocities should be similar. However, because the velocity vectors shown in Fig. 7.12 represent an average velocity for all droplets measured in the sample, the varied droplet sizes and their corresponding velocities could account for the difference in the measured peak droplet velocity.

Despite the difference in magnitudes, the direction of the velocity vectors nearly coincide for the sprays produced by both hole sizes. The wider opening of the 4.22 mm-dia. hole simply allows the spray to fan out across a wider angle.

The larger hole orifice was designed to increase the mass flow rate of air through the orifice while maintaining the same pressure drop (and hence, velocity magnitude) as a smaller orifice. As the hole size is varied at a set air velocity, the *ALR* can thus be independently varied. The importance of the *ALR* in affecting spray formation via airblast atomization has been noted by Lefebvre (1989), and can be seen by the use of this parameter in D_{32} correlations (e.g., see Eq. 4.1).

If the droplet D_{32} along the same $y=0$ mm axis at the $x=10$ mm plane are compared for the different orifice cases, it is seen that an increase in the spray orifice diameter enhanced spray atomization. This is presented more clearly in Fig. 7.13 for the 1.9 kg/h fuel flow case. Even though the *ALR* increases by 60-80% when using the 4.22 mm-dia. orifice instead of the 3.18 mm-dia. orifice, the overall D_{32} levels per airblast flow rate improve at most, by 40%. The D_{32} distribution, however, does verify that the spray tends to spread out farther when a larger orifice is used.

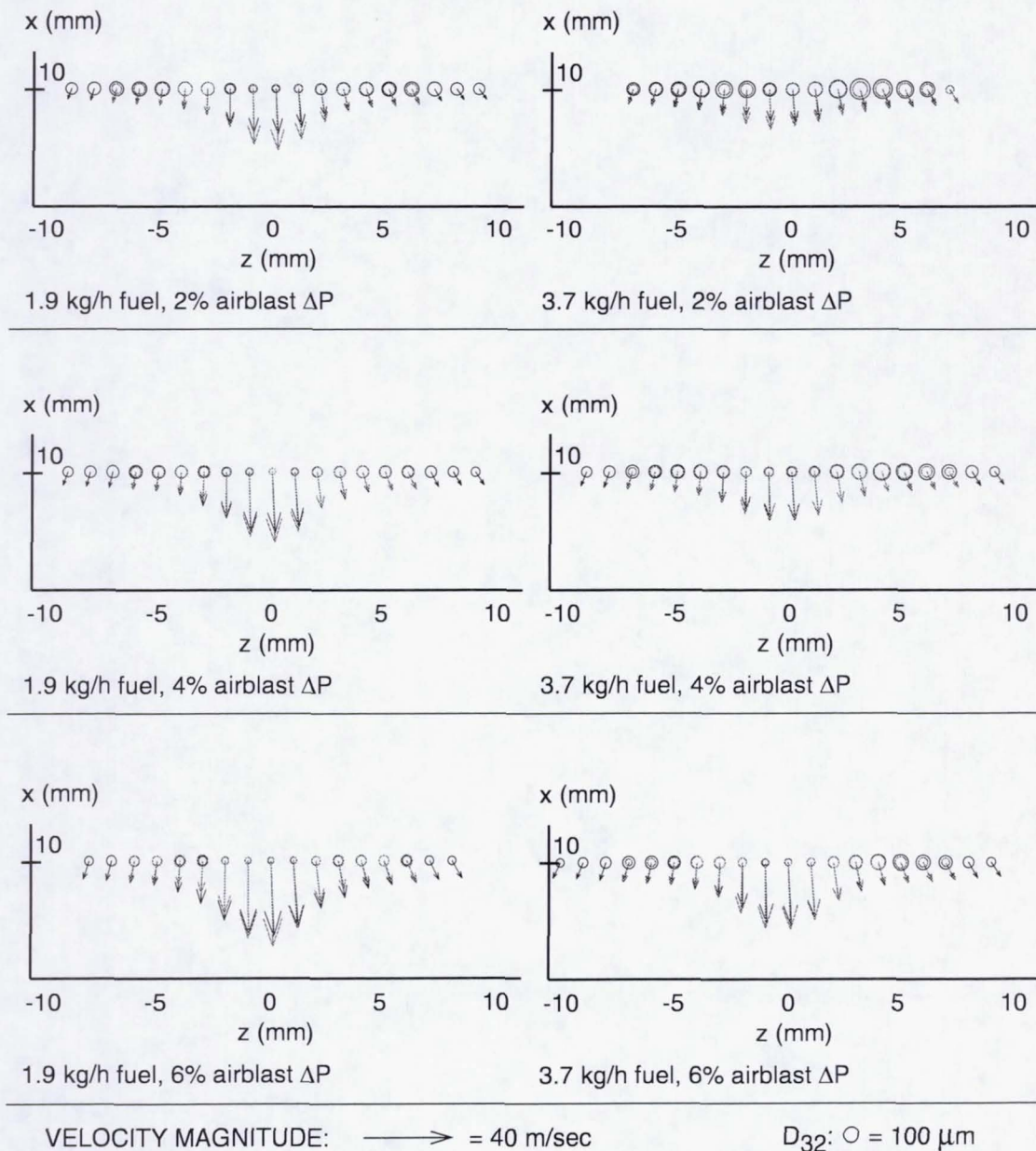
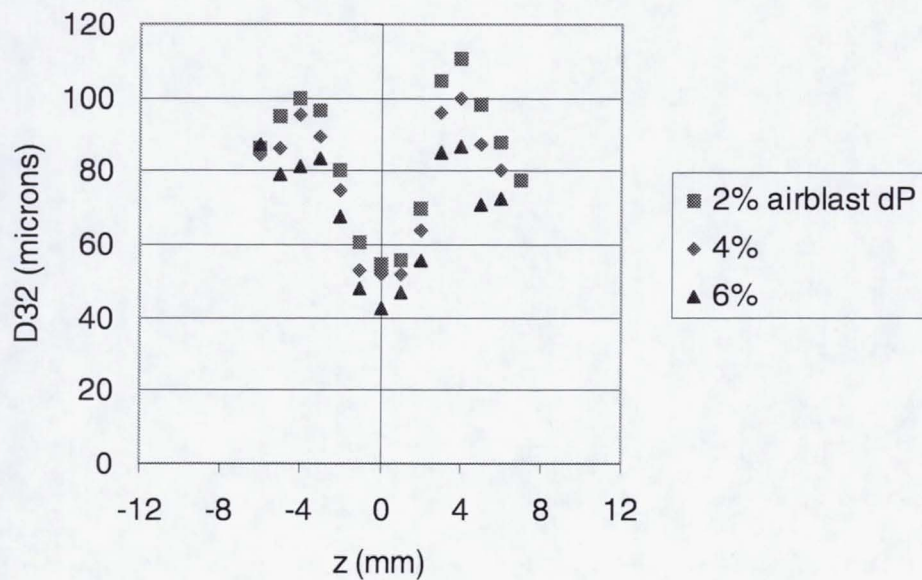
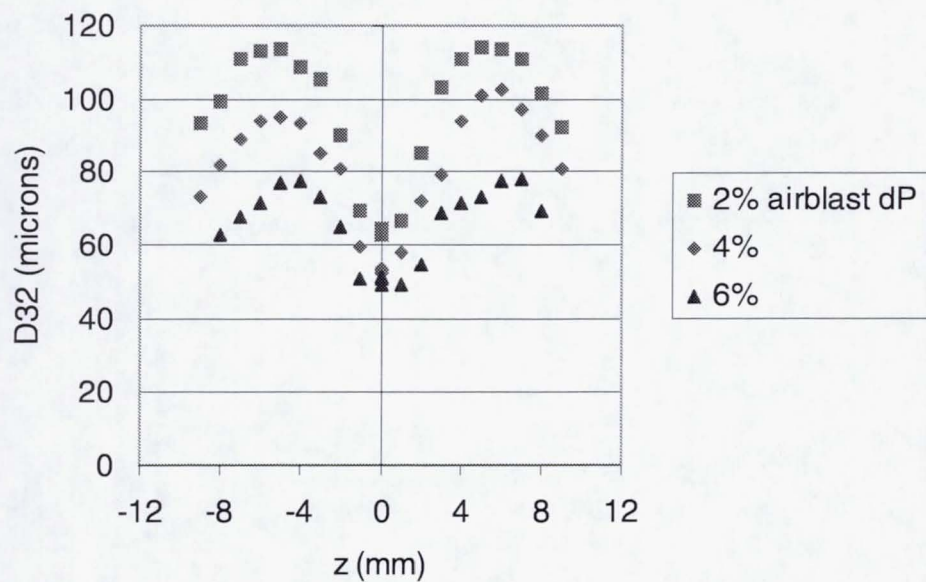


Fig. 7.12 Mean velocity and D_{32} plots across the longitudinal section ($y=0$ axis) of the airblast spray, at the $x=10$ mm plane, for the 3.18 mm-dia. spray orifice case (red), and the 4.22 mm-dia. case (black).



spray orifice diameter: 3.18 mm



spray orifice diameter: 4.22 mm

Fig. 7.13 Droplet D_{32} measured along the spray centerline parallel to the axis through the air circuits, at $y=0$ mm and $x=10$ mm, for the 1.9 kg/h fuel flow condition.

7.4 Summary

The airblast spray was investigated for its breakup mechanism and also for its spray angle in a non-crossflow configuration. The primary objective of these tests was to survey a wide range of conditions in order to assess their effect on the behavior of the spray in the absence of a crossflow.

Using high speed video imaging, 130 conditions that varied the injector geometry and flow rates were tested. The images were classified according to the mechanism leading to the breakup of the jet and plotted on charts with the relevant dimensionless parameters of Re_L , We_{airbl} , and ALR on the axes. The breakup of the airblast-atomized jet follows either a Rayleigh-type mode, a membrane-type mode, or prompt atomization. Because of the myriad parameters that can be varied in the system (e.g., the fuel and spray orifice sizes, the fuel and air flows), the regime maps can help to predict the type of jet breakup that will occur for a given combination of parameters.

The spray angles were also measured for various flow conditions operating under two orifice sizes. For the fully-atomized spray formed via prompt atomization, the geometry plays a role in affecting spray dispersion. At a constant atomizing air pressure drop, the larger hole size allows the spray to expand further. An increase in the ALR also arises from an increase in hole size, and leads to enhanced atomization. For the fully-formed spray, the increase in hole size affects the spray expansion more so than its atomization. However, there is a limit to increasing the hole size: an increase beyond a certain diameter will allow a higher percentage of atomizing air to issue through the orifice without participating in the liquid breakup process, as shown in the results from the 6.35 mm-dia. orifice case.

CHAPTER 8

PLANAR CHARACTERIZATION OF THE AIRBLAST SPRAY WITHOUT CROSSFLOW

This chapter extends the work performed in the previous chapter by probing selected spray conditions in more detail. High speed video allowed for the quick viewing of instantaneous images of the spray at a high resolution, and under a multitude of conditions. While the high speed video images show the jet structure in terms of, for example, the breakup mode and spray angle, these video images represent an integrated light scattering field that cannot be resolved into liquid mass distributions at specific planes. With the development of the UV planar imaging techniques in Chapters 5-6, the internal spray structure in terms of its liquid distributions, and the extent of the atomizing air in the spray, can be visualized. The objective of the present chapter is to perform a more detailed characterization of the airblast spray without crossflow using the UV planar imaging techniques.

8.1 Experimental Conditions

The setup of the UV planar imaging diagnostic, as applied to the airblast spray in the non-crossflow configuration, is depicted in Fig. 8.1. The spray injection panel is oriented in the same horizontal position as it was in the high speed video tests. A vertical laser sheet consisting of the 266 nm wavelength passes through the spray along the xz -plane along the positive z -axis. The intensified CCD camera is oriented normal to the sheet, and is focused on the plane of the laser sheet. While the laser and camera

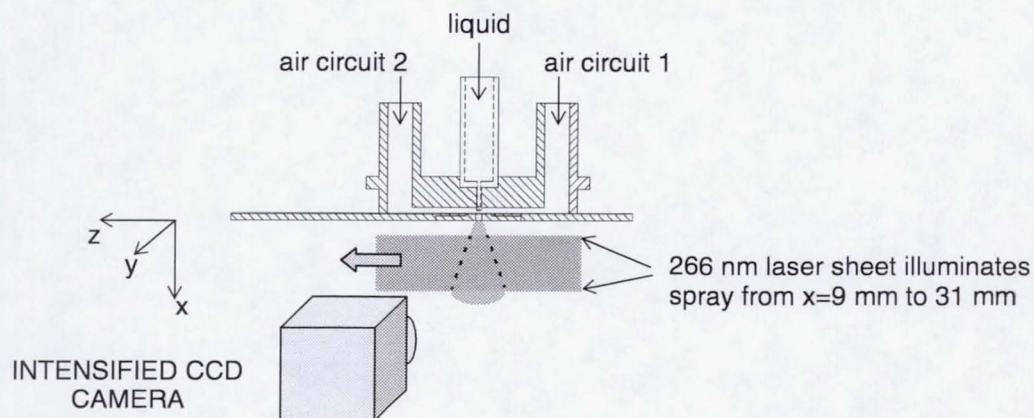


Fig. 8.1 Positioning of the intensified CCD camera relative to the vertical laser sheet passing through the spray experiment in the non-crossflow configuration.

remained fixed to the optical bench top, the injection panel was traversed along the y-axis from -10 mm to 10 mm to capture the different cross-sectional distributions in the spray. The -10 mm to +10 mm y-values were arbitrarily chosen limits that still captured the bulk of the spray.

Although the planar images canvassed a 21 mm-wide region, the image processing techniques that were applied (see Chapter 6) resulted in a 19.2 mm-wide region. The overall dimensions of the processed image in the horizontal yz-plane, shown in Fig. 8.2, are 19.2 mm x 25.2 mm, with the center of the image coinciding with the spray origin. All of the images are scaled by the maximum level of intensity measured for the particular imaging technique. For example, the intensities for the calibration fluid PLLIF images were normalized by the maximum PLLIF intensity

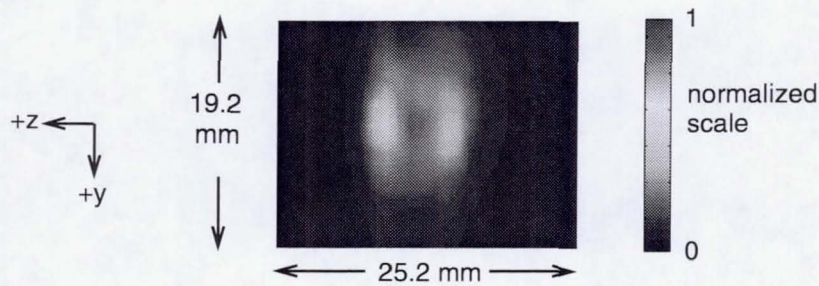


Fig. 8.2 Sample horizontal planar section extracted from the set of vertical slices.

measured for the entire batch of cases tested. The color scale in the images runs from blue to red, representing the range of normalized values from 0 to 1.

The set of conditions that were tested in this phase of the experiment are listed in Table 8.1. The conditions represent a subset of the high speed video tests. Two fuel flow rates, three airblast pressure drops, and two spray orifice sizes were chosen to yield 12 combinations of parameters ($2 \times 3 \times 2 = 12$).

The fuel flow rates, which differ by a factor of two, still fall within the practical operating conditions of a gas turbine engine power cycle. The airblast pressure drops of 2%, 4%, and 6% also are reasonable conditions for gas turbine engine operation. The three pressure drop conditions were chosen to produce sprays that were judged from the high speed video tests to be “poorly” atomized (the 2% airblast ΔP condition), “well” atomized (the 4% airblast ΔP condition), and “fully” atomized (the 6% airblast ΔP condition). The spray orifice diameters of 3.18 mm and 4.22 mm were selected based on past experiments (Leong et al., 2000) and on future full-injector tests under

Table 8.1 Operating and geometric conditions for the planar imaging of the airblast spray experiment in the non-crossflow configuration.

Parameter	Range of Variation
Ambient pressure (kPa)	101.3
Fuel flow (MIL-C-7024D) (kg/h)	1.8, 3.7
Airblast pressure drop (%)	2, 4, 6
Airblast velocity, U_{airbl} (m/sec)	43.6 - 80.4
Airblast air to liquid mass flow ratio, ALR	0.29 - 1.87
$Re_L = \frac{\rho_L U_L d_f}{\mu_L}$	$1.26 \times 10^3 - 2.59 \times 10^3$
$We_{airbl} = \frac{\rho_g (U_{airbl} - U_L)^2 d_f}{\sigma_L}$	88 - 425
$Re_{airbl} = \frac{\rho_g U_{airbl} d_{spray}}{\mu_g}$	$1.09 \times 10^4 - 2.90 \times 10^4$
Fuel orifice diameter, d_f [corresponding l/d in brackets]	0.66 mm (0.0260 in.) [$l/d = 2.5$]
Spray orifice diameter, d_{spray} [corresponding l/d in brackets]	3.18 mm (0.125 in.) [$l/d = 1.0$], 4.22 mm (0.166 in.) [$l/d = 0.75$]

Notes:

- $\rho_L = 764 \text{ kg/m}^3$ for MIL-C-7024D; $\rho_g = 1.19 \text{ kg/m}^3$ for air at room temp. and pressure
- $\mu_L = 7.96 \times 10^{-4} \text{ kg/m-sec}$ for MIL-C-7024D; $\mu_g = 2.00 \times 10^{-5} \text{ kg/m-sec}$ for air at room temp. and pressure
- $\sigma_L = 0.0245 \text{ kg/sec}^2$ for MIL-C-7024D
- For reference, hardware dimensions are also given in English units, which were the primary units used in the machining process.

reacting conditions. The placement of these conditions on the breakup regime map developed in Chapter 7 for the airblast spray injector is shown in Fig. 8.3. The 2% airblast ΔP ranges fall in the membrane-type regime, and the 6% airblast ΔP ranges fall

in the prompt atomization regime. The 4% ΔP condition straddles both regions, with the 4% condition for the 3.7 kg/h fuel flow rate falling in the membrane-type region, and 4% condition for the fuel flow rate of 1.8 kg/h falling in the prompt atomization region.

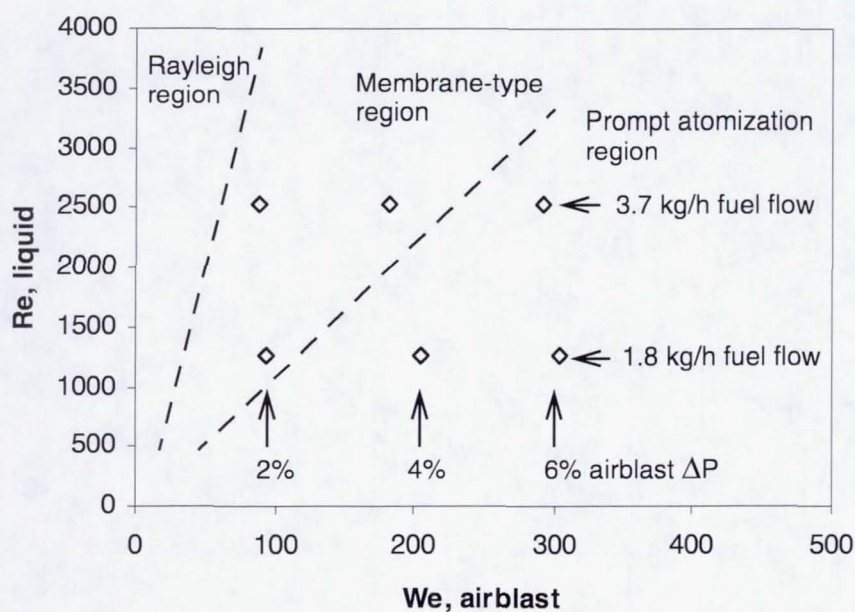


Fig. 8.3 Classification of the case conditions tested on the breakup regime map for the airblast spray.

The rest of this chapter focuses on characterizing the distribution of liquid in the spray—qualitatively through image comparisons, and quantitatively using calculated parameters. The extent of the air in affecting and in being affected by its interaction with the liquid in the spray is also characterized via the planar imaging techniques.

8.2 Distribution of the Liquid Component of the Spray

The canvassing of a volume of the spray enables the characterization of its evolution along the axial direction. The imaged volume does not represent the spray in “real-time,” but because the spray operates under steady-state conditions, the volume of images is presumed to portray the spray adequately.

The effect of the parameters on the dispersion of the liquid in the spray is first observed by comparing the cases at the cross-sectional plane parallel to the injector panel and located 10 mm from the spray orifice exit. Thereafter, the evolution of the spray along its axial direction is reviewed for the different cases.

8.2.1 Comparison at the $x=10$ mm Plane

8.2.1a PLLIF and Planar D_{32} Images

Calibration fluid PLLIF images are used to view the liquid mass distributions in the spray. The PLLIF images for the 1.8 kg/h fuel flow, 3.18 mm-dia. orifice case are presented in Fig. 8.4 for the $x=10$ mm plane. The images are arranged from left to right by increasing airblast pressure drop. Overlaid on these images are PDI-measured values of liquid volume concentration that were obtained along the yz -axes of the spray at this plane. The PDI data are represented by filled magenta circles of varying sizes that are proportional to the magnitude of the measured concentration. The size of the circle representing $1.0 \times 10^9 \mu\text{m}^3$ per cubic centimeter of the probe volume is shown at the bottom of the figure. The primary intent of presenting the PDI data alongside the images is to calibrate the images with measured quantities. The inclusion of the PDI

data also serves to verify the comparison between the PLLIF images and the point-based spray measurements of the PDI.

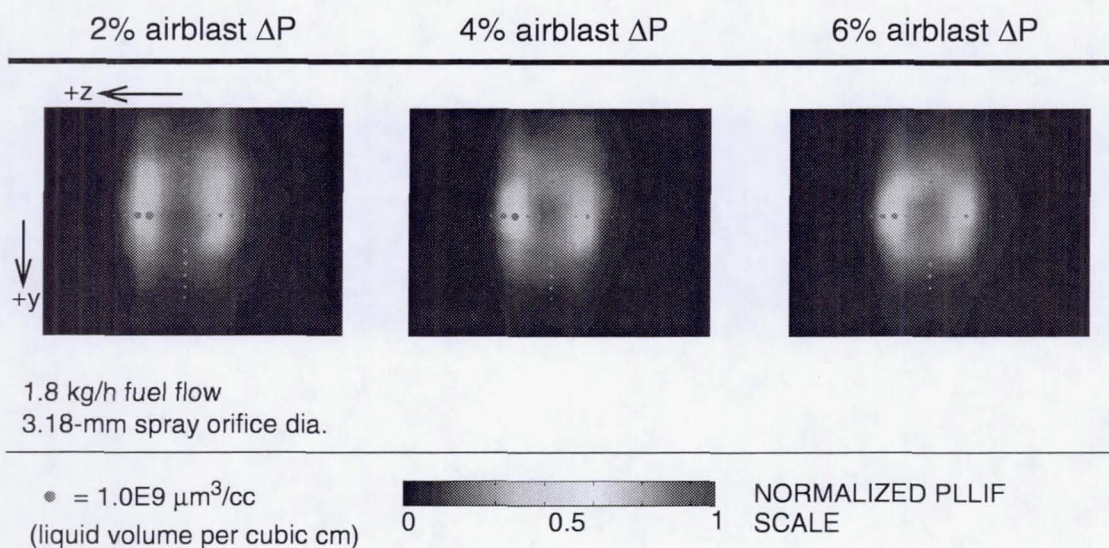


Fig. 8.4 PLLIF liquid concentration images with overlaid PDI-based volume concentration distributions at the $x=10$ mm plane for the 1.8 kg/h fuel flow, 3.18-mm spray orifice dia. condition.

Overall, the sprays shown in Fig. 8.4 are not axisymmetric, but instead are symmetric with respect to the y - and z -axes. The presence of two lobes of high liquid concentration results in the non-axisymmetric structure of the spray. The occurrence of the lobes corresponds to the design of the injector, which utilizes two air circuits to impinge on the emerging liquid jet from opposing z -directions (see Fig. 8.1). The opposing air-flow paths cause the liquid jet to break up and accumulate in two spots along the z -axis.

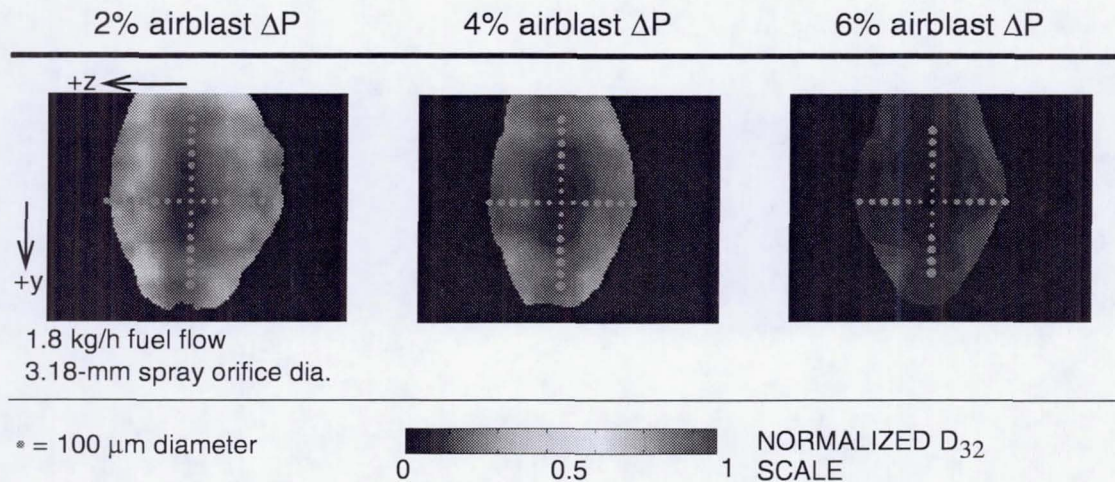


Fig. 8.5 Planar D_{32} images with overlaid PDI-measured D_{32} values at the $x=10$ mm plane for the 1.8 kg/h fuel flow, 3.18-mm spray orifice dia. condition.

Evidence of an increasing atomization trend with increasing airblast pressure drop is shown in Fig. 8.5. The planar D_{32} images, derived by taking a ratio of PLLIF and Mie scattering images, are shown for the same 1.8 kg/h fuel flow, 3.18 mm-dia. case. Overlaid on these plots are the values of D_{32} measured at positions along the y - and z -axes as shown. The size of a 100 μm drop is shown at the bottom of the figure for reference. The images and the PDI data show that smaller D_{32} values are achieved as the airblast air is increased for a set fuel flow rate. It can also be seen for each condition that smaller values of D_{32} occur toward the center of the spray. However, the planar D_{32} images and the PDI-measurements of D_{32} do not reveal any correlation to the two lobes of high liquid concentrations observed in Fig. 8.4.

From Figs. 8.4 and 8.5, the overall size of the spray is observed to decrease with an increase in air flow. The spray formed at a 2% pressure drop is rectangular in shape,

but tends toward a circular shape as the pressure drop increases. The spray coverage also decreases with an increase in the air flow. The increased air flow forces the droplets in the spray to exit the orifice at a higher velocity, and causes the jet cross-section to become more compact.

The PLLIF and D_{32} images of the sprays produced by the twelve case conditions are presented in Figs. 8.6 and 8.7. Each row presents spray images obtained for a certain fuel flow and spray orifice combination. The top row of each of these figures includes the images for the 1.8 kg/h fuel flow, 3.18 mm-dia. case that were presented in Figs. 8.4 and 8.5. The second row of images contains the sprays produced using the same 1.8 kg/h fuel rate, but with the larger 4.22 mm-dia. orifice. The third and fourth rows present images obtained at the fuel flow rate of 3.7 kg/h, with the third row corresponding to the 3.18 mm-dia. orifice and the fourth row corresponding to the 4.22 mm-dia. orifice.

The PLLIF images in Fig. 8.6 are all shown with the overlaid PDI-measured liquid concentration data. The PDI data for the twelve different spray cases verify the utility in using the PLLIF images to characterize the liquid concentration distribution in the spray. In the cases where the two-lobed structure occurs, a definite correlation can be seen between the larger circles representing higher liquid concentrations measured by PDI, and the location of the lobed structures.

The two-lobed concentration of liquid mass occurs in virtually all of the PLLIF images presented in Fig. 8.6. The exceptions appear to be the 4% and 6% ΔP conditions in the 1.8 kg/h, 4.22 mm-dia. case, and the 2% ΔP condition for the 3.7 kg/h, 3.18 mm-dia. case. The two-lobed structures, however, are still present in the

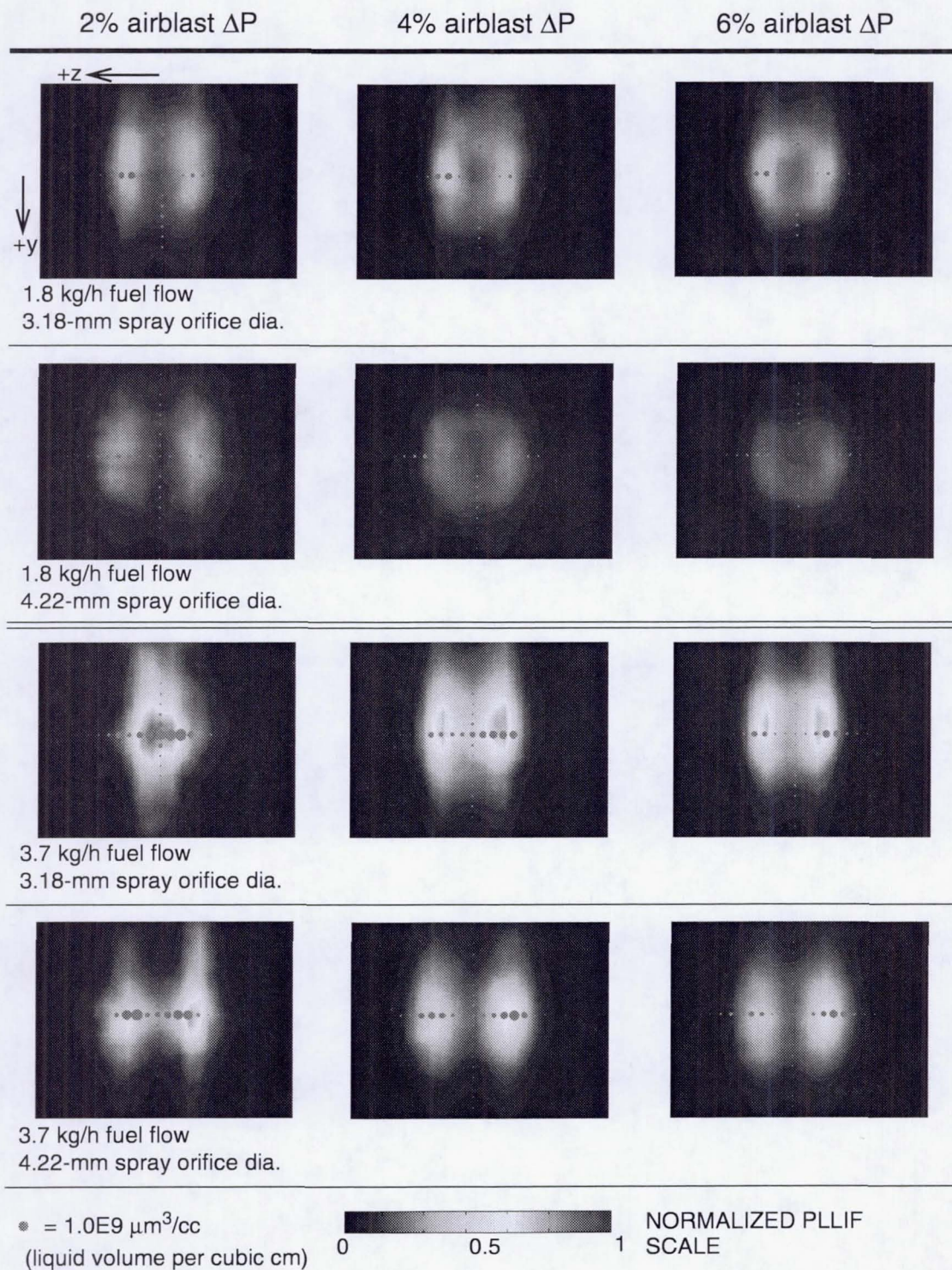


Fig. 8.6 Comparison of PLLIF images with overlaid PDI-based volume concentration distributions at the $x=10$ mm plane for the different spray conditions.

1.8 kg/h, 4.22 mm-dia. cases, but appear indistinguishable because the lower range of intensities and the color scale do not prominently enhance this feature in the images. The 3.7 kg/h, 3.18 mm-dia., 2% ΔP case, on the other hand, definitely shows the liquid mass concentrating toward the center of the spray. The centralized mass in this case, which occurred at a low We_{airbl} of 87 and a high Re_L of 2.53×10^3 , probably resulted from the inability of the relatively low momentum of the atomizing air to separate the spray into the two lobes. However, with an increase in the airblast pressure drop (to 4%) or an increase in the ALR (by using the 4.22-mm spray orifice diameter), the two-lobed structure appears.

The effect of increasing the orifice diameter causes the spray to expand in area and to tend toward a more circular shape. The expansion of the spray with increased orifice size was also observed in the high-speed video images presented in Chapter 7. From the PLLIF images in Fig. 8.6, the coverage of the spray is seen to increase with spray orifice size, as observed from comparisons drawn at the same fuel flow rate (e.g., by comparing the images in rows 1 and 2, and the images in rows 3 and 4). The expanded spray area also disperses the fuel mass, as seen in the overall lower intensities found in the PLLIF images for the larger 4.22 mm-dia. cases.

Increasing the fuel flow rate instead of the jet orifice size decreases the relative fuel-air velocity. The decrease in relative fuel-air velocity, which is an important parameter in spray atomization, reduces the degree of atomization. This effect is shown by comparing the images of rows 1 and 3, and the images of rows 2 and 4 in Fig. 8.6. For the 3.18 mm-dia., 2% airblast ΔP case, an increase in the fuel flow causes the spray to lose its two-lobed structure and to collapse toward the center. The PDI-

measured volume concentrations for the 3.7 kg/h fuel flow also show a high concentration of liquid occurring in the axis running through the two lobes, whereas the distribution of PDI-measured volume concentrations across the y- and z- axes in the 1.8 kg/h fuel flow case are more balanced. The sprays formed from the injection panel apparently tend to disperse in the $\pm z$ -axis.

While the spray is generally symmetric about both the z- and y-axes, the sprays show a modest asymmetry in the magnitude of the lobes. For the 1.8 kg/h fuel flow cases, the left lobe contains a higher concentration of liquid, while for the 3.7 kg/h flow, the concentration in the right lobe dominates. Laser sheet attenuation by the spray would result in a reduced fluorescence intensity in the left side of the spray because the sheet travels in the $+z$ -direction (from right to left in the image). This phenomenon could explain the dominant right lobe in the 3.7 kg/h case, but not the dominant left lobe in the 1.8 kg/h case. The PDI data, however, corroborate the asymmetric spray distributions of the PLLIF images for both sets of fuel flow cases. As seen in Fig. 8.6, higher liquid concentrations measured by the PDI diagnostic generally occur in the left lobe for the 1.8 kg/h fuel flow case, and in the right lobe for the 3.7 kg/h case. Any asymmetries inherent in the injector geometry are probably inducing the asymmetric liquid distributions in the spray.

While the PLLIF images characterize the liquid mass distributions in the plane, they do not reveal any information on the atomization quality. However, the atomization quality can be inferred from the planar images of D_{32} . The planar D_{32} images in Fig. 8.7 are overlaid with the circles representing the size of the D_{32} measured at each point location using PDI. The D_{32} sizes ranged from 40 μm to

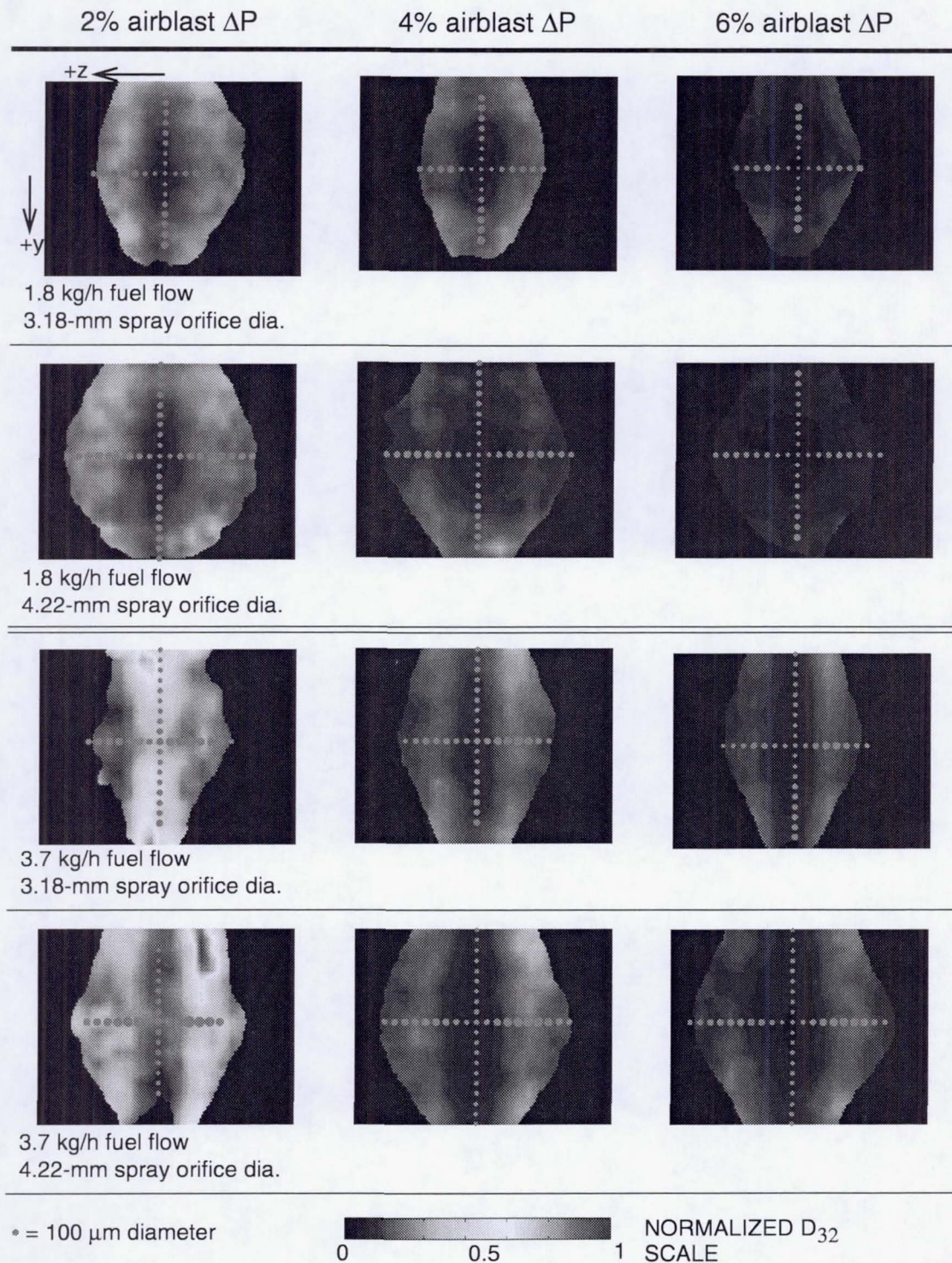


Fig. 8.7 Comparison of planar D_{32} images with overlaid PDI-measured D_{32} values at the $x=10$ mm downstream plane for the different spray conditions.

160 μm along the z -axis passing through the lobed structures, and from 40 μm to 100 μm along the y -axis. A comparison of the planar D_{32} with the PDI-measured D_{32} values shows good agreement in general, with the smaller circles corresponding to the lower intensity levels in the planar D_{32} images. The one exception is the 3.7 kg/h, 3.18 mm-dia., 2% airblast ΔP case, which produced a concentrated distribution of liquid mass toward the center because of insufficient atomization resulting from the low relative velocity (due to the combination of a low air flow and high fuel flow) and low ALR (due to the smaller orifice diameter).

The discrepancy between the PDI-measured D_{32} values and the planar D_{32} image for the 3.7 kg/h, 3.18 mm-dia., 2% airblast ΔP case can be explained by the difference in the sampling basis of the diagnostics used. If the large droplets occurring in the poorly-atomized spray are intermittent, the imaging process, which samples 25 images over the span of one minute, may not sufficiently capture these larger droplets. The PDI diagnostic, which measures at least 10,000 droplets, is not time-constrained, and can thus capture more of the larger droplets. If the imaging sampling interval were longer, the resultant image would capture a more accurate representation of the large droplet population that would better match the PDI data. Sankar et al. (1999) produced this result by showing that the derived planar D_{32} and the PDI data had similar profiles, if the PDI data were measured at a lower data rate to match that of the planar imaging diagnostic. Alternatively, if the imaging technique used a sampling time that obtained a minimum of 10,000 droplets—a setting that can take up to 3 hours to measure—a good fit between the PDI data and the planar D_{32} can be obtained (Le Gal et al., 1999). The lack of a good correlation between the PDI data and the planar D_{32} for the 3.7 kg/h

fuel flow, 3.18 mm-dia. orifice, 2% airblast ΔP case suggests that the PLLIF and planar D_{32} methods may be limited to well-atomized sprays.

If the 3.7 kg/h, 3.18 mm-dia., 2% ΔP case is ignored, the other planar D_{32} images confirm the trends seen in the PLLIF images of Fig. 8.6 and also depict the atomization quality of the sprays. In general, the images show that the atomization quality of the spray increases—by virtue of the decrease in D_{32} intensities—as the airblast pressure drop increases. As the air flow is increased, the D_{32} distributions become more evenly dispersed although the extent of the spray decreases.

Increasing the orifice diameter also leads to a decrease in the droplet D_{32} distributions, a trend that is seen especially in the 1.8 kg/h case. According to the D_{32} correlation by Lorenzetto and Lefebvre (1977) for plain-jet airblast atomization (see Eq. 4.1), an increase in ALR should decrease the D_{32} for the spray. At the larger orifice diameter in the 1.8 kg/h case, the higher air flow rates used to maintain the same pressure drop lead to a 60%-80% increase in ALR. However, the D_{32} images as well as the PDI values do not reflect a comparable decrease in the D_{32} magnitude. From the PDI data, the use of the 4.22 mm-dia. hole size only decreased the droplet D_{32} by a maximum value of 16% over the 3.18 mm-dia. case. Hence, the larger hole size mainly serves to expand the spray jet sooner rather than enhance its atomization.

Finally, an increase in the fuel flow rate for a given air flow condition results in a lower relative velocity and a decreased quality of atomization. This is reflected in Fig. 8.7 by the increased intensity levels present in the sprays formed at the higher fuel flows for each corresponding airblast ΔP and spray orifice diameter condition.

8.2.1b Effect of the Airblast ΔP and Spray Orifice Diameter on the Airblast Velocity

The comparison of planar D_{32} images showed that the increase in airblast pressure drop for a set fuel flow leads to several observations. First of all, the resulting increase in air velocity increases the degree of atomization and produces lower D_{32} values. Secondly, the extent of the spray decreases as well, although the 3.7 kg/h case does not reflect this trend between the 2% and 4% ΔP conditions because the spray is not fully atomized at the 2% condition. In fact, the breakup regime chart in Fig. 8.3 shows that these two conditions correspond to the “membrane-type” breakup mode, which is not considered to produce a fully-atomized spray. However, once full spray atomization is attained by increasing the air flow for the particular fuel flow setting, any additional increase in air velocity reduces the expansion of the jet. The spread of the spray decreases, as seen in the images in Fig. 8.7 and also by the decrease in the spray angle in the fully-atomized sprays (e.g., the plots for the cases of fuel flows less than 5.0 kg/h and airblast ΔP greater than 6% that were presented in Figs. 7.9 and 7.10).

The difference between either increasing the airblast ΔP or enlarging the spray orifice diameter on affecting both the degree of atomization and the spread of the spray can be explained by considering the mean airblast air velocity in a simplified analysis of the control volume at the spray orifice. Figure 8.8 depicts a force diagram of the control volume, which is within the spray orifice of length L and diameter D . The direction of flow is downward, with a pressure differential of $\Delta P = P_1 - P_2$ driving the flow. If the flow at the spray orifice is simplified by assuming that it is fully developed,

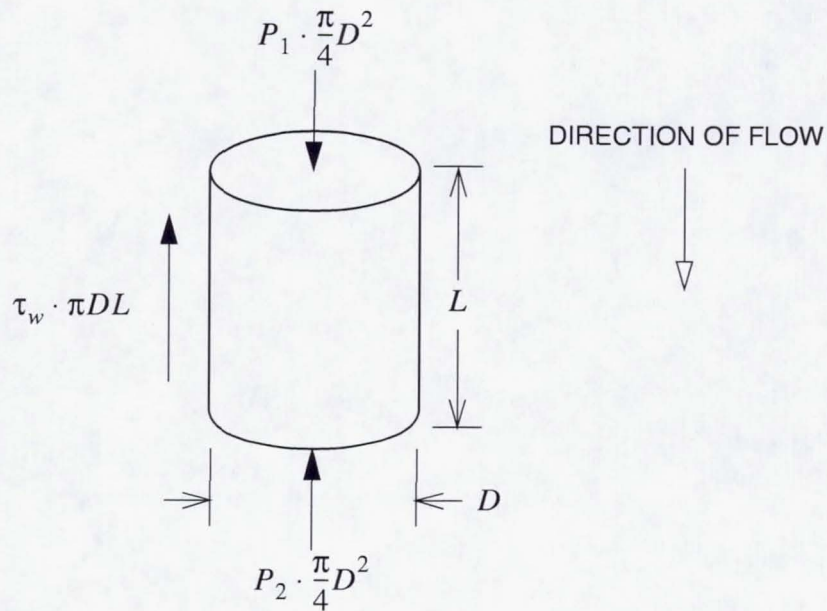


Fig. 8.8 Force diagram on the control volume at the spray orifice.

the pressure gradient will not change along the length of the orifice, and can then be represented by $\Delta P/L$.

The airblast air flow is turbulent through the spray orifice, given that the airblast Reynolds number, Re_{airbl} , ranges from 1.09×10^4 to 2.90×10^4 as noted in Table 8.1. While the velocity profile cannot be obtained analytically for a turbulent pipe flow, the mean velocity, U_m , can be approximated by the empirical relationship $U_m^2 \sim \Delta P$ (Schlichting, 1979). The pressure differential per unit length can thus be related to the dynamic pressure divided by its corresponding characteristic length, the orifice diameter D , by the relationship

$$\frac{\Delta P}{L} = \frac{\lambda}{D} \cdot \frac{1}{2} \cdot \rho U_m^2 \quad (8.1)$$

where λ is the “resistance coefficient of pipe flow” (Schlichting, 1979).

For a constant orifice length L and constant λ and ρ , Eq. 8.1 can be reduced to

$$U_m \propto \sqrt{\Delta P \cdot D} \quad (8.2)$$

For a constant orifice diameter, an increase in the airblast ΔP from 2% to 4% leads to a 41% increase in U_m while a 4% to 6% increase in the airblast ΔP leads to a 22% increase in U_m . On the other hand, for a constant airblast ΔP , an increase in the orifice diameter from 3.18 mm to 4.22 mm results in a 15% increase in U_m . Based on these findings, the increase in the airblast ΔP produces a larger increase in the mean airblast velocities than does an increase in the orifice diameter. This finding explains the higher degree of atomization as well as the decreased extent of the spray area when the planar D_{32} images are compared in relation to increasing airblast ΔP (i.e., across the rows in Fig. 8.7) against the images obtained in relation to an increase in orifice diameter (i.e., comparing the images of row 1 to row 2, and of row 3 to row 4 in Fig. 8.7).

Despite the increased atomization, it is interesting to note that the liquid concentration distributions appear more widely dispersed with an increase in the orifice diameter rather than with an increase in the airblast ΔP (see Figs. 8.6 and 8.7). The dispersion of the liquid in this case may be more of a function of the injector geometry rather than of the air flow.

8.2.2 Axial Evolution of the Liquid Distribution

Images at various downstream positions offer a sense of the spray structure. A feature such as the persistence of the two-lobed structure in the spray can be gleaned from the downstream distributions. The evolving liquid concentration distributions of the different spray conditions shown in Figs. 8.9 through 8.12 are drawn from planes at the $x=10$ mm, 20 mm, and 30 mm positions. In each of these figures, the top row of images are reproduced from the images at the $x=10$ mm plane that were shown earlier in Fig. 8.6.

The first set of conditions produced by the 1.8 kg/h fuel flow, 3.18 mm-dia. spray orifice are presented in Fig. 8.9. From the $x=10$ mm plane, the sprays produced at the different airblast flow conditions increase in coverage as the sprays continue to diverge over the downstream distance. The dispersion of the liquid not only increases in area, but also distributes the liquid more uniformly and with an overall lower average intensity. Remnants of the two-lobed structure still exist, although the gradients are not as large as those occurring at the $x=10$ mm plane.

The effect of the airblast ΔP on the sprays at the initial plane is the same along the downstream planes. The extent of the spray decreases with an increase in pressure drop. In addition, the liquid distributions of the spray become more uniformly dispersed with an increase in the airblast pressure drop, which is postulated to result from the dual effect of the smaller D_{32} and the higher airblast velocity magnitudes. Similar trends are produced for the 4.22-mm spray orifice diameter at the same fuel flow rate of 1.8 kg/h (see Fig. 8.10). An increased uniformity in spray distribution as well as a decreased extent of spray area are both observed as the airblast flow is

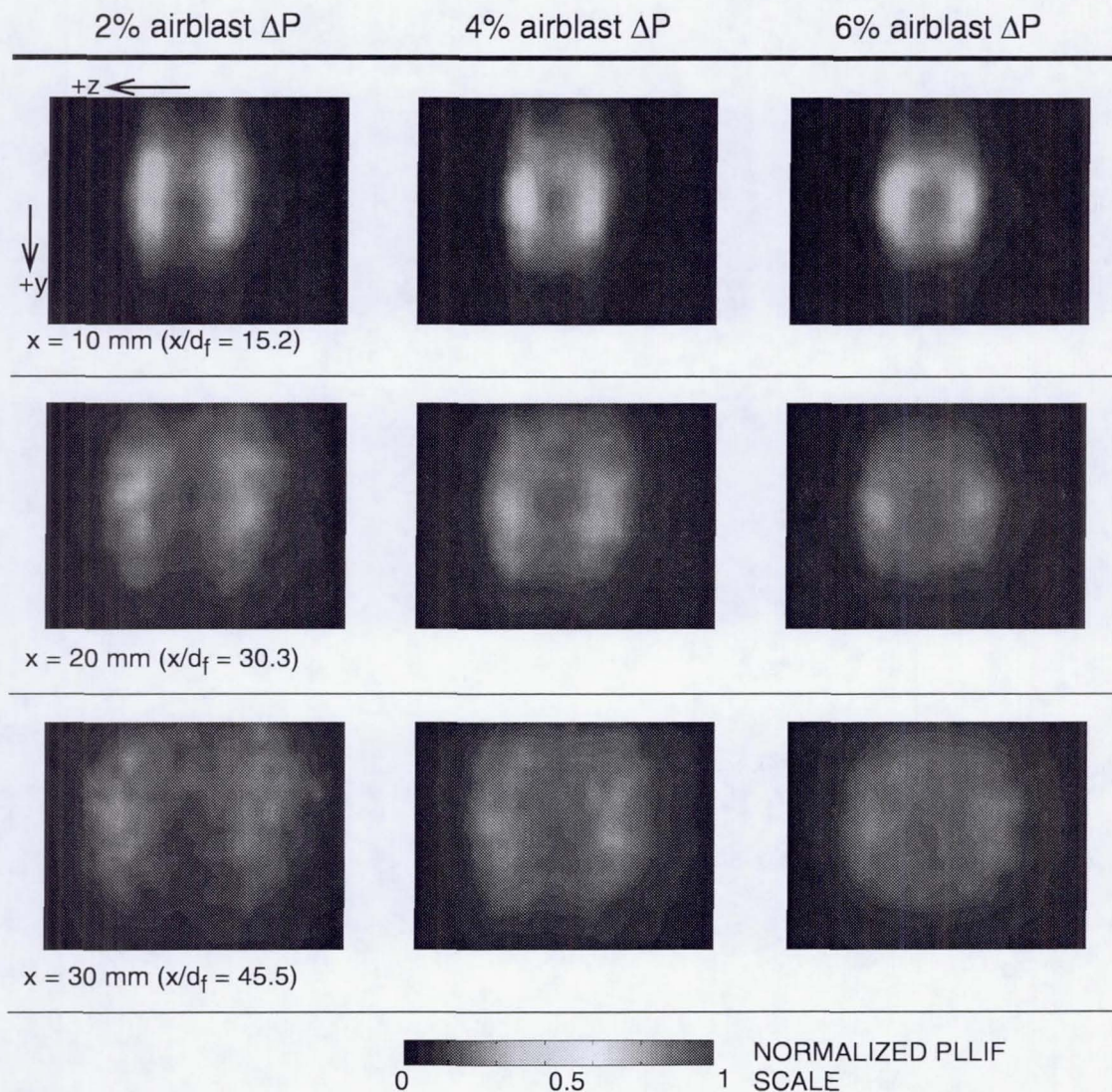


Fig. 8.9 Evolution of the liquid concentration distributions for the 1.8 kg/h fuel flow, 3.18-mm spray orifice diameter case.

increased. Between the sets of images obtained for the 3.18 mm-dia. and the 4.22 mm-dia. cases, it can be seen that the sprays produced by the larger hole diameter lead to a more dispersed spray mass across a larger area.

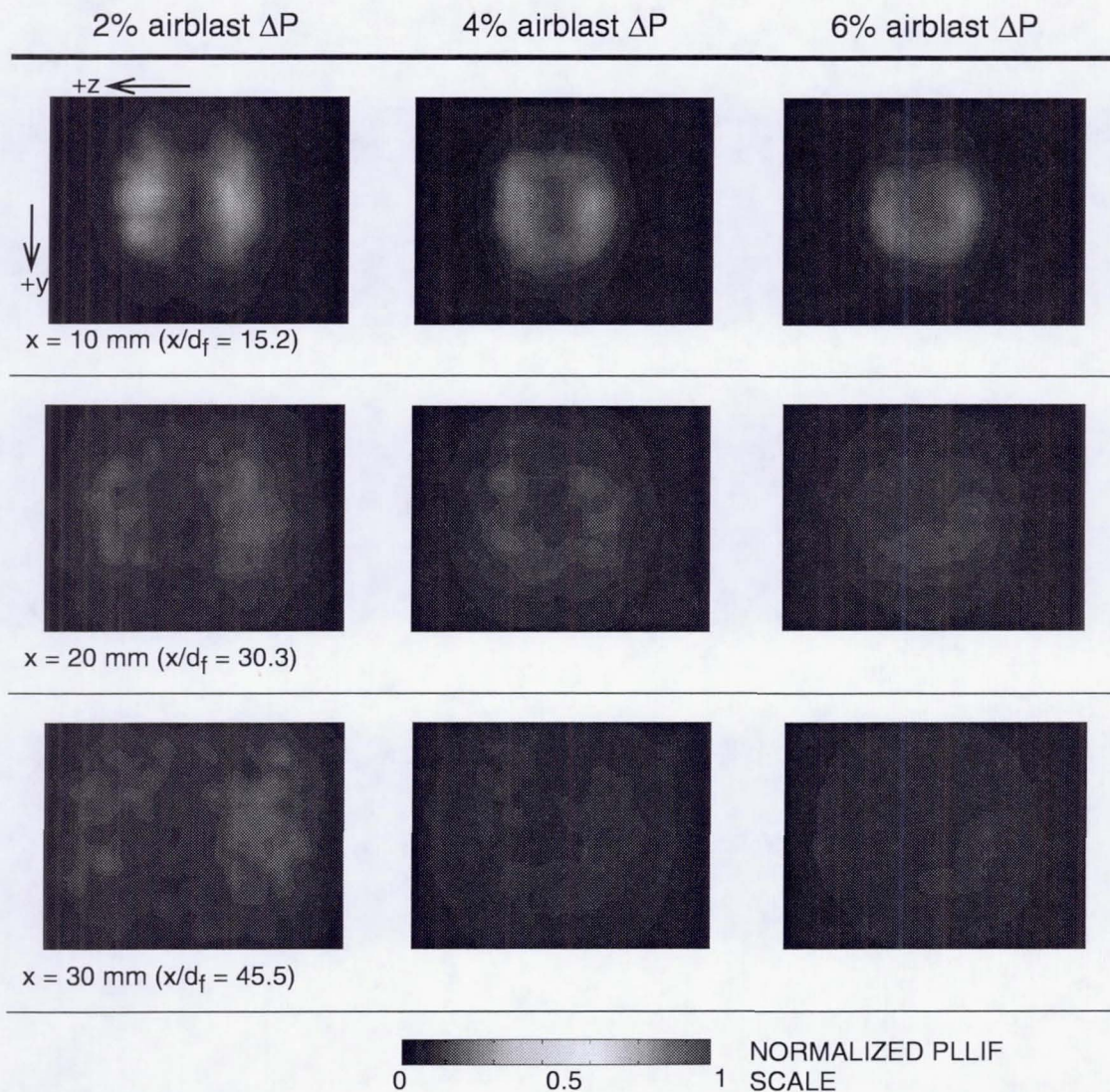


Fig. 8.10 Evolution of the liquid concentration distributions for the 1.8 kg/h fuel flow, 4.22-mm spray orifice diameter case.

The spray distributions for the higher fuel flow rate of 3.7 kg/h (see Figs. 8.11 and 8.12), also evolve in a similar fashion. Because of the presence of a higher concentration of liquid in the cross-section, the intensities encompass the entire range of the scale, which produces clearer divisions in the distributions as compared to the

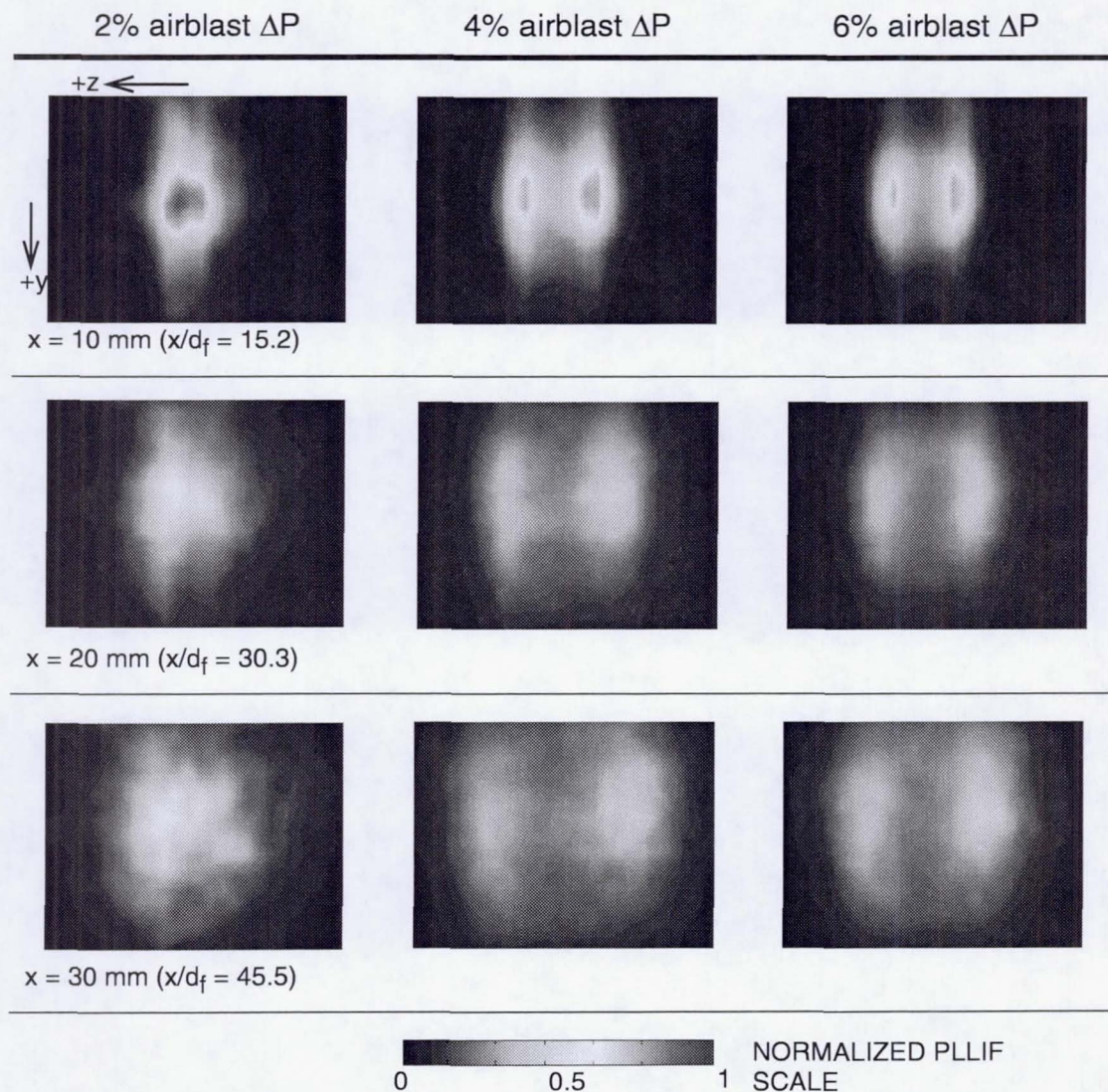


Fig. 8.11 Evolution of the liquid concentration distributions for the 3.7 kg/h fuel flow, 3.18-mm spray orifice diameter case.

1.8 kg/h fuel flow case. Except for the 3.7 kg/h, 3.18 mm-dia., 2% airblast ΔP case, the two-lobed structure that appears in the spray persists to the $x=30$ mm plane. The separation between the lobes increases along the axial direction of the spray, with the lobes in the sprays formed in the 4.22 mm-dia. orifice case spreading farther apart

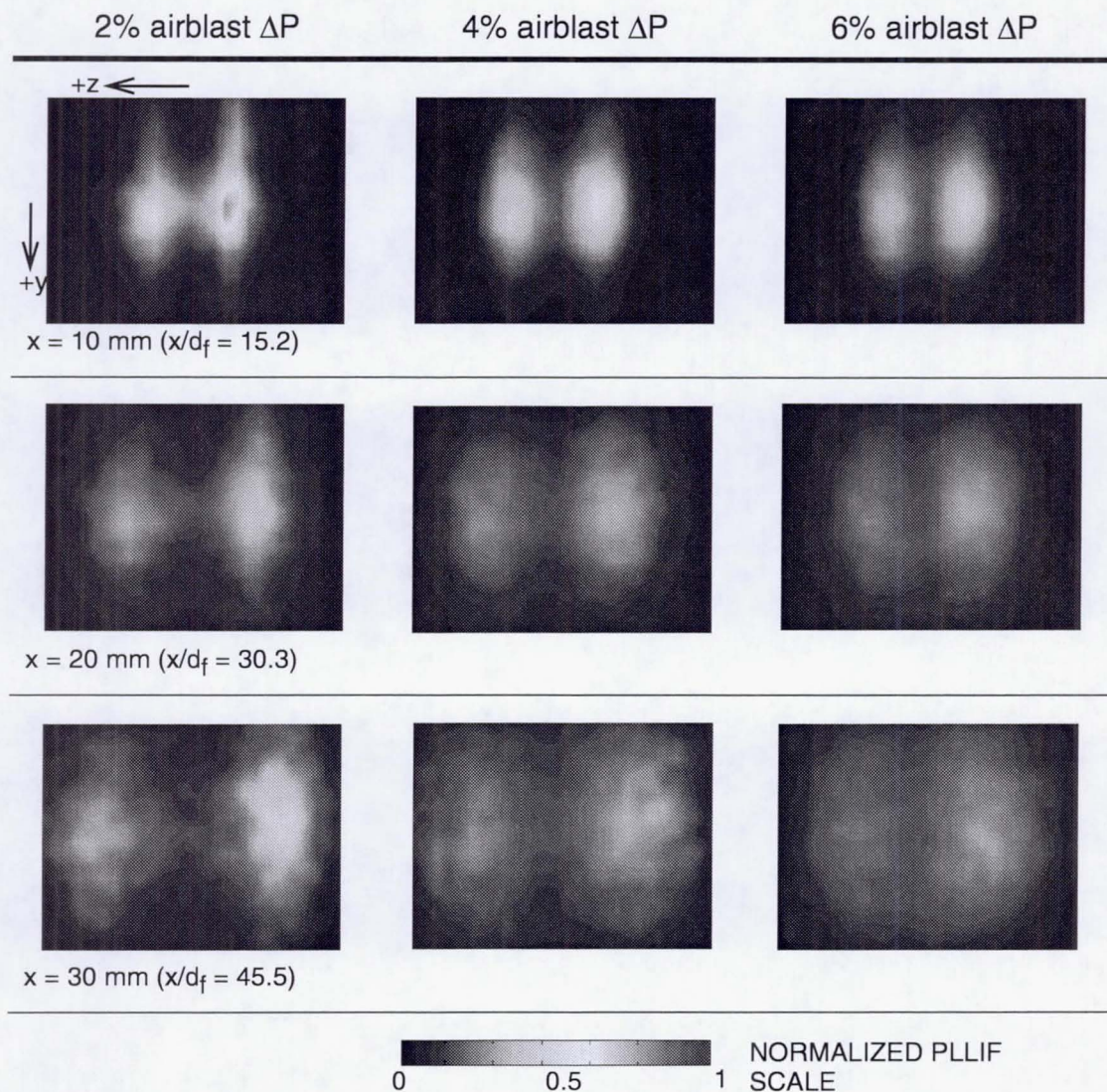


Fig. 8.12 Evolution of the liquid concentration distributions for the 3.7 kg/h fuel flow, 4.22-mm spray orifice diameter case.

than those corresponding to the 3.18 mm-dia. orifice. The two-lobed spray structures in the 3.7 kg/h case also consistently show the dominance of the right lobe, which is probably caused by any asymmetries inherent in the injector geometry. As for the 3.7 kg/h, 3.18 mm-dia., 2% ΔP case shown in Fig. 8.11, which is the only case that did

not produce the two-lobed structure, the liquid concentration distributions show the spray continuing to expand, with similar centralized distributions of the liquid mass present at each downstream plane.

8.3 Planar D_{32} Correlation and Comparison

In Fig. 8.7, planar distributions of the normalized droplet D_{32} values were presented at the $x=10$ mm plane. These images were presented on a normalized scale with limits corresponding to a range between 0 and the maximum ratio of PLLIF to Mie scattering intensities that was obtained at that plane. A calibration constant, K , can be used to relate the non-dimensional intensity ratio using Eq. 6.9:

$$\frac{I_{PLLIF}(i,j)}{I_{Mie}(i,j)} = K \cdot D_{32}(i,j) \quad (6.9)$$

The calibration constant can be determined if point measurements of the droplet D_{32} are obtained, as Sankar et al. (1999) did by using the PDI-measured D_{32} at the center of a spray in order to determine K .

In the present experiment, PDI measurements were obtained across two axes for the twelve case conditions. These measurements, overlaid atop the planar D_{32} images in Fig. 8.7, showed good qualitative agreement overall. Instead of utilizing a single measurement point to obtain the calibration constant, all of the PDI point measurements were used to find a correlation between the PDI-measured D_{32} values and the D_{32} intensity ratios.

To pinpoint the intensity ratio at a (y, z) location, the planar D_{32} images were condensed by replacing bins of 6-pixel x 6-pixel dimensions with its average intensity. The bin dimensions were chosen to correspond to the 6 pixel/mm resolution of the images. Each “super”-pixel in the condensed image thus represented an average value at a 1-mm x 1-mm grid space in the yz -plane. The collection of average intensity ratios and their corresponding PDI measurements are shown in Fig. 8.13. Note that the intensity ratios are greater than 1 in this plot, because the ratios have not been normalized with respect to the maximum intensity ratio for the purpose of this calibration. The plot in Fig. 8.13 also does not include the data from the 3.7 kg/h, 2% airblast ΔP cases, since the images in these cases did not show a good qualitative correlation to the PDI measurements as seen in Fig. 8.7.

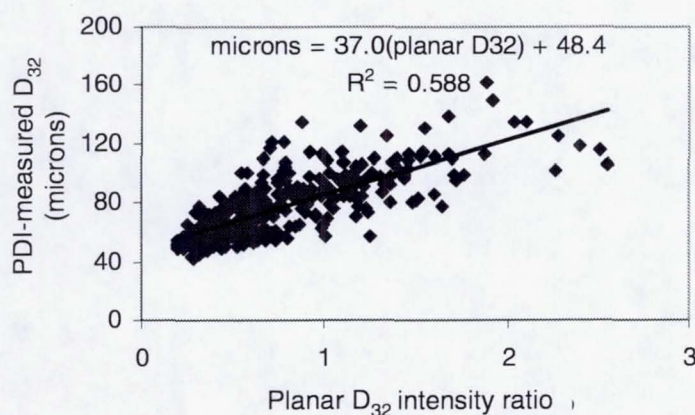


Fig. 8.13 Correlation between the planar mean D_{32} intensity ratio and the corresponding point-based PDI measurement for the airblast spray.

The linear correlation of the PDI-measured D_{32} to the planar D_{32} intensity ratio produced a slope of 37.0 and an offset of 48.4. For an offset of 0, the slope represents the reciprocal of the calibration constant, K . The presence of the linear offset may represent uncertainties associated with the measurement technique.

Plane-averaged D_{32} intensity values were determined at each downstream plane from $x=9$ mm to 31 mm. The values were converted to a micron basis using the D_{32} correlation that was elicited from Fig. 8.13. The evolution of the plane-averaged D_{32} is shown in Figs. 8.14 and 8.15.

Figure 8.14 depicts the trends of the cases for the low fuel flow rate of 1.8 kg/h while Fig. 8.15 shows the results from conditions at the high fuel flow rate of 3.7 kg/h. In each of these figures, the cases utilizing the different spray orifice diameters are grouped by symbols. The cases which used the 3.18 mm-dia. orifice are represented by hollow symbols while the 4.22 mm-dia. cases are denoted by solid symbols.

As expected for both fuel flow cases, the 6% airblast ΔP condition produced sprays with the lowest D_{32} values. The average planar D_{32} subsequently increases as the airblast pressure drop decreases. These observations also follow the trends shown by the D_{32} planar images in Fig. 8.7. The poorly-atomized spray formed by the 3.7 kg/h, 2% conditions observed in Fig. 8.7 is also reflected by the large difference between the average D_{32} curves for the 2% and 4% cases as seen in Fig. 8.15.

The effect of the spray orifice diameter is more pronounced at the 1.8 kg/h fuel flow rate, and for the 2% airblast ΔP case for the 3.7 kg/h fuel flow condition. The increase in orifice diameter for these conditions increases the ALR , which improves the atomization of the spray and results in a decrease in the mean D_{32} values. On the other

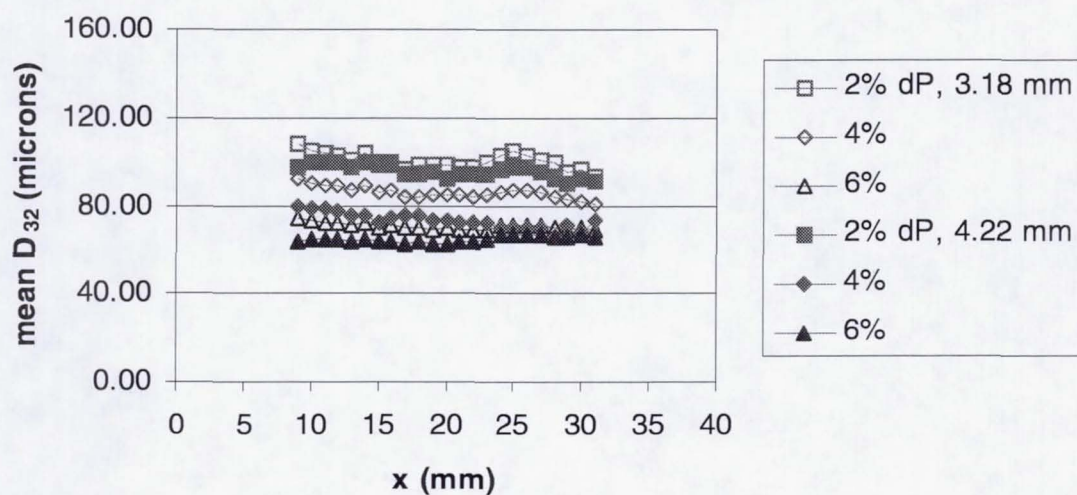


Fig. 8.14 Comparison of the planar mean D_{32} for the different cases at various downstream x -positions for the 1.8 kg/h case.

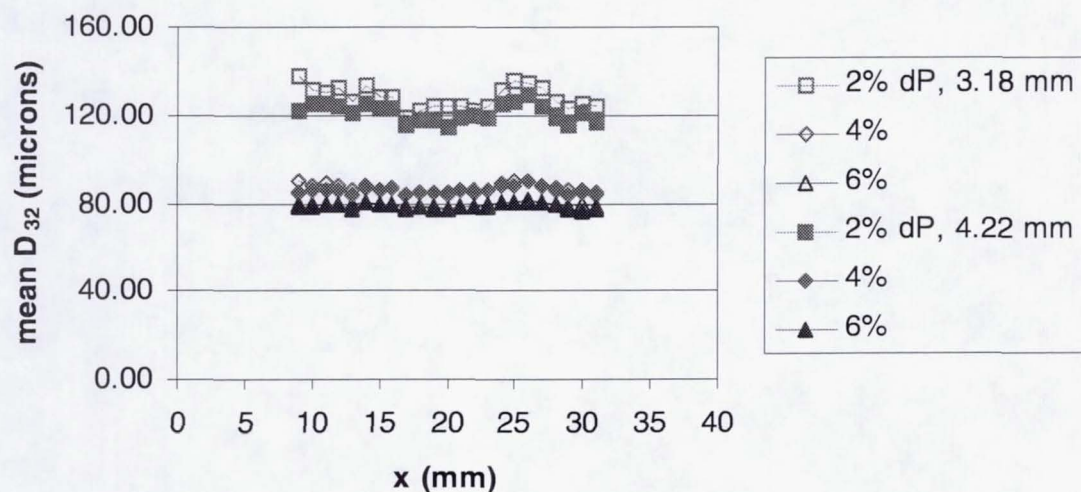


Fig. 8.15 Comparison of the planar mean D_{32} for the different cases at various downstream x -positions for the 3.7 kg/h case.

hand, the 4% and 6% airblast ΔP conditions for the 3.7 kg/h case do not show any significant improvement in atomization with respect to an increase in spray orifice diameter.

If each corresponding airblast ΔP case is compared between the 1.8 kg/h fuel flow case in Fig. 8.14 and the 3.7 kg/h case in Fig. 8.15, the increase in the fuel flow rate generally produced higher plane-averaged D_{32} values. This trend is expected because of the decrease in the fuel-air relative velocity caused by the increase in the fuel velocity.

The evolution of the plane-averaged D_{32} values along the axial x -direction of the spray shows the curves either varying about a constant level, or exhibiting a slight decreasing trend of the mean D_{32} . The cases which show a fairly constant D_{32} across the axial direction of the spray are primarily conditions in which the sprays are well-atomized. In the well-atomized sprays formed at the 6% airblast ΔP conditions, for instance, the mean D_{32} does not greatly decrease from the first measured plane of $x=9$ mm. The 2% conditions, on the other hand, initially produce a poorly-atomized spray with larger droplets and ligaments that break up further as the spray progresses farther in distance.

From the plane-averaged D_{32} values, a correlation can be obtained in terms of the operating variables as well as the measurement plane position. A correlation for the planar D_{32} can serve as a design tool that assesses the importance of varying different operating parameters on affecting the atomization quality. If the plane-averaged D_{32} , or $D_{32,avg}$, is normalized with respect to a pertinent characteristic length such as the fuel orifice diameter d_f , then the quantity $D_{32,avg}/d_f$ can be cast as a function of the

non-dimensional flow parameters Re_L , We_{airbl} , and Re_{airbl} . In addition, to evaluate the variation of $D_{32,avg}/d_f$ with respect to the downstream distance, x/d_f is also included in the function. The resultant correlating equation takes the form of

$$\frac{D_{32,avg}}{d_f} = c_0 \cdot Re_L^{c_1} \cdot We_{airbl}^{c_2} \cdot Re_{airbl}^{c_3} \cdot \left(\frac{x}{d_f}\right)^{c_4} \quad (8.3)$$

where c_0 , c_1 , c_2 , c_3 , and c_4 are constants. To solve for these constants, a nonlinear multivariate analysis was performed, the details of which are contained in Appendix B. The analysis of the plane-averaged D_{32} from the images yielded the coefficients $c_0=0.841$, $c_1=0.204$, $c_2=-0.258$, $c_3=-0.199$, $c_4=-0.034$. These coefficients for the correlation in Eq. 8.3 are applicable for the flow conditions listed in Table 8.1.

The coefficients for the correlation match the expected trends in the variation of the parameters. The positive exponent for Re_L verifies that an increase in the liquid velocity, for a set fuel orifice diameter and constant liquid density and viscosity properties, leads to an increase in the droplet D_{32} as a result of a decreased relative fuel-air velocity. The negative exponents for We_{airbl} and Re_{airbl} reflect the decrease in D_{32} for an increase in the airblast air velocity, given a constant spray orifice diameter and constant air properties. An increase in the air velocity increases the relative fuel-air velocity, which increases the degree of atomization and leads to smaller D_{32} values. The relatively small negative coefficient for the downstream distance x/d_f shows that the droplet D_{32} does not vary greatly in the measured region of $x=9$ mm to 31 mm.

The goodness of the fit can be assessed with a plot of the predicted versus the measured values of $D_{32,avg}/d_f$. As depicted in Fig. 8.16, such a plot shows that the

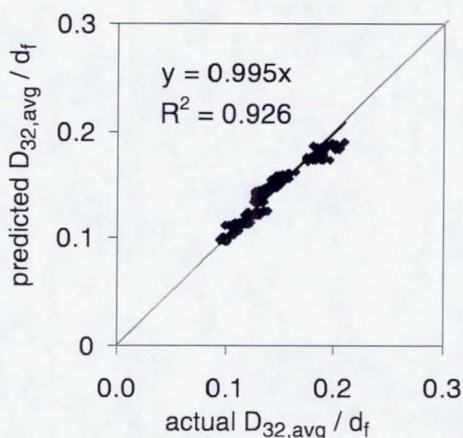


Fig. 8.16 Comparison between the values of $D_{32,avg}/d_f$ predicted by Eq. 8.3 and the measured values.

correlation of Eq. 8.3 produces a good fit of the data. The predicted and measured values produce a near one-to-one correspondence that is reflected in a slope of the fitted line that is near unity. A review of the curve fit revealed that the average deviation between the predicted and measured $D_{32,avg}/d_f$ values was 4.2%.

8.4 Quantitative Assessment of the Spray Quality

8.4.1 Definitions

In Section 8.2, the qualitative comparison of the images offered insight into the effect of different parameters on the evolution of the liquid mass distribution of the spray. The goal of this section is to quantify the comparison using parameters that assess the quality of the spray. While the present case does not correspond to the LBI

injection system because of the absence of the crossflow of air, the analysis presented here can later be applied to the spray jet in crossflow case.

The primary objective of fuel injectors for lean premixed combustion is to produce a well-mixed fuel and air mixture prior to the combustion process. The spray should thus

- produce a well-atomized droplet distribution in order to accelerate droplet vaporization and the subsequent mixing of the fuel vapor and air
- distribute the fuel across a large spray area
- disperse the fuel as uniformly as possible.

Among the parameters that can be used to represent these qualities are the mean D_{32} values, which indicate the atomization quality in the spray, the extent of area (EA), which represents the spray coverage across a given area, and the spatial unmixedness (U_s), which quantifies the uniformity of the liquid spray distribution. From the volume of planar images, these summary statistics can be calculated at each downstream x -plane. A quantitative succinct history of the spray evolution for each case can then be used to compare the effect of the different conditions in eliciting the desired spray dispersion.

The plane-averaged D_{32} values that were obtained in Section 8.3 are normalized with respect to the maximum D_{32} value in the data set. The normalized D_{32} are used to compare the atomization quality of the sprays formed under different conditions.

The extent of area, EA , is a parameter that gauges the fraction of spray coverage across a given area. The extent of area is defined as the sum of all pixels in the image

with intensities above a threshold value, normalized by the area of the region of interest, which is constant for each condition. The use of a threshold value eliminates the pixels representing the background of the image in order to yield the area covered by the spray. Under some conditions, particularly in the latter axial planes, the actual extent of the spray is larger than the region of interest. However, it is assumed that this should not greatly affect a comparison of this parameter for the different cases. For the planes in which the spray coverage increases beyond the bounds of the region of interest, the spray is likely to cover the entire region and result in an *EA* of 1.

The spatial unmixedness U_s of a spray quantifies concentration mixing in a planar image (Liscinsky et al., 1993), and is a modified version of the definition of temporal unmixedness U obtained at a point in space (Danckwerts, 1952). Vranos et al. (1991) validated the use of U_s by showing that the value of U calculated across a planar image from an ensemble of instantaneous intensity levels at each pixel produced a value that was nearly identical to the spatial variance of an image of time-averaged intensities. The spatial unmixedness of an $m \times n$ image with a plane-averaged intensity of I_{avg} is defined as

$$U_s = \frac{I_{var}}{I_{avg}(1 - I_{avg})} \quad (8.4)$$

where the variance I_{var} of the image is computed by

$$I_{var} = \frac{1}{(m \cdot n)} \sum_{i=1}^m \left(\sum_{j=1}^n (I(i,j) - I_{avg})^2 \right) \quad (8.5)$$

The spatial unmixedness is a normalized variance parameter, with the denominator in Eq. 8.4 representing the maximum fluctuation that could occur in the system. By this definition, U_s is bounded between 0 and 1, with $U_s=0$ representing a fully-mixed system, and $U_s=1$ representing a totally segregated system. Note that the intensities must be normalized to produce values that fall within the bounded range.

For this experiment, the bounded area across which the EA and U_s values were calculated was arbitrarily but uniformly applied to all of the cases. The left and right boundaries of the cropped image were set such that all of the sprays were contained in the image. For the non-crossflow spray experiment, the EA and U_s values were calculated across the image area shown in Fig. 8.2.

8.4.2 Application of the Defined Spray Parameters

The spray coverage, denoted by the extent of area (EA) parameter, is compared in Figs. 8.17 and 8.18 for the different cases. The EA for each case approaches a value of 1, which is expected since the spray expands with distance as it encompasses the entire region of interest. Among the 1.8 kg/h cases (see Fig. 8.17), the magnitude of the EA curves decrease with an increase in airblast ΔP . The shrinkage in spray area was observed with the planar PLLIF images in Fig. 8.6, and was attributed to the twofold effect of the high airblast flows in producing smaller droplets and in inducing these smaller droplets to follow the direction of the increased axial velocity of the airblast air. If the 2% airblast condition were ignored as in previous comparisons, the sprays in the 3.7 kg/h fuel flow and 4.22 mm-dia. cases (see Fig. 8.18) also generally follow this trend. The 3.18 mm-dia. cases at the 3.7 kg/h condition show no significant effect on

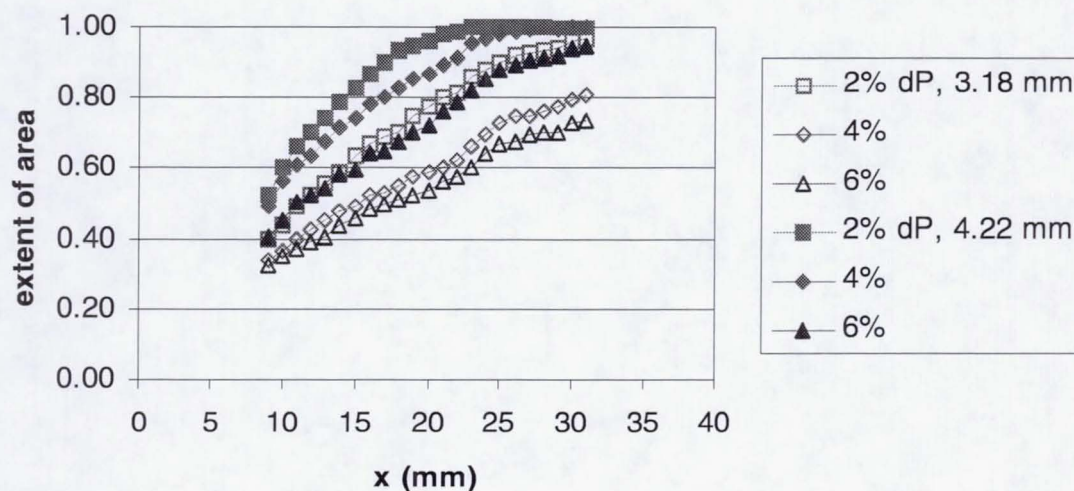


Fig. 8.17 Comparison of the spray extent of area for the different cases at various downstream x-positions for the 1.8 kg/h case.

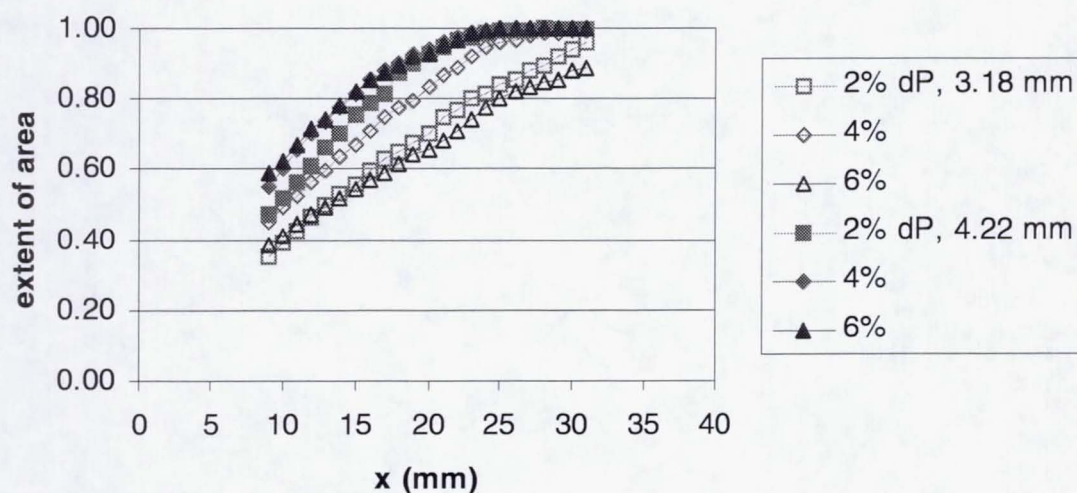


Fig. 8.18 Comparison of the spray extent of area for the different cases at various downstream x-positions for the 3.7 kg/h case.

the extent of area. The effect of the orifice diameter size on the spray coverage can be seen in both cases, as the apparent internal flow patterns produced by the 4.22 mm-dia. spray orifice greatly enhance the expansion of the spray for each corresponding airblast ΔP and hole size condition.

The uniformity of the spray across a plane is gauged by the spatial unmixedness U_s . The calculated U_s values per cross-sectional plane are presented in Figs. 8.19 and 8.20 for the respective 1.8 kg/h and 3.7 kg/h fuel flow cases. As shown in both figures, the U_s values decrease with increasing downstream distance. This is expected since the expansion of the spray caused by the initial momenta of the atomized droplets disperses the liquid across a larger area. Any additional breakup mechanisms that occur will further dilute the liquid concentrations in the region.

The sprays produced at the lower fuel flow rate (Fig. 8.19) exhibit lower U_s values than their higher fuel flow counterparts (Fig. 8.20). However, this is a function of the calculated U_s being based on intensities normalized by the overall maximum PLLIF intensity, which in this set of experiments, corresponds to the maximum recorded intensity for the 3.7 kg/h fuel flow rate. The 1.8 kg/h fuel flow case tends toward a uniform distribution more quickly than does the 3.7 kg/h flow rate because the case has a lower concentration of fuel to disperse across the region of interest.

The only other clear trend that can be elicited from the U_s curves in Figs. 8.19 and 8.20 is related to the effect of the spray orifice diameter. At each fuel flow condition, increasing the spray orifice diameter from 3.18 mm to 4.22 mm produces lower U_s values. The 4.22 mm-dia. case benefits from a faster expansion of the spray over that produced by the 3.18 mm-dia. orifice.

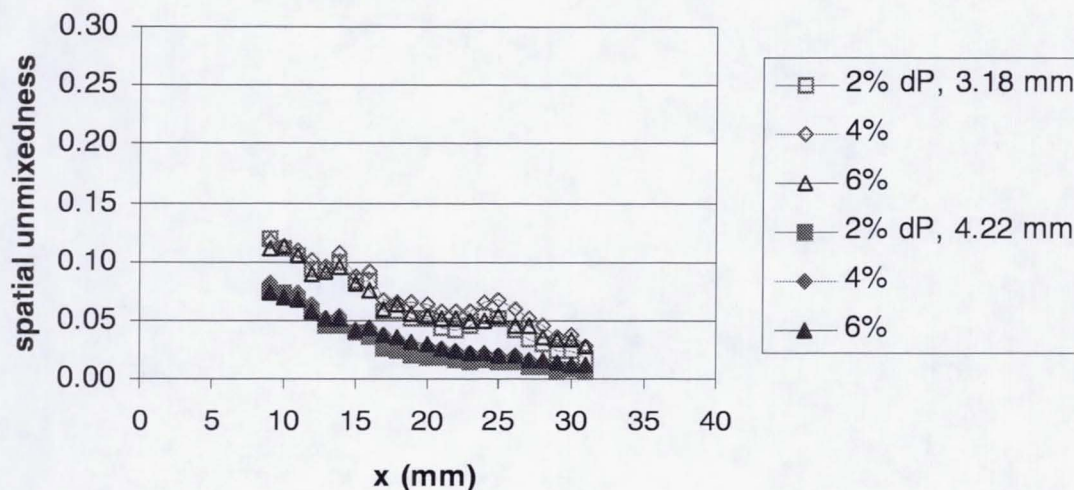


Fig. 8.19 Comparison of the spatial unmixedness in the horizontal planar sections of the spray at different downstream x-positions for the 1.8 kg/h case.

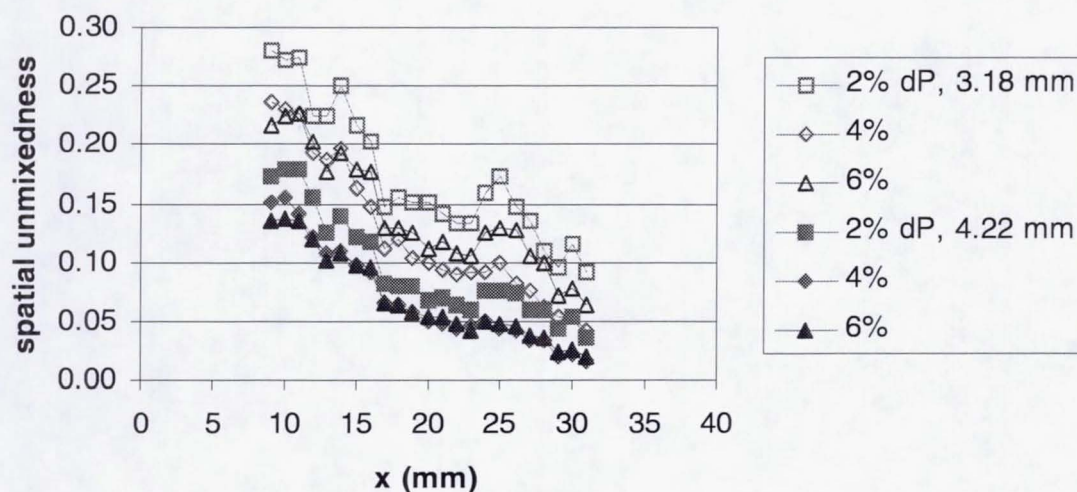


Fig. 8.20 Comparison of the spatial unmixedness in the horizontal planar sections of the spray at different downstream x-positions for the 3.7 kg/h case.

The desired fuel spray for combustion should be well-atomized, dispersed across a large area, and distributed uniformly in concentration. Based on these requirements, a mean D_{32} (normalized with respect to the maximum value in the tests) tending toward 0, an EA tending toward 1, and a U_s tending toward 0 are highly desirable. If a "spray quality" (SQ) parameter is defined as follows

$$SQ = [(1 - (D_{32, avg}/D_{32, max})) + EA + (1 - U_s)]/3 \quad (8.6)$$

then a spray that possesses the desired qualities will have an SQ approaching 1, while a spray of poor quality will have an SQ near 0. The SQ is essentially an equally-weighted average of the three parameters, but can be formulated to weight specific parameters differently depending on their importance to the user.

Calculations of the spray quality function at each downstream x location for each of the twelve conditions are depicted in Figs. 8.21 and 8.22. The SQ approaches 1 with increasing axial distance x in all cases, as D_{32} and U_s decrease while EA increases. Although the trends within the 1.8 kg/h fuel flow condition (Fig. 8.21) are more difficult to discern, the conditions utilizing the 4.22 mm-dia. spray orifice do appear to achieve a higher spray quality than do the corresponding airblast ΔP cases that use the spray orifice diameter of 3.18 mm. The effect of the different parameters in the 3.7 kg/h fuel flow case can be seen more clearly (see Fig. 8.22). As observed in the 1.8 kg/h fuel flow set of conditions, the use of the 4.22 mm-dia. orifice produces sprays with higher SQ values. The 2% airblast ΔP conditions also produce a lower SQ curve in their respective orifice diameter group. For each respective spray orifice diameter group, the 4% and 6% airblast ΔP conditions produce sprays of comparable qualities,

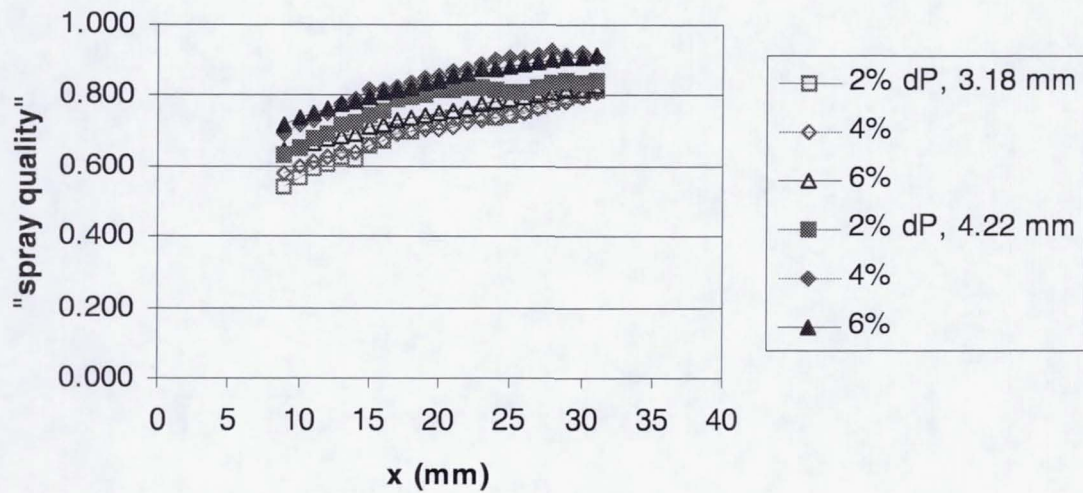


Fig. 8.21 Comparison of the spray quality in the horizontal planar sections of the spray at different downstream x-positions for the 1.8 kg/h case.

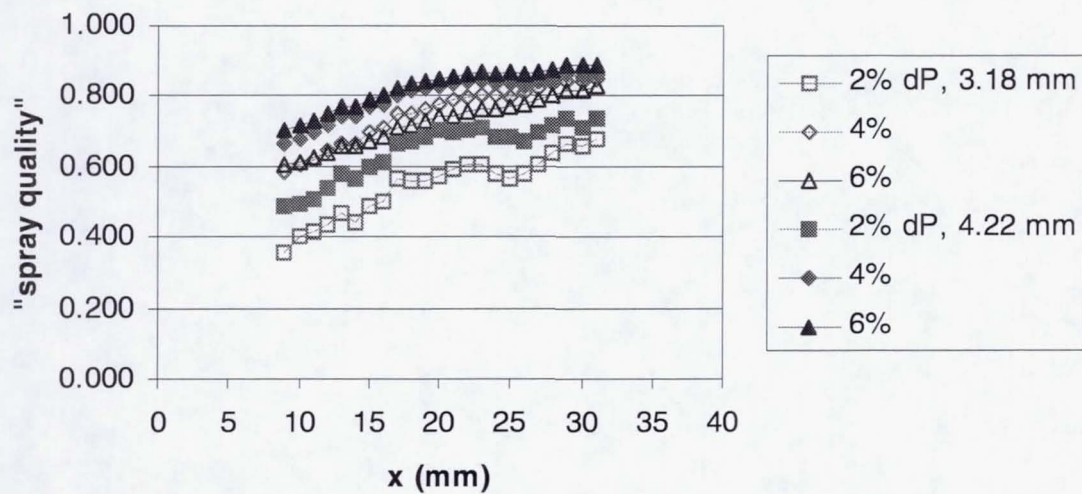


Fig. 8.22 Comparison of the spray quality in the horizontal planar sections of the spray at different downstream x-positions for the 3.7 kg/h case.

which suggests that the airblast flow need only be set at 4% to achieve the desired SQ . However, it remains to be seen in the how the 4% airblast ΔP condition performs when the spray is injected into a crossflow.

8.5 Extent of the Atomizing Air in the Spray

In the airblast spray, the air flow helps to atomize the liquid jet as well as to transport the resultant ligaments and droplets. Planar imaging and PDI measurements demonstrated the dual role of the air flow both in the atomization of the spray and in the subsequent transport of the droplets. An increase in airblast pressure drop increased the air velocity, which was shown by the PLLIF and PDI data to result in both a decrease in the droplet size and the formation of a more compact spray jet. Such a coupling suggests a close interaction between the air and the liquid, which is the subject of this section. Through acetone PLIF techniques, the atomizing air is imaged to reveal the permeation of the air within the spray.

The application of acetone PLIF to image the airblast flow in the spray has not been entirely perfected. As noted in Chapter 6, the droplets in the spray appear to scatter the fluorescence from the excited acetone molecules that are seeded into the air stream. Although a temporal filter was applied to the images to remove the discernible droplets, the overall intensity levels of the acetone PLIF images remain higher than those levels produced for a plain acetone-seeded air jet operating under comparable air flow conditions. For the 1.8 kg/h case, the overall intensities are almost twice that of the air jet case, while the intensities in the 3.7 kg/h case are three times as high. The increase in intensity level with an increase in fuel flow rate suggests that residual

contamination of the captured signal by the scattering of acetone fluorescence by the droplets may still be occurring. While the acetone PLIF images obtained under a 3.7 kg/h flow condition appear to be greatly affected by the effects of this scattering, the images from the 1.8 kg/h case appeared to produce reasonable results.

Figures 8.23 and 8.24 present a series of images depicting the vertical $y=0$ mm plane illuminated by the laser sheet for the 1.8 kg/h fuel flow condition. The results for the 3.18-mm spray orifice diameter are presented in Fig. 8.23, while the results for the 4.22 mm-dia. case are shown in Fig. 8.24.

Within each figure are three sets of images which are grouped in rows. The first two rows contain acetone PLIF images, and are presented on a color scale normalized to the highest acetone PLIF intensity recorded in the batch of non-crossflow spray tests. The first row contains PLIF images of the acetone-seeded air injected without the liquid flow, while the second row contains acetone PLIF images of the air with the liquid flow present. As discussed earlier, the scattering phenomenon that illuminates the droplets once the liquid flow is present results in higher intensity levels in the acetone PLIF images of the spray, even after applying the temporal filtering procedure of Chapter 6. However, the extent to which the acetone-laden air pervades the spray can still be observed by comparing the edge of the acetone PLIF distributions in the images. Near the edge of the spray, the concentration of liquid is lower, as indicated by the PLIF images in the third row. Consequently, the propensity for interference by the droplets in scattering the acetone fluorescence should be minimized near the spray edges.

In each figure, the acetone PLIF spray tests were run under conditions corresponding to a 3% and 6% airblast pressure drop in the spray. While the 6% cases are shown in its respective right most column, the 3% cases are shown straddling the 2% and 4% airblast ΔP columns.

In the 1.8 kg/h fuel flow, 3.18 mm-dia. spray orifice case shown in Fig. 8.23, the acetone PLIF images of the pure air jet show that the air is concentrated toward the center of the jet. From the 3% to the 6% airblast ΔP case, the air jet can be seen to decrease in its angle of spread, which corresponds to the increase in air velocity with pressure drop setting. When the liquid flow is present, the airblast air pervades the spray as observed in the increased width of the air concentration boundaries. The cross-sectional images also show a decreased extent of the air concentration boundaries as the airblast pressure drop setting increases from 3% to 6%.

The PLLIF images in the third row of the figure are used to gauge the extent of the airblast air boundaries with respect to the liquid spray boundaries. The boundaries of the acetone PLIF images in the 3% airblast ΔP case fall between the extent of the PLLIF-imaged sprays produced by the 2% and 4% airblast ΔP conditions, which suggests that the extent of air follows that of the liquid component in the spray. This is verified by a direct comparison at the 6% airblast ΔP condition, in which the boundaries of the air concentration in the spray follow the liquid concentration boundaries. The results for the 4.22 mm-dia. case in Fig. 8.24 show similar trends in the results.

Interestingly, in both Figs. 8.23 and 8.24, the acetone-laden air in the spray (middle row in each figure) exhibits a more continuous distribution, as compared to the

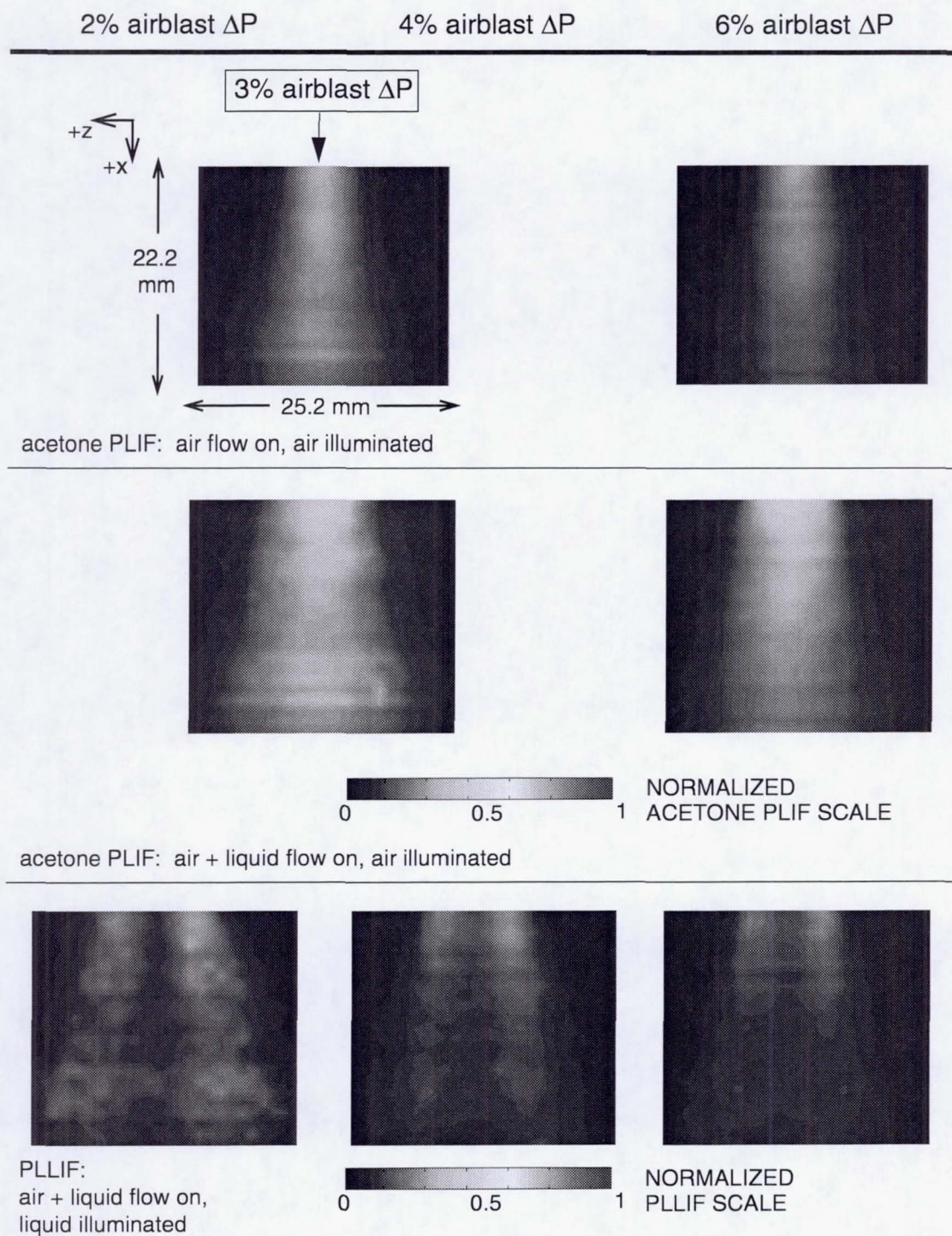


Fig. 8.24 Comparison between the distributions of air and liquid, with and without the presence of liquid, for the 1.8 kg/h fuel flow, 4.22-mm spray orifice diameter case, at the $y=0$ mm plane.

lobed structures in the liquid distributions (bottom row in each figure). However, it is unclear whether the continuous distributions seen in the acetone-laden spray images result entirely from Mie scattering by the droplets, since Mie scattering distributions exhibit the same type of continuous distribution (see Fig. 6.11). Until an investigation into the impact of the droplets on the scattering of acetone fluorescence is performed, any observation made from the acetone-laden spray images should be limited to determining the farthest extent that the atomizing air pervades the spray.

8.6 Summary

This chapter extends the work presented in Chapter 7 in characterizing the spray issuing into a quiescent environment. Whereas the previous chapter dealt with characterizing the overall structure of the spray by classifying the spray conditions into breakup regimes and by using spray angles to describe its expansion, the focus of this chapter was to characterize the internal structure of the spray.

PLLIF images revealed the presence of a two-lobed structure of liquid concentration occurring in the fully-atomized spray cases. The magnitude of the concentrated lobes and their extent depended on the flow conditions, as an increase in the degree of atomization induced by increasing the airblast ΔP , compounded with the rapid expansion of the spray by increasing the spray orifice diameter, led to a more diffuse liquid distribution that covered a larger area. A correlation was found that described the plane-averaged D_{32} as a function of the liquid and airblast Reynolds number, the airblast Weber number, and the downstream distance. The correlation fit the expected trends with respect to an increase in fuel or airblast air velocity, and

showed that the spray D_{32} was largely invariant between the $x=9$ mm and 31 mm planes.

To quantitatively compare the overall quality of the different sprays that were tested, a “spray quality” (SQ) function was developed. The SQ quantity incorporated a planar mean D_{32} value that reflected the atomization quality of the spray, an extent of area parameter (EA) that determined the spread of the spray, and a spatial unmixedness parameter (U_s) that indicated the uniformity in liquid distribution.

The parametric variation of the airblast flow, fuel flow, and spray orifice diameter revealed general trends involving the cases that were fully atomized. The fully-atomized cases encompassed all conditions except the lowest We_{airbl} number case corresponding to the 3.7 kg/h fuel flow, 3.18 mm-dia. spray orifice, 2% airblast ΔP set of conditions. With the exception of this case, an increase in the airblast pressure drop resulted in increased atomization and increased uniformity of distribution, but at the expense of a decreased extent of area.

An increase in the spray orifice diameter for a constant airblast ΔP supplies a higher mass flow rate of air while maintaining the same airblast velocity. The result of increasing the spray orifice diameter was to improve the atomization of the spray, as revealed by the lower intensities observed in the planar D_{32} images. However, the primary effect of using an increased spray orifice diameter was to enable the spray to expand faster and to cover a larger spray area. This corroborates similar observations made from the spray angle measurements obtained from the high speed video images in Chapter 7.

The characterization of the spray without crossflow through video, plane-specific laser imaging, and PDI yielded information about the overall and internal structure of the spray. How these results relate to the penetration and dispersion of the spray jet in a crossflow remain to be seen in Chapters 9 and 10.

CHAPTER 9

GLOBAL STRUCTURE OF THE AIRBLAST SPRAY JET IN A CROSSFLOW

The subject of the present and the following chapter concerns the dispersement of the airblast-atomized spray into a subsonic, high velocity crossflow of air. The present chapter focuses on characterizing the global structure while the next chapter characterizes the internal structure of the dispersed spray jet in a crossflow.

This chapter presents images of bulk spray scattering captured by high magnification video under various operating conditions, including tests performed at elevated ambient pressures. The images are used to develop correlations that quantify the extent of the spray in the crossflow.

This chapter first describes the experimental configuration and the operating conditions used to obtain the spray images. The spray images are then compared and assessed for trends, with specific spray conditions identified for additional PDI measurements. Finally, the development of the spray trajectory correlations is addressed at the end of the chapter.

9.1 Experimental Conditions

The spray jet in crossflow experiment was installed in the elevated pressure facility (see Fig. 4.6) in order to vary the ambient pressure in the tests. The hardware for the crossflow configuration consisted of the injection panel and the crossflow transition section. The injection panel was installed with the panel oriented vertically

in order to inject the spray in the positive x -direction as shown in Fig. 9.1. A steel back panel and two quartz windows formed the rest of the rectangular duct that confined the crossflow of air. The cross-stream of air flowed along the $+z$ -direction, with the origin of the axes located at the center of the exit plane of the spray orifice.

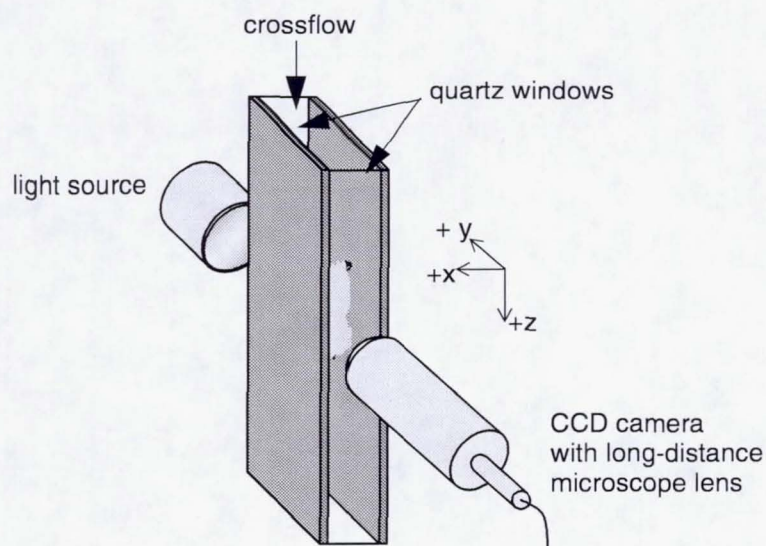


Fig. 9.1 Orientation of the test section in the crossflow configuration.

High magnification video was used to characterize the global behavior of the sprays produced over a wide range of conditions. The orientation of the video system with respect to the crossflow test section is also depicted in Fig. 9.1. The light source illuminated the spray from the rear. The CCD camera captured an 8-bit image of the back-lit spray in the xz -plane. The spray is injected into the crossflow from the right side of the image, as shown in Fig. 9.2. The time-averaged image is cropped to a field

of view measuring 13.9 mm x 8.9 mm. The left edge of the images corresponds approximately to the midpoint of the crossflow channel. The images are represented by a blue (low) to red (high) intensity scale, normalized with respect to the maximum intensity level recorded for the full set of tests.

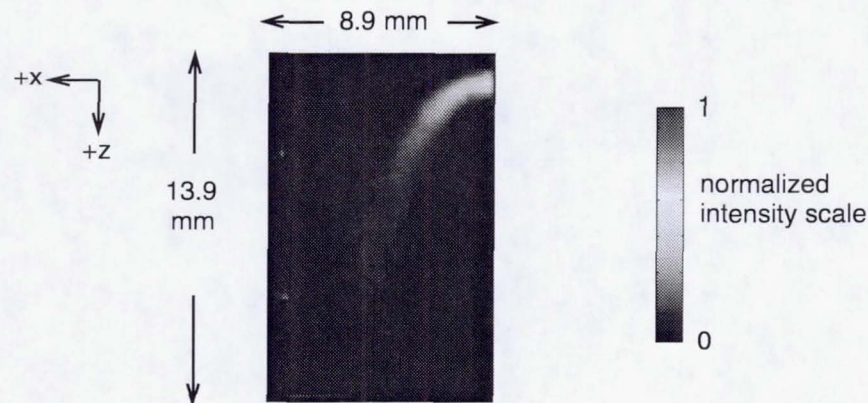


Fig. 9.2 Image obtained from the high magnification video system.

The operating and geometric conditions for these global characterization tests are noted in Table 9.1. As with the non-crossflow cases in Chapter 7, the global visualization of the spray injected into the crossflow utilized jet-A as the test liquid. The fuel flow was maintained at a constant mass flow rate of 0.66 kg/h. The main conditions that were varied included the ambient pressure and the airblast pressure drop. Although the baseline crossflow velocity magnitude was set at 38 m/sec, it was also varied for several cases at each ambient pressure condition.

Table 9.1 Operating and geometric conditions for the global visualization of the airblast spray experiment in the crossflow configuration.

Parameter	Range of Variation
Ambient pressure (kPa)	101.3, 304.0, 506.6
Fuel flow (jet-A) (kg/h)	0.66
Airblast pressure drop (%)	0 - 4.8
Airblast velocity, U_{airbl} (m/sec)	0 - 90.1
Airblast air to liquid mass flow ratio, ALR	0 - 11.2
Crossflow velocity, U_{cross} (m/sec)	31 - 54
$Re_L = \frac{\rho_L U_L d_f}{\mu_L}$	509
$We_{airbl} = \frac{\rho_g (U_{airbl} - U_L)^2 d_f}{\sigma_L}$	0 - 552
$Re_{airbl} = \frac{\rho_g U_{airbl} d_{spray}}{\mu_g}$	0 - 5.97×10^4
$Re_{cross} = \frac{\rho_g U_{cross} d_{cross}}{\mu_g}$	5.29×10^4 - 4.61×10^5
Fuel orifice diameter, d_f [corresponding l/d in brackets]	0.34 mm (0.0135 in.) [$l/d = 6.7$]
Spray orifice diameter, d_{spray} [corresponding l/d in brackets]	2.26 mm (0.089 in.) [$l/d = 1.4$]
Crossflow length x width	76.2 mm x 18.0 mm (3.0 in. x 0.71 in.)
Crossflow hydraulic diameter, d_{cross}	29.2 mm

Notes:

- $\rho_L = 822 \text{ kg/m}^3$ for jet-A; $\rho_g = 1.19 \text{ kg/m}^3$ for air at room temp. and pressure
- $\mu_L = 1.32 \times 10^{-3} \text{ kg/m-sec}$ for jet-A; $\mu_g = 2.00 \times 10^{-5} \text{ kg/m-sec}$ for air at room temp. and pressure
- $\sigma_L = 0.0277 \text{ kg/sec}^2$ for jet-A
- For reference, hardware dimensions are also given in English units, which were the primary units used in the machining process.
- d_{cross} , the hydraulic diameter of the crossflow section, is computed by the formula $4A/P$, where A and P are the area and wetted perimeter, respectively, of the crossflow cross-section.

The uniformity of the crossflow velocity profile was gauged with PDI measurements at atmospheric conditions. A mist of silicone oil droplets, with presumed droplet sizes of less than $10\text{ }\mu\text{m}$ to yield Stokes numbers less than 1 for the range of crossflow velocities tested, were seeded into the crossflow of air to track the path of the high velocity flow. The transverse and axial velocity components of these particles were measured with the PDI system across a grid of points located at a plane above the orifice, at $z = -5\text{ mm}$. The grid of points was limited in scope by the potential clipping of either the laser beams from the transmitter, or the collection cone of the receiver. As a result, the grid was confined to a cross-section limited to $-25\text{ mm} < y < 25\text{ mm}$, and $5\text{ mm} < x < 11\text{ mm}$. Within this confined grid, spatial deviations of the axial velocity were found to be within 2.5% of the mean value, with a maximum turbulent fluctuation of $u_{rms}/\bar{U} = 14\%$. The transverse velocity component was also determined to be 0.5% of the mean axial component. Although the y-directional component of the crossflow velocity was not measured, it was assumed that this component was negligible. These measurements thus indicate that the crossflow velocity profile was primarily comprised of the axial velocity component, and was uniform in both magnitude and direction.

9.2 Two-Phase Definition of the Momentum-Flux Ratio

In order to compare results from the various test combinations of ALR , crossflow velocity, and ambient pressure, a non-dimensional parameter was sought to cast the flow conditions on a common basis. For a jet in a crossflow, an important flow parameter that determines jet penetration is the jet to crossflow momentum-flux ratio

(Holdeman, 1993). For a single-phase jet, the definition of the momentum-flux ratio q_1 was presented earlier as Eq. 2.14:

$$q_1 = q = \frac{\rho U^2|_{jet}}{\rho U^2|_{crossflow}} \quad (2.14)$$

where the jet refers to either the gaseous or liquid phase, and the subscript for q refers to the number of phases in the jet. Although the present definition of q suitably defines single-phase jets, this definition does not represent very well a two-phase jet such as that encountered in the current experiment. Because the penetration of the jet into the crossflow depends primarily on a jet to crossflow momentum-flux ratio, a similar parameter was developed in order to produce correlations describing the airblast spray penetration into the crossflow.

For this study, a composite definition of the two-phase jet momentum flux is obtained to represent the numerator of Eq. 2.14. Assuming negligible fuel vaporization as well as negligible kinetic energy losses, the exiting momentum of the spray upon leaving the injection plate is presumed to be equal to the initial momentum of both fluids prior to their entering the control volume (see the control volume in Fig. 9.3). The total momentum entering the control volume is given by

$$\text{spray jet momentum} = \rho_L U_L^2 A_{fuel} + \rho_g U_{airbl}^2 A_{airbl} \quad (9.1)$$

where A_{fuel} refers to the area associated with the orifice in the fuel injector, and A_{airbl} corresponds to the difference between the area of the spray orifice, A_{spray} , and A_{fuel} .

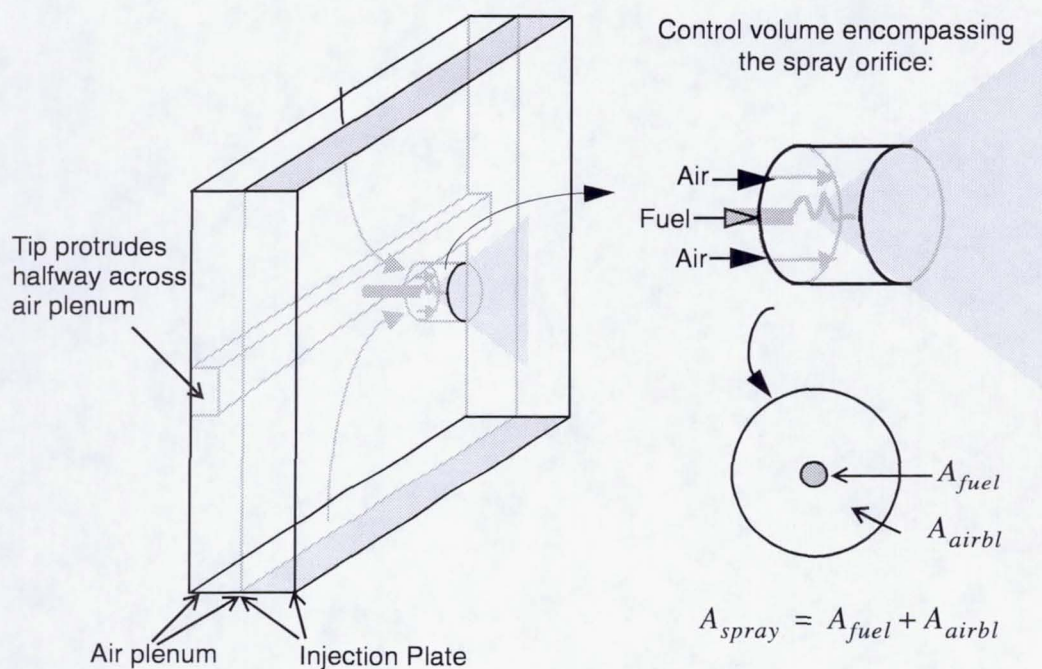


Fig. 9.3 Schematic of the control volume encompassing the spray orifice.

To obtain the momentum flux of the two-phase jet, the spray jet momentum in Eq. 9.1 is divided by A_{spray} . The momentum-flux formulation for the two-phase jet, q_2 , can thus be defined as

$$q_2 = \frac{(\rho_L U_L^2 A_{fuel} + \rho_g U_{airbl}^2 A_{airbl}) / A_{spray}}{\rho_g U_{cross}^2} \quad (9.2)$$

In the q_2 expression, the airblast contribution dominates over the fuel contribution. Although the air to liquid density ratio is on the order of 10^{-3} , the velocity of the airblast stream is 25 times as high as the fuel velocity. When squared, the atomizing air velocity nearly compensates for its low density factor. In addition,

the area associated with the fuel stream is only 2.3% of the area associated with the atomizing air, which further decreases the impact of the fuel momentum contribution to q_2 .

9.3 Baseline Case: Liquid Jet (Airblast $\Delta P=0\%$)

A baseline comparison of a pure liquid jet injected into a crossflow at the different ambient pressure conditions is presented in Fig. 9.4. Because the cases shown in Fig. 9.4 involve a single phase jet, the q_1 momentum-flux ratio definition is given. For comparison, the q_2 definition is also provided for each of these cases. The q_2 values are 42 times less than q_1 because the momentum flux of q_2 is obtained by dividing the liquid momentum by the spray orifice area A_{spray} instead of A_{fuel} . In addition, the Weber number, We_{cross} , based on the crossflow air velocity is noted.

In the 1-atm case, the outer and inner surfaces of the jet are distinct. However, in the 3-atm and 5-atm cases, the inner spray surface is not distinctly seen because the spray attaches to the near wall. The increasing air density due to the increase in ambient pressure causes the liquid jet penetration to decrease. The decreasing liquid jet penetration corresponds to a decrease in the q_1 and q_2 values.

The extent of atomization by the high-velocity crossflow can be inferred by the expansion of the spray width with increasing downstream distance, since it is presumed that this expansion can only occur if the liquid jet is disintegrating. Beginning with the 1-atm case, the spray width progressively increases with ambient pressure, which indicates a higher level of spray formation. For a constant crossflow and liquid

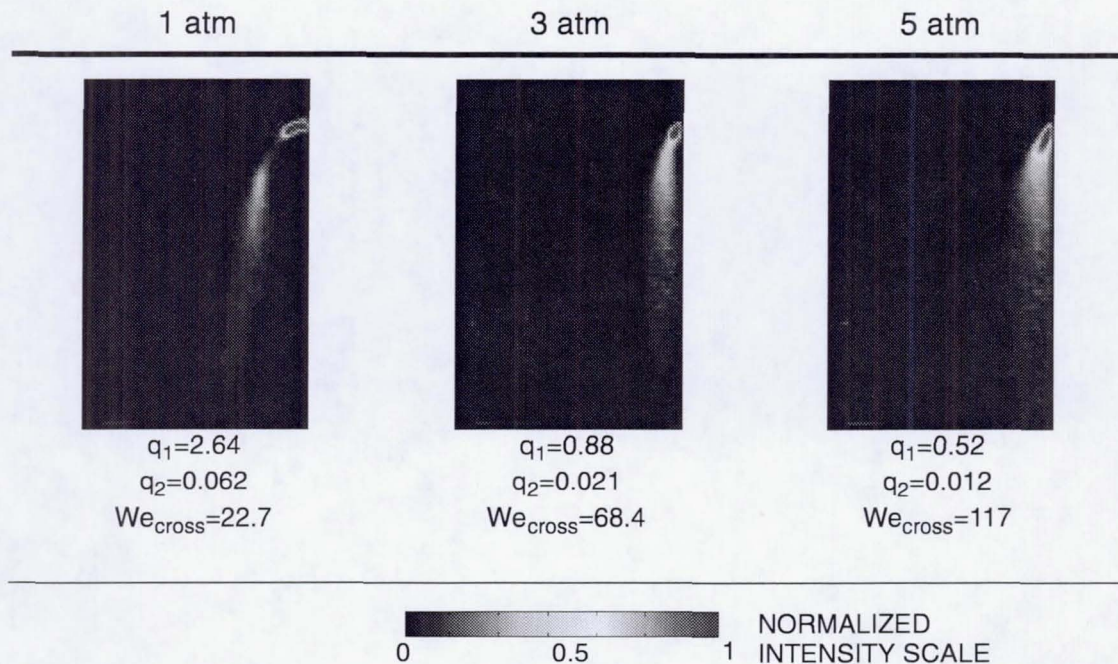


Fig. 9.4 Pure liquid jet injection with 0% airblast ΔP and $ALR=0$.

velocity, the increase in ambient pressure results in an increase in We_{cross} , and in turn, an increased tendency toward breakup.

9.4 Effect of Airblast Air at Different Ambient Pressure Conditions

The introduction of airblast air into the system increases spray atomization, as observed in the set of images shown in Fig. 9.5. The images in Fig. 9.5 are presented at each ambient pressure case for three groups of atomizing air pressure drop ranges: a 1.2-1.5% range, a 2.0-2.3% range, and a 2.9-3.3% range. For the purpose of this comparison, these three groups will be referred to as the 1%, 2%, and 3% ranges,

respectively. Each image is also labeled with its two-phase momentum-flux ratio, q_2 , and its atomizing air to liquid mass-flow ratio, or ALR .

Within each ambient pressure condition, the sprays follow the expected trend of increasing jet penetration with increasing q_2 . However, in comparing the sprays at each pressure condition, the spray penetration relationship to q_2 does not follow a linear function. For example, the q_2 values for the 1- and 3-atm cases at the 1% and 3% airblast ΔP conditions differ only by 0.03 and 0.01, respectively, but these differences produce a large change in the penetration of the spray. However, a larger difference in q_2 between the 3- and 5-atm sprays does not affect the jet penetration to the same degree.

The effect of introducing the airblast air can be seen by comparing the images from Fig. 9.4 (for $\Delta P=0\%$) to those in the 1% ΔP range, which are presented in the first row of Fig. 9.5. The presence of the atomizing air at an airblast ΔP of 1% helps to propel the liquid jet farther into the crossflow. The atomizing air especially affects the jets in the 3- and 5-atm cases, where the increase in jet penetration lifts the jet away from the near wall, which exposes more of the jet to entrain the crossflow and aids in dispersing the spray. A comparison between the $\Delta P=0\%$ and $\Delta P=1\%$ images, however, does not reveal any significant improvement in atomization.

With a continued increase in the atomizing air pressure drop, the airblast air begins to atomize the liquid before it is injected into the crossflow. The 2% group of cases shows an atomized jet leaving the exit plane of the orifice. Increasing the airblast pressure drop to 3% yields a fully-atomized spray that extends across the orifice exit.

A nodule of liquid occurs at the trailing edge of the orifice, and is thought to form

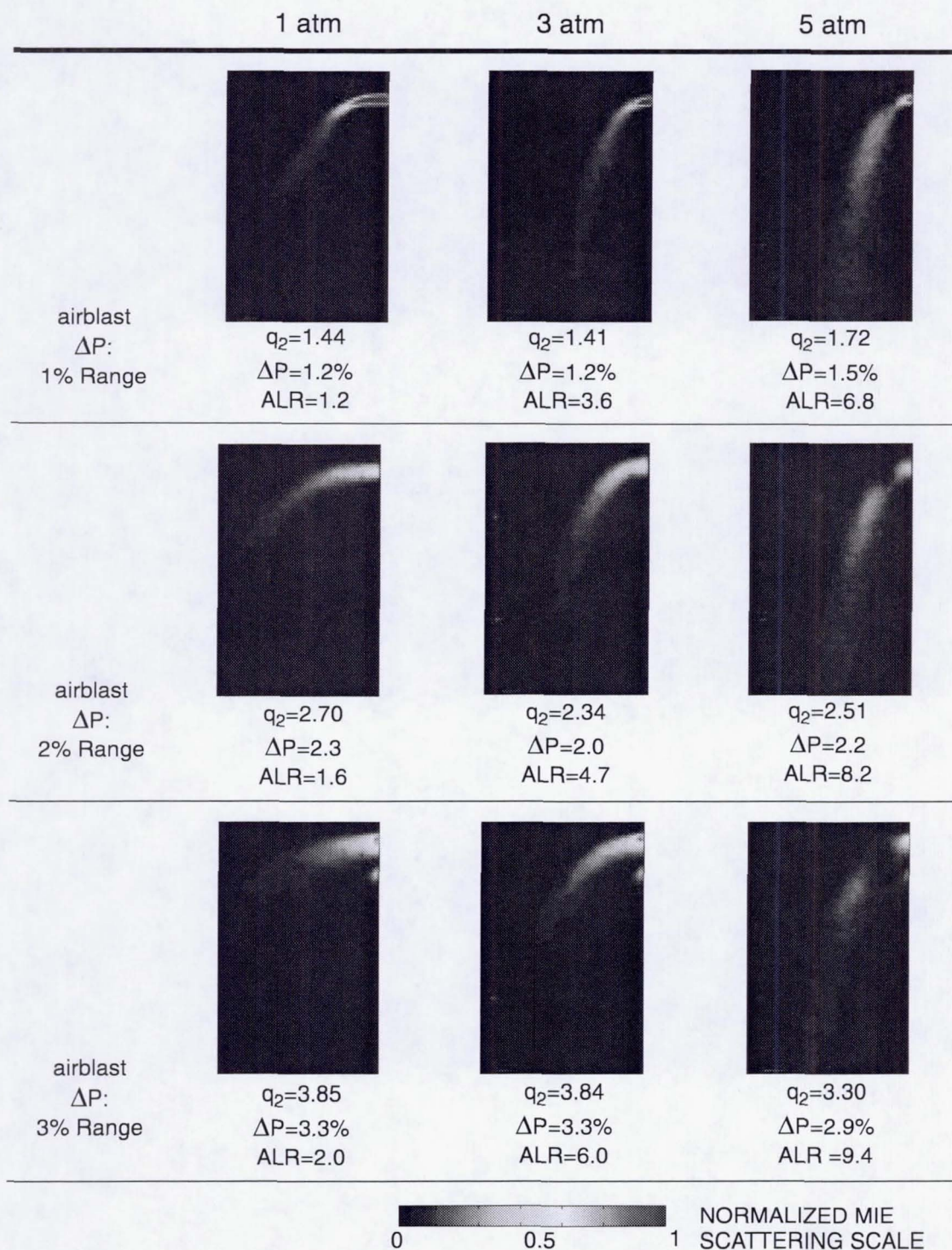


Fig. 9.5 Effect of atomizing air pressure drop on spray structure for various ambient pressures.

because of a separation-induced, internal flow pattern in the orifice of the injection panel as pictured in Fig. 7.11.

From these observations, three distinct jet shapes occur for similar atomizing air pressure drops at the different ambient pressure cases. The first regime, which occurs for airblast pressure drops less than 2%, yields an intact jet structure at the orifice exit plane similar to the intact liquid jet for the 0% airblast ΔP case in Fig. 9.4. The second regime, occurring for airblast pressure drops between 2-3%, forms an atomized spray across the orifice exit plane. The third regime, which accounts for air pressure drops greater than 3%, produces a fully-atomized spray across the exit plane with the appearance of a liquid nodule at the trailing edge of the jet orifice. It is postulated that the presence of this liquid nodule leads to the formation of larger droplets near the injector wall in an otherwise well-atomized field of small droplets (Seay et al., 1995; Leong et al., 1997). The 2% airblast ΔP condition appears to be optimal in producing sprays that are well-atomized and devoid of the liquid nodule that is a potential source of large droplets near the injection wall. However, a more detailed characterization of the internal spray distributions is needed in order to verify this observation.

Figure 9.6 compares these breakup regimes to the regime map obtained for the spray without crossflow, which was presented in Fig. 7.7. The operating conditions for the 1-, 3-, and 5-atm cases are plotted on their respective Re_L vs. We_{airbl} graphs. The three breakup divisions are noted on each of the graphs, and the markers corresponding to the airblast ΔP ranges of 1%, 2%, and 3% are labeled. In the graph for the 1-atm condition, the regime map divisions predict the atomization mode exhibited by the jet

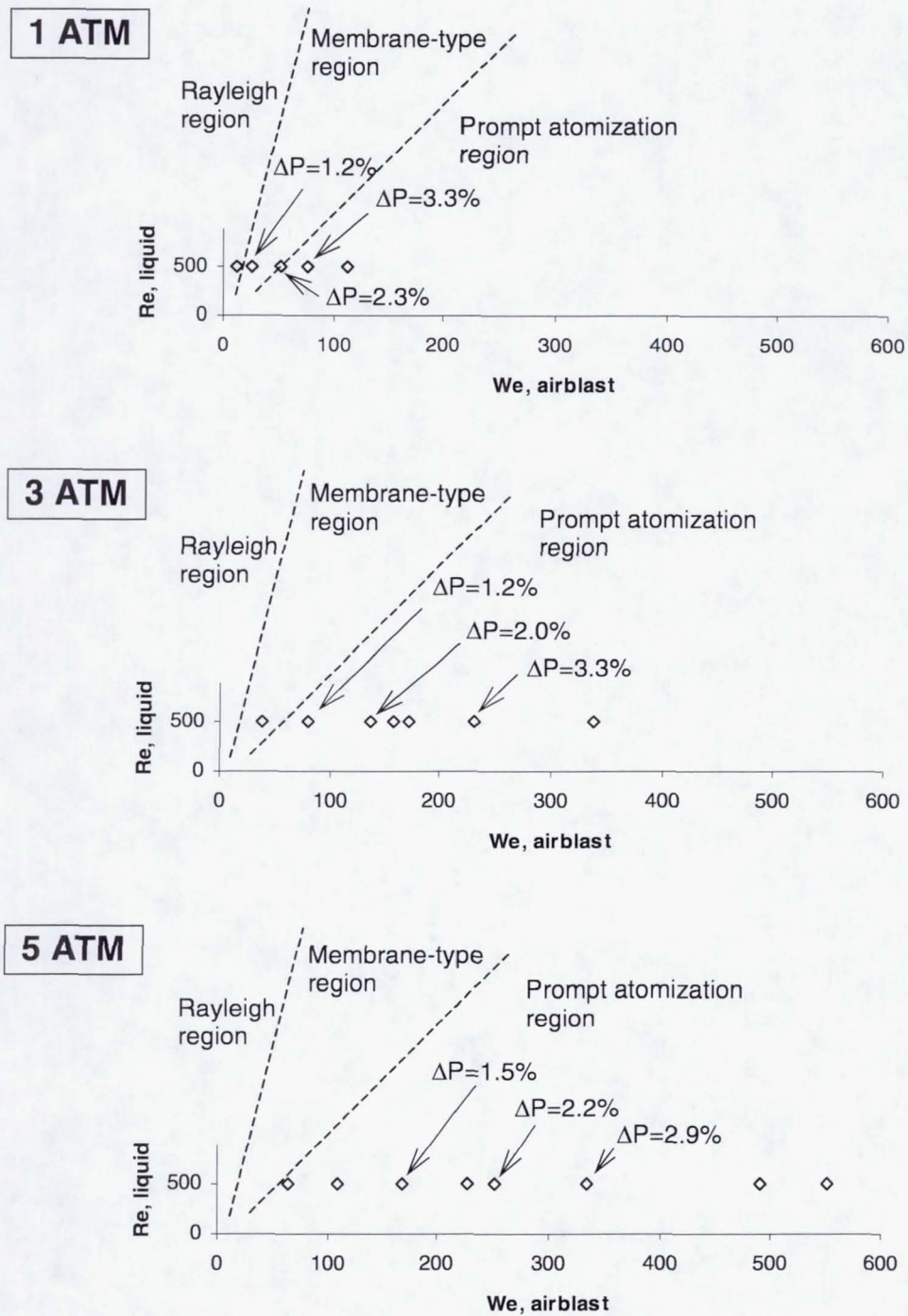


Fig. 9.6 Plots of the Re_L to We_{airbl} for the elevated pressure tests, relative to the breakup regime maps obtained in Chapter 7.

fairly well. The intact jet structure, which corresponds to the 1.2% ΔP marker, occurs in the membrane-type region. The transition regime, which occurs at a 2% airblast ΔP , straddles the membrane-type and prompt-atomization modes. The fully-atomized spray, obtained at the 3% airblast ΔP , falls under the prompt mode in the chart.

As the ambient pressure is increased, however, the 1%, 2%, and 3% pressure drop conditions shift into the prompt atomization regime of the map. The shift is induced by the increase in ambient pressure, which increases the air density parameter in We_{airbl} . While the regime map does not correspond well to the conditions in the 3- and 5-atm cases, it should be remembered that the breakup regime map for the airblast spray system was derived under atmospheric conditions.

9.5 Development of a Spray Trajectory Equation

A correlation relating the spray trajectory to flow conditions is useful for determining conditions that lead to optimal spray penetration. Correlations describing the jet penetration into a crossflow of air have been obtained for both gaseous (e.g., Kamotani and Greber, 1972) and liquid jets (e.g., Wu et al. (1997) and Schetz and Padhye (1977)). Based on phenomenological considerations, the jet in crossflow correlations adhere to the following general equation, whether the centerline of gaseous jets or the upper surface of liquid jets is being described:

$$\frac{x}{d_f} = c_0 \cdot (q_2)^{c_1} \cdot \left(\frac{z}{d_f} \right)^{c_2} \quad (9.3)$$

In this equation, c_0 , c_1 , and c_2 are empirically-derived constants, x/d_f and z/d_f represent the penetration and downstream distance, respectively, normalized with respect to the

fuel orifice diameter d_f . Correlations for liquid jet and for gaseous jet penetration were applied to the airblast spray images without much success. Correlations derived from the spray images, and which implemented the two-phase definition of q_2 to account for the operating conditions of the experiment, were thus sought.

A multivariate, nonlinear regression was performed on the data, using Eq. 9.3 as the basic equation. Details regarding the regression can be found in Appendix B. The method essentially involved casting Eq. 9.3 as a linear equation through a substitution of variables, and applying a least squares fit on the resulting linear equation. The solved coefficients are then substituted back into the original equation.

For this experiment, the main operating conditions that were varied were the ambient pressure and the airblast ΔP . Although the crossflow air velocity was maintained at 38 m/sec, images were also obtained at two additional crossflow velocity magnitudes at each ambient pressure condition.

The trajectory of the upper and lower surfaces of the spray for selected cases are shown in Fig. 9.7. The plots are arranged by column according to their ambient pressure condition. The q_2 conditions that were selected corresponded to values of q_2 approaching 0.70 (top row), 2.5 (middle row), and 5.5 (bottom row). The plots are oriented such that the spray originates from the bottom axis, with the crossflow entering from the left. The outer and inner spray surfaces are represented by the blue lines. The tracing of the spray surfaces excluded the liquid nodules that appeared in the 3% airblast ΔP cases. Superimposed on each plot are the curve fits, shown in red, for the outer and inner surfaces. The coefficients obtained from the regression were

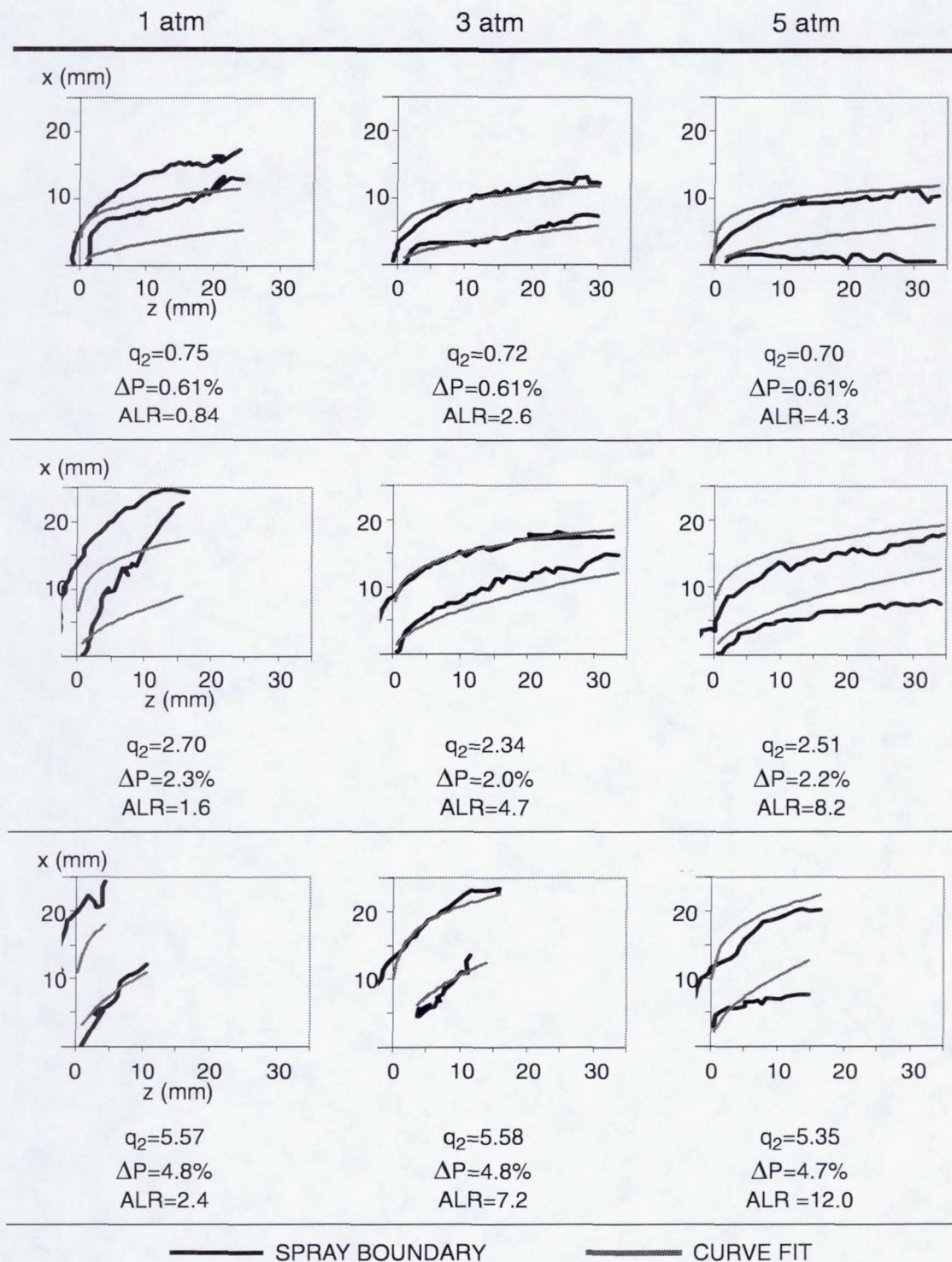


Fig. 9.7 Comparison between the spray surface trajectories and the outer and inner spray surface curve fit from Eq. 9.3 for selected cases.

$c_0=7.15$, $c_1=0.375$, and $c_2=0.182$ for the outer surface, and $c_0=1.20$, $c_1=0.570$, and $c_2=0.519$ for the inner surface correlation.

As observed in the plots, the trajectories in the 3-atm case are well-described by the curve fits. However, the curve fits underpredict the spray trajectories at the 1-atm condition, and overpredict the trajectories at the 5-atm condition. One reason for the insufficient fit lies in the lack of a term to account for the atomization quality of the spray, since droplets of varying sizes experience different drag forces which would affect their trajectory. Because the ambient pressure affects the degree of atomization of the spray, one of the additional factors that was considered was a ratio of pressure normalized by a baseline pressure of $P_0=1$ atm. The resulting equation that was fitted in the second iteration was

$$\frac{x}{d_f} = c_0 \cdot (q_2)^{c_1} \cdot \left(\frac{z}{d_f} \right)^{c_2} \cdot \left(\frac{P}{P_0} \right)^{c_3} \quad (9.4)$$

Table 9.2 summarizes the coefficients that describe the outer and inner surface trajectories that were derived for Eq. 9.4 as well as for the original curve fit in Eq. 9.3. In general, the power coefficients of q_2 for each of the four fitted equations are low (less than 1), but are greater than the powers of x/d_f . While the power coefficients of q_2 and x/d_f are positive, the powers associated with the pressure ratio are negative. These trends make sense, given that the penetration of the spray should increase with an increase in the momentum-flux ratio and the downstream distance, and should decrease with an increase in the ambient pressure.

The results of the modified curve fits are shown in Fig. 9.8. The spray surfaces are represented by the blue lines, while the pink lines correspond to the fit with the

Table 9.2 Coefficients for the outer and inner spray surface trajectory fits.

Equation type		constant: c_0	power of q_2 : c_1	power of (z/d_f): c_2	power of (P/P_0): c_3
Basic (Eq. 9.3)	outer	7.15	0.375	0.182	-
	inner	1.20	0.570	0.519	-
P -correction (Eq. 9.4)	outer	6.13	0.430	0.230	-0.336
	inner	0.809	0.664	0.631	-0.687

added pressure ratio factor. The plots in Fig. 9.8, which are representative of the results for the other spray conditions, show that the addition of the correction factor helped to collapse the fits unto the surface trajectories. The 17% average deviation of the outer edge curve fit associated with the basic trajectory correlation in Eq. 9.3 decreased to 7.8% for the pressure-corrected correlation in Eq. 9.4. For the inner spray edge, the average deviation was 69.5% for the basic trajectory correlation and 50.6% for the pressure-corrected correlation. The pressure correction improved the fit but was still deficient in predicting the inner edge of the spray, which is a region most likely populated by smaller droplets that are detrained by the crossflow from the lee side of the spray jet. For the lower edge of the spray, a factor such as the Stokes number (Eq. 2.11), may need to be incorporated to account for the behavior of droplets that are being entrained into the crossflow.

The spray trajectory correlations that were obtained are valid for the operating and geometric conditions listed in Table 9.1. Because of the limited range of

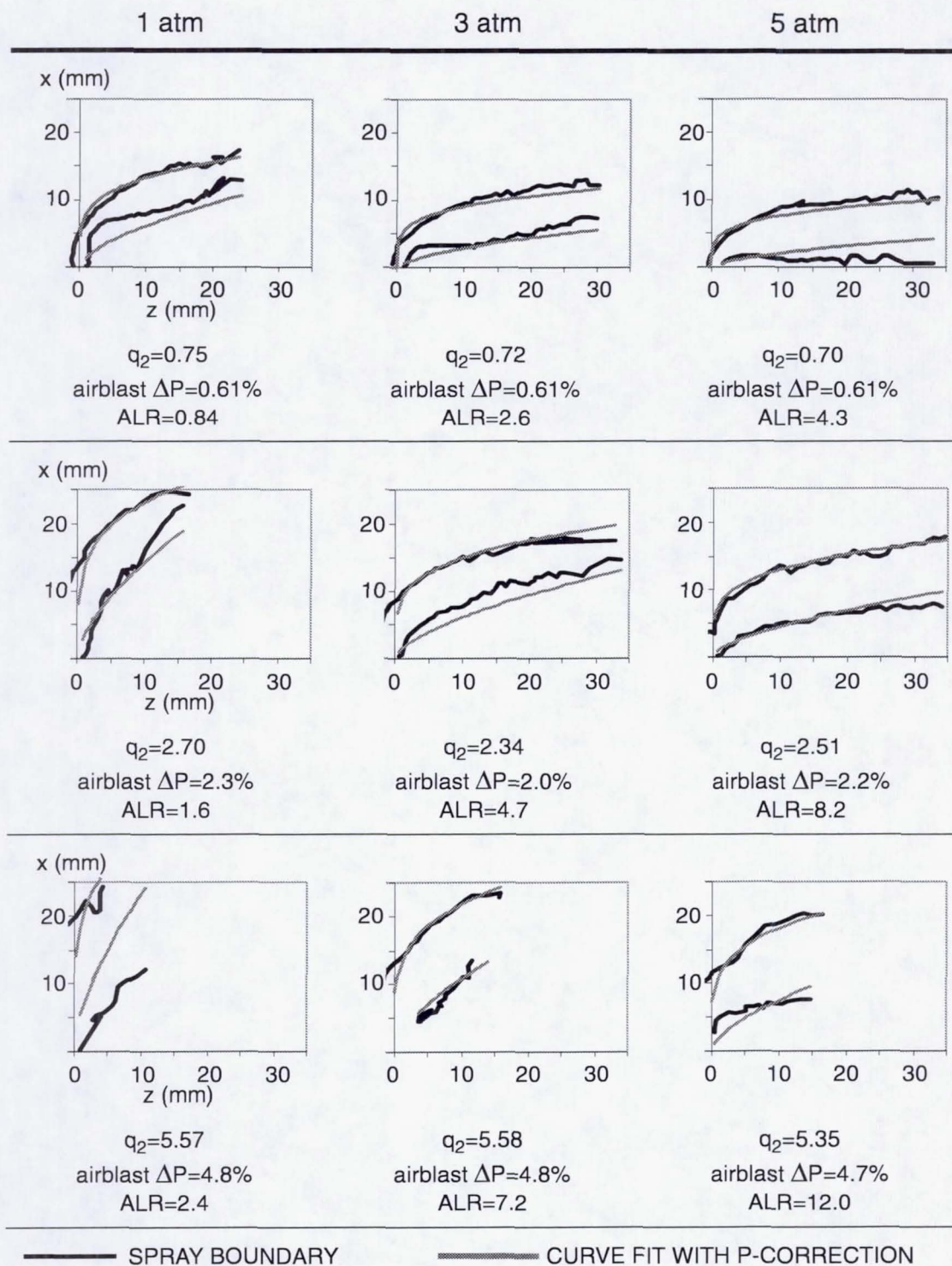


Fig. 9.8 Comparison between the spray surface trajectories and the modified curve fit from Eq. 9.4 for selected cases.

parameters such as the fuel flow rate, future tests should encompass a wider range of these variables and include other parameters as well in order to produce a more robust correlation.

9.6 Summary

Spray scattering images were used to investigate the structure of the airblast-atomized spray jet injected into a crossflow of air under varying ambient pressure conditions. At each ambient pressure, the airblast air flow rate was varied to yield airblast pressure drops ranging from 0%-4.8% across the injector orifice. The crossflow velocity magnitude was varied between 31-54 m/sec around a baseline of 38 m/sec. An increase in the spread of the spray width as well as an increase in the maximum spray penetration, as denoted by the upper surface trajectory, occurred with an increase in the airblast ΔP . The increased velocity of the airblast air imparted a higher momentum on the spray of droplets, which caused the droplets to penetrate farther into the crossflow.

A transition in spray structure at the injector orifice exit plane was also observed. At an airblast ΔP between 2-3%, the spray transitioned from an intact liquid jet to a fully-atomized spray that showed the presence of a liquid nodule at the orifice trailing edge. The presence of the liquid nodule is presumed undesirable because of the tendency for large droplets to shed from the pooled liquid. Based on this criteria, the operation of the airblast injector within the transitional 2-3% airblast ΔP range appears desirable in producing a well-atomized and widely-dispersed spray. The sprays in this

airblast pressure drop range were subjected to additional PDI measurements that will be presented in Chapter 10.

To characterize the general structure of the spray, the images were analyzed to fit empirical equations to the outer and inner surfaces of the spray jet. A two-phase definition of the jet to crossflow momentum-flux ratio, q_2 , was utilized in the equation. Curve fits of the penetration x/d_f as a function of q_2 and the downstream distance z/d_f underpredicted the surface trajectories in the 1-atm case, and overpredicted the trajectories in the 5-atm case. A normalized pressure-correction factor improved the fits that described both spray surfaces, although the inner spray surface correlation can still be further improved.

The correlations were obtained by varying the ambient pressure, airblast air, and crossflow velocity conditions. However, additional measurements need to be obtained to incorporate more combinations of conditions that include different fuel flow rates, spray orifice diameters, ambient temperatures, and other crossflow velocity settings in order to produce a comprehensive parametric variation of q_2 . Nonetheless, the ability to fit an equation to spray jets using a bulk parameter such as q_2 at various ambient pressure conditions is encouraging, especially given the fact that varying degrees of atomization are obtained at the different conditions. Additional correction factors that take into account the droplet dynamics within the spray jet should especially help to improve the correlations describing the inner surface trajectory.

CHAPTER 10

PLANAR CHARACTERIZATION OF THE AIRBLAST SPRAY JET IN A CROSSFLOW

The overall structure of the spray jet injected into a crossflow was characterized in Chapter 9. A two-phase momentum-flux ratio that represented the initial conditions that form the spray was defined in order to correlate the penetration of the outer and inner spray surfaces. The penetration of the spray could not be characterized solely by the momentum-flux ratio, as an additional factor that took into account the droplets in the sprays was needed to produce a better correlation. To help understand how the airblast sprays disperse into the crossflow, additional characterization of the flow field is needed.

This chapter begins with the planar characterization with phase Doppler interferometry (PDI) of the conditions selected from the global screening tests of Chapter 9. The time-intensive characterization of planar distributions using PDI leads to the use of the UV planar imaging techniques developed in Chapters 5 and 6 to characterize the distributions of the spray jet in crossflow for a wide range of cases. To bridge the results from the UV planar imaging techniques with the PDI measurements from the non-crossflow tests, a simplified droplet trajectory analysis is performed to predict the spray dispersion into the crossflow. The droplet trajectory analysis of the measurements also serves to identify areas in which further refinements to the model can be made.

10.1 Spray Measurements in Transition Regime of $\Delta P=2\%$

In Chapter 9, the 2% airblast ΔP condition was identified as being an optimal range in the atomization and dispersion of the spray into the crossflow. The sprays at this condition correspond to the transitional regime between the intact liquid jet and the nodule-forming spray regimes. Droplet size and velocities were measured across a grid of points at three axial z -planes with the PDI system (Phase Doppler Particle Analyzer, Aerometrics).

To maintain continuity in the experiment, the same experimental conditions that were used in the global visualization tests of Chapter 9 were used in the PDI tests. The dimensions of the hardware included a fuel orifice diameter of 0.34 mm, a spray orifice diameter of 2.26 mm, and a crossflow cross-section measuring 76.2 mm x 18.0 mm, with the latter dimension representing the maximum distance across which the spray can penetrate. The fuel flow of jet-A was set at 0.66 kg/h, and the crossflow velocity was maintained at 38 m/sec. To achieve the ambient pressure conditions, the experiment was installed in an elevated pressure facility (see Fig. 4.6).

Contour plots of the spray volume flux cross-sections are shown in Fig. 10.1. At the top of the figure, the vertical spray scattering images corresponding to the 2% airblast ΔP condition are shown. As a reference point, the left edge of the spray image coincides with the mid-plane of the crossflow section. A horizontal dashed line indicating the first downstream PDI measurement plane at $z=6.35$ mm is also noted on the images.

The liquid volume flux contour plots, which are sized to the same scale as the spray scattering images, are positioned beneath and aligned with each image. The

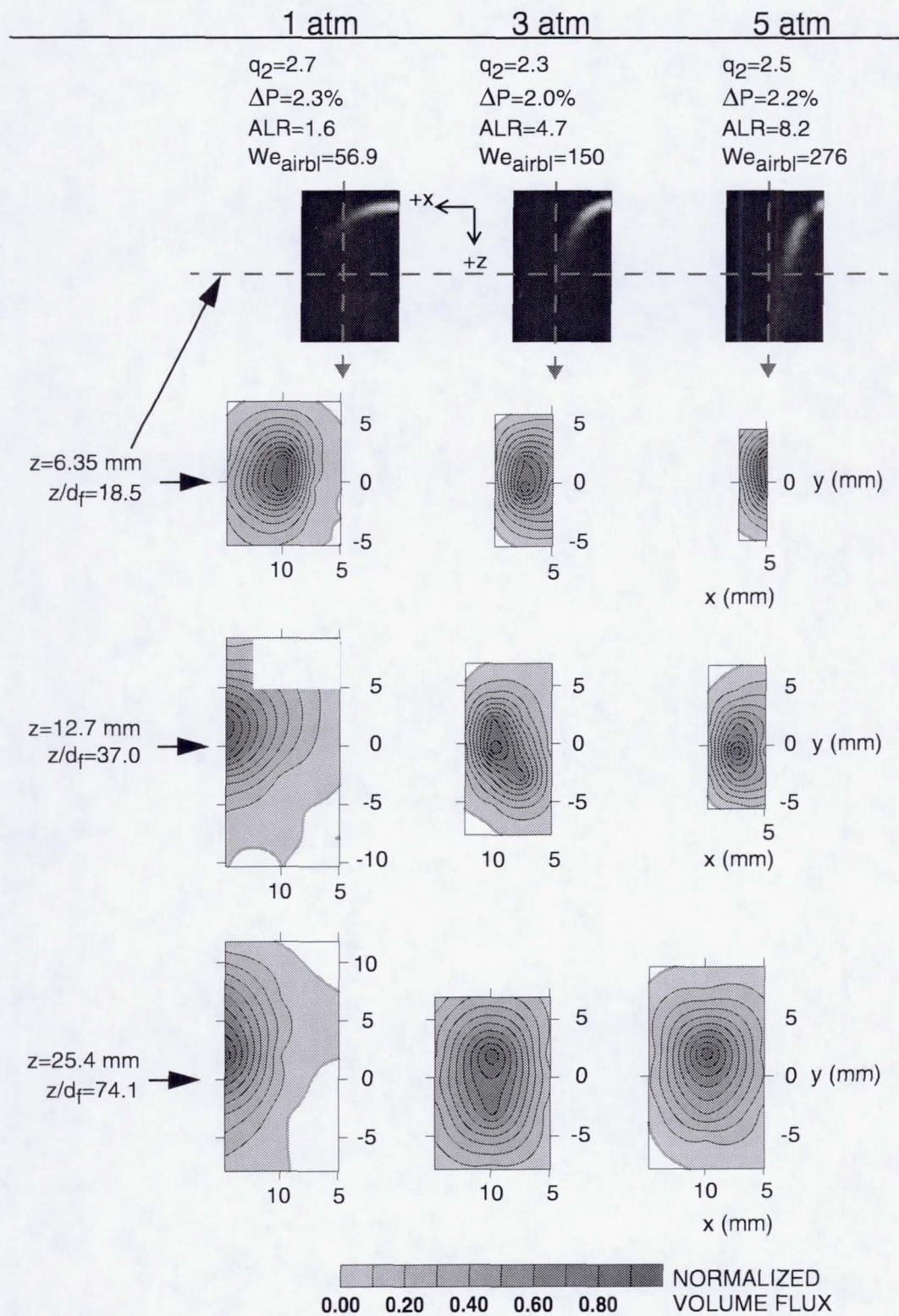


Fig. 10.1 Contour plots of normalized volume flux at various downstream z-planes.

orange lines appearing in the plots separate the lowest band level from the white areas, and denote the extent of the spray. The volume fluxes are normalized with respect to the highest volume flux recorded in each respective plane, and thus give an indication of the relative liquid volume fraction per plane. If the spray trajectory in the side profile image is traced to the plane of $z=6.35$ mm, the intersection of the spray at this plane can be compared to the corresponding volume flux measurements. The 1- and 5-atm cases show peak volume flux images corresponding to the trajectory of the spray image. The volume flux for the 3-atm case, however, slightly overshoots the intersection point of the spray in the image. It should be noted, though, that the images show light scattering by the spray, and are not representative of the mass distribution in the spray. As a result, exact alignment of the spray image with the spray volume flux measurements is not expected. The main purpose in comparing the images with their respective volume flux distributions at the $z=6.35$ mm plane is to show the general agreement between the two sets of data.

The liquid volume flux plots in Fig. 10.1, which can also be referred to as liquid mass flux plots, show the spray being aligned with the $y=0$ mm centerplane at the first measured plane of $z=6.35$ mm. However, at farther downstream planes, the spray shifts toward the positive y -direction, which could be caused by the development of non-uniformities in the crossflow as the air flows around the spray jet. The 3- and 5-atm cases also exhibit this same shift in the peak volume flux occurring by the last measured plane of $z=25.4$ mm.

In Fig. 10.1, the penetration of the center of mass, which approximately corresponds to the red peaks, increases with downstream distance for each ambient

pressure case, and decreases as the ambient pressure is increased. The penetration of the center of mass observed in Fig. 10.1 corresponds to regions of relatively larger droplet size classes, as seen in the D_{32} contour plots of Fig. 10.2.

Between the different downstream planes, the atomization quality as indicated by the D_{32} contour plots (Fig. 10.2) does not appear to change noticeably, which suggests that the crossflow contribution to secondary atomization may be minimal. However, the D_{32} contour plots do show that the atomization quality improves as the ambient pressure is increased. While the relative velocity between the atomizing air and the liquid fuel is constant at a given airblast ΔP setting, the atomization quality improves with increasing ambient pressure because the increasing air density results in an increase in Weber number (from 56.9 to 150 to 276 for the respective 1-atm, 3-atm, and 5-atm cases). A higher degree of atomization occurs between the 1- and 3-atm cases than occurs between the 3- and 5-atm cases.

Contour plots of the mean transverse velocity components presented in Fig. 10.3 contain nonzero distributions with contour levels that increase with increasing distance from the wall. The higher transverse velocities that occur in the regions farthest from the wall correspond to the droplets that penetrate farthest into the crossflow. Otherwise, the transverse velocity profiles of the droplets in the spray field do not show much variation in distribution between the 1-, 3-, and 5-atm cases.

While the transverse velocity plots in Fig. 10.3 do not exhibit large differences in the shape and distribution of the contours, the distributions for the axial velocity component in Fig. 10.4 are varied within each case and within the different z -planes. The axial components of the droplets change according to the jet interaction with the

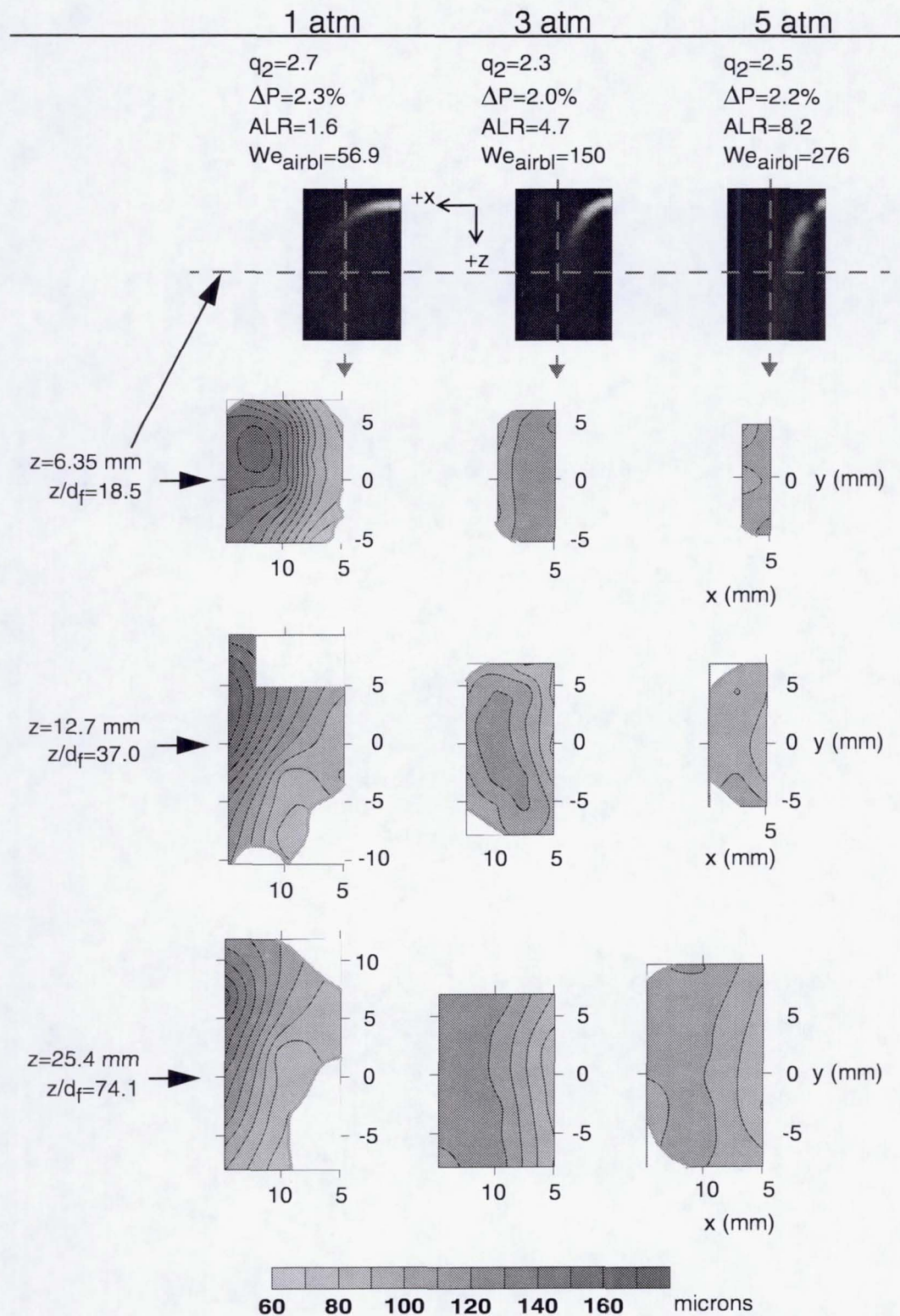


Fig. 10.2 Contour plots of D_{32} at various downstream z -planes.

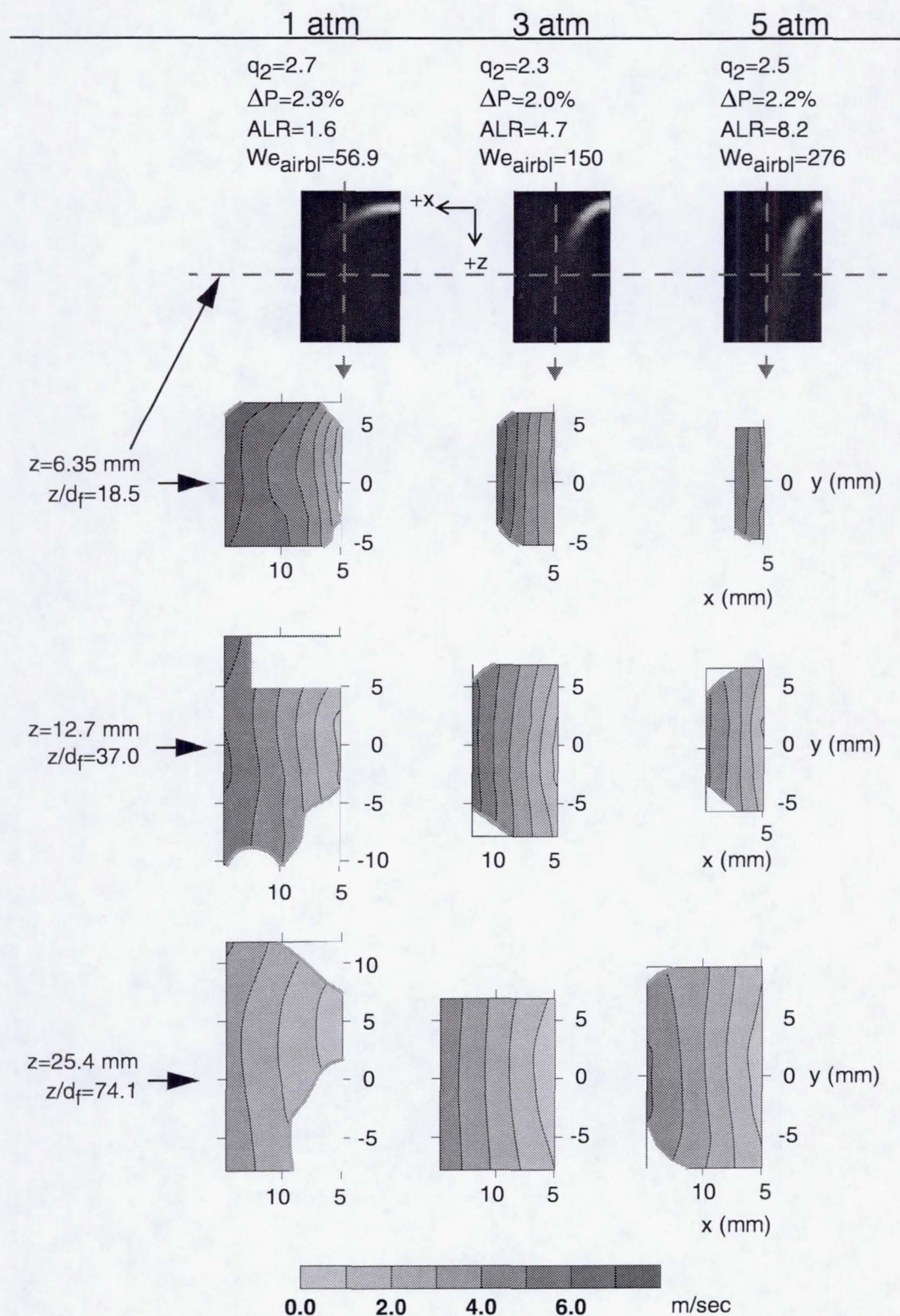


Fig. 10.3 Contour plots of the transverse velocity component (parallel to the x-axis) at various downstream z-planes.

crossflow. In the near-field region, the body of the dense spray jet can induce regions of high velocity as the crossflow travels around the jet. The high velocity regions that form end up flanking a low-velocity region that is induced by the wake of the jet. The presence of a pair of lobes of high axial velocity formed by this mechanism was observed by Wu et al. (1998) in their planar characterization studies of a liquid jet in a crossflow, and is also observed in the present study.

At the $z=6.35$ mm plane for the 1-atm case, a high velocity band between 15 m/sec and 17 m/sec is observed, as well as a distinctive notch of a lower axial velocity range of 13 m/sec to 15 m/sec that manifested at the (x,y) coordinate of $(5,0)$. The absence of this characteristic in the 3- and 5-atm cases at the $z=6.35$ mm plane is attributed to the fact that the PDI measurement plane misses the wake region of the jet spray in these cases, as seen in the alignment of the images with the PDI measurement planes. At the downstream plane of $z=12.7$ mm, however, the notched structure is observed in the 3 atm case, but not in the 5-atm case. At this same z -plane, the PDI measurement grid may still miss the wake region of the lower-penetrating 5-atm case.

All three cases show an increase in the mean axial velocity magnitudes with increasing downstream distance. By the $z=25.4$ mm downstream plane, all of the spray cases attain a maximum mean axial velocity approaching 24 m/sec, which is still less than the 38 m/sec crossflow velocity condition. In comparing the axial velocity distributions with corresponding contour plots of D_{32} in Fig. 10.2, the regions with lower axial velocities occur where larger droplet distributions are present, while higher axial velocities occur in regions where smaller droplet distributions are present.

The kidney-shaped cross-section associated with jet-crossflow dynamics are not represented or suggested in the contour plots presented in Figs. 10.1 through 10.4. The droplet distribution may contain larger diameter droplets that are more likely to penetrate the crossflow rather than become entrained in the vortical structures produced by the jet-crossflow interaction. In addition, the interaction between the jet and crossflow may not be strong enough to generate the vortex pair necessary for the kidney-shape deformation of the spray by the $z=25.4$ mm plane. A finely-atomized spray, such as a spray with a plane-averaged D_{32} value of $24.5\text{ }\mu\text{m}$, can exhibit the characteristic kidney-shape (Leong et al., 1997) because the spray droplets are more amenable to following the dynamics of the gaseous flow field.

10.2 Experimental Conditions for the Planar Imaging Tests

While the PDI measurements yielded insightful information from the planar characterization of the spray, the diagnostic requires a considerable amount of time to acquire a planar grid of data. To increase the efficiency in surveying sprays of different parametric variations, the planar imaging techniques developed in Chapters 5 and 6 were applied to the spray jet in crossflow cases. Although the planar imaging techniques do not measure droplet velocities, the diagnostic does offer the ability to visualize the atomizing air component of the spray. The planar imaging diagnostic can also be used to screen conditions for additional PDI measurements.

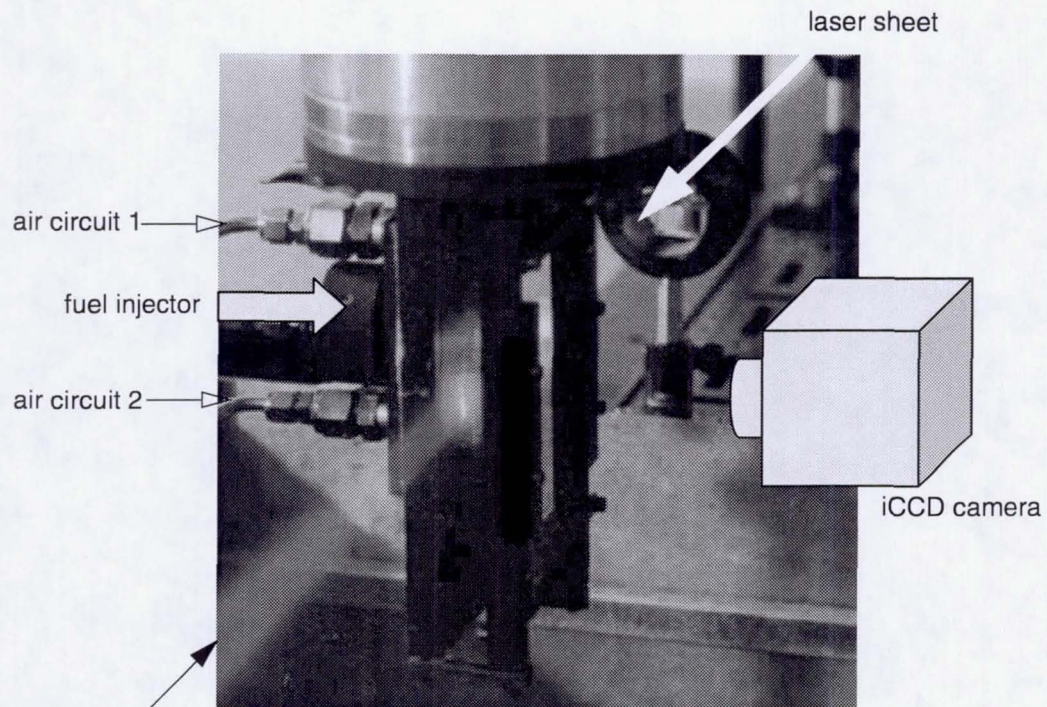
For the planar imaging tests, the spray injection hardware used the same crossflow configuration as the elevated pressure tests in Chapter 9 and in Section 10.1. However, because of issues related to the dependence of the fluorescence signal on the

ambient pressure, the UV planar imaging techniques were only applied to tests conducted at atmospheric pressure. As a result, the hardware was installed in the atmospheric test facility for these tests.

In the crossflow configuration, the injection panel is oriented so that the spray is injected from the side, transversely into the downward-flowing, high velocity crossflow of air. The vertical laser sheet passes through the side windows in the test section, along the $+y$ -direction, to illuminate the yz -plane of the spray (see Fig. 10.5). The camera focuses on the plane of the laser sheet through a pane of quartz glass installed on the side of the test section opposite the injector panel. The spray is canvassed by traversing the experiment along the x -axis in order to capture the yz -planes of the spray from $x=2$ mm to $x=16$ mm, in 1-mm increments.

The collection of vertical planar images is processed to produce horizontal cross-sections at downstream distances ranging from $z=8$ mm to $z=30$ mm. After reconstructing the horizontal planes and applying a smoothing filter, the resultant image measured 13.2 mm x 18.2 mm. A majority of the images in this chapter are presented in the orientation shown in Fig. 10.6. The viewpoint of the image is from a position upstream of the jet, with a view of the dispersed spray in the $+z$ -direction. From this point of view, the spray is injected from the top of the image.

The planar imaging results are presented on a normalized intensity scale. Each measurement type (e.g., PLLIF, acetone PLIF) was normalized by the maximum intensity value that was recorded. However, where noted, the results for some sets of images are displayed on a different normalized intensity scale in order to enhance the distributions shown in the images.



*Note: The green 532 nm light that is normally filtered out of the experiment is only present in this picture for the express purpose of illustrating the path of the laser sheet.

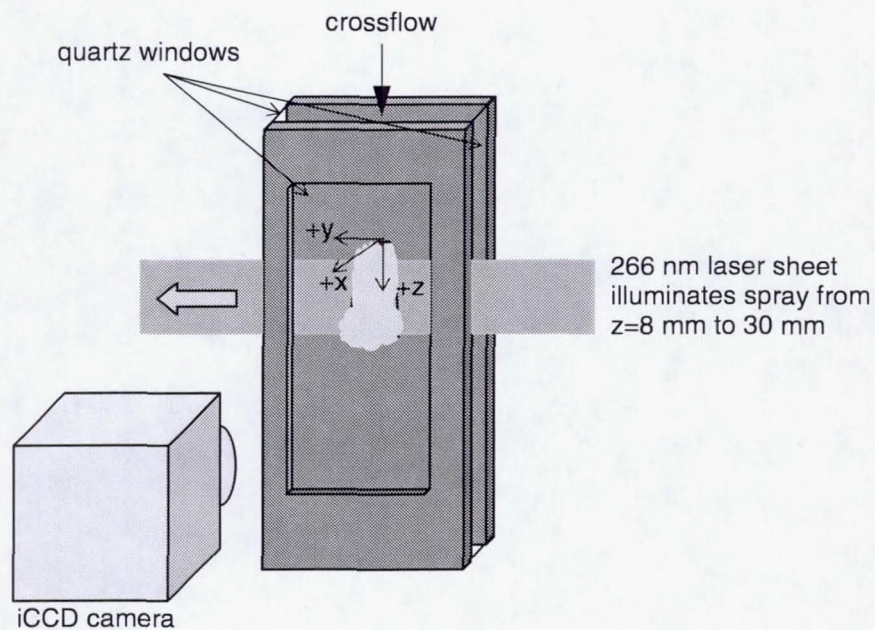


Fig. 10.5 Picture and schematic depicting the orientation of the UV laser sheet and camera with respect to the spray jet in crossflow experiment.

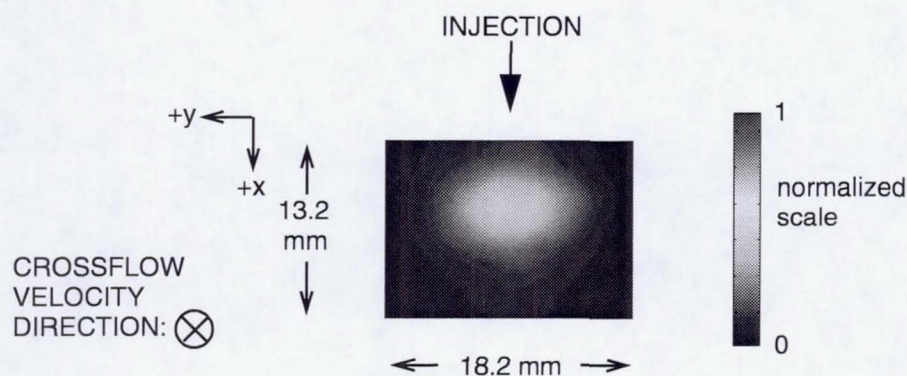


Fig. 10.6 Sample horizontal planar section extracted from the set of vertical slices.

The twelve conditions that were investigated in the non-crossflow tests of Chapter 8 resulted from a combination of two fuel flow rates (1.8 kg/h and 3.7 kg/h), three airblast pressure drop settings across the spray orifice (2%, 4%, 6%), and two spray orifice diameters (3.18 mm, 4.22 mm). The sprays formed by these conditions were subjected to a 70 m/sec crossflow of air with maximum turbulent fluctuations (u_{rms}/\bar{U}) approaching 14%. In addition to these cases, the crossflow velocity magnitude was increased to 78 m/sec and 87 m/sec for selected cases. A full list of the ranges of conditions encompassed in the planar characterization tests is listed in Table 10.1.

In addition to the planar imaging results, PDI (Real Time Signal Analyzer, Aerometrics) was used to obtain data for the sprays injected into the crossflow velocity of 70 m/sec. The droplet size and velocities in the spray were measured across a grid of points at the $z=10$ mm plane. The two velocity components that were measured are in

Table 10.1 Operating and geometric conditions for the planar imaging of the airblast spray experiment in the crossflow configuration.

Parameter	Range of Variation
Ambient pressure (kPa)	101.3
Fuel flow (MIL-C-7024D, MIL-PRF-7024E) (kg/h)	1.8, 3.7
Airblast pressure drop (%)	2, 4, 6
Airblast velocity, U_{airbl} (m/sec)	32.1 - 82.6
Airblast air to liquid mass flow ratio, ALR	0.29 - 1.92
Crossflow velocity, U_{cross} (m/sec)	70, 78, 87
$Re_L = \frac{\rho_L U_L d_f}{\mu_L}$	$1.26 \times 10^3 - 2.59 \times 10^3$
$We_{airbl} = \frac{\rho_g (U_{airbl} - U_L)^2 d_f}{\sigma_L}$	111 - 303
$Re_{airbl} = \frac{\rho_g U_{airbl} d_{spray}}{\mu_g}$	$1.22 \times 10^4 - 2.56 \times 10^4$
$Re_{cross} = \frac{\rho_g U_{cross} d_{cross}}{\mu_g}$	$1.21 \times 10^5, 1.35 \times 10^5, 1.50 \times 10^5$
Fuel orifice diameter, d_f [corresponding l/d in brackets]	0.66 mm (0.0260 in.) [$l/d = 2.5$]
Spray orifice diameter, d_{spray} [corresponding l/d in brackets]	3.18 mm (0.125 in.) [$l/d = 1.0$], 4.22 mm (0.166 in.) [$l/d = 0.75$]
Crossflow length x width	76.2 mm x 18.0 mm (3.0 in. x 0.71 in.)
Crossflow hydraulic diameter d_{cross}	29.2 mm

Notes:

- $\rho_L = 764 \text{ kg/m}^3$ for MIL-C-7024D; $\rho_L = 762 \text{ kg/m}^3$ for MIL-PRF-7024E;
 $\rho_g = 1.19 \text{ kg/m}^3$ for air at room temp. and pressure
- $\mu_L = 7.96 \times 10^{-4} \text{ kg/m-sec}$ for MIL-C-7024D; $\mu_L = 7.57 \times 10^{-4} \text{ kg/m-sec}$ for MIL-PRF-7024E;
 $\mu_g = 2.00 \times 10^{-5} \text{ kg/m-sec}$ for air at room temp. and pressure
- $\sigma_L = 0.0245 \text{ kg/sec}^2$ for MIL-C-7024D; $\sigma_L = 0.0280 \text{ kg/sec}^2$ for MIL-PRF-7024E
- For reference, hardware dimensions are also given in English units, which were the primary units used in the machining process.
- d_{cross} , the hydraulic diameter of the crossflow section, is computed by the formula $4A/P$, where A and P are the area and wetted perimeter, respectively, of the crossflow cross-section.

the transverse x -direction, which runs parallel to the initial spray injection velocity, and the axial z -direction, which is aligned with the crossflow velocity.

10.3 Distribution of the Liquid Component of the Spray Injected into a Crossflow

PLLIF images of the liquid volume concentrations showed that the airblast spray without the crossflow contained a two-lobed structure that corresponded to the design of the atomizing air passageways in the injector. For reference, the orientation of the lobes in the current configuration is pictured in Fig. 10.7 to show the spray prior to introducing the crossflow.

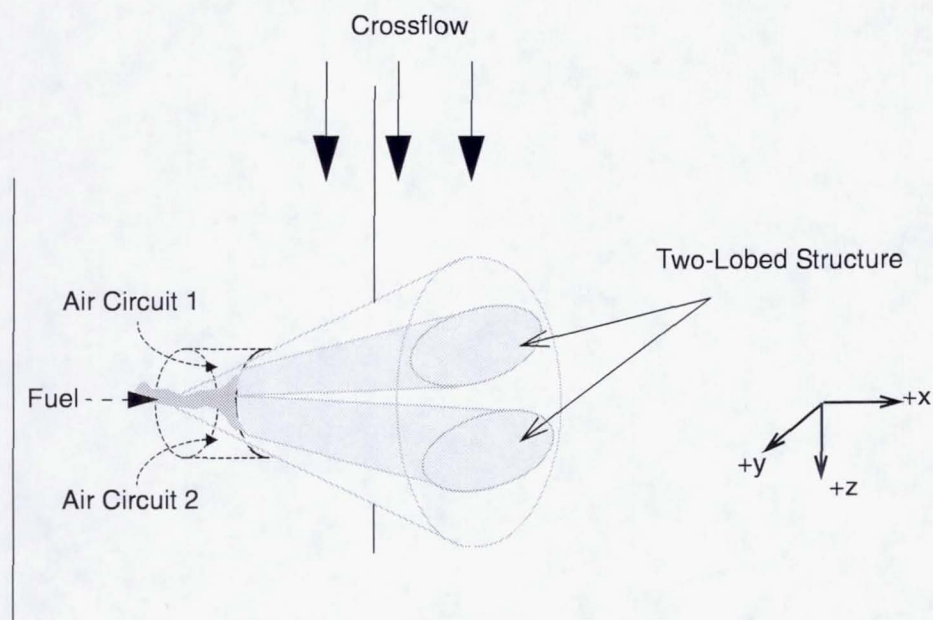


Fig. 10.7 Schematic depicting the orientation of the two-lobed spray structure prior to introducing the crossflow.

In the spray jet in crossflow system, initial PDI measurements at various downstream planes of the spray jet showed no evidence suggesting the presence of the twin-lobed structure in the volume-flux distributions (see Chapter 9). However, these measurements were only obtained for three conditions. In this section, planar images are used to view the cross-section of the sprays for evidence of the lobes as well as for other structural phenomena.

10.3.1 Effect of Injection Parameters on the Spray Jet Injected into a Crossflow at 70 m/sec

10.3.1a Distributions in the $z=10$ mm plane

General Observations of the Liquid Concentration Distributions

The PLLIF images of the sprays injected into the baseline crossflow velocity condition of 70 m/sec are shown in Fig. 10.8. The images, which represent the cross-sections at the $z=10$ mm plane, are arranged in rows according to their fuel flow rate and spray orifice diameter, and in columns according to their airblast ΔP . The first two rows of images correspond to the 1.8 kg/h fuel flow condition while the third and fourth rows correspond to the 3.7 kg/h fuel flow rate. Within each fuel flow group, the rows are divided according to the different spray orifice diameters.

Each image is labeled with the two-phase momentum-flux ratio, q_2 , based on the operating conditions in the experiment. The q_2 values increase with an increasing airblast ΔP . Within each column of cases, q_2 is largely invariant, since the atomizing air and crossflow are kept constant within each column, and since the change in the fuel flow rate has only a slight effect on q_2 . Although the trends in the penetration of the

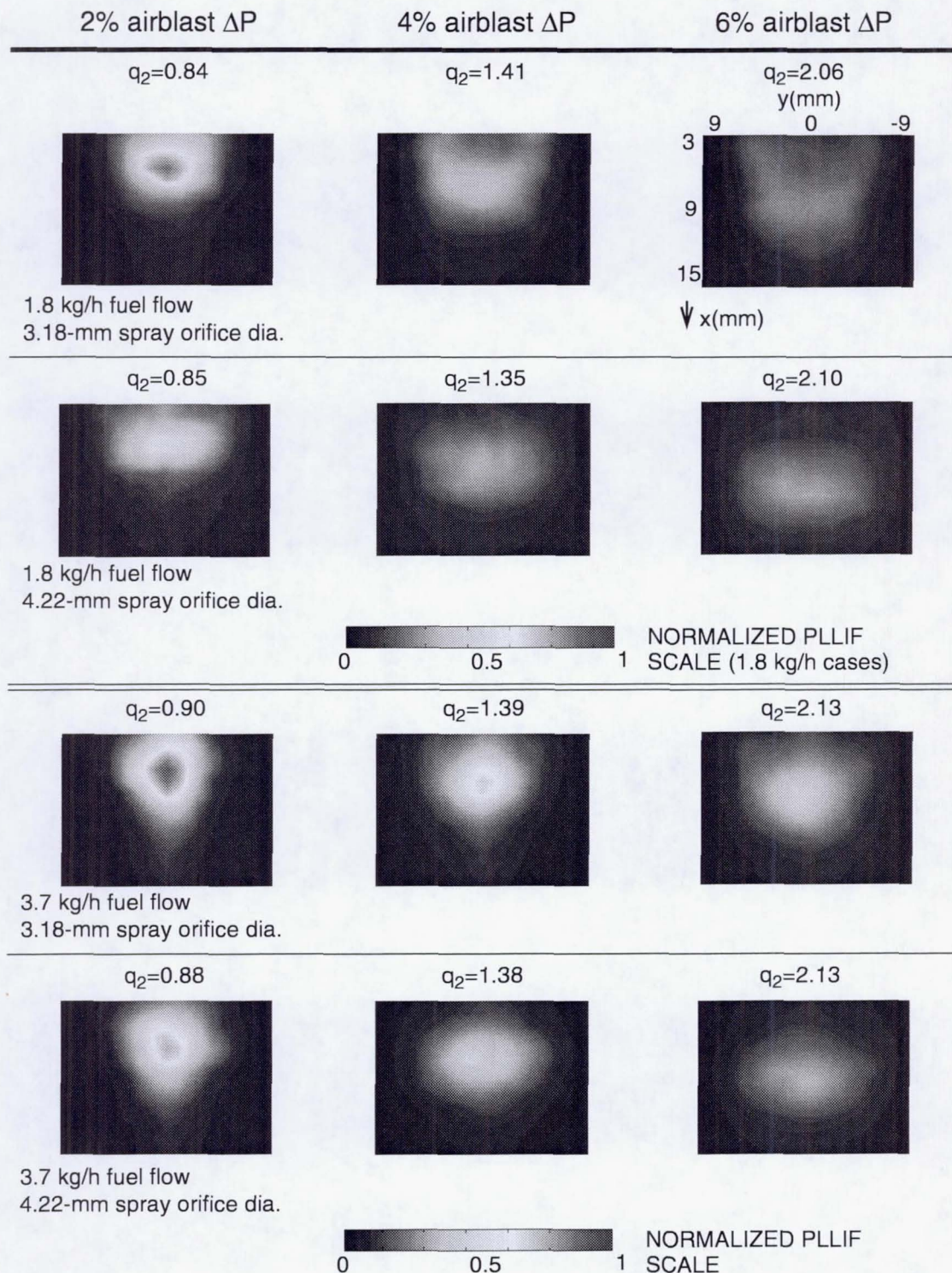


Fig. 10.8 PLLIF images depicting volume concentration distributions at the $z=10$ mm plane for the twelve spray conditions, after injection into a crossflow of 70 m/sec.

upper surface of the sprays (i.e., the surface of the spray farthest from the injection wall) correspond well with the q_2 values, it is clear from the images that the extent of the lower surface (i.e., the surface of the spray closest to the injection wall) as well as the width and internal distributions of the sprays vary within each group of q_2 conditions.

In the group of images for the 1.8 kg/h fuel flow rate, the emitted maximum fluorescence signal was half of the maximum level collected for the 3.7 kg/h case. This observation makes sense, given that the fluorescence signals in the PLLIF measurement are proportional to the liquid volume concentration in the plane. Because of this difference, the two groups of fuel flow rates are presented on different normalized intensity scales in order to better observe the structures in the 1.8 kg/h case.

The cross-sections of the liquid distributions can be classified as possessing either a circular shape, an elliptical shape, or a “kidney”-shaped distribution typically seen in gaseous jet in crossflow mixing (e.g., Kamotani and Greber (1972), Zaman and Foss (1997), Smith and Mungal (1998)). The circular cross-sections are mainly seen in the sprays where a lower degree of atomization is expected, such as at the 3.7 kg/h, 2% ΔP cases. As the degree of atomization is increased by increasing the relative velocity between the airblast and fuel streams, the spray forms a flattened elliptical cross-section after injection into the crossflow, as seen in the row of images formed at the 1.8 kg/h, 4.22 mm-dia. conditions.

For a subset of the sprays with elliptically-shaped cross-sections, a kidney-shaped distribution is observed. The kidney-shaped distribution is primarily seen in the 1.8 kg/h, 3.18 mm-dia. case for the 4% and 6% airblast ΔP conditions. Interestingly,

these cases did not produce the lowest initial D_{32} distributions in the non-crossflow cases. Rather, in the non-crossflow condition, the 4.22 mm-dia. geometry produced the lowest D_{32} distributions that were most uniformly dispersed across a large area (see Fig. 8.7). On the other hand, although the planar D_{32} distributions were higher in the non-crossflow, 3.18 mm-dia. case, the velocity distributions were also higher (see Fig. 7.12). The initial droplet and velocity distributions apparently play an important role in affecting the penetration of the spray: a spray with a uniformly low droplet D_{32} is not necessarily advantageous if an effective dispersement of the spray across the crossflow is desired.

In the images for all of the case conditions, the two-lobed structure is not preserved in the cross-sections of the spray. The crossflow apparently causes the lobed structure to merge upon impacting the spray jet.

Trends in the Liquid Concentration and D_{32} Distributions

The effect of the airblast ΔP on the liquid volume distributions is observed by comparing the sprays formed by the three airblast ΔP conditions within each row of Fig. 10.8. An increase in the airblast ΔP correlates to a liquid mass dispersion that increases in coverage across the cross-section and that also decreases in mean concentration. This observation is opposite of the trend seen in the non-crossflow cases, where an increase in the airblast ΔP resulted in a decrease in the spray area (see Fig. 8.6). In the non-crossflow case, the increase in airblast ΔP produced a higher atomizing air velocity which had the dual effect of producing a well-atomized spray while forcing the spray through the orifice with a high velocity component along the

injection direction. The same high velocities that decrease the extent of spray area in the non-crossflow case also help to distribute the droplet distributions across the crossflow.

The increase in fuel flow rate produced a decreased dispersion of the spray into the crossflow, as seen by the decreased spray coverage and increased non-uniformity in spatial distributions. The cause of the increased non-uniformity can be attributed to the higher concentration of fuel that needs to be dispersed in the higher fuel flow case.

Increasing the spray orifice diameter did not drastically change the area covered by the spray. However, the shape of the cross-sections tended toward a more flattened, elliptical shape as the orifice diameter was increased from 3.18 mm to 4.22 mm. This observation may be related to the combination of a lower initial droplet velocity and a smaller droplet distribution in the 4.22 mm-dia. case that prohibits the spray from penetrating across a wide section of the crossflow.

To obtain an idea of the atomization quality of the sprays, which will help in interpreting the trends elicited from the liquid concentration distributions, planar D_{32} images were derived, and are presented in Fig. 10.9. The format of the figure follows the same format used to present the PLLIF images in Fig. 10.8.

In each image, the sprays are observed to produce increasing D_{32} values with increasing distance from the wall. These droplet distributions result from the higher momentum of the larger drops, which causes the drops to penetrate farther into the crossflow. Interestingly, the regions of higher liquid concentrations do not necessarily correspond to the regions of large droplet D_{32} . For example, in the 1.8 kg/h, 2% airblast ΔP , 3.18 mm-dia. case, which corresponds to the leftmost image in the top row

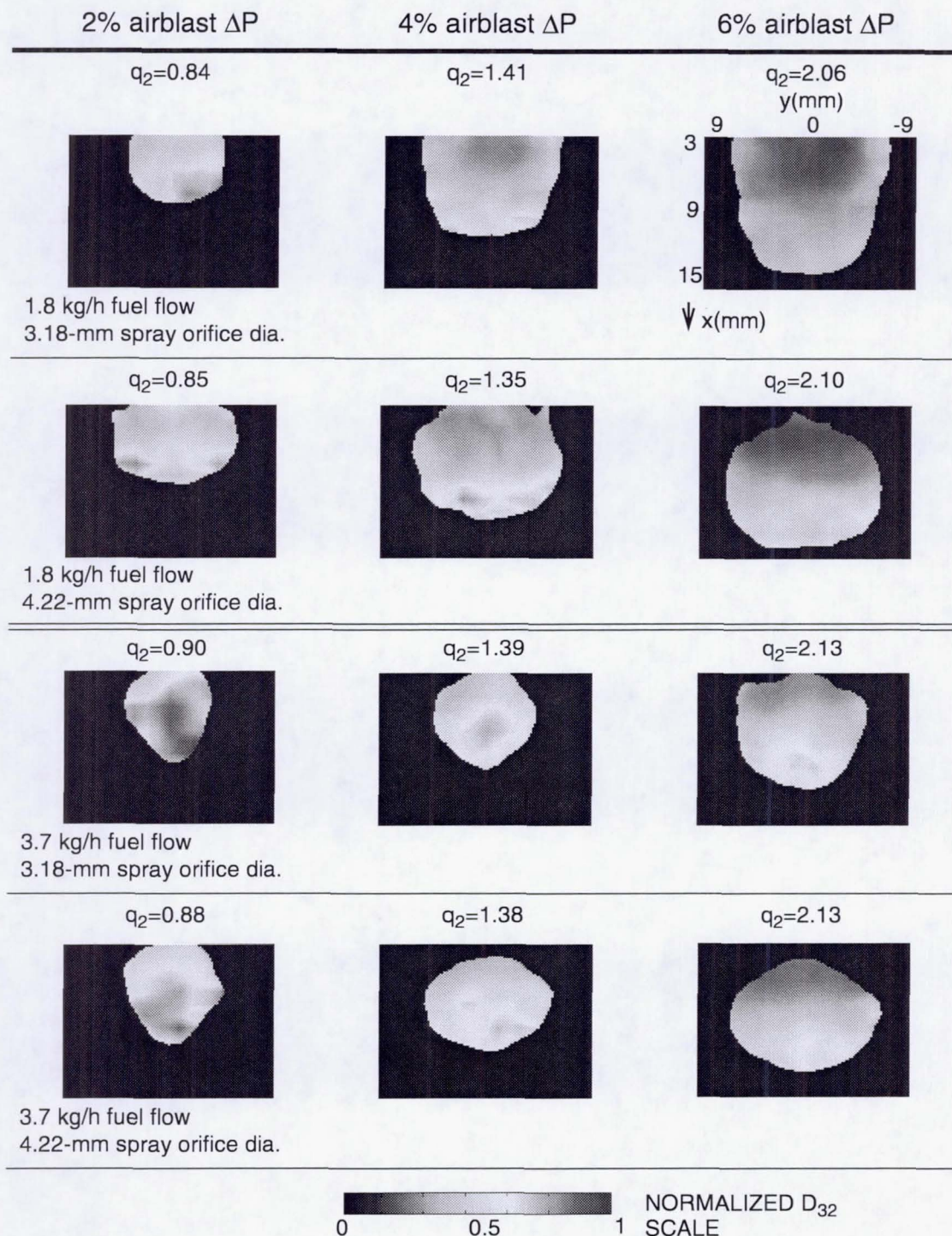


Fig. 10.9 Planar D_{32} images at the $z=10$ mm plane depicting D_{32} distributions of the twelve spray conditions, after injection into a crossflow of 70 m/sec.

of Figs. 10.8 and 10.9, the highest concentration of liquid occurs in the center of the spray (see Fig. 10.8), but the largest D_{32} are found along the outer edge of the spray (see Fig. 10.9). This observation holds for a majority of the conditions tested. On the other hand, in the 1.8 kg/h fuel case, the indentation in the kidney-shaped structure between the wall and the jet shows a region containing a low liquid volume concentration that corresponds to a region of smaller D_{32} .

The D_{32} distributions of the sprays injected into the crossflow show similar trends that to those found in the non-crossflow cases. An increase in the relative velocity between the airblast and fuel streams, produced by either increasing the airblast ΔP or by operating at a lower fuel flow rate, produced smaller D_{32} distributions. The effect of increasing the spray orifice diameter appeared to largely enhance the spread of the spray rather than increase the atomization of the spray.

In order to draw comparisons with the images and to gain a sense of the range of droplet sizes indicated by the planar D_{32} distributions, PDI-measured D_{32} values obtained across a grid of points at the $z=10$ mm plane are presented in Fig. 10.10. The grid of points is shown overlaid on the contour plot of the measured D_{32} values for each case condition. The grid varied according to the extent of the spray, with points obtained in 2-mm increments along the y -direction, and in 1-mm increments along the x -direction.

A comparison of the range of magnitudes between the D_{32} measurements at the $x=10$ mm plane from the non-crossflow case and the $z=10$ mm plane for the crossflow case can be made, assuming that the distance traveled by the spray to both planes is nearly the same. In the non-crossflow tests, the overall minimum and maximum

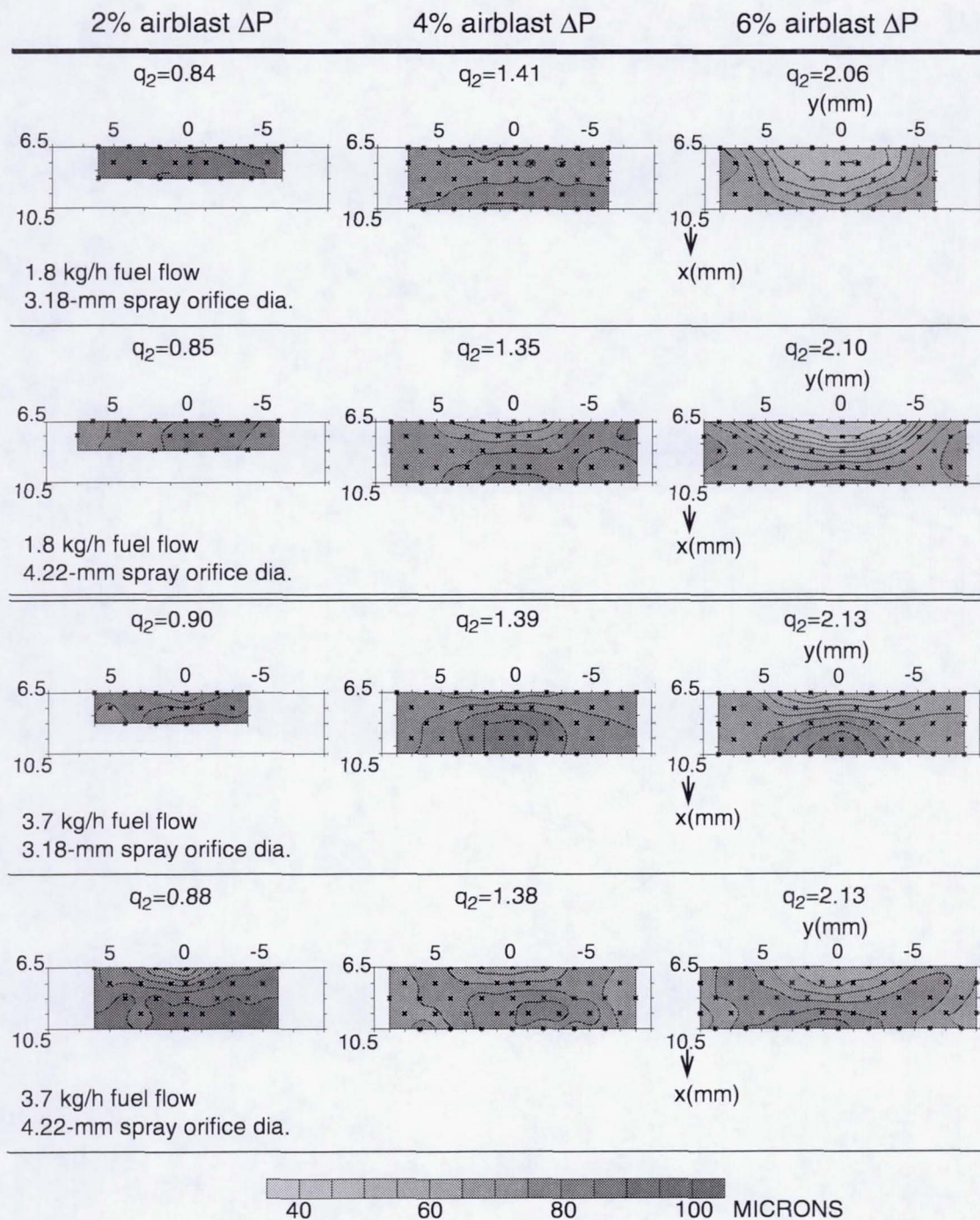


Fig. 10.10 Droplet D_{32} distributions at the $z=10$ mm plane for the twelve spray conditions at the 70 m/sec crossflow velocity case.

droplet D_{32} values that were measured across the y- and z-axes ranged from 43 μm to 162 μm . In the crossflow case shown in Fig. 10.10, the D_{32} across the planar cross-section of the spray varied between 36 μm and 100 μm . The lower range of D_{32} measured for the crossflow case suggests additional droplet breakup caused by the crossflow. In Eq. 2.5, the critical relative velocity, $U_{R,critical}$, at which a drop of diameter d_0 is induced to break up, is given by

$$U_{R,critical} = \sqrt{\frac{8\sigma}{C_D \rho_A d_0}} \quad (2.5)$$

where the drag coefficient C_D for a rigid sphere is used. For the flow conditions in the experiment, the calculated Reynolds numbers for the droplets are between 1 and 1000, a range for which the following empirically derived relationship for a rigid sphere (Wallis, 1969) applied:

$$C_D = \frac{24}{Re_d} (1 + 0.15 \cdot Re_d^{0.687}) \quad (10.1)$$

For a droplet diameter of 160 μm , which is the maximum D_{32} measured in the non-crossflow experiment, $U_{R,critical}=36$ m/sec, which suggests that the crossflow (which has a velocity of 70 m/sec) does induce a secondary breakup of large droplets in the spray. However, the presence of the 100 μm drops (with a calculated $U_{R,critical}=45$ m/sec) appears to contradict the suggested occurrence of secondary breakup. The survival of a 100 μm drop in the 70 m/sec crossflow velocity could possibly occur if the crossflow velocity decelerates to a value that is less than the

$U_{R,critical}$ of 45 m/sec. If the 100 μm drops reside within the jet structure, the drops could also avoid secondary breakup processes, as they would be sheltered from the dynamic force of the crossflow.

The contours from the D_{32} distributions obtained from PDI measurements in Fig. 10.10 are compared to the distribution of the planar D_{32} images in Fig. 10.9 to validate the derived planar D_{32} images. Because of limitations in the ability of the PDI setup to capture data along the injection panel and the far wall, the grid could only encompass a region that extended between $x=6.5$ mm and 10.5 mm. The PDI-based D_{32} contour plots thus represent approximately one-half of the field of view presented in the planar D_{32} images. The larger flow field obtained by the planar imaging technique illustrates the benefit of using this diagnostic to characterize the spray.

If a case by case comparison is made between the $x=6.5$ mm to $x=10.5$ mm subset of the planar D_{32} images in Fig. 10.9 and the D_{32} contour plots in Fig. 10.10, the distributions agree very well in the trend of magnitudes as well as in the shape of the contours. Distinct examples of the agreement in the contours can be seen in the 1.8 kg/h, 6% airblast ΔP cases and in the 3.7 kg/h, 4% airblast ΔP cases.

Summary of the Trends Observed in the Parametric Variation Tests

Table 10.2 summarizes the trends that were observed in the characterization of the sprays before and after exposure to a crossflow of air. The main parameters that were varied included the airblast pressure drop, the fuel flow rate, and the spray orifice diameter, and are shown in the first column of the table. The second and third columns classify the trends in the spray uniformity, coverage, and degree of atomization that

were observed for the non-crossflow and crossflow cases. In general, the characterized sprays in the absence of and in the presence of the crossflow follow similar trends, with the exception of the effect of the airblast ΔP on affecting spray coverage in both systems.

Table 10.2 Summary of the effects of varying the spray injection parameters on the liquid distributions before and after introducing the crossflow of air.

Injection parameter	Spray without Crossflow (Chapter 8 Results)	Spray with Crossflow
increase in airblast ΔP (increases relative velocity)	<ul style="list-style-type: none"> • increased uniformity about a lower mean • decreased spray coverage • increased atomization 	<ul style="list-style-type: none"> • increased uniformity about a lower mean • increased spray coverage • increased atomization
increase in fuel flow rate (decreases relative velocity to delay onset of breakup mechanisms)	<ul style="list-style-type: none"> • decreased uniformity • decreased spray coverage • decreased atomization 	<ul style="list-style-type: none"> • decreased uniformity • decreased spray coverage • decreased atomization
increase in spray orifice diameter (increases airblast to liquid ALR , increases exit orifice area)	<ul style="list-style-type: none"> • increased uniformity about a lower mean • increased spray coverage • increased atomization 	<ul style="list-style-type: none"> • increased uniformity about a lower mean • comparable and/or slight increase in spray coverage; flattened cross-section • increased atomization

The crossflow velocity appears to induce secondary atomization in the injected spray droplets, as seen in the calculation of the critical relative velocity. However, the crossflow also most likely affects the dispersion of the spray, as observed from the kidney-shaped cross-sections generated in the highly-atomized sprays which are reminiscent of gaseous jet in crossflow mixing, and from the flattened cross-sections of the 4.22 mm-dia. cases. Despite the roles that the crossflow plays in atomizing and dispersing the spray, the similarities in trends observed and summarized in Table 10.2 suggest that the formation of the airblast spray prior to its injection into the crossflow plays a dominant role in affecting spray dispersion.

As a final note, because the trends observed in the 1.8 kg/h and 3.7 kg/h fuel flow cases are similar, the presentation of the rest of the results will focus primarily on the higher flow rate case. For reference, results from the 1.8 kg/h set of cases that correspond to Sections 10.3.1b and 10.7.3 are presented in Appendix C.

10.3.1b Downstream Evolution of the Liquid Distributions

Figures 10.11 and 10.12 present the images of the spray cross-sections at three different axial locations for the 3.7 kg/h fuel flow cases. The sprays formed by the 3.18 mm-dia. case are shown in Fig. 10.11 while the 4.22 mm-dia. results are shown in Fig. 10.12. In each figure, the 2%, 4%, and 6% airblast pressure drop cases are grouped in columns, with each row corresponding to cross-sections at the $z=10$ mm, 20 mm, and 30 mm planes. The $z=10$ mm images for each case are reproduced from the set of images first presented in Fig. 10.8.

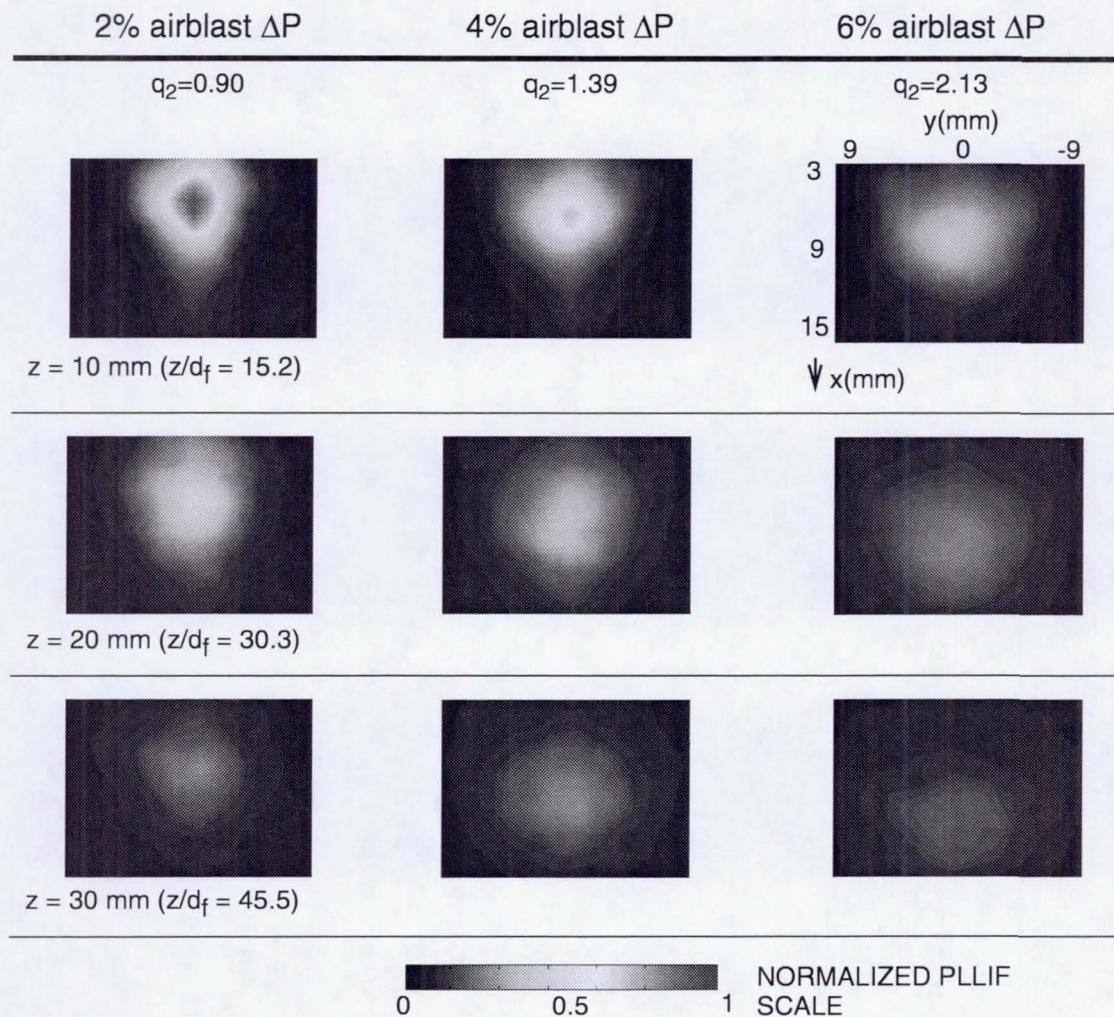


Fig. 10.11 Evolution of the liquid concentration distributions for the 3.7 kg/h fuel flow, 3.18-mm spray orifice diameter case at a crossflow velocity of 70 m/sec.

In comparing the distributions in the different z -planes for the 2% airblast ΔP condition in Fig. 10.11, two observations can be made. The liquid mass disperses across the field of view, and the penetration of the spray increases as the distance from the point of injection increases. The increased dispersion in liquid mass is inferred

from the increasingly lower intensity levels in the cross-section, as well as from the increased spread of the spray across the plane.

At the 4% and 6% ΔP conditions in Fig. 10.11, similar trends are observed in the spread and in the increasingly diffuse distribution of the spray with downstream distance. The images at the $z=20$ mm and 30 mm planes also show the same trends that were noted in the comparison of $z=10$ mm planar images in Fig. 10.8. These observations, resulting from the effect of increasing the airblast flow, included an increased uniformity of the spray at a lower mean magnitude, and an increased spray area coverage. These observations also hold true for the 4.22 mm-dia. spray orifice case in Fig. 10.12. Other than the decrease in magnitude and the increase in the spray coverage, the images generally show similar shapes and distributions of the liquid spray after the $z=10$ mm plane, so any comparison made of these parameters between the cases should hold true downstream of this plane.

From the images of the downstream planes, the penetration of the spray into the crossflow can be observed. In the cross-sectional images, the penetration of the inner boundary of the spray, which is nearest the injector wall, is obtained by tracking the edge of the spray toward the top of the image, which corresponds to $x=2.4$ mm. The outer spray boundary, which denotes the farthest extent of the spray into the crossflow, occurs toward the bottom of each image, which corresponds to a distance that is $x=15.6$ mm from the injection panel.

The effect of changing the orifice size does not affect the penetration of the outer spray surfaces, but does affect the lower surface penetration. As seen in both Figs. 10.11 and 10.12, the outer spray surface location at the corresponding planes for

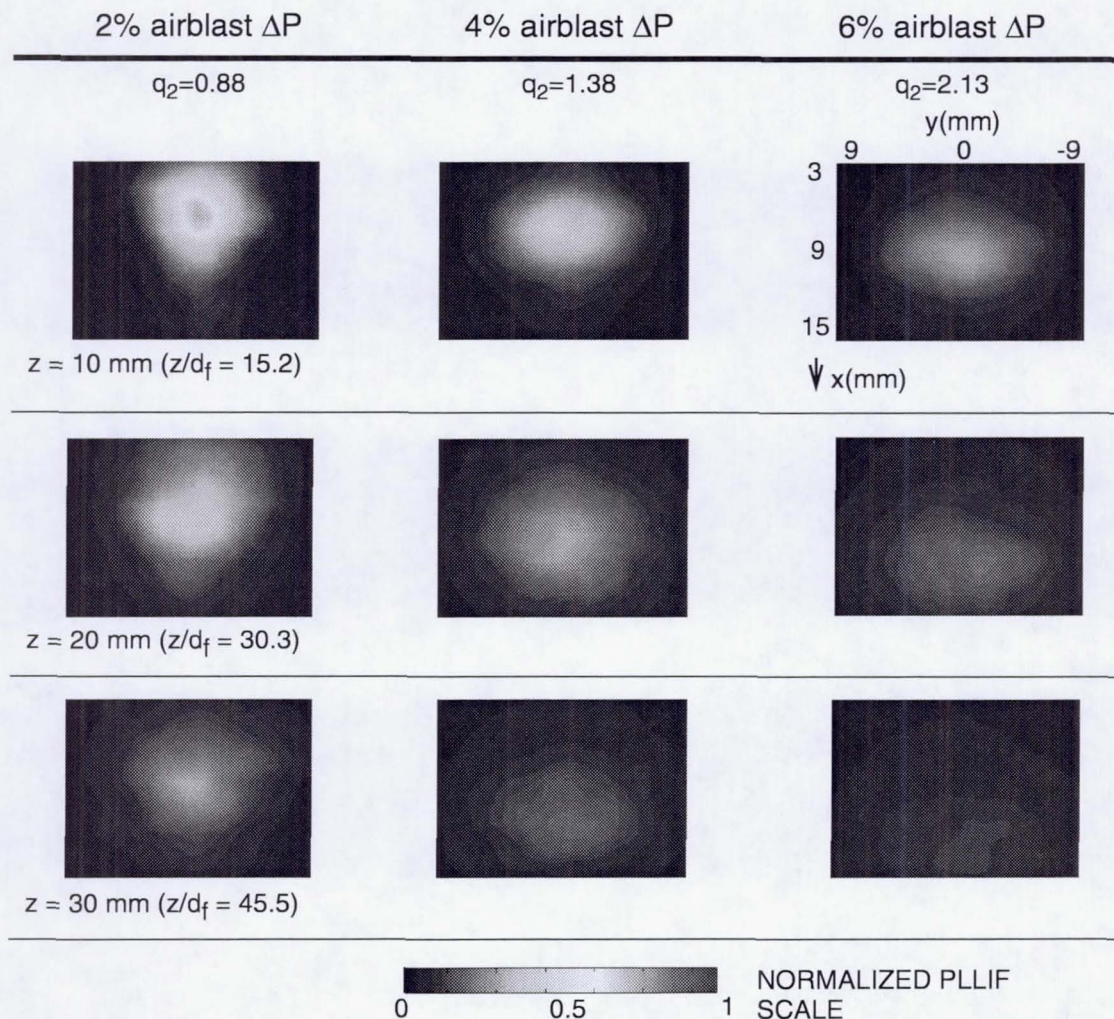


Fig. 10.12 Evolution of the liquid concentration distributions for the 3.7 kg/h fuel flow, 4.22-mm spray orifice diameter case at a crossflow velocity of 70 m/sec.

each airblast ΔP condition is nearly the same. The edge of the inner spray surface, however, consistently increases in distance away from the wall. Because the atomizing air velocity is constant at a set pressure drop for the two different orifice sizes, the mean velocity that propels the drops into the crossflow should be the same. From the

planar D_{32} distributions presented in Fig. 10.9, the sprays produced by the 4.22 mm-dia. orifice have lower D_{32} distributions than do the 3.18 mm-dia. cases. Larger drops would have a higher momentum than smaller drops traveling at the same velocity because of the difference in mass. Based on this information, the sprays produced with the 3.18 mm-dia. orifice, which have a higher D_{32} than the 4.22 mm-dia. sprays, should penetrate farther into the crossflow. However, the images show the opposite occurring—the better-atomized sprays from the 4.22 mm-dia. orifice have an inner surface boundary that penetrates farther than the 3.18 mm-dia. sprays. The initial droplet size and velocity distributions—rather than the mean values—need to be considered in explaining the results.

An increase in the airblast ΔP causes the spray to penetrate farther into the crossflow. The inner spray boundary in the 2% ΔP case for both orifice diameter cases barely lifts off from the injection wall, while the outer spray boundary also hardly changes with respect to the $z=10$ mm plane. As the airblast ΔP increases to 4% and 6%, the penetration of the outer spray surface increases noticeably. While the outer spray boundaries for the 4% and 6% cases appear to be comparable, there is a difference in the penetration of the inner spray surface between both airblast ΔP cases. The penetration of the inner spray boundary in the 4% ΔP condition increases with distance, but does not penetrate as far as the inner spray surface for the 6% ΔP case. The difference in the orifice size does not affect the airblast ΔP trend with respect to the spray surface penetration.

The dispersion of the liquid into the crossflow can be affected by secondary breakup processes which transfer more liquid mass across a larger area. Alternatively,

or perhaps in conjunction with the secondary atomization process, the entrainment of crossflow air by the spray jet increases the cross-sectional area of the jet, which spreads the drops.

10.3.2 Effect of the Crossflow Velocity Magnitude

The magnitude of the crossflow velocity was varied in order to determine its effect on the penetration and dispersion of the spray. Four conditions from the baseline of twelve injection conditions were selected for the crossflow variation tests. The four conditions, all at a fuel flow rate of 3.7 kg/h, resulted from combinations of the two airblast ΔP conditions of 4% and 6%, and the two spray orifice diameters of 3.18 mm and 4.22 mm. The sprays were subjected to crossflow velocities of 78 m/sec and 87 m/sec, to yield a total of ($2*2*2=8$) eight additional conditions.

To compare the effect of the crossflow velocity on the distribution of the liquid into the crossflow, images of the liquid volume concentration and of the planar D_{32} distribution are compared. The set of images for Fig. 10.13 represents the sprays injected into the baseline crossflow velocity of 70 m/sec. These images were previously presented in Figs. 10.8 and 10.9, and are compiled in Fig. 10.13 to serve as a basis for comparison with the other crossflow conditions. The main observations that were noted within the set of 70 m/sec cases were the effect of the airblast ΔP and the size of the spray orifice diameter on the dispersion of the droplets within the crossflow. When the airblast ΔP was increased, the atomization of the spray increased, as noted by the overall lower D_{32} ranges. The increase in airblast ΔP also caused the outer surface of the spray as well as its peak mass concentration to penetrate farther into the

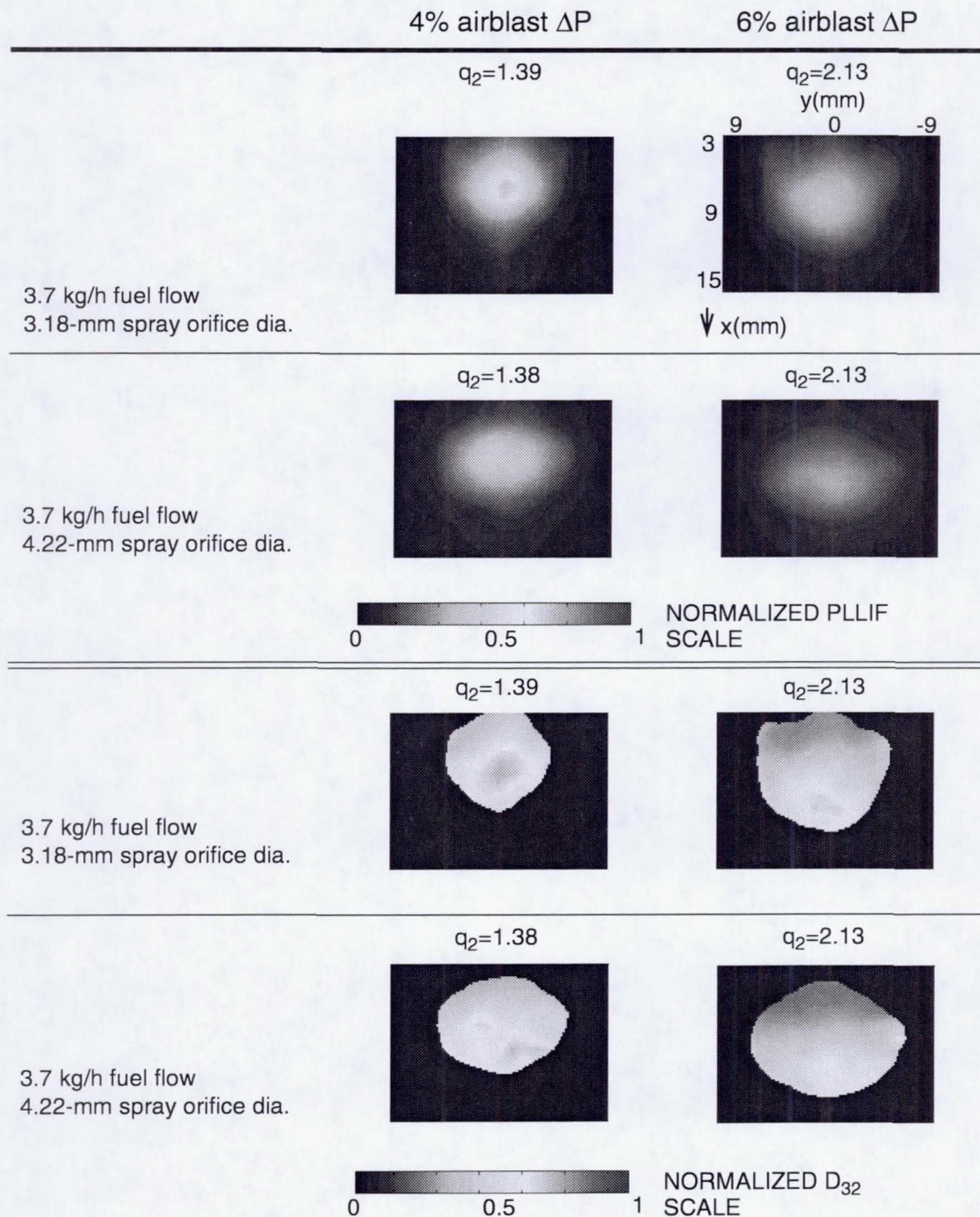


Fig. 10.13 Liquid concentration and planar D_{32} distributions at the $z=10$ mm plane for the 3.7 kg/h fuel flow, 4% and 6% airblast ΔP sprays injected into a crossflow at 70 m/sec.

crossflow. On the other hand, an increase in the spray orifice diameter mainly increased the penetration of the inner surface of the spray and enhanced spray dispersion along the width-wise y -direction, but did not greatly decrease the D_{32} levels. The net result of increasing the spray orifice diameter was to produce a spray with a more flattened spray cross-section. Within each airblast ΔP group, the penetration of the outer surface of the sprays is comparable, and correlates well with the similar q_2 values.

The trends produced by increasing the airblast ΔP and spray orifice diameter also hold at the higher crossflow velocities of 78 m/sec (see Fig. 10.14) and 87 m/sec (see Fig. 10.15). The liquid distributions become more diffuse for a higher airblast ΔP as well as for an increased spray orifice diameter. The penetration of the sprays increases with increasing airblast ΔP . Larger droplets penetrate farthest into the crossflow, with the regions of large D_{32} showing no correlation to the peak mass concentration.

To determine the main effect of increasing the crossflow velocity, the images in Figs. 10.14 and 10.15 are compared to the baseline 70 m/sec case in Fig. 10.13. Overall, the distributions of each corresponding spray injection condition, in terms of its magnitude and shape, are preserved, but the size of the cross-sections is reduced as the crossflow velocity is increased. Spray penetration also decreases with increasing crossflow velocity.

The only apparent anomaly in the trends produced by increasing the crossflow velocity arises from a comparison of the normalized D_{32} distributions. An increase in the crossflow velocity is more likely to induce a higher degree of secondary

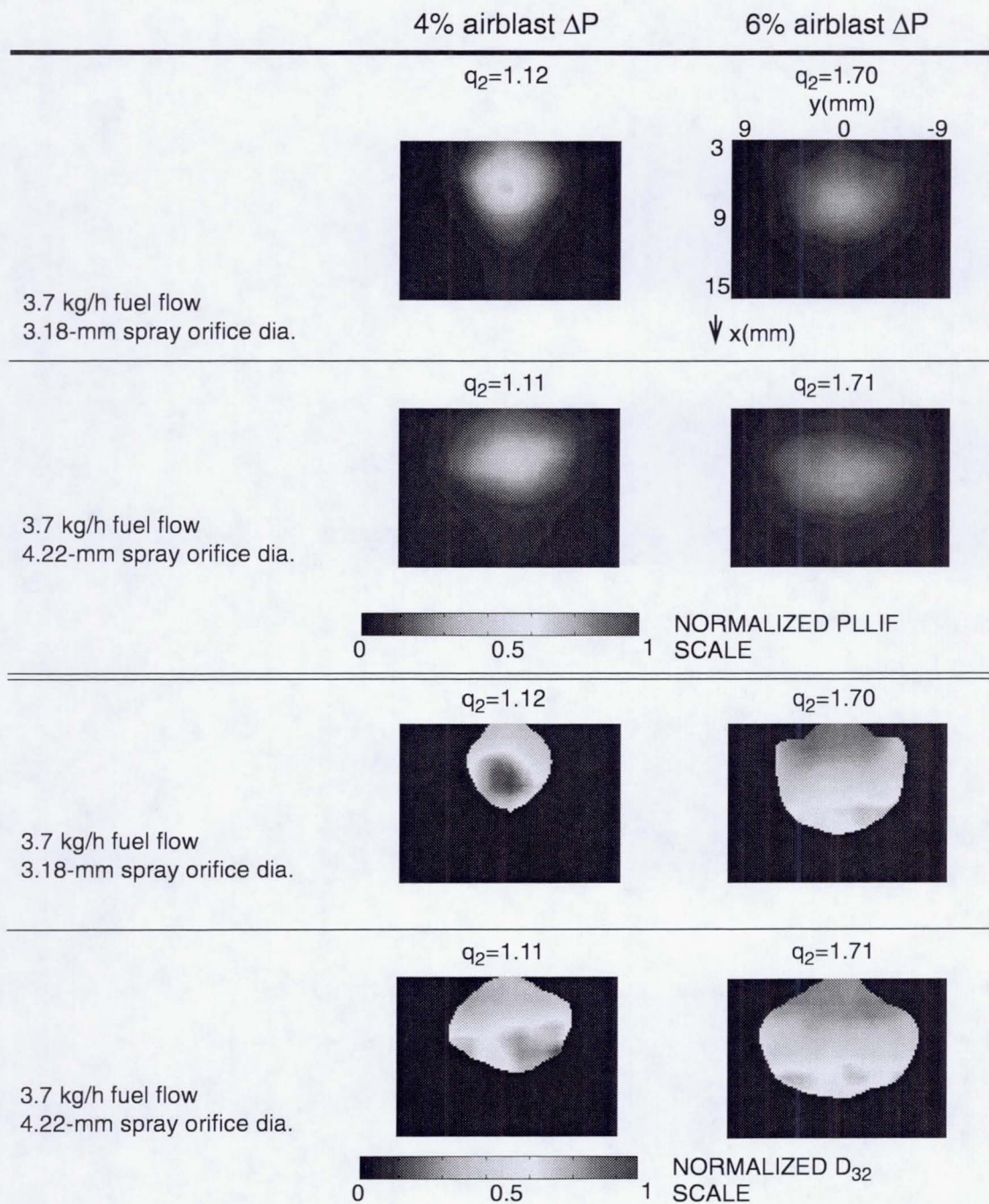


Fig. 10.14 Liquid concentration and planar D_{32} distributions at the $z=10$ mm plane for the 3.7 kg/h fuel flow, 4% and 6% airblast ΔP sprays injected into a crossflow at 78 m/sec.

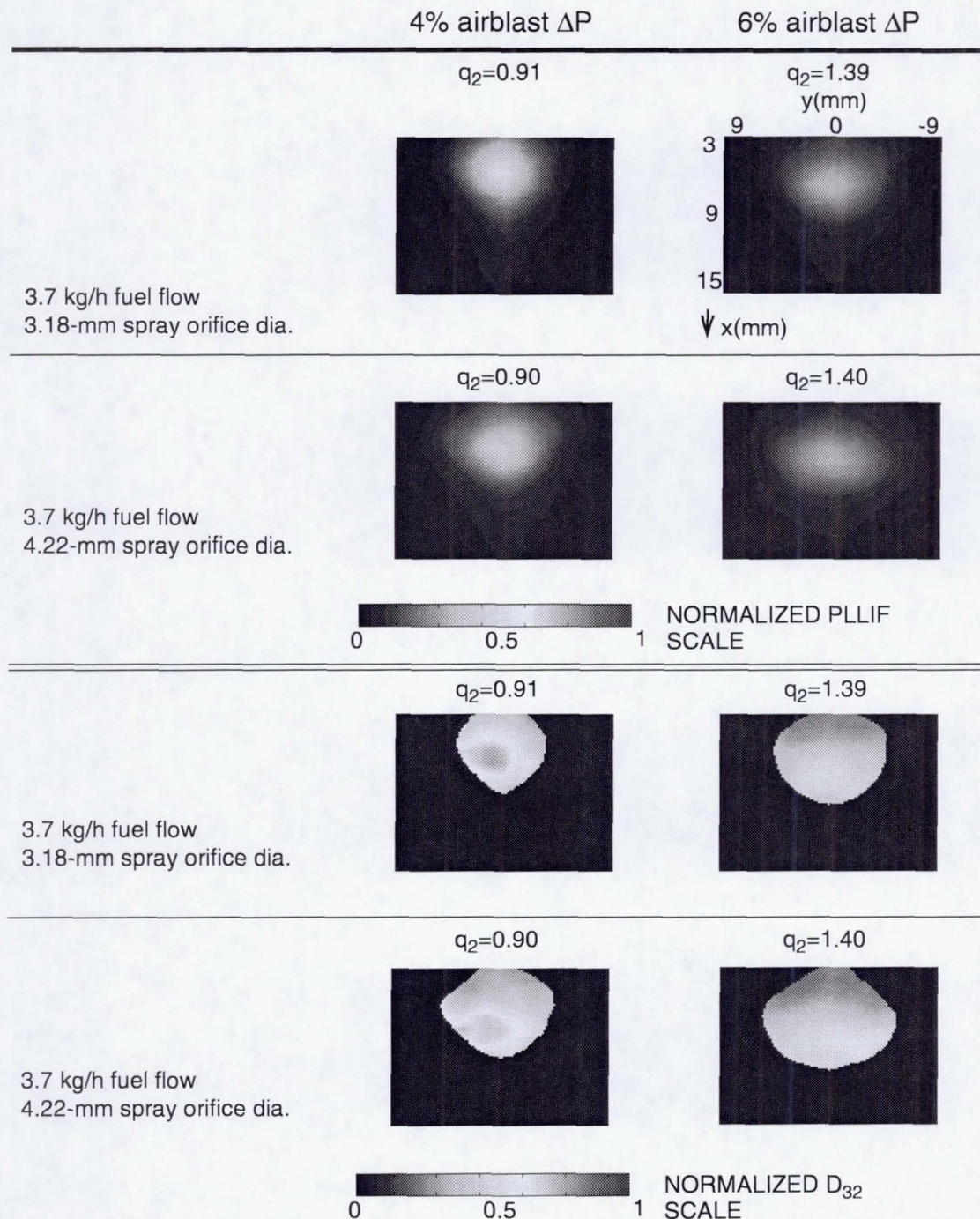


Fig. 10.15 Liquid concentration and planar D_{32} distributions at the $z=10$ mm plane for the 3.7 kg/h fuel flow, 4% and 6% airblast ΔP sprays injected into a crossflow at 87 m/sec.

atomization, which would thus produce a steady decrease in the D_{32} levels. However, it is observed that the D_{32} levels in the images of the baseline 70 m/sec case (see Fig. 10.13) are lower than the D_{32} magnitudes in the sprays subjected to the crossflow velocity of 78 m/sec (see Fig. 10.14). This trend may be attributed to the change in calibration fluid during the course of the experiment. While all of the PLLIF studies were conducted using the calibration fluid MIL-C-7024D, the calibration fluid supply was switched to MIL-PRF-7024E for the Mie scattering tests that were conducted at the higher crossflow velocity conditions of 78 m/sec and 87 m/sec. The planar D_{32} images are derived from the Mie scattering images as well as the PLLIF images. The change from MIL-C-7024D to MIL-PRF-7024E should ideally form sprays of similar quality because of the similarities in their physical properties, as discussed in Section 4.4.1. However, any slight difference in the physical properties could have affected the Mie scattering result, which in turn, would affect the D_{32} magnitudes.

10.4 Planar D_{32} Correlation and Comparison

In Section 10.3, the planar D_{32} images at the $z=10$ mm plane in Fig. 10.9 qualitatively agreed with the corresponding point-based PDI measurements of D_{32} presented in Fig. 10.10. To make the planar D_{32} results more meaningful, the intensity ratios were correlated to the PDI measurements, following the procedure of Section 8.3. The result of this correlation is presented in Fig. 10.16. Not all of the points that were measured by the PDI instrument could be correlated. In particular, the points near the edge of the spray were not sufficiently captured by the UV planar

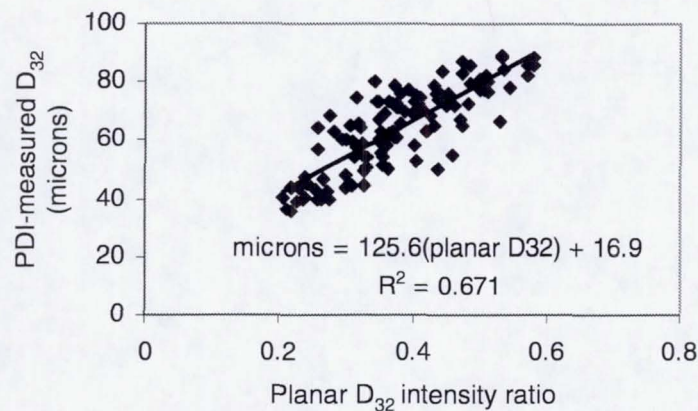


Fig. 10.16 Correlation between the planar mean D_{32} intensity ratio and the corresponding point-based PDI measurement for the airblast spray injected into a crossflow of 70 m/sec.

imaging technique. The PDI diagnostic, on the other hand, is able to capture these edge points because of the longer time period that is afforded to this measurement technique.

The result of the correlation of the PDI data to the planar D_{32} intensity ratios produced a slope of 125.6 and a linear offset of 16.9. This correlation was applied to the plane-averaged D_{32} values that were obtained for the image planes between $z=8$ mm and 30 mm. The results are presented in Fig. 10.17 for the 1.8 kg/h fuel flow case, and in Fig. 10.18 for the 3.7 kg/h fuel flow case.

For both fuel flow cases, the increase in the spray orifice diameter produces less of an effect on spray atomization than does the increase in the airblast pressure drop, which was explained by the analysis performed in Section 8.2.1b. The average D_{32} approaches an asymptotic limit in both fuel flow cases, starting from the downstream plane of $z=20$ mm. Interestingly, the values do not differ greatly between the 1.8 kg/h

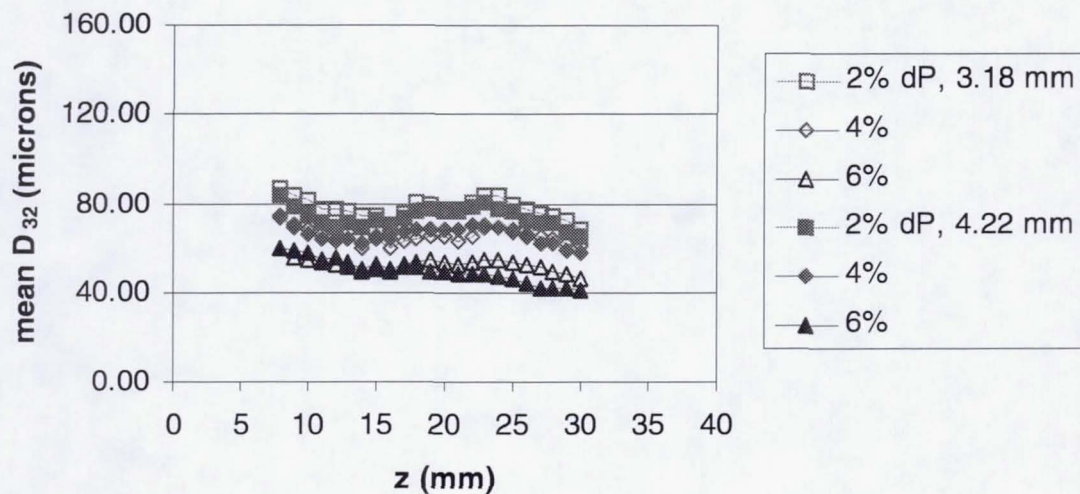


Fig. 10.17 Comparison of the planar mean D_{32} for the different cases at various downstream z -positions for the 1.8 kg/h case.

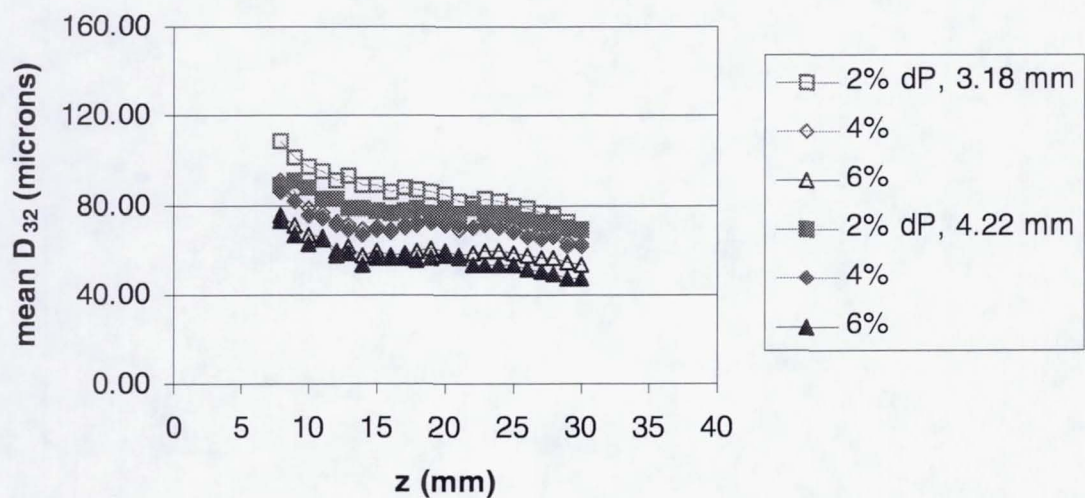


Fig. 10.18 Comparison of the planar mean D_{32} for the different cases at various downstream z -positions for the 3.7 kg/h case.

and the 3.7 kg/h fuel flow cases beyond this plane. Prior to the $z=20$ mm plane, the crossflow velocity appears to contribute to the secondary atomization of the spray, especially in the higher fuel flow case in which a larger decrease in the plane-averaged D_{32} occurs. Further evidence suggesting secondary atomization can be seen in a comparison of the plane-averaged D_{32} for the crossflow cases in Figs. 10.17 and 10.18 and the corresponding non-crossflow cases presented in Figs. 8.14 and 8.15. The range of planar D_{32} values vary between 60 and 140 μm in the non-crossflow case, and decreases to a range of values between 40 and 110 μm in the crossflow case.

In the non-crossflow spray case, a correlation for the plane-averaged D_{32} normalized by the characteristic length of the fuel orifice diameter d_f was obtained. The correlation obtained in Eq. 8.3 was a function of the non-dimensional flow parameters Re_L , We_{airbl} , and Re_{airbl} , and the downstream distance normalized by d_f . With the introduction of the crossflow, the effect of its velocity on spray quality needs to be accounted for. Because the crossflow velocity is suggested to induce secondary atomization, the Weber number of the crossflow, We_{cross} , is included in the correlation.

To determine the applicability of the correlation from the non-crossflow case to the crossflow case, the following equation was fitted using the nonlinear multivariate regression outlined in Appendix B:

$$\frac{D_{32, avg}}{d_f} = c_0 \cdot Re_L^{c_1} \cdot We_{airbl}^{c_2} \cdot Re_{airbl}^{c_3} \cdot \left(\frac{z}{d_f} \right)^{c_4} \quad (10.2)$$

Equation 10.2 is essentially the same equation as that used in the non-crossflow correlation of Eq. 8.3, except that the downstream distance is now along the z -axis.

The results from the regression are listed in the middle row of values in Table 10.3 while for comparative purposes, the coefficients for Eq. 8.3 for the spray without crossflow are listed in the top row. Given that the only variable that changes in the Reynolds and Weber numbers is the fuel and airblast air velocity, the coefficients for correlation Eq. 10.2 follow the expected trends of producing a positive exponent for Re_L and negative exponents for We_{airbl} and Re_{airbl} . Hence, an increase in Re_L due to an increase in fuel velocity leads to a decreased atomization quality (i.e., higher D_{32}) while an increase in We_{airbl} and Re_{airbl} resulting from an increased airblast air velocity increases the atomization quality (i.e., lower D_{32}). The negative exponent for z/d_f reflects the decrease in D_{32} that is postulated to result from secondary atomization by the crossflow.

In comparing the power coefficients of Eq. 10.2 to those obtained from the non-crossflow case for Eq. 8.3, it can be seen that the signs of the exponents are the same. With respect to the magnitude of the exponents, the power coefficient of Re_{airbl} reflects a weaker dependence in the crossflow case than in the non-crossflow case while the exponent for the downstream distance shows a stronger dependence of D_{32} on this variable in the crossflow case. Although the latter observation may be attributed to the effect of the crossflow in inducing secondary atomization, the reason for the decreased dependency of Re_{airbl} after the addition of the crossflow is unclear.

The effect of adding a crossflow-related factor to the correlation can be determined by solving for the coefficients of the following correlating equation:

$$\frac{D_{32, avg}}{d_f} = c_0 \cdot Re_L^{c_1} \cdot We_{airbl}^{c_2} \cdot Re_{airbl}^{c_3} \cdot \left(\frac{z}{d_f} \right)^{c_4} \cdot We_{cross}^{c_5} \quad (10.3)$$

where the fuel hole diameter represents the characteristic diameter in We_{cross} . The solved coefficients for Eq. 10.3, which are listed in the bottom row of Table 10.3, are similar in magnitude and sign to the values obtained for the “basic” Eq. 10.2. The exponent of 0.0881 for the additional We_{cross} factor is positive, yet low in magnitude. The positive sign of the exponent for We_{cross} is contrary to the expectation that an increase in We_{cross} should lead to the occurrence of secondary atomization and a subsequent decrease in D_{32} . However, the low magnitude of the exponent suggests that We_{cross} does not play a great role in the correlation of D_{32} . This is evidenced in evaluating the correlation quality of both Eqs. 10.2 and 10.3. Fig. 10.19 shows plots that compare the predicted and measured $D_{32,avg}/d_f$ values. The left plot (Fig. 10.19a), which contains the results from the correlation of the “basic” Eq. 10.2, produces as comparable a fit to the data as does the correlation in Eq. 10.3, the results of which are shown in the right plot (Fig. 10.19b). The similar results produced by both correlations

Table 10.3 Curve fit coefficients for the plane-averaged D_{32} for the non-crossflow and crossflow cases.

Condition	Equation type	constant: c_0	power of Re_L : c_1	power of We_{airbl} : c_2	power of Re_{airbl} : c_3	power of (z/d_f) : c_4	power of We_{cross} : c_5
SPRAY W/OUT CROSS- FLOW	Basic (Eq. 8.3)	0.841	0.204	-0.258	-0.199	$[(x/d_f)=]$ -0.034	-
SPRAY WITH CROSS- FLOW	Basic (Eq. 10.2)	0.493	0.164	-0.316	-0.0778	-0.119	-
	Basic + We_{cross} (Eq. 10.3)	0.392	0.142	-0.326	-0.0777	-0.119	0.0881

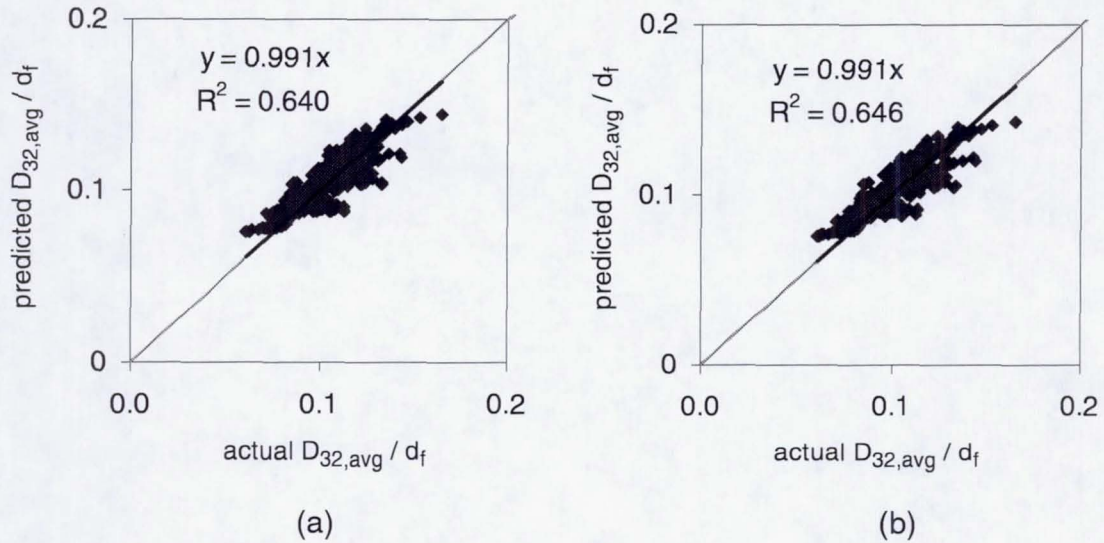


Fig. 10.19 Comparison between the predicted and actual values of plane-averaged D_{32} in a crossflow of 70 m/sec for (a) the basic correlating Eq. 10.2 and (b) the basic correlation with an additional We_{cross} factor (Eq. 10.3).

appear to suggest that the crossflow does not play a large role in determining the plane-averaged D_{32} . A more detailed characterization of the flow field using PDI measurements is required in order to define the role of the crossflow velocity in affecting spray atomization. PDI measurements of the crossflow velocity in the presence of the jet could identify any likelihood of secondary breakup occurring, while PDI measurements of the spray at different downstream planes could verify the observed decrease of the plane-averaged D_{32} with increasing distance.

10.5 Quantitative Assessment of the Spray Quality

The sprays produced in the non-crossflow tests were compared in terms of a “spray quality” parameter (Eq. 8.6) that was formulated in Chapter 8, Section 8.4. The

“spray quality” (SQ) parameter was defined by three qualities that were judged as important in spray mixing—the normalized average D_{32} , the extent of area (EA) covered by the spray, and the spatial unmixedness (U_s). The current formulation of SQ weights each of these parameters equally, and is repeated here for convenience:

$$SQ = [(1 - (D_{32, avg}/D_{32, max})) + EA + (1 - U_s)]/3 \quad (8.6)$$

In a well-atomized spray, the normalized mean D_{32} tends toward 0. To induce rapid mixing between the spray and the crossflow of air, the spray should cover as much area as possible, or have an EA tending toward 1. A well-mixed fuel-air mixture exhibiting uniform mixing with a low average concentration (e.g., across a large area) produces a U_s tending toward 0. A desired spray that is finely-atomized and distributed uniformly across a large area about a low average concentration results in an SQ that tends toward 1.

The SQ parameter does not directly account for the penetration of the spray jet into the crossflow. However, for under- and over-penetrating sprays, the spray coverage (represented by the EA parameter) and the spatial unmixedness U_s would be compromised, and thus would affect the final SQ value.

SQ values were computed at different downstream cross-sections in the spray for each spray condition, the results of which are presented in Figs. 10.20 through 10.24. In each figure, the SQ values for the 3.18 mm-dia. case are denoted by hollow markers, while the results associated with the 4.22 mm-dia. orifice are denoted by solid markers.

The SQ values for the 1.8 kg/h and 3.7 kg/h fuel flow conditions are presented

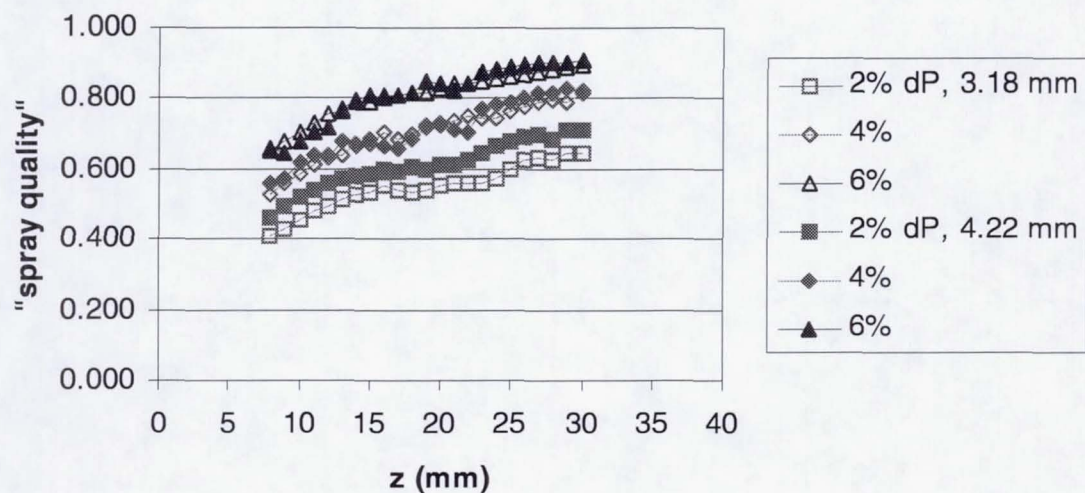


Fig. 10.20 Comparison of the spray quality in the horizontal planar sections of the spray at different downstream z -positions for the 1.8 kg/h case at 70 m/sec.

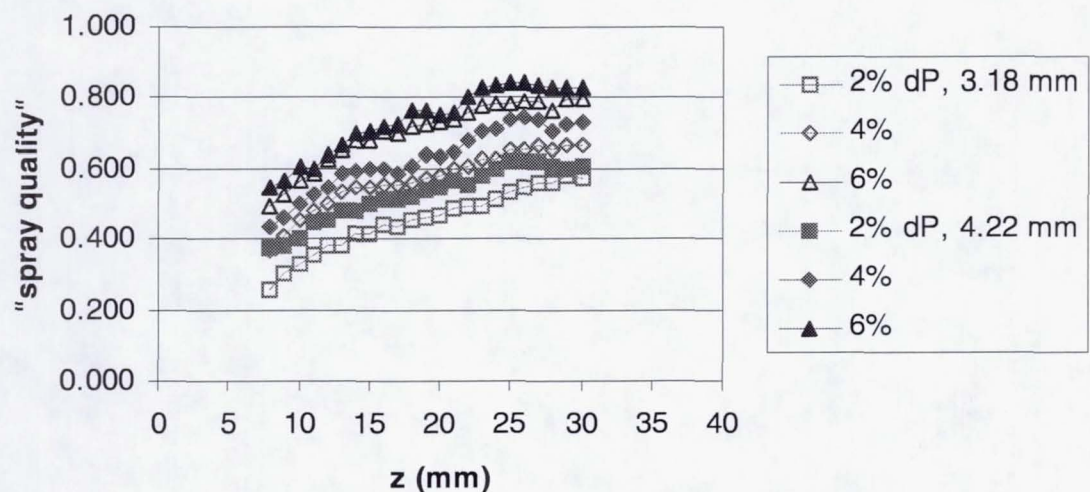


Fig. 10.21 Comparison of the spray quality in the horizontal planar sections of the spray at different downstream z -positions for the 3.7 kg/h case at 70 m/sec.

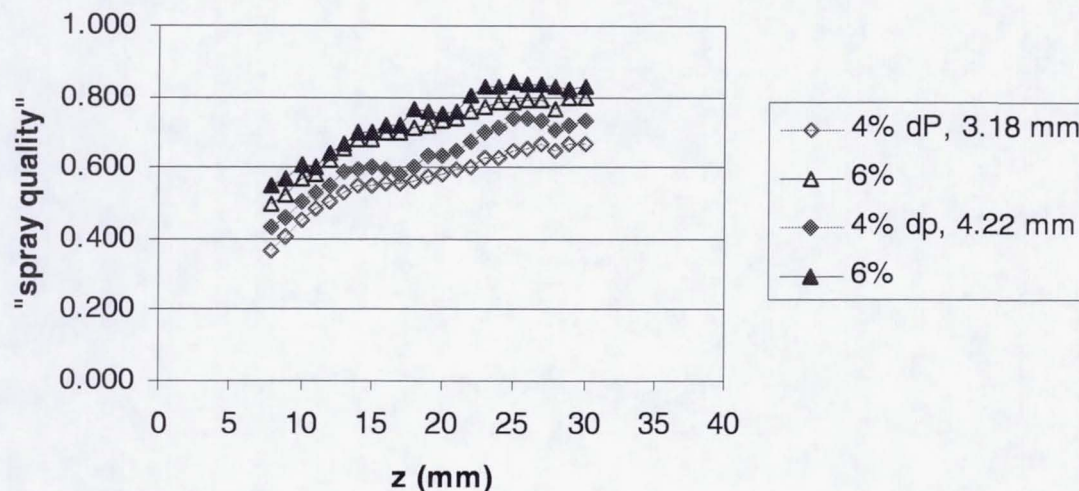


Fig. 10.22 Comparison of the spray quality in the horizontal planar sections of the spray at different downstream z positions for the 3.7 kg/h case at 70 m/sec.

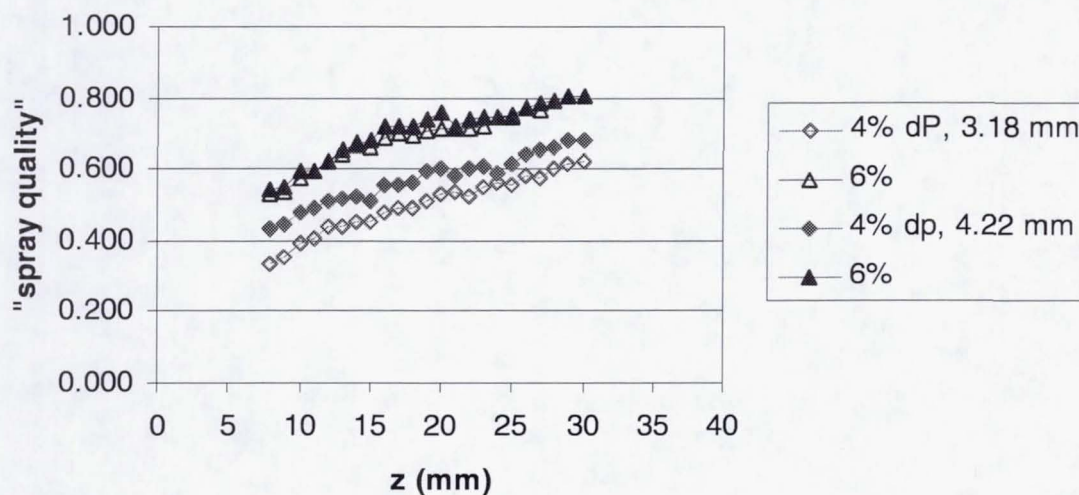


Fig. 10.23 Comparison of the spray quality in the horizontal planar sections of the spray at different downstream z -positions for the 3.7 kg/h case at 78 m/sec.

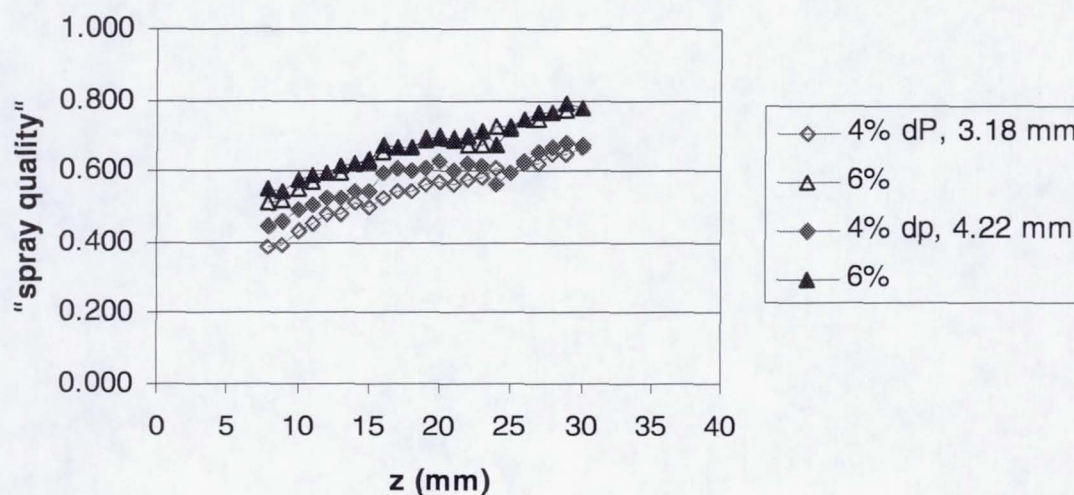


Fig. 10.24 Comparison of the spray quality in the horizontal planar sections of the spray at different downstream z -positions for the 3.7 kg/h case at 87 m/sec.

in Figs. 10.20 and 10.21, respectively. The graphs in both Figs. 10.20 and 10.21 show a clear trend in the effect of the airblast ΔP and the spray orifice diameter on SQ .

Increasing the airblast pressure drop consistently increased the SQ value of the spray.

An increase in the spray orifice diameter generally yielded higher SQ values. The trends in the SQ curves reiterate what has been observed repeatedly in the spray characterization results—that a more dispersed, well-mixed, and well-atomized spray is obtained by using a high airblast pressure drop and a larger spray orifice diameter.

For both fuel flow cases, the SQ values appear to approach an asymptotic limit near the $z=25$ mm plane.

The effect of the crossflow air velocity in affecting the SQ of the sprays was minimal. The SQ curves for the baseline 3.7 kg/h fuel flow, 70 m/sec crossflow

velocity at the 4% and 6% airblast ΔP conditions are replotted in Fig. 10.22. Sprays produced for the same injection conditions, but at a crossflow velocity of 78 m/sec and 87 m/sec, are depicted in Figs. 10.23 and 10.24, respectively. In comparing the SQ curves for the three crossflow velocities, no substantial difference in the ordering of the trendlines or in the magnitude of the spray quality parameter was observed. The crossflow velocity did not drastically affect the average spray characteristics that were examined.

10.6 Extent of the Atomizing Air in the Spray

In the non-crossflow spray results presented in Chapter 8, acetone PLIF was used to show the extent of the atomizing air within the spray. The atomizing air was observed to increase in its extent when the droplets were present, indicating a coupling between the atomizing air and liquid flows in the spray. The intent of this section is to determine whether the same phenomenon occurs for the spray jet in crossflow system by visualizing the atomizing air with the same procedure that was applied in the non-crossflow case.

Figure 10.25 presents a set of images that compares the cross-section of the jet at the $y=0$ mm plane, for the 3.7 kg/h fuel flow, 3.18 mm-dia. spray orifice cases. The images are organized by columns, according to the airblast ΔP . Each image is positioned between two lines which represent the walls of the test section. Injection occurs at $z=0$, from the left side of the images.

Each row contains a different test result in order to compare the distributions of each component of the spray. In the top row of images, a jet of air, flowing at the same

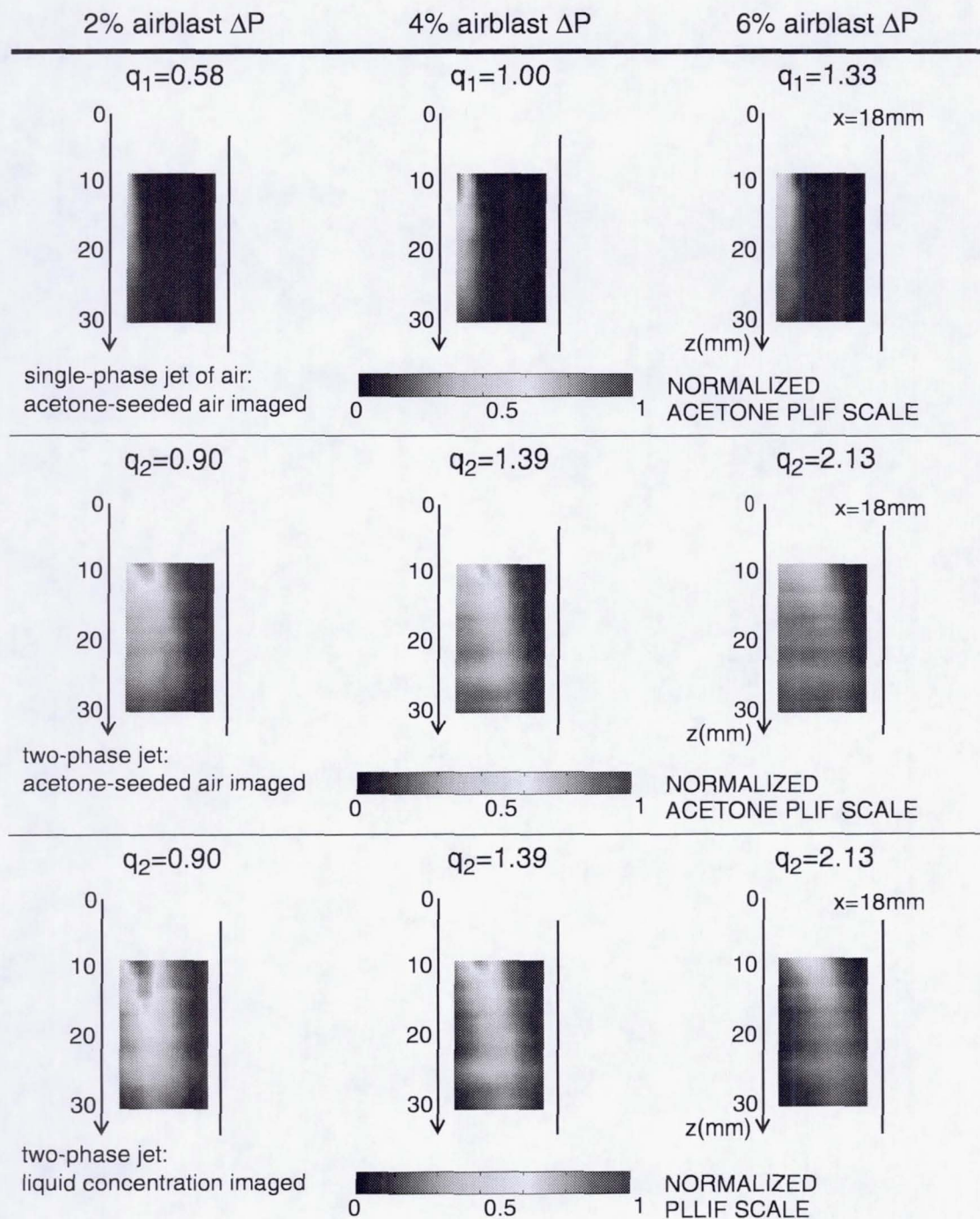


Fig. 10.25 Distributions of the atomizing air without and with the liquid phase (top and middle rows), at the $y=0$ mm centerplane for the 3.7 kg/h fuel flow, 3.18 mm-dia. orifice, 70 m/sec crossflow. For comparison, the liquid volume distribution is also presented (bottom row).

mass flow rate that was used to atomize the spray at the specified airblast ΔP condition, is captured using the acetone PLIF technique. The second row of images also present acetone PLIF results that show the atomizing air, but with the presence of the liquid in the spray. Although the same acetone PLIF technique was used in both cases, the images are represented by different normalized intensity scales. The higher overall intensities captured in the acetone PLIF images in the presence of the liquid, which are thought to occur because of the droplet scattering of acetone fluorescence, led to the representation of the images on different intensity scales. The third row of images, which contains the results of the PLLIF imaging technique, is used to compare the liquid concentration distribution with respect to the atomizing air in the spray.

The images of the single-phase jet of atomizing air (presented in the first row of images) show that an increase in airblast ΔP increases the penetration of the jet into the crossflow. However, in all of the images that were acquired, the pure air jet does not penetrate to the middle of the crossflow test section, and its inner edge is not visible in the images.

With the addition of the liquid flow (refer to the second row of images), the imaged atomizing air appears to increase in its extent. The atomizing air distribution begins near the injection wall, and is out of the range covered by PLIF imaging. The outer surface of the air component of the spray jet penetrates beyond the midpoint of the crossflow width.

The atomizing air within the spray jet appears to follow the distribution of the liquid component, as seen in the imaged liquid volume distributions (refer to the third row of images). As mentioned in Chapter 8, the scattering of fluorescence by the

droplets may be contributing to the increased intensity of the atomizing air within the spray. Thus, the high intensities measured within the acetone spray may be an artifact of the droplet scatter rather than of the atomizing air concentration. This is observed in the close correspondence in the regions of high intensities visualized in the atomizing air images in the second row, to similar regions in the liquid concentration images of the third row. However, since the primary objective of this section is to gauge the extent of the atomizing air within the spray, only the edges of the jet are of interest. At the edges of the jet, the concentration of droplets is not as high, and it is assumed that the effect of the droplet scatter of fluorescence is negligible in this region. This assumption is justified by comparing the inner edges of the jet near the wall in the acetone PLIF and calibration fluid PLLIF images, for the 4% and 6% airblast ΔP sprays. The acetone PLIF images of the atomizing air show the presence of acetone persisting to the left edge of each of the images in the second row. On the other hand, the boundary representing the inner edge of the liquid component of the spray can be seen in the PLLIF images.

The acetone fluorescence signal near the wall is probably not affected by the droplets because of the lower liquid fluorescence signals recorded in that region, and also because the larger droplets, which scatter more light, should penetrate farther into the crossflow. Hence, the acetone-laden spray images reveal that the atomizing air adheres toward the wall on the lee side of the jet, which suggests its entrainment into the crossflow.

The results for the 3.7 kg/h, 4.22 mm-dia. case, presented in Fig. 10.26, show similar trends. The single-phase jet of atomizing air did not penetrate as far into the

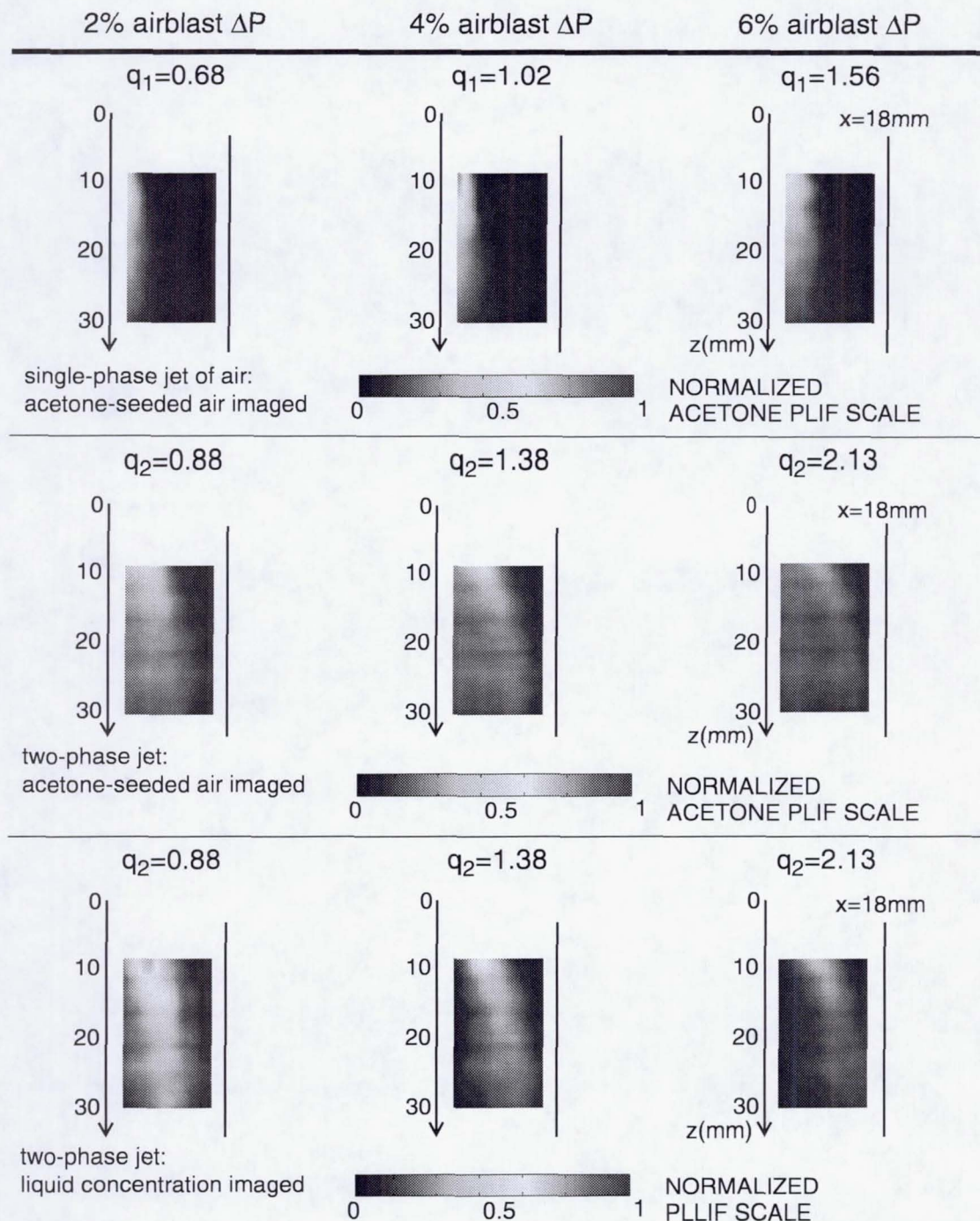


Fig. 10.26 Distributions of the atomizing air without and with the liquid phase (top and middle rows), at the $y=0$ mm centerplane for the 3.7 kg/h fuel flow, 4.22 mm-dia. orifice, 70 m/sec crossflow. For comparison, the liquid volume distribution is also presented (bottom row).

crossflow as did the air in the two-phase jet. Curiously, the single-phase jet of air also shows a higher concentration region in the 4% airblast ΔP condition (see top row). The high concentration region may be present near the wall in the 2% case, but could not be imaged, while in the 6% airblast ΔP case, the higher penetration of the jet may have lifted the jet away from the wall region to enhance entrainment of the crossflow air through the lee side of the jet.

10.7 Spray Dispersion into the Crossflow of Air

10.7.1 Droplet Trajectory Analysis

It has been observed that the droplet size and velocity distributions, rather than their mean values, should be considered in describing the dispersement of the spray. To aid in understanding how the spray disperses into the crossflow, an analysis which utilized the measured PDI data was performed. The droplet size and velocity distributions furnished the initial conditions to the equations of motion for a droplet which were subsequently solved to obtain the droplet trajectories in the crossflow.

In this analysis, droplet breakup was neglected because it was assumed that the airblast air induced most of the spray atomization. Droplet vaporization was also neglected in this non-preheated system, since the droplet residence time within the measured control volume attains a maximum time of 0.43 msec. The only forces acting on the droplets that were considered were the drag-related and the gravitational and buoyant forces. Though the gravitational and buoyant forces were left in the momentum equation, these forces did not have a large effect on the droplet motion, as it

was subsequently observed from the solutions. The present analysis did not consider jet entrainment of the crossflow or changes in the crossflow velocity flow field, but the results should indicate general trends and should also point to deficiencies that could be rectified in a more stringent analysis.

Based on the assumptions, the system of momentum equations in Eqs. 2.21 through 2.24 were applied. The relationship for the drag coefficient of a rigid sphere (see Eq. 10.1), which was used by Ghosh and Hunt (1998) in their spray jet in crossflow analysis, was used in the present calculations. The drag coefficient for a rigid sphere should produce sufficient results, as a study by Nguyen et al. (1991) had shown in producing comparable droplet trajectory results using various drag coefficient relationships.

The system of first order ODEs were solved with a fourth-order Runge-Kutta routine in MATLAB (see Appendix D for the associated MATLAB codes). The time step chosen was 10^{-6} sec, and the equations were integrated for a duration of 0.003 sec to ensure that all of the droplets traversed a downstream distance of 30 mm.

Although the analysis was applied to all of the spray conditions, only the results from the sprays produced at the 3.7 kg/h fuel flow rate, at the baseline crossflow velocity of 70 m/sec, are presented. The corresponding results for the 1.8 kg/h fuel flow rate are presented in Appendix C. The parametric variations of the airblast ΔP and of the spray orifice diameter had a far greater effect than the fuel flow or crossflow velocity on the dispersion and penetration of the spray jet into the crossflow.

10.7.2 Initial Conditions

The droplet size and velocity distributions obtained from the PDI measurements were utilized. The analysis is confined to the xz -plane at the $y=0$ centerplane. The PDI data from the non-crossflow condition, reported earlier in Chapter 7, contain the droplet size and velocity distributions at a distance of $x=10$ mm from the injection panel, at the $y=0$ mm spray centerline, and at various z -coordinates. This axis of data corresponds to the axis that traverses through the two concentrated lobes of liquid in the non-crossflow tests (see Fig. 10.7).

The raw time series data were classified according to their size. The average velocities and data rate (the number of drops measured per unit time) were computed for each size class, and at each $(x=10$ mm, $y=0$, z) coordinate. The mean diameter of the bin size and the mean transverse and axial velocities corresponding to the droplets in the bin were treated as initial conditions.

Fig. 10.27 presents the velocity vectors and D_{32} values measured in the non-crossflow experiment for the 3.7 kg/h fuel flow case. Although the data were obtained in the non-crossflow configuration, the graphs are rotated by 90° to correspond visually to the crossflow experiment. Each velocity vector and circle plot of D_{32} represents the values averaged across the entire sample measured at each point. The data were obtained across a range of z -values varying at most between -10 mm and +10 mm. The extent of the spray is inferred from the number of points at which data were acquired, and its extent generally increased when the larger orifice was used.

A core of peak velocity magnitudes centered about $z=0$ occurs in each condition. The magnitude of the peak velocities increase with increasing airblast ΔP .

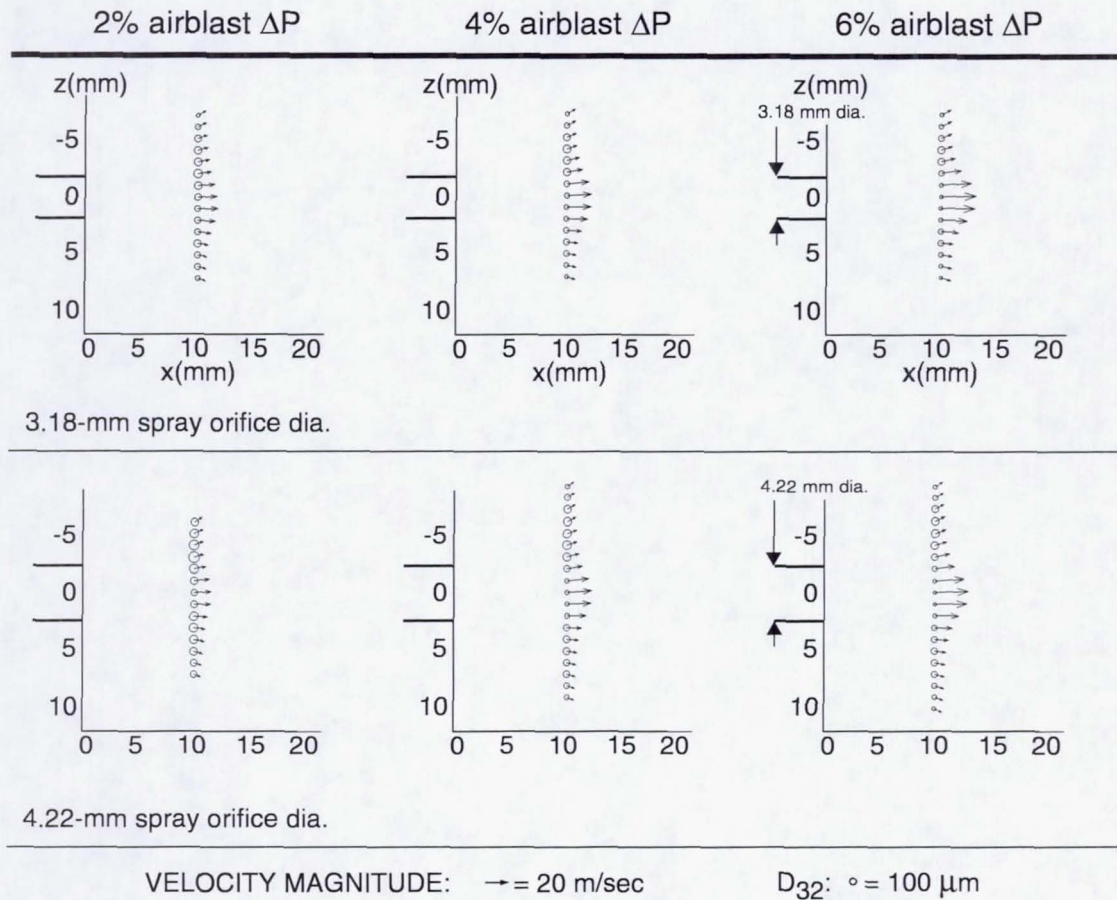


Fig. 10.27 Initial mean velocities and D_{32} obtained at the $y=0 \text{ mm}$ centerplane for the 3.7 kg/h fuel flow sprays before introducing the crossflow.

However, within each airblast ΔP group, the peak velocity decreases as the spray orifice diameter is enlarged. Note that the purpose in enlarging the spray orifice diameter was to increase the ALR parameter while maintaining the same relative velocities at the same airblast ΔP . The decrease in the mean droplet velocities with increasing orifice size suggests that more energy is expended in forming and dispersing the spray across a wider area rather than in propelling the droplets transversely into the crossflow.

The plots in Fig. 10.27 also show the mean droplet D_{32} distribution across the z -axis. The droplet size is proportional to the diameter of the circles, the relative size of which can be obtained from the legend at the bottom of the figure. The plots show that the center core of high velocity magnitudes corresponds to smaller droplet sizes. An increase in airblast ΔP generally decreased the D_{32} values in the spray, but an increase in the spray orifice diameter did not induce significantly lower D_{32} values.

To explore the relationship between the droplet size and correlating velocities, the plots in Fig. 10.27 are further divided to show the mean velocities for the different drop size classes. Figures 10.28 and 10.29 present the breakdown of mean velocities for the 3.18 mm-dia. and 4.22 mm-dia. spray orifice configurations, respectively. The plots in Figs. 10.28 and 10.29 are arranged by column, according to the airblast ΔP condition, and by row, according to the different size classes of 11-20 μm , 41-50 μm , and 76-90 μm .

Each plot contains a set of velocity vectors corresponding to the droplet size class for the particular condition. Superimposed on these vector plots are circles which represent the data rate of the spray. The legend located toward the bottom of the figures shows the size of the circle corresponding to the data rate of 5000 drops/sec. The data rate indicates the number of drops measured at the particular point in space for a unit of time.

In the results for the 3.18 mm-dia. spray orifice (see Fig. 10.28), the data rate is highest for the droplets in the 11-20 μm range, and decreases for larger droplet sizes, which implies that most of the droplets in the spray are comprised of smaller droplets. The data rate of the smaller droplets also increase as the airblast ΔP increases,

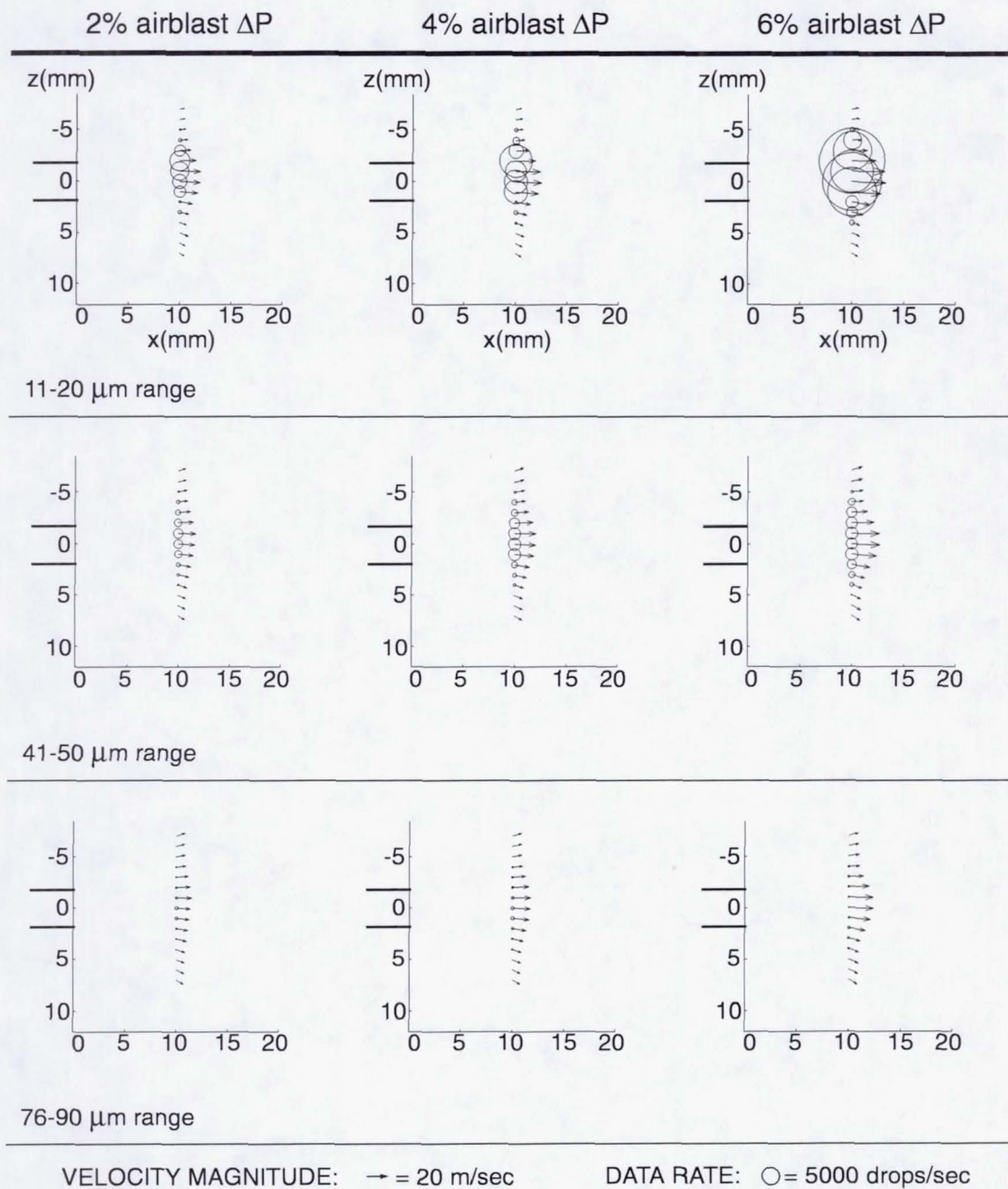


Fig. 10.28 Initial velocities and data rates obtained at the $y=0$ mm centerplane for the 3.7 kg/h fuel flow, 3.18 mm-dia. spray orifice case without crossflow.

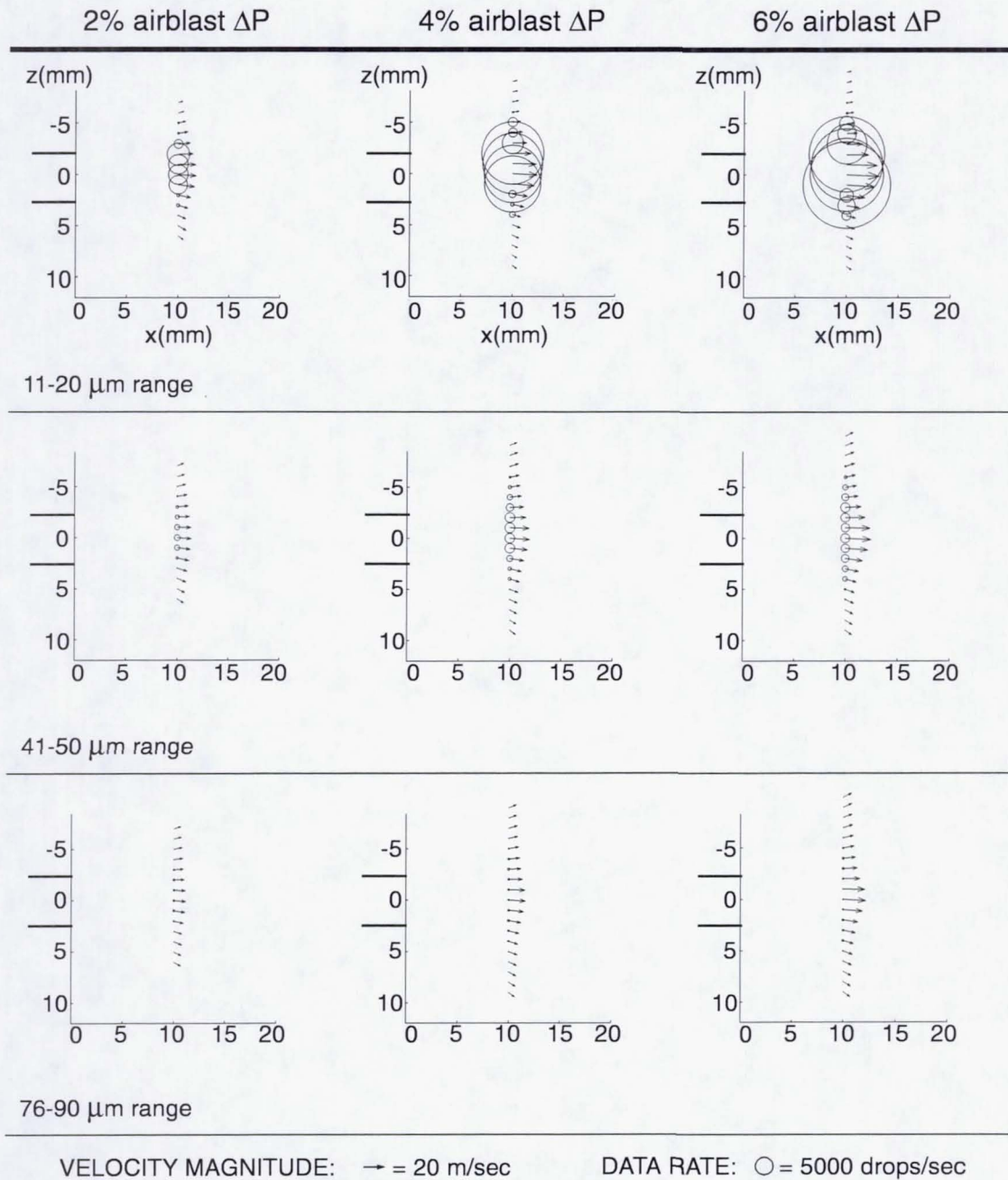


Fig. 10.29 Initial velocities and data rates obtained at the $y=0$ mm centerplane for the 3.7 kg/h fuel flow, 4.22 mm-dia. spray orifice case without crossflow.

particularly in the small droplet diameter ranges. The plots also show a correspondence between the droplet size range and the velocity magnitudes. Smaller droplets correspond to higher velocities, and larger droplets correspond to lower velocities. The same trends are observed in the plots for the different size classes for the 4.22 mm-dia. spray orifice case (see Fig. 10.29). The 4.22 mm-dia. case, however, produced higher data rates for the 11-20 μm range, but lower peak droplet velocities, as compared with the 3.18 mm-dia. configuration in Fig. 10.28.

10.7.3 Predicted Trajectories and Volume Distributions

To solve the droplet trajectory equations of motion, the droplet and velocity measurements from the non-crossflow case were used as the initial conditions at $x=0$. Because droplet interactions were not considered in this analysis, there was only a slight difference in results produced either by leaving the spray measurements as discretely-injected points or by combining the discrete measurements into a set of initial conditions at a single injection point. Thus, the plots presented in Figs. 10.30 and 10.31 are shown with the trajectories traced for each discrete point in order to track the different path of the droplets.

Figure 10.30 depicts the solutions for the predicted trajectories of the droplet size classes at each point, for the 3.7 kg/h, 3.18 mm-dia. condition. Each column corresponds to an airblast ΔP condition. The trajectories are presented according to the different size classes in order to determine how the droplet distributions disperse into the crossflow. The data rates are also superimposed at the point of injection in order to provide a sense of the frequency in the occurrence of the droplet size at a particular

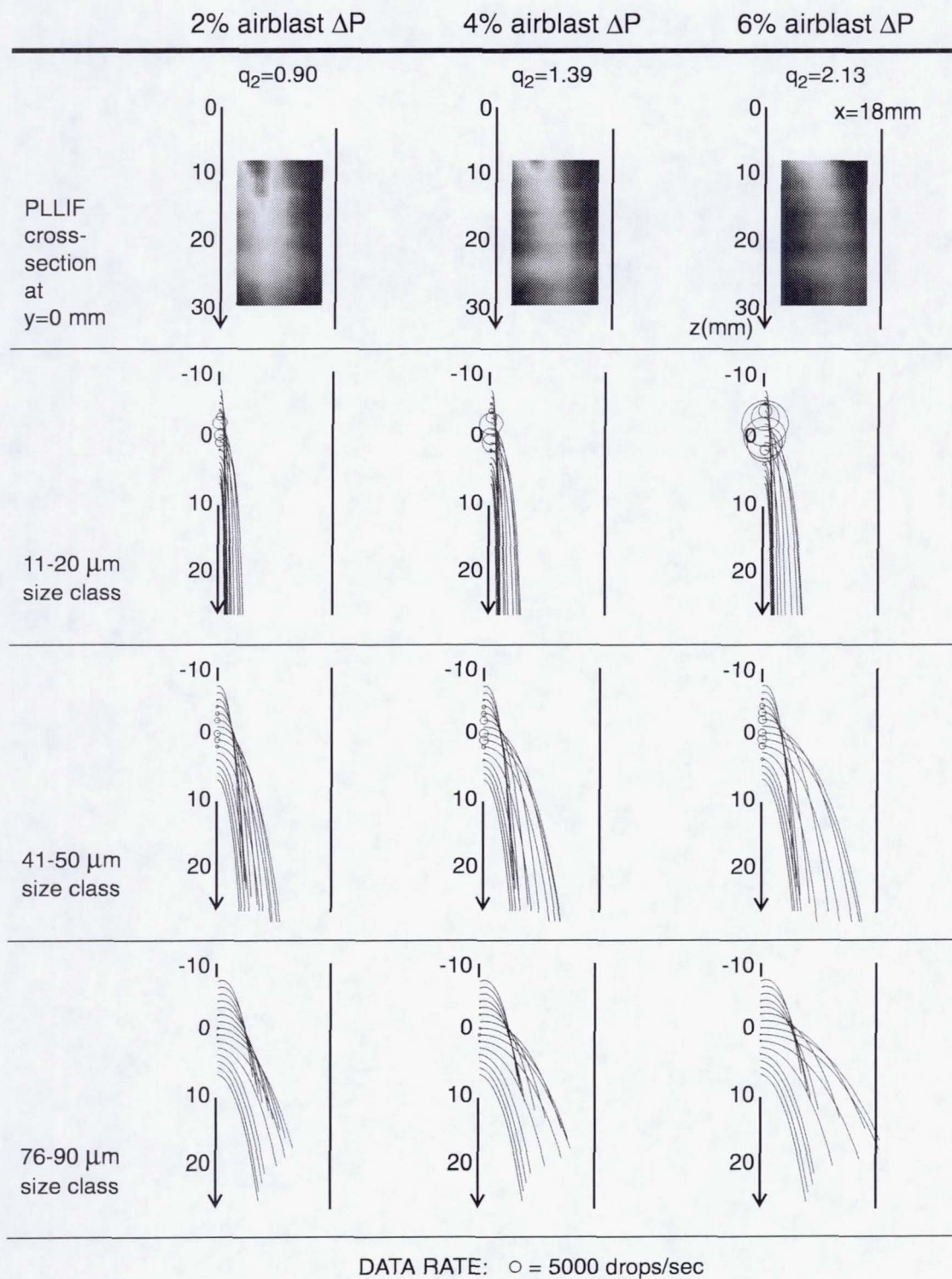


Fig. 10.30 Trajectories of three droplet size classes in a 70 m/sec crossflow, obtained using the initial conditions measured in the 3.7 kg/h fuel, 3.18 mm-dia. sprays without crossflow.

point. For comparison, the first row in the figure contains the corresponding vertical PLLIF images of the liquid concentration distribution.

Drops in the 11-20 μm range do not penetrate far, and instead, tend to travel along the wall. The smaller drops are immediately entrained by the crossflow velocity, attaining an axial velocity component equivalent to the 70 m/sec crossflow velocity almost immediately upon injection. The drops that correspond to the higher data rates in this 11-20 μm range are located in the center of the spray jet where the highest droplet velocities were measured. The 11-20 μm drops occurring at the center of the spray jet tend to penetrate farther into the crossflow, and correspond to the lower edge of the sprays in the images. In general, an increase in the airblast ΔP does not appreciably increase the penetration of the 11-20 μm drops.

The penetration of the drops does increase with an increase in the size class of the drops. A wider dispersion of the jet is achieved across the crossflow for the 41-50 μm and 76-90 μm range. The center of the spray, which yields higher data rates and which contains the peak droplet velocities for these size classes, penetrates farthest into the crossflow. The larger droplets, despite having a lower initial transverse velocity component (see Fig. 10.28), penetrate farther into the crossflow than the smaller droplets, which have a higher initial transverse velocity. The droplet momentum depends on the droplet volume and its velocity. Because the volume is related to the cube of the droplet diameter, a larger droplet will penetrate farther by virtue of its larger mass.

The penetration of the sprays formed in the 3.7 kg/h, 4.22 mm-dia. case are shown in Fig. 10.31. The same trends noted in the effect of droplet size on the

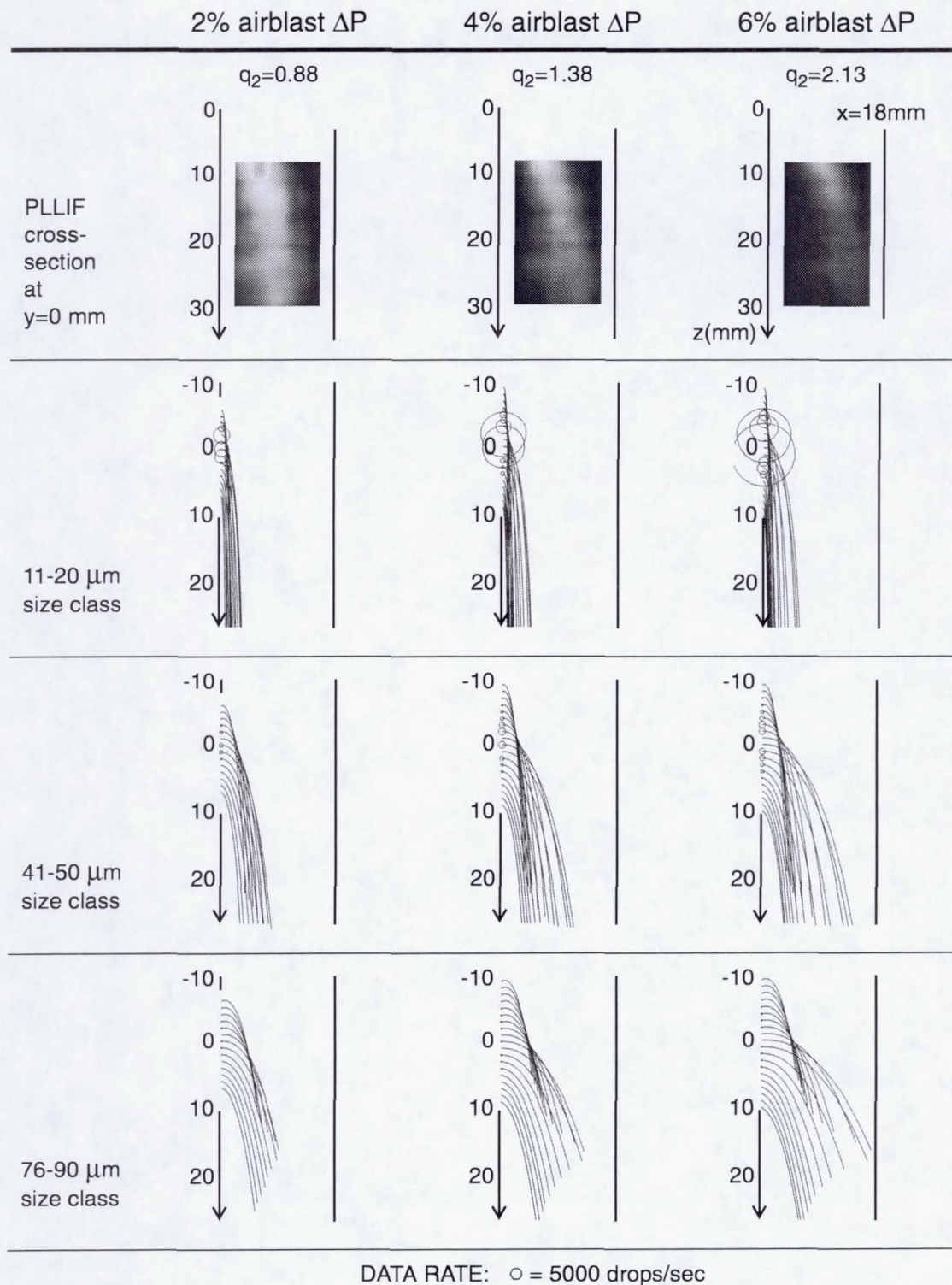


Fig. 10.31 Trajectories of three droplet size classes in a 70 m/sec crossflow, obtained using the initial conditions measured in the 3.7 kg/h fuel, 4.22 mm-dia. sprays without crossflow.

penetration of the spray also hold in the larger hole diameter case. In comparing the results from the two spray orifice diameter cases, however, it can be seen that the initial conditions affect the penetration of the droplets into the crossflow. Recall that a comparison of the initial conditions in Figs. 10.28 and 10.29 showed that the maximum droplet velocity magnitudes obtained in the 4.22 mm-dia. cases were lower than those achieved per size class in the 3.18 mm-dia. configuration. Because of these initial conditions, the trajectories of the sprays formed by the 4.22 mm-dia. orifice do not penetrate as far as the trajectories of the droplets formed by the 3.18 mm-dia. orifice. However, the predicted decrease in the overall penetration of droplets in the 4.22 mm-dia. case is contrary to the PLLIF results, which show that the 4.22 mm-dia. case produces higher penetrating sprays.

While the trajectories and data rates given for the different size classes in Figs. 10.30 and 10.31 offer information on the dispersion of the different droplet sizes into the crossflow, the results do not represent a volume distribution as do the PLLIF images. The PLLIF images, which capture the fluorescence of the droplets passing through the laser sheet thickness, biases the slower droplets because they reside in the laser sheet for a longer time period than faster moving droplets. The PDI data, on the other hand, measures all drops passing through the probe volume, for different time durations until a minimum droplet count is satisfied. It is thought that the difference in the basis of the PLLIF and PDI measurements resulted in the discrepancy between the jet penetration observed in the PLLIF images and the predicted droplet trajectories which used the PDI-measured data.

To reconcile the PLLIF images, which are a spatial-frequency-based sampling result, with the PDI data, which are based on a temporal-frequency sampling basis, either result can be converted to the other with a velocity factor (Dodge, 1988). The droplet trajectory results were thus converted to a volume concentration basis to enable a direct comparison between the PDI and PLLIF results. The procedure involved a series of steps that included:

1. Tracking the position of each droplet range initiating from the original set of spatial coordinates. At the specified downstream z -planes, the penetration distance x was obtained for each droplet size range from the trajectory curves.
2. Computing the volume V_{ij} associated with the number of drops measured in size range i that originated from coordinate $(x, y, z)=(0, 0, j)$. The mean value of bin i represented the diameter of the droplet in the volume calculation.
3. Correcting the volume calculation to obtain $V_{ij, corrected}$, which places more weight on the slower droplets, by applying the following equation:

$$V_{ij, corrected} = DR_{ij} \cdot (\bar{U}_{planar} / \bar{U}_{ij}) \cdot V_{ij} \quad (10.4)$$

DR_{ij} is the data rate of drops measured per unit time, \bar{U}_{planar} is the average velocity obtained across the z -plane of interest, and \bar{U}_{ij} is the average velocity, with the ij -subscripts in DR_{ij} and \bar{U}_{ij} as previously defined for V_{ij} (see above in line item 2).

4. Discretizing the corrected volumes as a function of penetration distance x , along each z -plane, in increments of $\Delta x = 0.1$ mm.

Applying this procedure to the generated droplet trajectory results yielded the volume distribution shown in Fig. 10.32, for the 3.7 kg/h fuel flow, 2% airblast ΔP , 3.18 mm-dia. condition. At the top of the figure, the vertical PLLIF image through the center of the jet is shown. The overall volume distribution calculated at the $z = 15$ mm plane is shown to the right of the image as a normalized volume. In comparing the profile of the PLLIF image along $z = 15$ mm to the calculated PDI-based volume distribution, it can be seen that the PDI-based data overpredicts the position of the peak volume in the crossflow width.

To determine the drop sizes that mainly contributed to the volume distribution, the volume distribution was divided according to the droplet size class. The results of the division, which are compiled below the PLLIF image in Fig. 10.32, show that the volume associated with the largest droplet size range of 106-200 μm comprised a major portion of the volume distribution. Despite the lower occurrence of these droplets as indicated by the lower data rates, these larger drops contain a large volume of liquid that is proportional to the cube of its diameter, d^3 .

The evolution of the PDI-calculated volume distribution for the 2% airblast condition is shown in Fig. 10.33. In addition, the corresponding 4% and 6% airblast ΔP conditions for this 3.7 kg/h, 3.18 mm-dia. case are compared in this figure. In general, the volume distribution shows an increased dispersion with increasing downstream distance. In each condition, the droplets are also predicted to impinge on

2% airblast ΔP

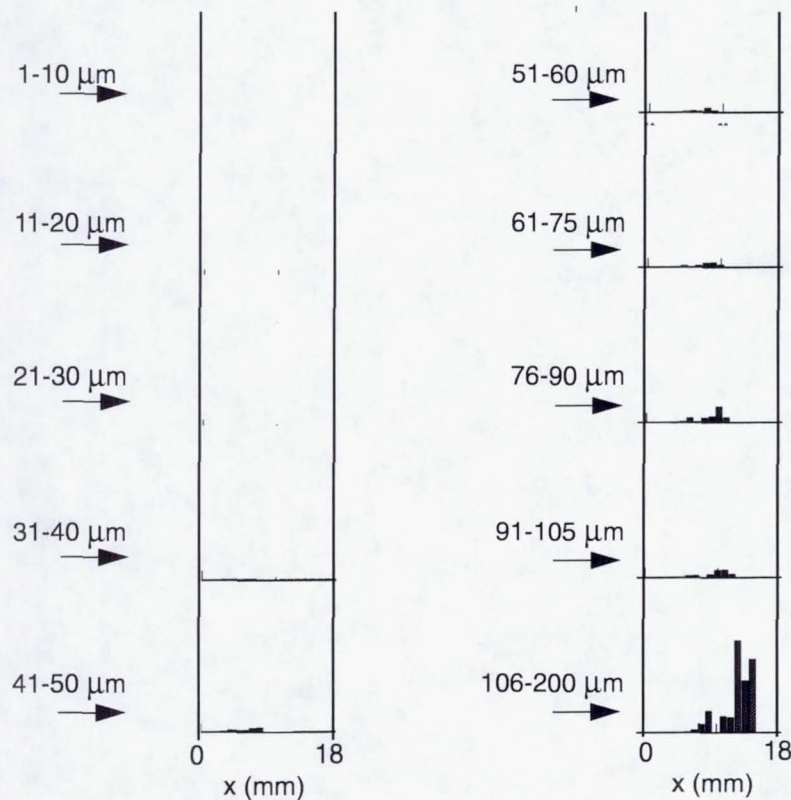
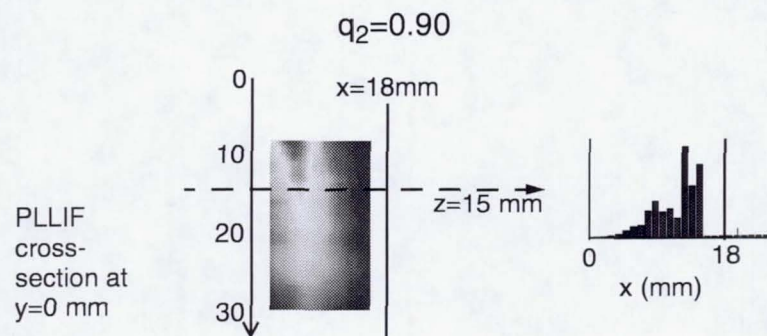


Fig. 10.32 Breakdown of volume distribution at the $z=15$ mm plane of predicted liquid volume distributions, compared to the liquid concentration distributions from PLLIF imaging for the 3.7 kg/h, 2% airblast ΔP , 3.18 mm-dia., 70 m/sec crossflow case.

the far wall, which is not suggested by the PLLIF images. As the airblast ΔP is increased, the droplet volume is dispersed across a larger area of the cross-section. In addition, the penetration of the peak volume in the spray decreases with increasing airblast ΔP .

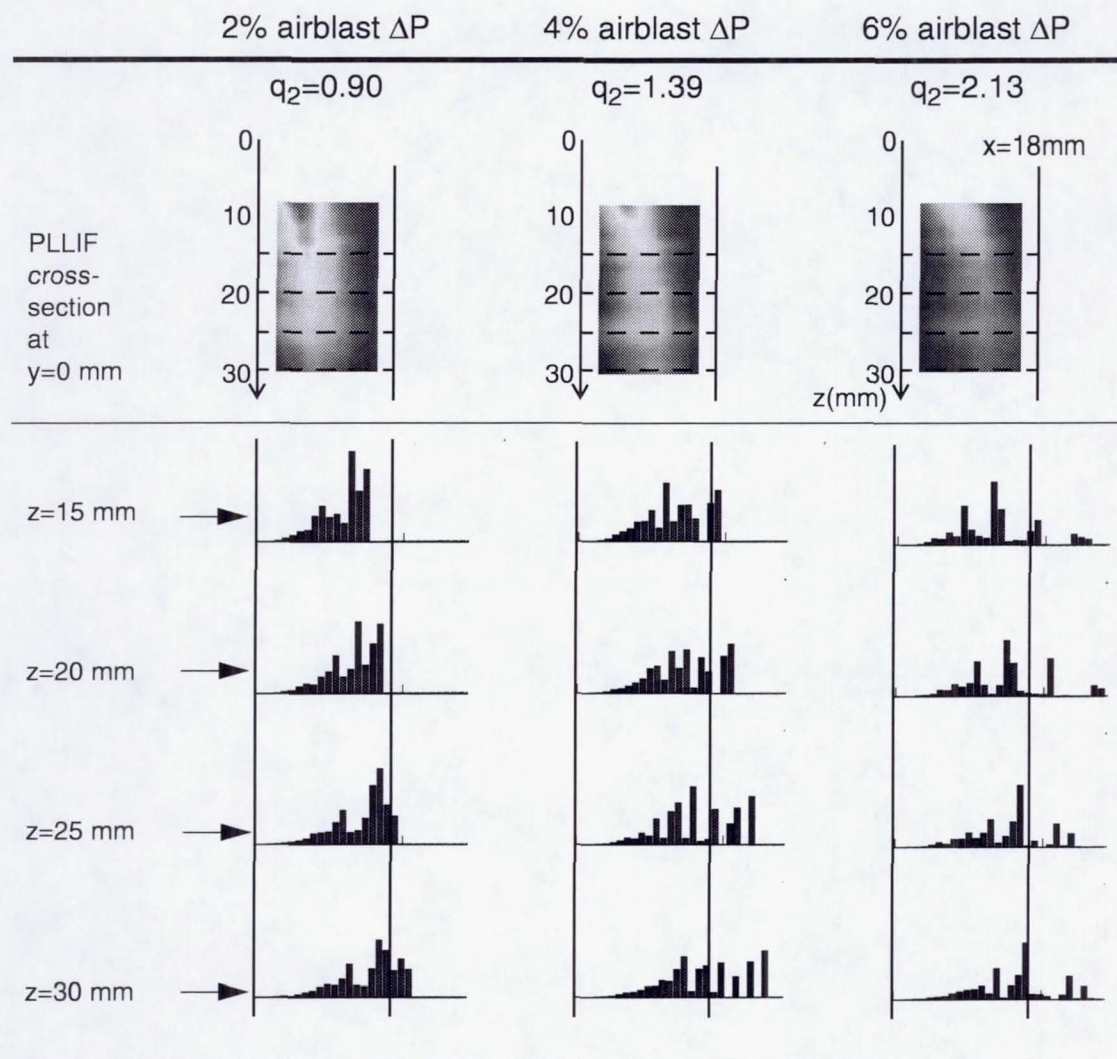


Fig. 10.33 Comparison of predicted liquid volume distributions to the liquid concentration distributions from PLLIF imaging for the 3.7 kg/h, 3.18 mm-dia., 70 m/sec crossflow cases.

Throughout the different downstream planes, the volume distribution for the 2% airblast ΔP case overpredicts the spray penetration depicted in the corresponding PLLIF image. The volume distributions also overpredict the trajectory at the 4% airblast ΔP condition. However, at the 6% airblast ΔP condition, the distributions begin to correlate to the PLLIF image distributions.

These same trends in the comparison of the predicted volume distribution with the PLLIF images are also observed in the results for the larger spray orifice diameter of 4.22 mm in Fig. 10.34. However, a comparison between the volume distributions in the 3.18 mm-dia. case shown in Fig. 10.33 with the 4.22 mm-dia. case in Fig. 10.34 shows the volume distributions from the smaller orifice diameter (3.18 mm-dia.) case penetrating farther, which is still contrary to the trends observed in the PLLIF images.

The higher penetration of the peak volume concentration predicted by the droplet data in the 3.18 mm-dia. case is not surprising, given that the initial conditions used in the analysis showed the smaller orifice diameter producing droplets with higher initial velocities. However, the reason for the deficiency in the present analysis probably lies in the oversimplification of the problem, which resulted in neglecting other forces involved in the mixing of the spray jet in the crossflow. The neglected phenomena include the varying crossflow velocity, particularly in the near field of the jet, the vortical structures induced by the jet in crossflow system, the entrainment of the crossflow air by the spray jet, interactions between droplets within the jet, and additional breakup processes. Consideration of these factors should enhance and improve the analysis. Droplet interactions, for instance, can be taken into account by following the method of Silverman and Sirignano (1994) to extend the single drop

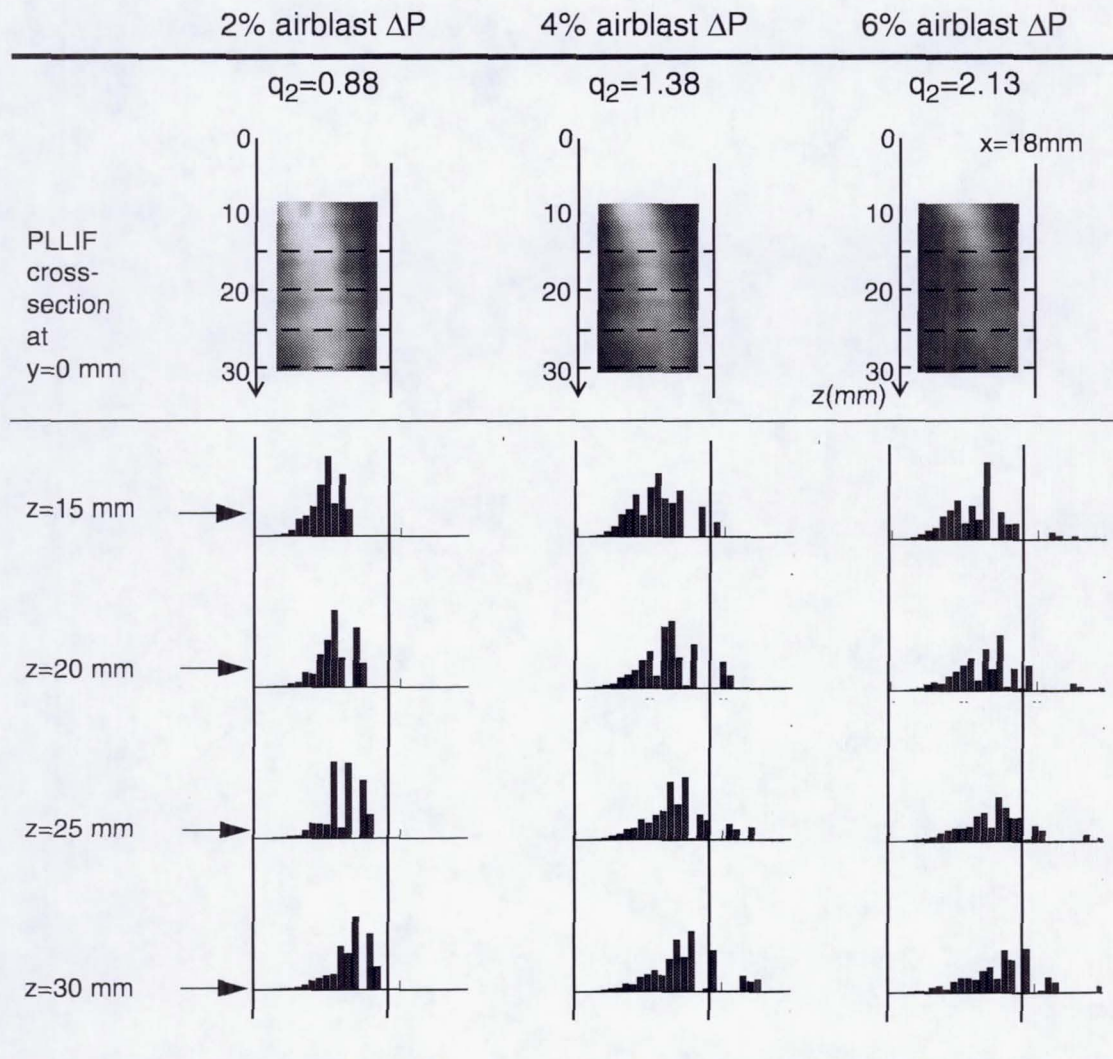


Fig. 10.34 Comparison of predicted liquid volume distributions to the liquid concentration distributions from PLLIF imaging for the 3.7 kg/h, 4.22 mm-dia., 70 m/sec crossflow cases.

trajectory analysis to a multi-droplet analysis with the formulation and application of a statistically-derived correction factor. The spray jet in crossflow system could also be separated into different regimes as Ghosh and Hunt (1998) performed in their model,

which also included equations describing the changing crossflow velocity field in the near-field region of the jet.

Crossflow entrainment by the jet may help to explain the higher penetration of the inner spray edge for the 4.22 mm-dia. orifice case as seen in a comparison of the PLLIF images in Fig. 10.8. The entrainment of the cross-flowing air by the jet depends on the dimensions of the jet, as demonstrated by the following entrainment function, E_f , used by Han and Chung (1992) in their gas-particle jet analysis:

$$E_f = \frac{A_f}{C_f} \rho_f E(U_f - U_\infty) \quad (10.5)$$

In this equation, the subscript f refers to the carrier gas properties, such as the atomizing air stream in the present experiment. The entrainment function describes the mass flow of crossflow air, per unit length, that is incorporated into the jet. The fluid properties of the jet and crossflow are represented by ρ_f and U_f , which refer to the density and velocity of the air flow in the jet, and U_∞ , which is the freestream velocity in the crossflow. E_f is also a function of the geometry of the jet, as seen in the inclusion of the cross-sectional area of the jet, A_f , the effective jet circumference, C_f , and the empirically-derived entrainment coefficient, E , which itself is a function of the jet diameter. Using the entrainment coefficient relationship obtained by Keffer and Baines (1963) for a gaseous jet in crossflow, the resultant dependence of E_f on the jet diameter d is given by $d^{0.63}$. Thus, in the present experiment, with the atomizing air and crossflow velocities maintained at constant settings, the entrainment of the crossflow mass into the spray jet should primarily depend on the spray orifice diameter.

A larger hole diameter should entrain more crossflow air into the spray jet, particularly in the lee side of the jet.

As more crossflow air is entrained into the inner spray surface by the counter-rotating vortex pair (CVP) induced in the gaseous phase of the spray jet, the drops along the lee side of the jet are convected farther outward into the crossflow. The CVP, induced by the crossflow of air that splits and flows around the jet, results in kidney-shaped distributions of velocity, as observed by Zaman and Foss (1997), as well as kidney-shaped distributions of concentration, as observed by Smith and Mungal (1998). Its presence in the spray jet is plausible, as the kidney-shaped distributions are especially evident in the liquid concentration images of the well-atomized sprays in Fig. 10.8.

10.8 Summary

In Chapter 9, the spray jet injected into a crossflow of air was examined in terms of its structure at the injection exit plane, and in terms of the penetration of the inner and outer surfaces of the spray jet. The screening of the global spray structure for those cases identified the 2% airblast ΔP as the condition contributing to a well-atomized and well-dispersed spray in the crossflow. The sprays at this pressure drop, and at different ambient pressure conditions, were subjected to additional planar characterization using PDI, which showed that the atomization quality of the spray varied significantly despite maintaining a constant fuel-air relative velocity by setting a constant atomizing air pressure drop and fuel flow rate.

PDI yielded detailed measurements of the spray, but is impractical for assessing the sprays formed under a wide range of conditions because of the amount of time required to obtain a planar grid of measurements. The planar imaging techniques developed in Chapters 5 and 6, which were applied to the non-crossflow case in Chapter 8, offers a means of quickly characterizing the internal distributions of a spray. The rest of this chapter subsequently presented the results obtained from applying the planar imaging techniques to the spray jet in the presence of a crossflow.

The internal distributions of the airblast spray were previously characterized in Chapter 8 under quiescent conditions in order to determine the parameters that affected the dispersion of the spray, independent of the crossflow velocity. The same variation in the injection parameters, which include the fuel flow rate, airblast ΔP , and spray orifice diameter, was performed in the crossflow cases using the planar imaging techniques as well as PDI measurements to supplement the images. The dual-lobed feature of the quiescent sprays did not appear in the cross-sections of the spray jet injected into the crossflow. Nonetheless, the tests yielded trends that were similar to those obtained in the non-crossflow case. For example, increasing the fuel flow rate continued to produce a poorly-atomized and dispersed spray, which indicates that the crossflow velocity cannot produce a well-mixed spray (as defined by good atomization and uniform dispersion across a large area of interest) if the spray was poorly-atomized and dispersed to begin with.

The airblast ΔP and the spray orifice diameter both produced favorable results in decreasing the D_{32} and increasing the spray coverage and liquid concentration uniformity. An increase in the airblast ΔP also produced an increase in the coverage by

the spray across the crossflow duct. This was the only quality that deviated from the non-crossflow test results, which showed a decreasing trend in spray area with respect to increasing airblast ΔP . The higher droplet velocities apparently helped to propel across the crossflow the droplet distributions that are produced in these flows.

The crossflow velocity magnitude was also varied in the tests. The increase in the crossflow velocity magnitude did not affect the structure of the liquid distributions in the spray. The main effect of the increased crossflow velocity was to shrink the size of the cross-sectional distributions.

Planar distributions of the D_{32} , obtained from both planar imaging and PDI diagnostics, showed that regions of large droplet sizes did not correspond to the peak volume concentrations suggested by the PLLIF images. The D_{32} profiles showed that the larger droplets penetrated farthest into the crossflow. A correlation relating the plane-averaged D_{32} to the Reynolds numbers of the liquid and airblast air streams, the Weber numbers of the airblast and crossflow air, and the downstream distance was obtained for the spray jet in crossflow cases. The crossflow Weber number factor did not have a significant impact on the D_{32} correlation, which indicated that the crossflow did not have a great effect in inducing secondary breakup of the spray.

The “spray quality” parameter (SQ) was assessed for the different flow conditions, and basically confirmed that (1) the well-atomized and dispersed sprays were mainly produced by the high airblast ΔP (6%) and larger spray orifice diameter (4.22 mm), and (2) the crossflow velocity magnitude did not impact the dispersion of the spray as much as the airblast ΔP and spray orifice diameter parameters. The SQ values, which were also calculated at different downstream axial locations, showed the

attainment of an asymptotic limit of SQ by a certain downstream plane within 25 mm from the point of injection (i.e., within $z/d_f = 37.9$). The PLLIF cross-sections at different downstream planes had also alluded to the attainment of a developed concentration distribution within the spray jet.

The atomizing air was imaged using the acetone PLIF technique. The atomizing air was observed to penetrate as far into the crossflow as the liquid spray mass, and to also become entrained by the crossflow along the inner edge of the spray.

A droplet trajectory analysis utilizing PDI measurements from the non-crossflow condition also showed that the larger droplets penetrated farthest into the crossflow. The larger droplets penetrated farther despite possessing lower initial velocities as compared to the velocity magnitudes corresponding to the smaller droplets. The PDI measurements were recast on a spatial-frequency basis to produce volume concentration distributions that could be compared with the PLLIF images. With the exception of the well-atomized sprays produced by the 6% airblast ΔP condition, the calculated volume distributions overpredicted the trajectory of the peak volume concentration shown in their corresponding PLLIF image. The overprediction of the peak volume concentration could be compensated in future analyses by incorporating such factors as the crossflow velocity field, droplet interactions, and crossflow entrainment by the jet.

Based on the observations made with the PLLIF images, PDI data, and the droplet trajectory analysis, the following description of the spray jet in crossflow is proposed, and is pictured in schematic form in Figure 10.35:

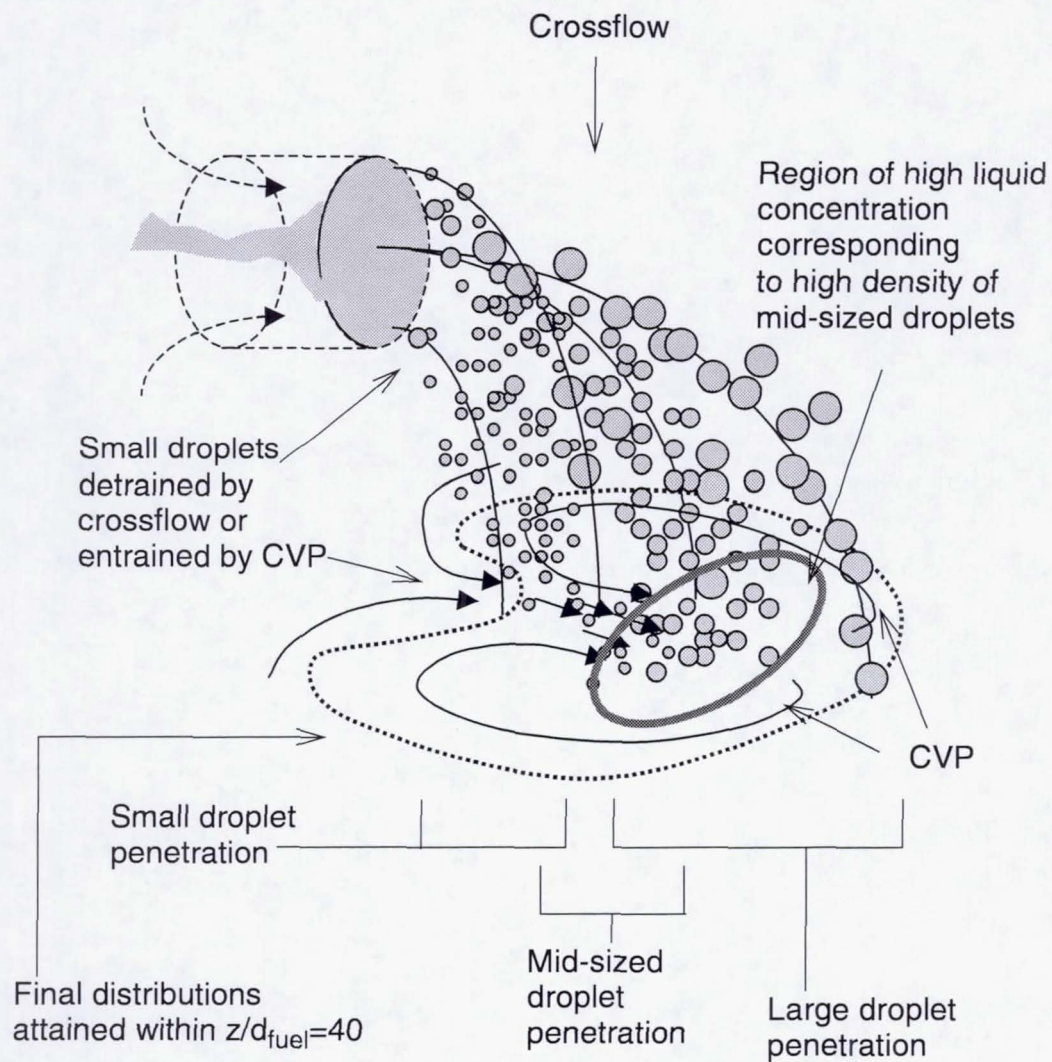


Fig. 10.35 Proposed model of the dispersion of the spray jet into the crossflow.

- The injected spray contains a high velocity core which disperses drops of different sizes across the crossflow.
- Smaller droplets lack the momentum to penetrate beyond the midpoint of the spray crossflow test section, and are immediately detrained from the jet by the crossflow.

- The increased penetration of the lower spray surface at the $y=0$ mm centerplane, as the spray orifice diameter or the airblast ΔP is increased, may be attributed to the CVP formed by the jet-crossflow interaction. The CVP causes air to be entrained through the centerline running along the lee side of the jet. The small droplets that are present near the inner edge of the jet follow the entrained air and are pushed farther into the jet cross-section by the CVP.
- Larger droplets occur less frequently than smaller droplets by two or more orders of magnitude, but contribute to a high percentage of the total volume in the spray. Although the regions of high D_{32} do not correspond directly with the peak volume concentration regions, the combination of large and mid-sized droplets contribute to the high concentration found within the spray cross-section, toward the outer spray surface.
- Beyond a certain downstream plane, the structure of the jet does not vary rapidly.

CHAPTER 11

SUMMARY, CONCLUSIONS, AND RECOMMENDATIONS

11.1 Summary

In order to characterize the dispersion of an airblast-atomized spray jet into a crossflow, the research problem was divided into three parts: Part I, which involved developing diagnostic techniques and procedures to probe the internal spray distribution; Part II, which characterized the spray without the presence of the crossflow; and Part III, which characterized the distribution of the spray injected into the crossflow. The major achievements and findings for each part are listed as follows:

Part I: UV Planar Imaging Diagnostic Development

- Liquid volume imaging of a calibration fluid via planar liquid laser-induced fluorescence (PLLIF) was developed as a tool for visualizing the distribution of the liquid phase in the spray, and verified with phase Doppler interferometry (PDI).
- The ratio of a PLLIF image and a Mie scattering image yielded a planar D_{32} distribution in the spray that was verified with PDI measurements.
- Acetone PLIF was used to visualize the atomizing air in the spray. Although the use of a temporal imaging filter helped to minimize the appearance of discrete droplets in the image, the scattering of the acetone fluorescence by the droplets produced a higher baseline intensity level in the images. Despite the interference,

the imaging of the atomizing air in the spray enabled a qualitative assessment of the extent of the atomizing air relative to the spray.

Part II: Characterization of the Airblast Spray without Crossflow

- A breakup regime map of Re_L vs. We_{airbl} similar to that developed by Farago and Chigier (1992) was obtained by classifying 130 spray conditions using high speed video imaging. Three main breakup modes were observed in the airblast atomization of the plain jet, and are listed in order of increasing severity, as follows: (1) Rayleigh-type mode, (2) membrane-type mode, and (3) “prompt” atomization.
- Based on an operating range of interest, tests were conducted primarily in the prompt atomization regime. A two-lobed liquid structure was observed. The formation of these structures corresponded to the design of the airblast passageways, which resulted in a high impingement angle of the atomizing air on the liquid jet.
- A parametric variation of the fuel flow, airblast ΔP , and spray orifice diameter was performed and assessed by characterizing such aspects as the liquid volume and D_{32} distributions, droplet size and velocity point measurements, and the spray angle. The resulting effects of these parameters on the atomization and dispersion of the spray showed that: (1) an increase in airblast ΔP produced the most effective change in the spray by increasing the atomization quality and the spread and uniformity in liquid mass dispersion, (2) the use of the larger spray orifice diameter

(4.22 mm-dia. versus the 3.18 mm-dia. orifice) also increased the dispersion and atomization of the spray, though it should be cautioned that there is a limit to enlarging the hole size before diminishing returns in spray quality occur (as observed with the 6.35 mm-dia. orifice in Chapter 7), and (3) an increase in fuel flow at the same airblast flow rates created poorly-atomized and poorly-dispersed sprays, as the decreased relative velocities between the fuel and air flows delayed the transition to higher-order breakup modes.

- The planar distributions of D_{32} were calibrated with the PDI point measurements of D_{32} . The computed plane-averaged D_{32} were subsequently used to derive a correlation for this parameter as a function of the Reynolds numbers of the liquid and atomizing air flows, the Weber number of the atomizing air flow, and the downstream distance.
- The “spray quality” (SQ) parameter was developed to summarize the spray performance across different spray conditions, and at different downstream planes. The SQ calculations quantitatively verified the trends that were observed in the parametric tests.

Part III: Characterization of the Airblast Spray Jet Injected into a Crossflow

- Video of the near-field of the spray jet showed the transition of the liquid jet from an intact structure (for airblast $\Delta P < 2\%$) to the onset of an atomized spray (for airblast ΔP between 2-3%), and thereafter to a fully expanded and atomized spray with liquid nodule formation (for airblast $\Delta P > 3\%$). The jet structures obtained at

elevated pressures, however, could not be classified under the breakup regime map obtained in Part II, which is reasonable given that the derived regime map was obtained at atmospheric conditions.

- Because of the importance of both the atomizing air and the liquid in affecting the spray penetration, and because the momentum-flux ratio q is a controlling parameter used to describe jet penetration, a definition of the two-phase momentum-flux ratio, q_2 , was developed. The definition generally conformed to the correct trend of increasing penetration with increasing q_2 .
- A spray trajectory equation was developed to describe the trajectories of the outer and inner surfaces of the spray jet in the crossflow, and was subsequently corrected with a normalized pressure factor in order to account for the effect of the atomization quality of the spray on its penetration into the crossflow.
- A correlation describing the droplet D_{32} as a function of the Reynolds numbers of the fuel and airblast air, and the Weber numbers of the airblast air and the crossflow air was obtained from the planar D_{32} images, after calibrating the images with PDI measurements.
- The atomizing air permeated the extent of the spray jet, but was also observed near the injection wall, in the absence of the droplets, as a result of crossflow entrainment processes.

- The effect of varying the different operating and geometric injection parameters on the dispersion of the spray jet into the crossflow was evaluated by examining the liquid concentration and D_{32} distributions, as well as the spray quality parameter. The results showed trends that were similar to those observed in the non-crossflow results, with the exception of the increased spray area coverage that was achieved with an increasing airblast ΔP . The high airblast velocities produced by the high airblast ΔP , which had led to a decreased spray area under quiescent conditions, were beneficial in aiding the penetration of the droplet distribution across a wider cross-sectional area.
- The effect of varying the crossflow velocity magnitude was minimal in relation to affecting the spray distributions. Under the range of crossflow velocities tested, the higher crossflow velocities decreased the penetration and the size of the cross-section of the spray, but did not affect the internal distributions.
- Single droplet trajectory models were applied to the system, using PDI measurements from the non-crossflow case as initial conditions, in order to predict droplet transport and compare the results with PLLIF liquid distributions. The analysis overpredicted the peak volume concentration penetration, especially in the lower airblast ΔP cases in which poor atomization was expected. In addition, the analysis could not reconcile the predictions with trends observed in the PLLIF images that included the increased inner spray surface penetration and increased peak volume penetration produced in the larger spray orifice diameter (4.22 mm) case. The single droplet trajectory equations do not account for droplet

interactions, crossflow velocity variation, and crossflow entrainment by the spray jet, all of which could affect the penetration of the sprays. However, the analysis performed here is a first step toward producing a full model that describes the dispersion of the spray jet into the crossflow.

In summary, the dispersion of the airblast-atomized spray in a crossflow is primarily governed by the initial conditions that form the spray. The initial droplet size and velocity distributions of the spray determine the extent of spray penetration and mass dispersion across the crossflow. To produce a widely dispersed, uniform, and well-atomized spray that disperses and mixes with the crossflow, the list of settings are, in order of importance: a high airblast ΔP to increase the relative fuel-air velocity, and a large spray orifice diameter (though not to the extent that a diminishing return in atomization occurs with respect to increasing atomizing air flow rates).

11.2 Conclusions

The characterization of the dispersion of the spray jet in a crossflow of air yielded the following conclusions:

- The liquid fuel and air components of a spray formed by twin-fluid atomization can be visualized with planar imaging techniques that enable the characterization of the internal structure of the spray jet.

- The insight gained in studying the breakup mode and internal structure of the spray issuing into a quiescent environment underscores the importance of characterizing the spray prior to introducing the crossflow.
 - A well-dispersed spray in a quiescent environment does not necessarily lead to a well-dispersed spray in a crossflow. Nonetheless, the overall “spray quality” trends from the non-crossflow case generally hold true in the crossflow case, which verifies that the dispersion of the spray into the crossflow primarily depends on the initial spray conditions elicited from the hardware design and the operating flow rates.
 - Measurements of the airblast-atomized spray can be used as initial conditions in modelling the dispersion of the spray into the crossflow. Distributions of the droplet size and velocities, rather than the mean values of these quantities, are used to represent the initial conditions of the spray.
- The dispersion of the spray jet into a crossflow is affected by the atomizing air flow and jet-crossflow interactions.
 - The penetration of the atomizing air is tied to the penetration of the liquid phase of the spray.
 - Secondary atomization by the crossflow does not play a major role if the sprays are already sufficiently atomized upon injection into the crossflow.

- The internal flow of the spray jet shows evidence of kidney-shaped contour distributions which are associated with the counter-rotating vortex pair (CVP) typically found in a gaseous jet in crossflow system. Kidney-shaped distributions of the liquid concentration are present in the well-atomized conditions because smaller drop size distributions occur in well-atomized sprays, and smaller drops tend to follow the surrounding flow field.
- The complexities associated with the spray jet in crossflow, which encompass both atomization and transport processes, are revealed by the difficulty in quantifying the flow field.
 - A two-phase momentum-flux ratio can be used to correlate the trajectories of the outer and inner surfaces of the spray jet. However, the varied drop size distribution in the spray creates difficulties in accounting for the dispersion along the inner surface of the spray jet.
 - Droplet trajectory calculations verify general observations such as the increased penetration of larger droplets in the crossflow. However, the single droplet analysis tends to overpredict the penetration of the volume distribution, especially for conditions in which larger droplets occur.

11.3 Recommendations

The suggestions for the continuation of this research problem are listed as follows, beginning with general recommendations and following with other recommendations corresponding to Parts I-III in the experiment:

General

- **Investigate sprays at higher pressures and temperatures.** Increasing the ambient pressures and temperatures affects the atomization and vaporization of the spray, which subsequently affects the penetration and dispersion of the spray droplets. Tests should be conducted to assess the effect of elevated pressures and temperatures on spray penetration and dispersion, as well as on the mixing of the vaporized fuel with air.
- **Apply a statistical design of experiment to optimize spray performance.** This experiment yielded parameters which quantify the spray quality and which can be used as response factors in a set of statistically-designed experiments that incorporate additional variables such as elevated pressures and temperatures.
- **Extend results to a full injector case.** A full injector case under both non-reacting and reacting conditions should be conducted using the same diagnostic techniques and analyses developed in this experiment. The full injector case increases the complexity of the single spray jet case by introducing the effects of multiple jet interaction and a nonuniform, swirling crossflow of air on the dispersion of the spray.

Diagnostics

- **Eliminate droplet scattering of acetone fluorescence.** To accurately track the acetone-laden atomizing air, the contamination of the signal by the droplet scattering of acetone fluorescence needs to be removed. A simple experiment that tests the interaction of a stream of non-UV absorbing droplets in a co-flow of acetone-laden air could help to show whether the droplet scattering of fluorescence can be avoided.
- **Apply techniques to visualize the vapor phase of the fuel in the spray.** The assessment of fuel vapor mixing becomes especially important as the ambient temperatures increase and enhance the droplet vaporization.

Spray Jet without Crossflow

- **Determine the effect of internal flow conditions on the atomized spray.**
Because of the importance in producing a well-atomized spray before its injection into the crossflow, a more thorough examination into the effect of the internal geometry of the injector on the production of the spray should be investigated.

Spray Jet with Crossflow

- **Extend the empirical and simplified models.** The jet penetration and droplet trajectory models would benefit from additional tests performed at varying ambient pressures and temperatures. The droplet trajectory model should be extended to accommodate such factors as the change in crossflow velocity as it flows around the jet, the effect of droplet vaporization, and the possible occurrence of additional secondary breakup of the droplets.

CHAPTER 12

REFERENCES

- Adelberg, M., 1967, "Breakup Rate and Penetration of a Liquid Jet in a Gas Stream," *AIAA Journal*, Vol. 5, No. 8, pp. 1408-1415.
- Adelberg, M., 1968, "Mean Drop Size Resulting from the Injection of a Liquid Jet into a High-Speed Gas Stream," *AIAA Journal*, Vol. 6, No. 6, pp. 1143-1147.
- Bachalo, W.D. and Houser, M.J. 1984, "Development of the Phase/Doppler Spray Analyzer for Liquid Drop Size and Velocity Characterizations," AIAA Paper 84-1199.
- Bachalo, W.D., 1994, "Spray Diagnostic Techniques and the Application to the Study of Spray Interactions with Turbulent Flows," IUTAM Symposium on Mechanics and Combustion of Droplets and Sprays, Taiwan.
- Bazile, R. and Stepowski, D., 1994, "Measurements of the Vaporization Dynamics in the Development Zone of a Burning Spray by Planar Laser Induced Fluorescence and Raman Scattering," *Experiments in Fluids*, Vol. 16, Nos. 3-4, pp. 171-180.
- Bazile, R. and Stepowski, D., 1995, "Measurements of Vaporized and Liquid Fuel Concentration Fields in a Burning Spray Jet of Acetone Using Planar Laser Induced Fluorescence," *Experiments in Fluids*, Vol. 20, No. 1, pp. 1-9.
- Beck, J.E., Lefebvre, A.H. and Koblish, T.R., 1991, "Airblast Atomization at Conditions of Low Air Velocity," *Journal of Propulsion and Power*, Vol. 7, No. 2, pp. 207-212.
- Berlman, I., 1971, *Fluorescence Spectra of Aromatic Compounds*, Academic Press: New York.
- Bowman, C.T., 1976, "Kinetics of Pollutant Formation and Destruction in Combustion," *Progress in Energy and Combustion Science*, Vol. 1, pp. 33-45.
- Bowman, C.T., 1992, "Control of Combustion-Generated Nitrogen Oxide Emissions: Technology Driven by Regulation," *Twenty-Fourth Symposium (International) on Combustion*, Vol. 24, pp. 859-878.
- Briffa, F.E.J. and Dombrowski, N., 1966, "Entrainment of Air into a Liquid Spray," *A.I.Chemical Engineering Journal*, Vol. 12, No. 4, pp. 708-717.

Chigier, N. and Reitz, R.D., 1996, "Regimes of Jet Breakup and Breakup Mechanisms (Physical Aspects)," in *Recent Advances in Spray Combustion: Spray Atomization and Drop Burning Phenomena*, edited by K.K. Kuo, Vol. 1, pp. 109-135.

Chin, J.S., Freeman, W.G. and Lefebvre, A.H., 1986, "Evaporation Histories of Fuel Sprays Injected Across a Flowing Air Stream," *Atomisation and Spray Technology*, Vol. 2, No. 2, pp. 135-149.

Clark, B.J., 1964, "Breakup of a Liquid Jet in a Transverse Flow of Gas," NASA TN D-2424.

Cowell, L.H. and Smith, K.O., 1993, "Development of a Liquid-Fueled, Lean-Premixed Gas Turbine Combustor," *Journal of Engineering for Gas Turbines and Power*, Vol. 115, No. , pp. 554-562.

Crowe, C.T., Sharma, M.P. and Stock, D.E., 1977, "The Particle-Source-In Cell (PSI-Cell) Model for Gas-Droplet Flows," *Journal of Fluids Engineering*, Vol. 99, No. 2, pp. 325-332.

Danckwerts, P.V., 1952, "The Definition and Measurement of Some Characteristics of Mixtures," *Applied Scientific Research, Section A*, Vol. 3, No. 4, pp. 279-296.

deNevers, N., 1995, *Air Pollution Control Engineering*, McGraw-Hill: New York.

Dodge, L.G., 1988, "Representation of Average Drop Sizes in Sprays," *Journal of Propulsion*, Vol. 4, No. 6, pp. 490-496.

Dutta, P., Gore, J.P. and Sojka, P.E., 1997, "Emissions Characteristics of Liquid-Fueled Pilot Stabilized Lean Premixed Flames in a Tubular Premixer-Combustor," *Journal of Engineering for Gas Turbines and Power*, Vol. 119, pp. 585-590.

Eastes, T.W. and Samuelsen, G.S., 1992, "Secondary Atomization by High Amplitude Pressure Waves," AIAA Paper 92-3120.

Eastes, T.W. and Samuelsen, G.S., 1993, "Temporally and Spatially-Resolved Imaging of Drop Response to a Shock," 6th ILASS Proceedings, Worcester, MA.

Edelman, R.B., Economos, C., and Boccio, J., 1971, "Mixing and Combustion in Two-Phase Flows with Application to the B-O-H-N System," *AIAA Journal*, Vol. 9, No. 10, pp. 1935-1940.

Eroglu, H. and Chigier, N., 1991, "Initial Drop Size and Velocity Distributions for Airblast Coaxial Atomizers," *Journal of Fluids Engineering*, Vol. 113, No. 3, pp. 453-459.

- Faeth, G.M., 1990, "Structure and Atomization Properties of Dense Turbulent Sprays," *Twenty-Third Symposium (International) on Combustion*, Vol. 23, pp. 1345-1352.
- Farago, Z. and Chigier, N., 1992, "Morphological Classification of Disintegration of Round Liquid Jets in a Coaxial Air Stream," *Atomization and Sprays*, Vol. 2, No. 2, pp. 137-153.
- Fenimore, C.P., 1971, "Formation of Nitric Oxide in Premixed Hydrocarbon Flames," *13th Symposium (International) on Combustion*, Vol. 13, pp. 373-380.
- Forde, J.M., Molder, S. and Szpiro, E.J., 1966, "Secondary Liquid Injection into a Supersonic Airstream," *Journal of Spacecraft*, Vol. 3, No. 8, pp. 1172-1175.
- Fric, T.F., 1993, "Effects of Fuel-Air Unmixedness on NO_x Emissions," *Journal of Propulsion and Power*, Vol. 9, No. 5, pp. 708-713.
- Ghosh, S. and Hunt, J.C.R., 1994, "Induced Air Velocity Within Droplet Driven Sprays," *Proceedings of the Royal Society of London, Part A*, Vol. 444, No. 1920, pp. 105-127.
- Ghosh, S. and Hunt, J.C.R., 1998, "Spray Jets in a Cross-Flow," *Journal of Fluid Mechanics*, Vol. 365, pp. 109-136.
- Gordon, S. and McBride, B.J., 1976, "Computer Program for Calculation of Complex Chemical Equilibrium Compositions, Rocket Performance, Incident and Reflected Shocks, and Chapman-Jouguet Detonations," NASA SP-273.
- Han, K.S. and Chung, M.K., 1992, "Numerical Simulation of Two-Phase Gas-Particle Jet in a Crossflow," *Aerosol Science and Technology*, Vol. 16, No. 2, pp. 126-139.
- Hanson, R.K., 1986, "Combustion Diagnostics: Planar Imaging Techniques," *Twenty-First Symposium (International) on Combustion*, Vol. 23, pp. 1677-1691.
- Harari, R. and Sher, E., 1997, "Optimization of a Plain-Jet Airblast Atomizer," *Atomization and Sprays*, Vol. 7, No. 1, pp. 97-113.
- Harari, R. and Sher, E., 1998, "Bimodal Drop Size Distribution Behavior in Plain-Jet Airblast Atomizer Sprays," *Atomization and Sprays*, Vol. 8, No. 3, pp. 349-362.
- Hecht, E., 1998, *Optics* (3rd ed.), Addison-Wesley: Reading, MA.
- Heister, S.D., Nguyen, T.T. and Karagozian, A.R., 1989, "Modeling of Liquid Jets Injected Transversely into a Supersonic Crossflow," *AIAA Journal*, Vol. 27, No. 12, pp. 1727-1734.

- Hinze, J.O., 1955, "Fundamentals of the Hydrodynamic Mechanism of Splitting in Dispersion Processes," *AIChE Journal*, Vol. 1, No. 3, pp. 289-295.
- Holdeman, J.D., 1993, "Mixing of Multiple Jets with a Confined Subsonic Crossflow," *Progress in Energy and Combustion Science*, Vol. 19, No. 1, pp. 31-70.
- Holterman, H.J., van de Zande, J.C., Porskamp, H.A.J. and Huijsmans, J.F.M., 1997, "Modelling Spray Drift from Boom Sprayers," *Computers and Electronics in Agriculture*, Vol. 19, No. 1, pp. 1-22.
- Hsiang, L.P. and Faeth, G.M., 1992, "Near-Limit Drop Deformation and Secondary Breakup," *International Journal of Multiphase Flow*, Vol. 18, No. 5, pp. 635-652.
- Igushi, T., McDonell, V.G. and Samuelson, G.S., 1993, "An Imaging System for Characterization of Liquid Volume Distributions in Sprays," 6th ILASS Proceedings, Worcester, MA.
- Inamura, T., 2000, "Trajectory of a Liquid Jet Traversing Subsonic Airstreams," *Journal of Propulsion and Power*, Vol. 16, No. 1, pp. 155-157.
- Inamura, T. and Nagai, N., 1997, "Spray Characteristics of Liquid Jet Traversing Subsonic Airstreams," *Journal of Propulsion and Power*, Vol. 13, No. 2, pp. 250-256.
- Inamura, T., Nagai, N., Watanabe, T. and Yatsuyanagi, N., 1993, "Disintegration of Liquid and Slurry Jets Traversing Subsonic Airstreams," in *Experimental Heat Transfer, Fluid Mechanics and Thermodynamics*, edited by M.D. Kelleher et al., pp. 1522-1529.
- Ingebo, R.D. and Foster, H.H., 1957, "Drop Size Distribution for Crosscurrent Breakup of Liquid Jets in Air Streams," NACA TN 4087.
- Jasuja, A.K., 1979, "Atomization of Crude and Residual Fuel Oils," *Journal of Engineering for Power*, Vol. 101, No. 2, pp. 250-258.
- Jeffreys, H., 1925, "On the Formation of Water Waves by Wind," *Proceedings of the Royal Society of London, Part A*, Vol. 107, pp. 189, 241.
- Kamotani, Y. and Greber, I., 1972, "Experiments on a Turbulent Jet in a Cross Flow," *AIAA Journal*, Vol. 10, No. 11, pp. 1425-1429.
- Keffer, J.F. and Baines, W.D., 1963, "The Round Turbulent Jet in a Cross-Wind," *Journal of Fluid Mechanics*, Vol. 15, pp. 401-496.
- Kihm, K.D., Lyn, G.M. and Son, S.Y., 1995, "Atomization of Cross-Injecting Sprays Into Convective Air Stream," *Atomization and Sprays*, Vol. 5, Nos. 4-5, pp. 417-433.

Kitamura, Y. and Takahashi, T., 1976, "Stability of a Liquid Jet in Air Flow Normal to the Jet Axis," *Journal of Chemical Engineering of Japan*, Vol. 9, No. 4, pp. 282-286.

Krzeczkowski, S.A., 1980, "Measurement of Liquid Droplet Disintegration Mechanisms," *International Journal of Multiphase Flow*, Vol. 6, No. 2, pp. 227-239.

Kundu, P.K., 1990, *Fluid Mechanics*, Academic Press: San Diego.

Lefebvre, A.H., 1989, *Atomization and Sprays*, Hemisphere: Washington, D.C.

Lefebvre, A.H., 1992a, "Twin-Fluid Atomization: Factors Influencing Mean Drop Size," *Atomization and Sprays*, Vol. 2, No. 2, pp. 101-119.

Lefebvre, A.H., 1992b, "Energy Considerations in Twin-Fluid Atomization," *Journal of Engineering for Gas Turbines and Power*, Vol. 114, No. 1, pp. 89-96.

Lefebvre, A.H., 1999, *Gas Turbine Combustion*, 2nd edition, Taylor & Francis: Philadelphia.

LeGal, P., Farrugia, N. and Greenhalgh, D.A., 1999, "Laser Sheet Dropsizing of Dense Sprays," *Optics and Laser Technology*, Vol. 31, No. 1, pp. 75-83.

Leong, M.Y., McDonell, V.G., and Samuelsen, G.S., 1997, "Cross-Sectional Spray Patternation of an Airblast-Atomized Liquid Jet Injected into a Crossflow," Proceedings of the 7th International Conference on Liquid Atomization and Spray Systems, Seoul, Korea.

Leong, M.Y., Smugeresky, C.S., McDonell, V.G., and Samuelsen, G.S., 2000, "Rapid Liquid Fuel Mixing for Lean-Burning Combustors: Low-Power Performance," ASME Paper 2000-GT-0116 (accepted for publication in the *Journal of Engineering for Gas Turbines and Power*).

Less, D.M. and Schetz, J.A., 1986, "Transient Behavior of Liquid Jets Injected Normal to a High-Velocity Gas Stream," *AIAA Journal*, Vol. 24, No. 12, pp. 1979-1986.

Li, H.S. and Karagozian, A.R., 1992, "Breakup of a Liquid Jet in Supersonic Crossflow," *AIAA Journal*, Vol. 30, No. 7, pp. 1919-1921.

Liscinsky, D.S., True, B. and Holdeman, J.D., 1993, "Experimental Investigation of Crossflow Jet Mixing in a Rectangular Duct," AIAA Paper 93-2037; also NASA TM-106152.

Locke, R.J., Hicks, Y.R., Anderson, R.C. and Zaller, M.M., 1998, "Optical Fuel Injector Patternation Measurements in Advanced Liquid-Fueled, High Pressure, Gas

- Turbine Combustors," *Combustion Science and Technology*, Vol. 138, Nos. 1-6, pp. 297-311.
- Lorenzetto, G.E. and Lefebvre, A.H., 1977, "Measurements of Drop Size on a Plain-Jet Airblast Atomizer," *AIAA Journal*, Vol. 15, No. 7, pp. 1006-1010.
- Lozano, A., Yip, B. and Hanson, R.K., 1992, "Acetone: A Tracer for Concentration Measurements in Gaseous Flows by Laser-Induced Fluorescence," *Experiments in Fluids*, Vol. 13, No. 6, pp. 369-376.
- Lyons, V.J., 1982, "Fuel/Air Nonuniformity--Effect on Nitric Oxide Emissions," *AIAA Journal*, Vol. 20, No. 5, pp. 660-665.
- Malte, P.C. and Pratt, D.T., 1974, "The Role of Energy-Releasing Kinetics in NO_x Formation: Fuel-Lean, Jet-Stirred CO-Air Combustion," *Combustion Science and Technology*, Vol. 9, Nos. 5-6, pp. 221-231.
- Mayer, E., 1961, "Theory of Liquid Atomization in High Velocity Gas Streams," *ARS Journal*, Vol. 31, No. 12, pp. 1783-1785.
- Mazallon, J., Dai, Z., and Faeth, G.M., 1999, "Primary Breakup of Nonturbulent Round Liquid Jets in Gas Crossflows," *Atomization and Sprays*, Vol. 9, No. 3, pp. 291-311.
- McDonell, V.G. and Samuelsen, G.S., 1988, "Application of Two-Component Phase Doppler Interferometry to the Measurement of Particle Size, Mass Flux, and Velocities in Two-Phase Flows," *Twenty-Second Symposium (International) on Combustion*, Vol. 22, pp. 1961-1971.
- Melton, L.A., 1993, "Planar Liquid and Gas Visualization," *Berichte der Bunsen-Gesellschaft für Physikalische Chemie*, Vol. 97, No. 12, pp. 1560-1567.
- Mugele, R.A. and Evans, H.D., 1951, "Droplet Size Distribution in Sprays," *Industrial and Engineering Chemistry*, Vol. 43, No. 6, pp. 1317-1324.
- Nejad, A.S. and Schetz, J.A., 1983, "Effects of Properties and Location in the Plume on Droplet Diameter for Injection in a Supersonic Stream," *AIAA Journal*, Vol. 21, No. 7, pp. 956-961.
- Nguyen, Q.V., Rangel, R.H., and Dunn-Rankin, D., 1991, "Measurement and Prediction of Trajectories and Collision of Droplets," *International Journal of Multiphase Flow*, Vol. 17, No. 2, pp. 159-177.
- Nguyen, T.T. and Karagozian, A.R., 1992, "Liquid Fuel Jet in Subsonic Crossflow," *Journal of Propulsion and Power*, Vol. 8, No. 1, pp. 21-29.

Nicol, D.G., Steele, R.C., Marinov, N.M. and Malte, P.C., 1995, "The Importance of the Nitrous Oxide Pathway to NO_x in Lean-Premixed Combustion," *Journal of Engineering for Gas Turbines and Power*, Vol. 117, No. 1, pp. 100-111.

Nukiyama, S. and Tanasawa, Y., 1939, "An Experiment on the Atomization of Liquid," *Transactions of the Society of Mechanical Engineers, Japan*, Vol. 5, No. 18, pp. 68-75.

Oda, T., Hiroyasu, H., Arai, M. and Nishida, K., 1994, "Characterization of Liquid Jet Atomization across a High-Speed Airstream," *JSME International Journal, Series B*, Vol. 37, No. 4, pp. 937-944.

Phillips, J.C. and Miller, P.C.H., 1999, "Field and Wind Tunnel Measurements of the Airborne Spray Volume Downwind of Single Flat-Fan Nozzles," *Journal of Agricultural Engineering Research*, Vol. 72, No. 2, pp. 161-170.

Phillips, J.C., Miller, P.C.H., and Thomas, N.H., 2000, "Air Flow and Droplet Motions Produced by the Interaction of Flat-Fan Sprays and Cross Flows," *Atomization and Sprays*, Vol. 10, No. 1, pp. 83-103.

Pratte, B.D. and Baines, W.D., 1967, "Profiles of the Round Turbulent Jet in a Cross Flow," *Journal of the Hydraulics Division*, Vol. 93, No. HY 6, pp. 53-64.

Ranger, A. A. and Nicholls, J. A., 1969, "The Aerodynamic Shattering of Liquid Drops," *AIAA Journal*, Vol. 7, No. 2, pp. 285-290.

Reitz, R.D., 1978, *Atomization and Other Breakup Regimes of a Liquid Jet*, Ph.D. Dissertation, Princeton University, Princeton, NJ.

Reitz, R.D. and Bracco, F.V., 1982, "Mechanism of Atomization of a Liquid Jet," *Physics of Fluids*, Vol. 25, No. 10, pp. 1730-1742.

Ricou, F.P. and Spalding, D.B., 1961, "Measurements of Entrainment by Axisymmetrical Turbulent Jets," *Journal of Fluid Mechanics*, Vol. 11, pp. 21-32.

Rizk, N.K. and Lefebvre, A.H., 1983, "Influence of Atomizer Design Features on Mean Drop Size," *AIAA Journal*, Vol. 21, No. 8, pp. 1139-1142.

Rizk, N.K. and Lefebvre, A.H., 1984, "Spray Characteristics of Plain-Jet Airblast Atomizers," *Journal of Engineering for Gas Turbines and Power*, Vol. 106, No. 3, pp. 634-638.

Rosin, P. and Rammler, E., 1933, "The Laws Governing the Fineness of Powdered Coal," *Journal of the Institute of Fuel*, Vol. 7, No. 31, pp. 29-36.

- Ross, S.M., 1987, *Introduction to Probability and Statistics for Engineers and Scientists*, John Wiley & Sons: New York.
- Rudinger, G., 1963, "Experiments on Shock Relaxation in Particle Suspensions in a Gas and Preliminary Determination of Particle Drag Coefficients," *Multi-Phase Symposium*, American Society of Mechanical Engineers.
- Russ, J.C., 1995, *The Image Processing Handbook* (2nd ed.), CRC Press: Boca Raton, FL.
- Salzman, R.N. and Schwartz, S.H., 1978, "Experimental Study of a Solid-Gas Jet Issuing into a Transverse Stream," *Journal of Fluids Engineering*, Vol. 100, No. 3, pp. 333-339.
- Samuelsen, G.S., Sowa, W.A. and Shaffar, S.W., 1995, Lean Burn Injector for Gas Turbine Combustor. U.S. Patent No. 5,477,685.
- Sankar, S.V., Maher, K.E., Robart, D.M. and Bachalo, W.D., 1999, "Rapid Characterization of Fuel Atomizers Using an Optical Patternator," *Journal of Engineering for Gas Turbines and Power*, Vol. 121, No. 3, pp. 409-414.
- Schetz, J.A., Kush, E.A. and Joshi, P.B., 1980, "Wave Phenomena in Liquid Jet Breakup in a Supersonic Crossflow," *AIAA Journal*, Vol. 18, No. 7, pp. 774-778.
- Schetz, J.A. and Padhye, A., 1977, "Penetration and Breakup of Liquids in Subsonic Airstreams," *AIAA Journal*, Vol. 15, No. 10, pp. 1385-1390.
- Schlichting, H., 1979, *Boundary-Layer Theory*, 7th edition, McGraw-Hill: New York.
- Seay, J.E., 1995, *Atomization and Dispersion of a Liquid Jet Injected into a Crossflow of Air*, M.S. Thesis, University of California, Irvine, CA.
- Seay, J.E., McDonell, V.G., and Samuelsen, G.S., 1995, "Atomization and Dispersion from a Radial Airblast Injector in a Subsonic Crossflow," AIAA Paper 95-3001.
- Seinfeld, J.H. and Pandis, S.N., 1998, *Atmospheric Chemistry and Physics*, John Wiley & Sons: New York.
- Seinfeld, J.H., 1986, *Atmospheric Chemistry and Physics of Air Pollution*, John Wiley & Sons: New York.
- Shaffar, S.W., 1993, *Reduction of Oxides of Nitrogen from a Liquid Fueled Gas Turbine Combustor*, M.S. Thesis, University of California, Irvine, CA.

Shaffar, S.W. and Samuelsen, G.S., 1998, "A Liquid Fueled, Lean Burn, Gas Turbine Combustor Injector," *Combustion Science and Technology*, Vol. 139, Nos. 1-6, pp. 41-57.

Shih, W.P., Lee, J.G. and Santavicca, D.A., 1996, "Stability and Emissions Characteristics of a Lean Premixed Gas Turbine Combustor," *Twenty-Sixth Symposium (International) on Combustion*, Vol. 26, pp. 2771-2778.

Silverman, I. and Sirignano, W.A., 1994, "Multi-Droplet Interaction Effects in Dense Sprays," *International Journal of Multiphase Flow*, Vol. 20, No. 1, pp. 99-116.

Smith, S.H. and Mungal, M.G., 1998, "Mixing, Structure and Scaling of the Jet in Crossflow," *Journal of Fluid Mechanics*, Vol. 357, pp. 83-122.

Sowa, W.A., 1992, "Interpreting Mean Drop Diameters Using Distribution Moments," *Atomization and Sprays*, Vol. 2, No. 1, pp. 1-15.

Suzuki, M., Nishida, K. and Hiroyasu, H., 1994, "Imaging of Drop and Vapour Clouds in an Evaporating Fuel Spray by Ultraviolet and Visible Lasers," *Particle and Particle Systems Characterization*, Vol. 11, No. 3, pp. 241-249.

Tacina, R.R., 1990, "Low NO_x Potential of Gas Turbine Engines," AIAA Paper 90-0550.

Thomas, R.H. and Schetz, J.A., 1985, "Distributions Across the Plume of Transverse Liquid and Slurry Jets in Supersonic Airflow," *AIAA Journal*, Vol. 23, No. 12, pp. 1892-1901.

Vranos, A., Liscinsky, D.S., True, B., and Holdeman, J.D., 1991, "Experimental Study of Cross-Stream mixing in a Cylindrical Duct," AIAA Paper 91-2459; also NASA TM 105180.

Wallis, G.B., 1969, *One-Dimensional Two-Phase Flows*, McGraw-Hill, New York.

Weiss, C. and Worsham, C., 1959, "Atomization in High Velocity Air Streams," *ARS Journal*, Vol. 29, pp. 252-259.

Wooler, P.T., 1969, "Flow of a Circular Jet into a Cross Flow," *Journal of Aircraft*, Vol. 6, No. 3, pp. 283-284.

Wu, P.K., Hsiang, L.P. and Faeth, G.M., 1995, "Aerodynamic Effects on Primary and Secondary Breakup," in *Liquid Rocket Engine Combustion Instability*, edited by V. Yang and W. Anderson, Vol. 169, pp. 247-279.

Wu, P.K., Kirkendall, K.A., Fuller, R.P. and Nejad, A.S., 1997, "Breakup Processes of Liquid Jets in Subsonic Crossflow," *Journal of Propulsion and Power*, Vol. 13, No. 1, pp. 64-73.

Wu, P.K., Kirkendall, K.A., Fuller, R.P. and Nejad, A.S., 1998, "Spray Structures of Liquid Jets Atomized in Subsonic Crossflows," *Journal of Propulsion and Power*, Vol. 14, No. 2, pp. 173-182.

Yatsuyanagi, N., Sakamoto, H. and Sato, K., 1998, "Empirical Calculation Model of the Atomization of a Liquid Sheet and a Round Liquid Jet in a Gaseous Flow Field," *Atomization and Sprays*, Vol. 8, No. 3, pp. 267-289.

Yuan, L.L. and Street, R.L., 1998, "Trajectory and Entrainment of a Round Jet in Crossflow," *Physics of Fluids*, Vol. 10, No. 9, pp. 2323-2335.

Yuen, L.S., Peters, J.E. and Lucht, R.P., 1997, "Pressure Dependence of Laser-Induced Fluorescence from Acetone," *Applied Optics*, Vol. 36, No. 15, pp. 3271-3277.

Zaman, K.B.M.Q. and Foss, J.K., 1997, "The Effect of Vortex Generators on a Jet in a Cross-Flow," *Physics of Fluids*, Vol. 9, No. 1, pp. 106-114.

Zeldovich, J.B., 1946, "Oxidation of Nitrogen in Combustion and Explosion," *Comptes Rendus (Doklady) de l'Academie des Sciences de l'URSS*, Vol. 51, No. 3, pp. 217-220.

Zelina, J. and Ballal, D.R., 1997, "Combustor Stability and Emissions Research Using a Well-Stirred Reactor," *Journal of Engineering for Gas Turbines and Power*, Vol. 119, No. 1, pp. 70-75.

APPENDIX A

IMAGE PROCESSING CODES

MATLAB (v. 5.3, MathWorks, Inc.) was the software package that was used to process and plot the images in this dissertation. The codes are divided into six main groups:

I. Processing of Raw Image Files

For the images that were captured via the planar imaging techniques, a *.spe file (a format native to the Princeton Instruments image acquisition software) obtained at each y-plane was imported into the MATLAB workspace. The *.spe file consisted of 25-layers of matrices containing intensity values recorded in a 16-bit unsigned integer data type. After storing the contents of the *.spe file as a 3-D workspace variable ($m \times n$ matrices, 25 layers in time), the block was averaged across the temporal dimension and subsequently stored in another matrix block of dimensions $m \times n \times p$, where p refers to the spatial dimension. For the acetone-laden spray images, the temporal filter was applied in this step, using a standard deviation of $\pm 2\sigma$ from the mean value at each pixel coordinate to filter out the high intensities associated with liquid droplet scattering.

II. Laser Sheet Profile Correction

The same procedure used to read in, store, and temporally average the *.spe images of the spray was used to process the laser sheet profiles. The laser sheet

profiles were obtained at the start of each day's tests by capturing the light that scattered off of a piece of glass placed obliquely to the path of the laser sheet. The oblique placement of the glass allowed the light to scatter off a wider section of the surface so that the signal could be averaged across the wide swath. After obtaining the time-averaged profile, the laser sheet scattering signal was averaged spatially and normalized. The single line-averaged, normalized profile was used to correct the images as the second step in the imaging processing procedure. The correction involved sweeping across the spray image, and dividing each column by the normalized laser sheet profile. The sections of the spray that were illuminated by a weaker section of the laser sheet would thereby be enhanced.

III. Extraction of Planar Cross-Sections

Codes were written to extract cross-sections in other planar dimensions. Vertical planes were imaged across the spray in 1-mm increments. Each vertical plane represented a thickness of one pixel, which resulted in a five-pixel gap between sheets because of the 6 pixel/mm resolution in this experiment. The blank pixels were filled by using a linear interpolation scheme between the corresponding $[i, j]$ pixels in each plane.

IV: Image Filtering

To produce a cleaner representation of the extracted images, the images were filtered. The filtering procedure consisted of averaging bins $a \times a$ large, across the extracted image. A value of $a=6$ was chosen to match the 6 pixels/mm resolution in this experiment. The averaging procedure resulted in a condensed image which was

then expanded back to its near-original dimensions by applying a bilinear interpolation scheme.

V: Calculation of Parameters to Assess the Spray Quality

After extracting and filtering the cross-sections of interest, calculations of the plane-averaged D_{32} values, the spray area coverage, and spatial unmixedness were obtained. The calculations were made after applying a threshold level on the images to elicit the spray boundaries.

VI: Edge Detection

Edge detection methods were applied to time-averaged images of the sprays in Chapter 7 in order to measure the spray angle. The edge detection method that was employed is essentially a Sobel edge detector which involves the calculation of the gradient across the rows and columns of the image. The sum of the square of the gradients is known as the squared gradient magnitude (*SGM*). Applying the squaring function results in the edge detection method being insensitive to the local orientation of the edge (Russ, 1995).

The MATLAB routines covered in the above discussion are included on the following pages. Unless otherwise noted, all codes were written by the author.

I. Code to Process Raw *.spe Files into Time-Averaged Images

```
% main.m

% PARAMETERS
numlayers = 25;
acetone_std = 2;

upper = 126;
lower = 300;
left = 121;
right = 264;

path = 'o:\setm_case1\acetone\'

[series,fuel,airdp,airdia,xflow,type,planemm,fileindex] = readscr;
[avgblock,stdblock]=processim(path,series,type,fileindex,upper,lower,
    left,right,numlayers,acetone_std);

function [fseries,ffuel,fairdp,fairdia,fxflow,ftype,fplanemm,findex]
    = readscr()

% Reads in script file of plane position and corresponding file name
% of FM spray images.
% Format of file:
% 1st line: fseriesf:file name format 'a_'
% 2nd line: ffuel: fuel mass flow rate (lbm/h)
% 3rd line: fairdp:atomizing air pressure drop (%)
% 4th line: fairdia:airblast hole diameter (in.)
% 5th line: fxflow:crossflow velocity (ft/sec)
% 6th line: ftype:type of measurement (milspec, mie, or acetone)
% 7th line: fcol1,2:titles of each column--'plane'; 'filenum'
% Subsequent lines: 1st column = plane position (mm);
%                   2nd column = file number.

fid=-1;
while fid == -1
    scriptfile=
        input('Type in case scriptfile (e.g., a_mil.dat): ', 's');
    fid = fopen(scriptfile,'rt');
    if fid == -1
        fprintf(1, 'File name invalid. Type in correct name.\n');
    end
end

fseries = fscanf(fid,'%s',1);
ffuel = fscanf(fid,'%f',1);
ffuelunit = fscanf(fid,'%s',1);
fairdp = fscanf(fid,'%f',1);
fairdpunit = fscanf(fid,'%s',1);
```

```

fairdia = fscanf(fid,'%f',1);
fairdiaunit = fscanf(fid,'%s',1);
fxflow = fscanf(fid,'%f',1);
fxflowunit = fscanf(fid,'%s',1);
ftype = fscanf(fid,'%s',1);
fcol1 = fscanf(fid,'%s',1);
fcol2 = fscanf(fid,'%s',1);
values = fscanf(fid,'%f',[2 inf]);
fclose(fid);

fplanemm=values(1,:);
findex=values(2,:);

```

```

function[avgblk,stdblk]=processim(fpath,fseries,ftype,findex,upper,
    lower,left,right,nlayers,ace_std)

```

```

% This function only reads in the images from files, and computes the
% time-averaged and standard deviation of the images. If the files
% are acetone PLIF images, then the images are filtered to eliminate
% the droplets.

```

```

nrows = lower - upper + 1;
ncols = right - left +1;

```

```

nfiles = length(findex);

```

```

% Initialize matrix block.

```

```

avgblk = zeros(nrows,ncols,nfiles);
stdblk = zeros(nrows,ncols,nfiles);
timeblk = zeros(nrows,ncols,nlayers);
for k=1:nfiles

```

```

    fname=[fpath fseries int2str(findex(k)) '.spe']

```

```

    if ~exist(fname), break,end

```

```

    timeblk=readtim(fname,timeblk,upper,lower,left,right,nlayers);

```

```

    avgmat = mean(timeblk,3);

```

```

    stdmat = std(timeblk,0,3);

```

```

    if strcmp(ftype,'acetone')

```

```

        [avgmatfilt, stdmatfilt]=

```

```

            tfilter(timeblk,avgmat,stdmat,ncols,nrows,nlayers,ace_std);

```

```

        avgmat = avgmatfilt;

```

```

        stdmat = stdmatfilt;

```

```

    end

```

```

    avgblk(:,:,k) = avgmat;

```

```

    stdblk(:,:,k) = stdmat;

```

```

end

```



```
function tblock=readtim(fname,plane,upper,lower,left,right,nlayers)
```

```
% This function reads in the multi-layered *.spe file and stores  
% all images in a matrix block of dimension plane x nlayers.
```

```
fidspe = fopen(fname,'r');  
status = fseek(fidspe, 4100,0);
```

```
for t = 1:nlayers  
    spemat = fread(fidspe,[384,576],'uint16');  
    spemat = spemat';  
    plane(:, :, t) = spemat(upper:lower,left:right);  
end  
fclose(fidspe);  
tblock=plane;
```

```
function [tmatavg,tmatstd]=  
    tfilter(block,blockavg,blockstd,col,row,numtimes,factorstd)
```

```
% Filters out high intensity "drops" passing through a pixel in time  
% by considering the time-based standard deviation of a point in  
% space.
```

```
upperlimit = blockavg + factorstd*blockstd;
```

```
for i=1:row  
    for j=1:col  
        tvector=[];  
        count=1;  
        for t=1:numtimes  
            if block(i,j,t) < upperlimit(i,j)  
                tvector(count)=block(i,j,t);  
                count=count+1;  
            end  
        end  
        tmatavg(i,j)=mean(tvector);  
        tmatstd(i,j)=std(tvector);  
        tmatcount(i,j)=length(tvector);  
    end  
end
```

```
maxstd=max(max(tmatstd))  
mincount=min(min(tmatcount))
```

Sample Script File "a_mil.dat" Read by "readscr.m"

```
a_  
4      lbm/h  
4      %dp  
0.166 in.dia  
0      ft/sec  
milplif  
plane filenum  
-10    1  
-9     2  
-8     3  
-7     4  
-6     5  
-5     6  
-4     7  
-3     8  
-2     9  
-1     10  
0      11  
1      12  
2      13  
3      14  
4      15  
5      16  
6      17  
7      18  
8      19  
9      20  
10     21
```

II. Function Used to Correct Images for Laser Sheet Profile Variation

```
function corrrdata = corrlaser(data,lineprofile)
```

```
% Function takes in [i,j,k]-dimensional array 'data' and  
% corrects with averaged laser line profile array 'lineprofile'  
% of length i.  
% Line profile is converted to array of [i,j,k] dimensions by  
% repeating column of data j times, then repeating the [i,j]  
% matrix k times.
```

```
[numrows,numcols,numdepth]=size(data);
```

```
for j=1:numcols  
    laserarray(:,j)=lineprofile;  
end  
for k=1:numdepth  
    laservol(:,:,k)=laserarray;  
end
```



```
% Following line divides each element in array 'data' by the
% corresponding element in array 'laservol'.
```

```
corrdata = data./laservol;
```

III. Functions Used to Extract Cross-Sections of Images

```
function plsection = xsection(block,pixpermm,slices,adim,bdim)
```

```
% 'block' is an [i,j,k] 3-D matrix consisting of k-slices of [i,j]
%   matrices.
% 'pixpermm' is a constant; in this experiment, pixpermm=6
% 'slices' is a vector of planes (in mm) in which to recreate slices.
% 'adim' and 'bdim' denote which dimension to obtain slices;
%   [adim,bdim]=[1,3] obtains a vertical slice;
%   [adim,bdim]=[3,2] obtains a horizontal cross-section.
% 'plsection' is a 3-D matrix consisting of matrices of total
%   length(slices).
```

```
[nrows,ncols,ndepth]=size(block);
nslices = length(slices);
```

```
% This section inserts matrices of zeros in between the measured
% planes to correct for the resolution.
```

```
realdepth = ndepth + (pixpermm - 1)*(ndepth-1);
newblock = zeros(nrows,ncols,realdepth);
for n = 1:ndepth
    newblockindex = (n-1)*pixpermm + 1;
    newblock(:,:,newblockindex) = block(:,:,n);
end
```

```
% This section recreates the slices specified by 'slices', taking the
% average of a slab of pixels 'pixpermm' width.
```

```
for p = 1:nslices
    minslice = (slices(p)-1)*pixpermm + 1;
    maxslice = minslice + (pixpermm-1);
    if adim==3 & bdim ==2
        % This case obtains a horizontal plane. Need to obtain slab of
        % matrices along a subset of rows. This slab is then averaged
        % along the rows to yield matrix 'avgslab'. The 'squeeze'
        % function produces a matrix that is transposed from the desired
        % form for the 1 x ncols x realdepth matrix (hence, need to
        % transpose matrix). Since this direction contains blank
        % values, need to interpolate using function 'int.m', which
        % requires that the input matrix be in column format (hence,
        % need to transpose matrix).
```

```

        slab = newblock(minslice:maxslice, :, :);
        avgslab = mean(slab, 1);
        avgslab = squeeze(avgslab)';
        intavgslab = int(avgslab');
        plsection(:, :, p) = intavgslab';
    elseif adim==1 & bdim==3
        % This case obtains a vertical plane.
        slab = newblock(:, minslice:maxslice, :);
        avgslab = mean(slab, 2); % mean of cols
        avgslab = squeeze(avgslab);
        intavgslab = int(avgslab);
        plsection(:, :, p) = intavgslab;
    end
end

```

function v = int(v)

```

% Given a matrix v that has gaps in some of the columns (value=0),
% this program interpolates between points to fill in the holes.

```

```

% Author: Erina Murakami

```

```

% Note from MYL: data must be in columns,
% and the first and last columns are filled.

```

```

disp('inside int')
[a,b] = size(v);

```

```

for r = 1:1:a
    i = 2;
    while i < b
        if v(r,i) == 0
            k=i;
            while v(r,k) == 0 & k < b
                k = k + 1;
            end

            % n = # pts between nonzero values surrounding i
            n = k - i + 1;
            dv = (v(r,k) - v(r,i-1))/n;
            for j = 0: 1: (n-2)
                v(r,i+j) = (j+1)*dv + v(r,i-1);
            end
            i = i + n;
        else
            i = i + 1;
        end
    end
end
end

```


IV. Functions Used to Filter Images

function fblock=imfilter(block,numbin)

% Function 'imfilter' works by shrinking and enlarging each image
% in the block of images. Bin size is 'numbin' by 'numbin' large.

[m,n,p]=size(block);

```
for k=1:p
    sm=condense(block(:,:,k),numbin);
    fblock(:,:,k)=expand(sm,numbin);
end
```

function smallmatrix=condense(matrix,pixpermm)

% Purpose of function "condense" is to shrink a high resolution
% picture down to 1 pixel per mm by representing each mm x mm block as
% an average of a pixpermm x pixpermm mask.

```
[m,n]=size(matrix);
nrows = floor(m/pixpermm);
ncols = floor(n/pixpermm);
```

```
for i=1:nrows
    for j=1:ncols
        mask=matrix(pixpermm*i-(pixpermm-1):pixpermm*i,
                    pixpermm*j-(pixpermm-1):pixpermm*j);
        smallmatrix(i,j)=mean(mean(mask));
    end
end
```

function expandmat=expand(smallmat,binsize)

% Program expands the condensed matrix of values, interpolating in 2
% dimensions. To use 'int.m', data must be in column form with zeros
% in between.

```
[m,n]=size(smallmat);
newm=m+(m-1)*(binsize-1);
newn=n+(n-1)*(binsize-1);
```

```
% Strategy for inserting zeros into the matrix:
% (1) create a matrix of zeros.
% (2) paste the data in the appropriate spot into the matrix of zeros.
```

```
% This section "inserts" rows of zeros.
```

```

bigmat=zeros(newm,n);
for i=1:m
    nonzeroindex=1+(i-1)*binsize;
    bigmat(nonzeroindex,:)=smallmat(i,:);
end

% This section "inserts" columns of zeros.

bigmat2=zeros(newm,newn);
for j=1:n
    nonzeroindex2=1+(j-1)*binsize;
    bigmat2(:,nonzeroindex2)=bigmat(:,j);
end

interpmat=int(bigmat2);
interpmat2=int(interpmat)';
expandmat=interpmat2;

```

V. Functions Used to Calculate Factors Contributing to the Spray Quality

function threshmat=blankit(block,threshold,blankvalue)

```

% Function 'thresh' sets the matrix values below a certain 'threshold'
% to the value 'blankvalue'.
% For D32 calculations, blankvalue=1. To elicit edges for spray
% boundary-related calculations, blankvalue=0.

[m,n,p]=size(block);

for k=1:p
    for i=1:m
        for j=1:n
            if block(i,j,k)<threshold
                threshmat(i,j,k)=blankvalue;
            else
                threshmat(i,j,k)=block(i,j,k);
            end
        end
    end
end
end

```


function blankd32=d32im(blankd3,blankd2)

% 'blankd3' represents the droplet volume concentration measurement
 % obtained using PLLIF, and processed using the function "blankit.m"
 % to filter values above a specified threshold.

% 'blankd2' represents the spray surface area measurement obtained
 % using planar Mie scattering, and has also been processed using the
 % function "blankit.m" to filter values above a specified threshold.

% Function "d32im" returns the D32 value, which is obtained by
 % taking the ratio of the PLLIF-related and Mie scattering-related
 % images, per the method of Sankar et al. (1999) and LeGal et al.
 % (1999).

[m,n,p]=size(blankd3);

```
for k=1:p
    for i=1:m
        for j=1:n
            if blankd3(i,j,k)==1 | blankd2(i,j,k)==1
                blankd32(i,j,k)=0;
            else
                blankd32(i,j,k)=blankd3(i,j,k)/blankd2(i,j,k);
            end
        end
    end
end
```

function fraction=computearea(block,thresh)

% Function "computearea" is used to calculate the extent of spray
 % coverage in terms of the fraction of the total area. The total
 % area is dictated by the m x n size of each matrix plane in 'block'.
 % The pixels included in the count must possess an intensity level
 % higher than 'thresh'.

[m,n,p]=size(block);
 totalarea=m*n;

```
for k=1:p
    count=0;
    for i=1:m
        for j=1:n
            if block(i,j,k)>thresh
                count=count+1;
            end
        end
    end
    fraction(k,1)=count/totalarea;
end
```

```
function us=uspatial(block)
```

```
% Function uspatial reads in a block of planes and calculates
% the spatial unmixedness value at each plane. The unmixedness
% is a normalized variance parameter which is used as a measure
% of spatial mixing.
```

```
[m,n,p]=size(block);
numpix=m*n;
maxI=65535;
```

```
% The following line normalizes the intensity by the maximum possible.
```

```
normblock=block/maxI;
```

```
for k=1:p
```

```
    % The following line obtains the normalized average intensity level
    % I in the plane.
```

```
    avgI=mean(mean(normblock(:,:,k)));
```

```
    % This loop calculates the sum of the squares of the
    % deviations of intensity from the mean intensity I in the plane.
```

```
    sumsq=0;
    for i=1:m
        for j=1:n
            sumsq=sumsq+(avgI-normblock(i,j,k))^2;
        end
    end
```

```
    % This section computes the spatial unmixedness in the plane.
```

```
    varI=sumsq/numpix;
    us(k,1)=varI/(avgI*(1-avgI));
end
```

VI. Functions Used in Edge Detection

```
function sobelmatrix=sobel(matrix)
```

```
sx=sobelx(matrix);
sy=sobely(matrix);
sobelmatrix=sx.^2+sy.^2;
```

```
function dmatrix=sobelx(matrix)
```



```
% Takes the derivative with respect to the x-direction.
```

```
dE_dx=[-1 0 1; -2 0 2; -1 0 1];
```

```
[row,col]=size(matrix);
```

```
dmatrix=zeros(row-2,col-2);
```

```
for i=1:row-2
```

```
    for j=1:col-2
```

```
        submatrix=matrix(i:i+2,j:j+2);
```

```
        prod=submatrix.*dE_dx;
```

```
        dmatrix(i,j)=sum(sum(prod));
```

```
    end
```

```
end
```

```
function dmatrix=sobely(matrix)
```

```
% Takes the derivative with respect to the y-direction.
```

```
dE_dy=[1 2 1; 0 0 0; -1 -2 -1];
```

```
[row,col]=size(matrix);
```

```
dmatrix=zeros(row-2,col-2);
```

```
for i=1:row-2
```

```
    for j=1:col-2
```

```
        submatrix=matrix(i:i+2,j:j+2);
```

```
        prod=submatrix.*dE_dy;
```

```
        dmatrix(i,j)=sum(sum(prod));
```

```
    end
```

```
end
```

```

function [edge1,edge2]=threshblock2(block,lowthresh)

% Extracts the edges by searching from the left and right edges, the
% coordinate at which the specified threshold value 'lowthresh'
% occurs.

[m,n,p]=size(block);
midpt=round(n/2);

for k=1:p
    % This i-for loop detects the left and right edges of the spray
    % based on an intensity threshold.

    for i=1:m
        % The following for loop searches for the lower edge to the left of
        % the penetration curve.

        for j=1:1:midpt
            if block(i,j,k)>lowthresh
                edge1(i,k)=j;
                break
            end
            if j==midpt
                edge1(i,k)=j;
            end
        end
    end

    % The following for loop searches for the upper edge to the right of
    % the penetration curve.
    for j=n:-1:midpt
        if block(i,j,k)>lowthresh
            edge2(i,k)=j;
            break
        end
        if j==midpt
            edge2(i,k)=j;
        end
    end
end
end
end

```


APPENDIX B

NONLINEAR MULTIVARIATE REGRESSION

For a nonlinear function of more than two dependent variables, a multivariate, nonlinear regression using the least squares method is applied to yield empirical curve fits. The following discussion uses the material presented by Ross (1987) to derive the procedures for producing regression curves for such equations such as the D_{32} correlations of Eqs. 8.3 and 10.3, and the spray trajectory correlations of Eqs. 9.3 and 9.4.

The regression is performed by using the least squares method to minimize the sum of the squared residuals, which are the differences between the set of responses (e.g., the plane-averaged D_{32} or the spray trajectory) and the estimated response given by the corresponding input parameters.

As an example, for the nonlinear spray trajectory equation

$$\frac{x}{d_f} = c_0 \cdot (q_2)^{c_1} \cdot \left(\frac{z}{d_f}\right)^{c_2} \quad (9.3)$$

a linear regression can be applied if the equation is recast in a linear form. The following equation is obtained after taking the logarithm of both sides of Eq. 9.3:

$$\log\left(\frac{x}{d_f}\right) = \log(c_0) + c_1 \cdot \log(q_2) + c_2 \cdot \log\left(\frac{z}{d_f}\right). \quad (B.1)$$

Substitution of the following variables $X = \log(x/d_f)$, $Q = \log(q_2)$, $Z = \log(z/d_f)$,

$b_0 = \log(c_0)$, $b_1 = c_1$, $b_2 = c_2$ leads to the linear regression equation

$$X = b_0 + b_1 \cdot Q + b_2 \cdot Z \quad (\text{B.2})$$

which is referred to as the regression equation of X on Q and Z . The sum of the squared differences, SS , between the response X and the estimate given by the linear regression is given by

$$SS = \sum (X - (b_0 + b_1 \cdot Q + b_2 \cdot Z))^2 \quad (\text{B.3})$$

To determine the coefficients b_0 , b_1 , and b_2 that minimize SS , partial derivatives of SS are taken with respect to the coefficients and set to zero. The following set of normal equations is subsequently obtained for n data points:

$$\begin{aligned} \sum X &= b_0 n + b_1 \sum Q + b_2 \sum Z \\ \sum XQ &= b_0 \sum Q + b_1 \sum Q^2 + b_2 \sum QZ \\ \sum XZ &= b_0 \sum Z + b_1 \sum QZ + b_2 \sum Z^2 \end{aligned} \quad (\text{B.4})$$

Substitution of the expressions $\tilde{x} = X - \bar{X}$, $\tilde{q} = Q - \bar{Q}$, and $\tilde{z} = Z - \bar{Z}$ into the set of equations in Eq. B.4 yields

$$\begin{aligned} \sum \tilde{x} &= b_1 \sum \tilde{q} + b_2 \sum \tilde{z} \\ \sum \tilde{x}\tilde{q} &= b_1 \sum \tilde{q}^2 + b_2 \sum \tilde{q}\tilde{z} \\ \sum \tilde{x}\tilde{z} &= b_1 \sum \tilde{q}\tilde{z} + b_2 \sum \tilde{z}^2 \end{aligned} \quad (\text{B.5})$$

The first equation of the set is called the regression equation of \tilde{x} on \tilde{q} and \tilde{z} . The unknowns b_1 and b_2 are the respective coefficients of \tilde{q} and \tilde{z} , and are calculated by solving the last two equations of Eqn. B.5. Once the coefficients are found for the regression, the original variables are substituted back into the first equation of Eqn. B.5, and the antilogarithm of the equation is obtained in order to convert the equation back to its original nonlinear form.

The same procedure was applied to determine the regression curves for Eq. 9.4:

$$\frac{x}{d_f} = c_0 \cdot (q_2)^{c_1} \cdot \left(\frac{z}{d_f}\right)^{c_2} \cdot \left(\frac{P}{P_0}\right)^{c_3} \quad (9.4)$$

The additional factor on the right hand side of Eqs. 9.4 increases the number of dependent variables to three, which adds another equation to the normal set of equations. In the general multivariable case, the normal set of $(k+1)$ equations for k variables is represented by

$$\begin{aligned} \sum X &= nb_0 + b_1 \sum Z_{i1} + b_2 \sum Z_{i2} + \dots + b_k \sum Z_{ik} \\ \sum XZ_{i1} &= b_0 \sum Z_{i1} + b_1 \sum Z_{i1}^2 + b_2 \sum Z_{i1}Z_{i2} + \dots + b_k \sum Z_{i1}Z_{ik} \\ &\dots \\ \sum XZ_{ik} &= b_0 \sum Z_{ik} + b_1 \sum Z_{ik}Z_{i1} + b_2 \sum Z_{ik}Z_{i2} + \dots + b_k \sum Z_{ik}^2 \end{aligned} \quad (B.6)$$

where X_i is the response variable, Z_{ik} represents the input variables, and $b_0 \dots b_k$ are the regression coefficients that are to be solved. Upon substitution of the expressions $\tilde{x} = X - \bar{X}$, $\tilde{q} = Q - \bar{Q}$, and $\tilde{z} = Z - \bar{Z}$ into Eq. B.6, the following form of the normal equations is obtained

$$\begin{aligned}
\sum \tilde{x} &= b_1 \sum \tilde{z}_{i1} + b_2 \sum \tilde{z}_{i2} + b_k \sum \tilde{z}_{ik} \\
\sum \tilde{x} \tilde{z}_{i1} &= b_1 \sum \tilde{z}_{i1}^2 + b_2 \sum \tilde{z}_{i1} \tilde{z}_{i2} + b_k \sum \tilde{z}_{i1} \tilde{z}_{ik} \\
&\dots \\
\sum \tilde{x} \tilde{z}_{ik} &= b_1 \sum \tilde{z}_{ik} \tilde{z}_{i1} + b_2 \sum \tilde{z}_{ik} \tilde{z}_{i2} + b_k \sum \tilde{z}_{ik}^2
\end{aligned} \tag{B.7}$$

which is a system of linear equations with regression coefficients that can be solved for using matrix algebra.

APPENDIX C

ADDITIONAL SPRAY JET IN CROSSFLOW RESULTS

The figures in this appendix present the results for the low fuel flow case of 1.8 kg/h that were not included in Chapter 10 because of the similarities in trends to the results of the 3.7 kg/h fuel flow case. Descriptions of the figures for the 1.8 kg/h cases are given below, along with the figure number corresponding to the 3.7 kg/h case. Note that the PLLIF images in Figs. C.1 through C.4 are presented on a scale normalized to the maximum intensity level obtained in the set of 1.8 kg/h cases.

- Figures C.1 and C.2 present the evolution of the liquid volume distribution over various downstream planes, as shown by the PLLIF images. Although Section 10.3.1b presents the results for the 3.7 kg/h case, the discussion of those results can be applied to the 1.8 kg/h cases. For this set of figures:
 - The 1.8 kg/h fuel flow, 3.18 mm-dia. spray orifice case in Fig. C.1 corresponds to Fig. 10.11 for the corresponding 3.7 kg/h condition.
 - The 1.8 kg/h fuel flow, 4.22 mm-dia. spray orifice case in Fig. C.2 corresponds to Fig. 10.12 for the corresponding 3.7 kg/h condition.
- Figures C.3 and C.4 compare the predicted liquid volume distributions, obtained by applying the spray trajectory analysis to droplet size and velocity data measured in the spray without crossflow, with the corresponding PLLIF cross-section through the spray centerplane. Although Section 10.7.3 discusses the results for the

3.7 kg/h case, the section can be referred to for a general description of the results that follow for the 1.8 kg/h fuel flow case. For this set of figures:

- The 1.8 kg/h fuel flow, 3.18 mm-dia. spray orifice case in Fig. C.3 corresponds to Fig. 10.33 for the corresponding 3.7 kg/h condition.
- The 1.8 kg/h fuel flow, 4.22 mm-dia. spray orifice case in Fig. C.4 corresponds to Fig. 10.34 for the corresponding 3.7 kg/h condition.

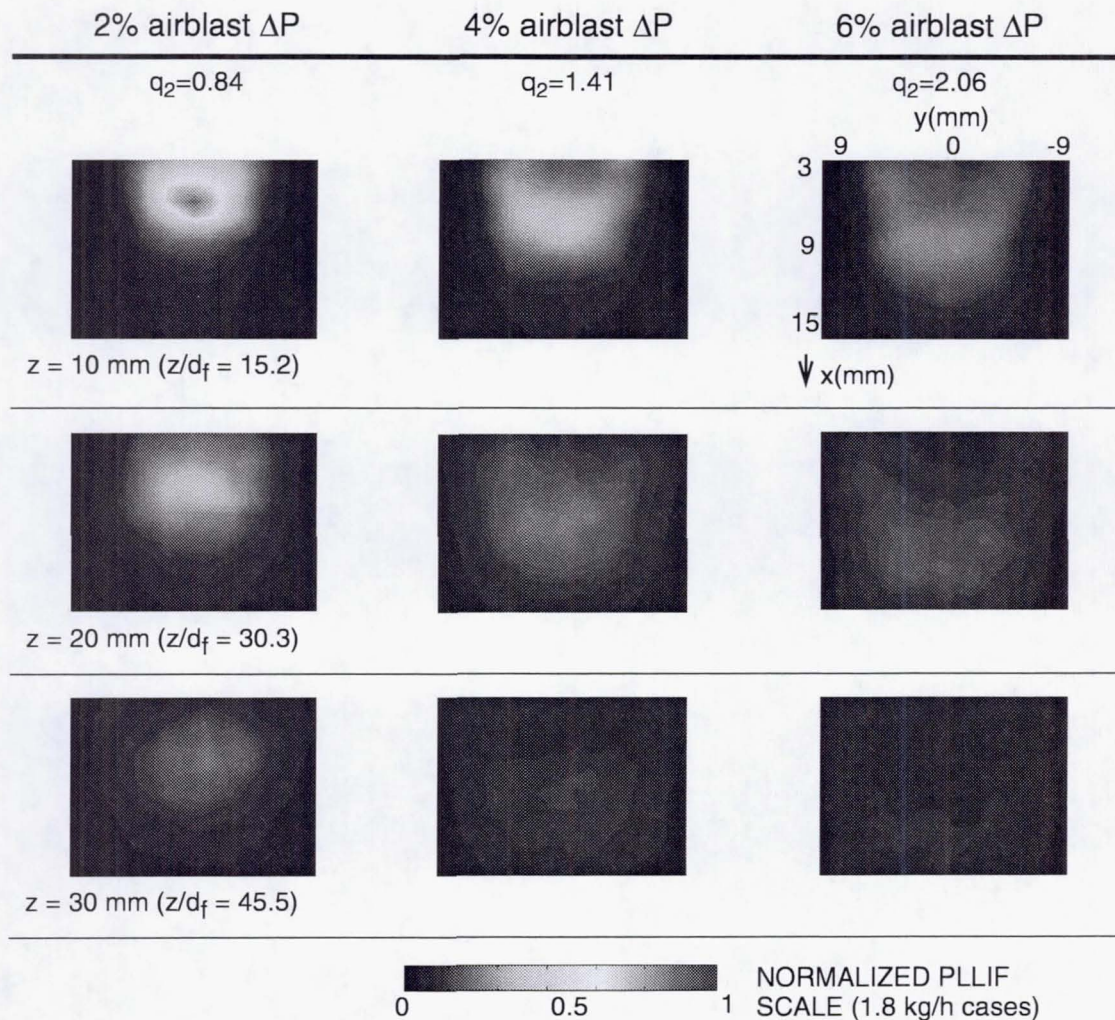


Fig. C.1 Evolution of the liquid concentration distributions for the 1.8 kg/h fuel flow, 3.18-mm spray orifice diameter case at a crossflow velocity of 70 m/sec.

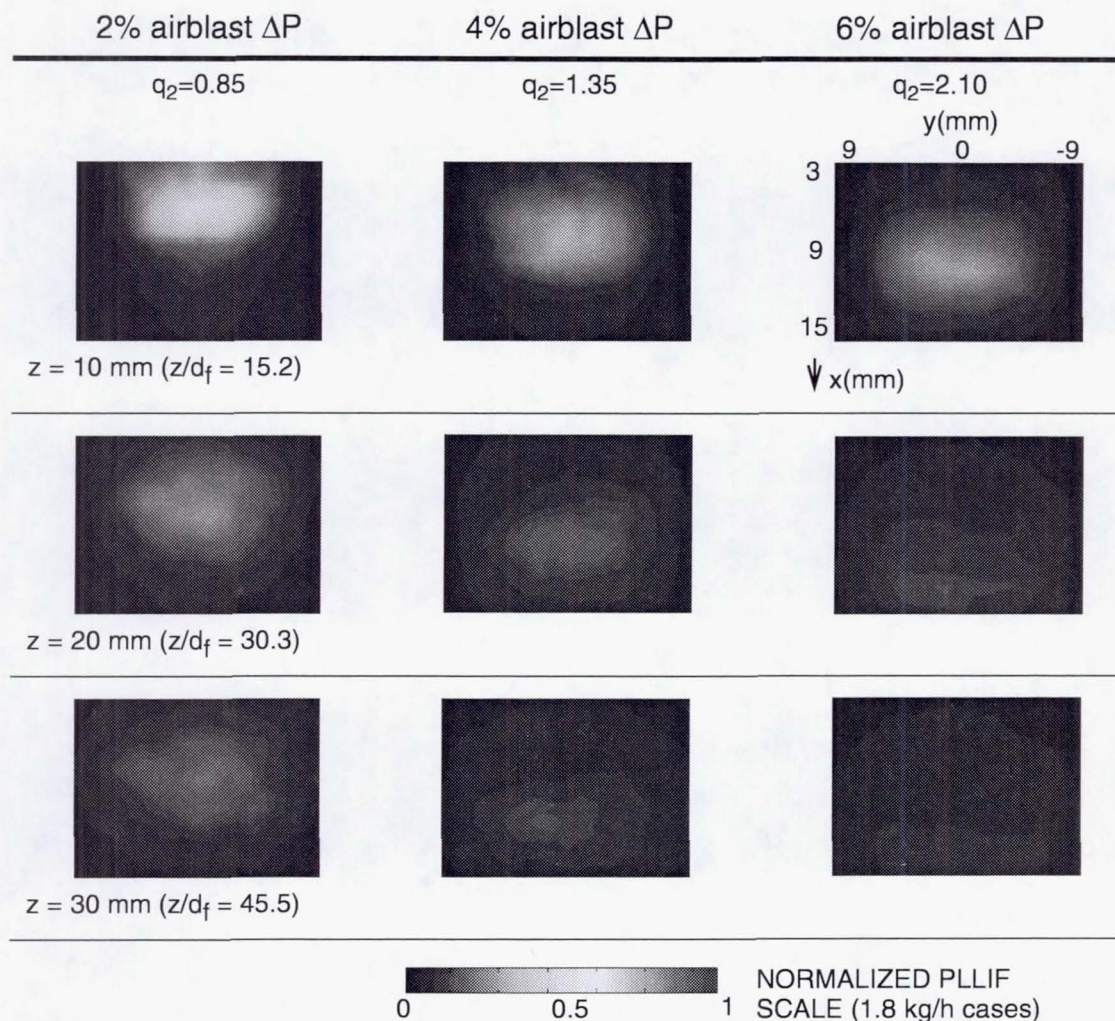


Fig. C.2 Evolution of the liquid concentration distributions for the 1.8 kg/h fuel flow, 4.22-mm spray orifice diameter case at a crossflow velocity of 70 m/sec.

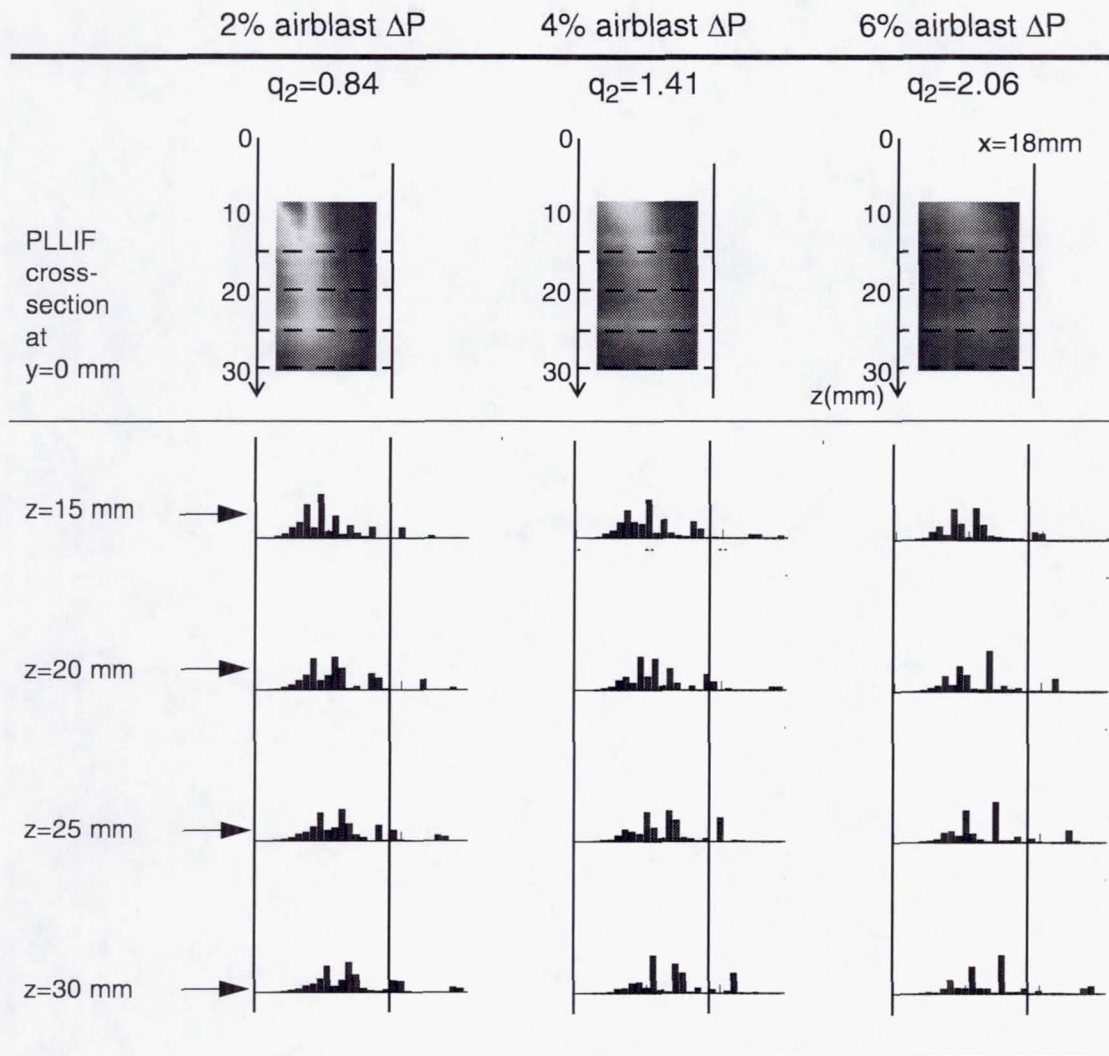


Fig. C.3 Comparison of predicted liquid volume distributions to the liquid concentration distributions from PLLIF imaging for the 1.8 kg/h, 3.18 mm-dia., 70 m/sec crossflow cases.

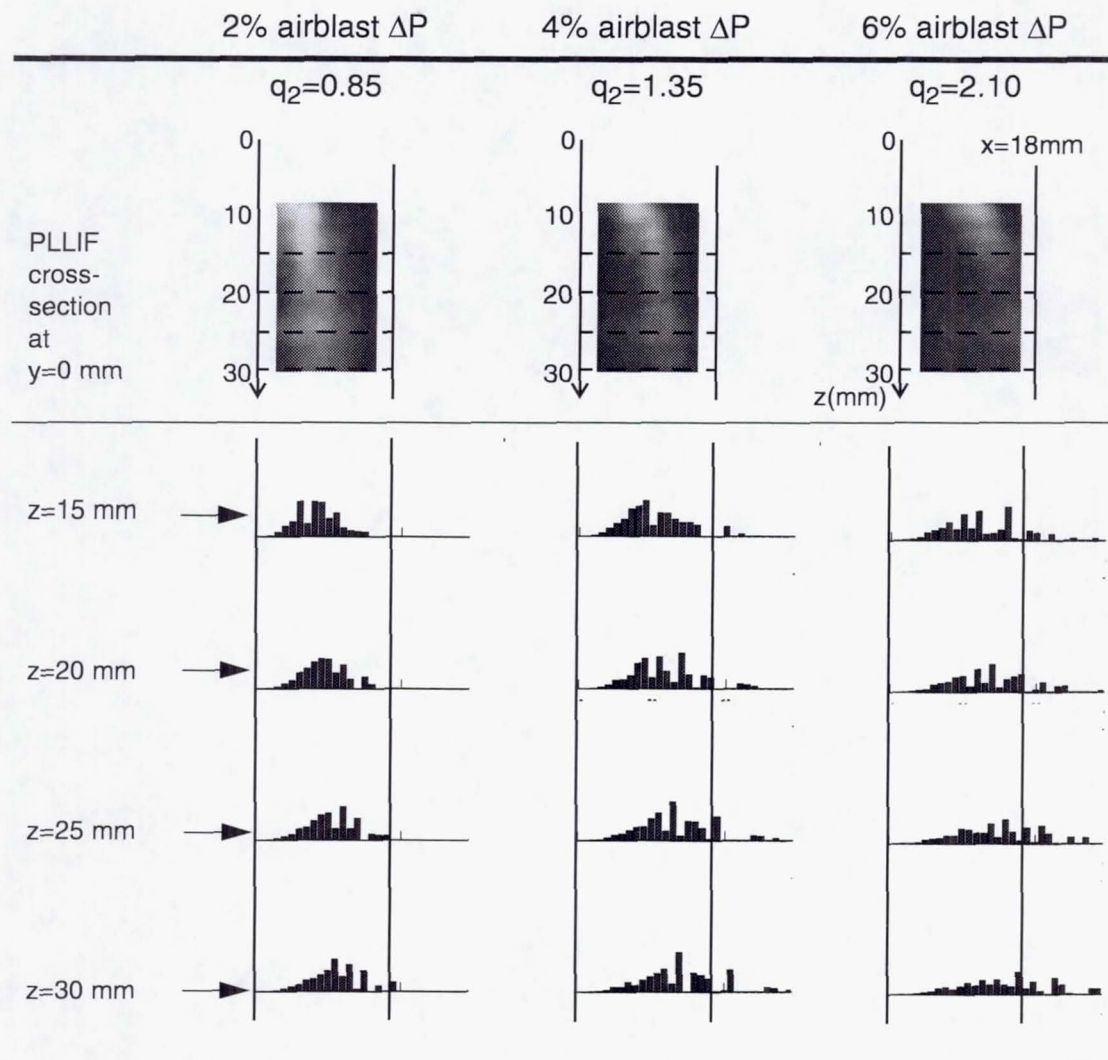


Fig. C.4 Comparison of predicted liquid volume distributions to the liquid concentration distributions from PLLIF imaging for the 1.8 kg/h, 4.22 mm-dia., 70 m/sec crossflow cases.

APPENDIX D

DROPLET TRAJECTORY PROGRAM FILES

The codes on the following pages were written to solve the droplet trajectory equations of motion from Eqs. 2.21-2.24. Function "calchist" served as the primary function that calls the function "droptraj." Function "droptraj" subsequently uses the function "trajderivs," which sets up the set of first-order linear ODEs. The system of equations are solved using the fourth-order Runge-Kutta routine "ode45," which is native to the MATLAB (v. 5.3, MathWorks, Inc.) software package. After solving for the droplet positions x and z , and the droplet velocity components u and w , the values corresponding to a specified plane are elicited using the function "evalatz."

```

function [tblock,xblock,zblock,ublock,wblock]=
    calchist(x,d30,meanv1,meanv2,xflowvel,zeval)

% Function input parameters:
% 'x' is a vector of [numcoords x 1] size which contains the
%   x-coordinate at the initial condition plane of z0=0.010 m
% 'd30' is a matrix of [numclasses x numcoords] size. Each row
%   contains the PVC D30 calculated for the prescribed droplet class
%   size. Each column corresponds to the x-coordinate where the run
%   was obtained. Units: [microns]
% 'meanv1' is similar to matrix 'd30', but contains mean transverse
%   velocities calculated for the particular size class at a
%   particular coordinate. Units: [m/sec]
% 'meanv2' is similar to matrix 'meanv1', except velocity component is
%   axial. units: [m/sec]
% 'xflowvel' is the crossflow velocity. Units: [m/sec]
% 'zeval' contains a vector of z-planes where the x-values and u- & w-
%   velocity components are to be obtained. Units: [m]

%---PARAMETERS

% Note: for tspan, axial velocities ~20-70 m/sec. If want to map a
% minimum of 50 mm, then need at least 0.050m/(20m/sec)=0.0025sec.

tspan=[0:.000001:.001]; % (sec)
z0=0.010; % (m)

numcoords=length(x);
numclasses=length(d30(:,1));
numzplanes=length(zeval);

tblock=zeros(numclasses,numcoords,numzplanes);
xblock=zeros(numclasses,numcoords,numzplanes);
zblock=zeros(numclasses,numcoords,numzplanes);
ublock=zeros(numclasses,numcoords,numzplanes);
wblock=zeros(numclasses,numcoords,numzplanes);

%---Determine PENETRATION OF EACH DROPLET CLASS i.
for n=1:numcoords
    for i=1:numclasses
        tc=[]; xc=[]; zc=[]; uc=[]; wc=[];
        diam=d30(i,n)*1E-6;% (m)
        if diam>0
            x0=x(n)*1E-3; % (m)
            udrop0=meanv1(i,n);% (m/sec)
            wdrop0=-1*meanv2(i,n);% (m/sec)
            [tc,xc,zc,uc,wc]=
                droptraj(diam,x0,z0,udrop0,wdrop0,xflowvel,tspan);
            % (tc[sec], xc[m], zc[m], uc[m/sec], wc[m/sec])

            tval=[]; xval=[]; zval=[]; uval=[]; wval=[];
            for k=1:numzplanes

```



```

        te=[]; xe=[]; ze=[]; ue=[]; we=[];
        [te,xe,ze,ue,we]=evalatz(tc,xc,zc,uc,wc,zeval(k));
        tval=[tval,te];
        xval=[xval,xe];
        zval=[zval,ze];
        uval=[uval,ue];
        wval=[wval,we];
    end
    tblock(i,n,:)=tval;
    xblock(i,n,:)=xval;
    zblock(i,n,:)=zval;
    ublock(i,n,:)=uval;
    wblock(i,n,:)=wval;
end
end
end

```

```

function [t,x,z,u,w]=
    droptraj(diam,x0,z0,udrop0,wdrop0,xflowvel,tspan)

```

```

% This program calculates the drop trajectory, given such input
% parameters as the initial positions 'x0' and 'z0', and the initial
% velocity components 'udrop0', 'wdrop0' of the droplet of diameter
% 'dia', injected into a crossflow with velocity 'w_cross'
% (the u-component u_cross=0).

```

```

% Units of dia, x0, z0:  m
% Units of udrop0,wdrop0,w_cross:  m/sec

```

```

% The 4th order Runge Kutta method is employed using the native
% MATLAB function 'ode45'.

```

```

% Notes:
% (1) +x axis corresponds to initial spray jet injection direction
%      (transverse), +z axis corresponds to direction aligned with
%      xflow (axial)
% (2) u-velocities in x-direction; w-velocities in z-direction

```

```

global dia density_drop density_air absvisc_drop absvisc_air
global u_cross w_cross g

```

```

dia=diam;
w_cross=xflowvel;

```

```

% PARAMETERS
%---Gravitational acceleration
g=9.81; % (m/sec2)

```

```

%---Fluid properties
density_drop=764; % (kg/m3)

```

```

% jet-A=822,
% MIL-C-7024D=764,
% MIL-PRF-7024E=762

density_air=1.185;      % (kg/m3), at 1-atm

absvisc_drop=7.76E-4;   % (kg/m-sec)
                        % jet-A=1.32E-3,
                        % MIL-C-7024D=7.76E-4,
                        % MIL-PRF-7024E=7.57E-4

absvisc_air=2.00E-5;    % (kg/m-sec)

%---Operating Conditions
u_cross=0;              % (m/sec)

% SET UP INITIAL CONDITION ARRAYS
%---Array of equations y
y(1)=x0;                % x(0)
y(2)=z0;                % z(0)
y(3)=udrop0;            % u(0)
y(4)=wdrop0;            % w(0)

% INTEGRATE USING RUNGE-KUTTA METHOD
[t,y]=ode45('trajderivs',tspan,y');
x=y(:,1);
z=y(:,2);
u=y(:,3);
w=y(:,4);

function dydt=trajderivs(t,y)

% Contains the system of first order ODEs that are to be solved
% via the Runge-Kutta method.

global dia density_drop density_air absvisc_drop absvisc_air u_cross
w_cross g

% Extract variables from incoming y-vector:
x=y(1);
z=y(2);
u=y(3);
w=y(4);

% Calculate new Reynolds numbers and drag coefficients
Vrel=relvel(u,u_cross,w,w_cross);
Re_drop = density_air * Vrel * dia / absvisc_drop;
CD=dragcoeff(Re_drop);

```



```

% Compute derivatives of x, z, u, w:
dxdt=u;
dzdt=w;
dudt=(-0.75*density_air*(u-u_cross)*Vrel*CD)/(density_drop*dia);
dwdt=(-0.75*density_air*(w-w_cross)*Vrel*CD)/
    (density_drop*dia)+g*(1-(density_air/density_drop));

% Input derivatives into dydt-vector:
dydt(1)=dxdt;
dydt(2)=dzdt;
dydt(3)=dudt;
dydt(4)=dwdt;

dydt=dydt';

```

```

function velocity=relvel(ud,ug,wd,wg)

```

```

% Computes the 2-D relative velocity.

```

```

velocity=sqrt(((ud-ug)^2)+((wd-wg)^2));

```

```

function CD=dragcoeff(Re)

```

```

% Function "dragcoeff" determines the drag coefficient for rigid
% spheres based on the particle Reynolds number.

```

```

if Re<=1                                % Stokes flow
    CD=24/Re;
elseif Re<=1000                          % Wallis (1969)
    CD=(24/Re)*(1+0.15*(Re^0.687));
elseif Re<3E5                            % Wallis (1969)
    CD=0.44;
elseif Re>=3E5
    CD=0;
    disp('Turbulent regime reached. Check flow');
end

```

```

function [te,xe,ze,ue,we]=evalatz(t,x,z,u,w,zeval)

% The goal of this function is to obtain the time ('te'), x-coord
% ('xe'), transverse & axial velocities ('ue' and 'we') of a droplet
% evaluated at a specified z-plane 'zeval'.

% The strategy here is to compare 'zeval' with 'z'. The value within
% +/- buffer of zeval is assigned tagged as the 'z' at which the
% evaluated 'te', 'xe', 'ue', and 'we' are obtained.

%---PARAMETERS
numvals=length(z);
diffz=abs(z-zeval);
mindiffz=min(diffz);

i=1;
while i<=numvals
    if mindiffz==diffz(i), break, end
    i=i+1;
end

te=t(i);
xe=x(i);
ze=z(i);
ue=u(i);
we=w(i);

```


REPORT DOCUMENTATION PAGE			Form Approved OMB No. 0704-0188	
Public reporting burden for this collection of information is estimated to average 1 hour per response, including the time for reviewing instructions, searching existing data sources, gathering and maintaining the data needed, and completing and reviewing the collection of information. Send comments regarding this burden estimate or any other aspect of this collection of information, including suggestions for reducing this burden, to Washington Headquarters Services, Directorate for Information Operations and Reports, 1215 Jefferson Davis Highway, Suite 1204, Arlington, VA 22202-4302, and to the Office of Management and Budget, Paperwork Reduction Project (0704-0188), Washington, DC 20503.				
1. AGENCY USE ONLY (Leave blank)	2. REPORT DATE October 2000	3. REPORT TYPE AND DATES COVERED Final Contractor Report		
4. TITLE AND SUBTITLE Mixing of an Airblast-Atomized Fuel Spray Injected Into a Crossflow of Air		5. FUNDING NUMBERS WU-714-02-20-00 NCC3-412		
6. AUTHOR(S) May Y. Leong, Vincent G. McDonell, and G. Scott Samuelsen				
7. PERFORMING ORGANIZATION NAME(S) AND ADDRESS(ES) University of California, Irvine Irvine, California 92697-3550		8. PERFORMING ORGANIZATION REPORT NUMBER E-12463		
9. SPONSORING/MONITORING AGENCY NAME(S) AND ADDRESS(ES) National Aeronautics and Space Administration Washington, DC 20546-0001		10. SPONSORING/MONITORING AGENCY REPORT NUMBER NASA CR-2000-210467 UCI-ARTR-00-05		
11. SUPPLEMENTARY NOTES Project Manager, James D. Holdeman, Turbomachinery and Propulsion Systems Division, NASA Glenn Research Center, organization code 5830, (216) 433-5846.				
12a. DISTRIBUTION/AVAILABILITY STATEMENT Unclassified - Unlimited Subject Category: 07 This publication is available from the NASA Center for AeroSpace Information, (301) 621-0390.			12b. DISTRIBUTION CODE Distribution: Nonstandard	
13. ABSTRACT (Maximum 200 words) The injection of a spray of fuel droplets into a crossflow of air provides a means of rapidly mixing liquid fuel and air for combustion applications. Injecting the liquid as a spray reduces the mixing length needed to accommodate liquid breakup, while the transverse injection of the spray into the air stream takes advantage of the dynamic mixing induced by the jet-crossflow interaction. The structure of the spray, formed from a model plain-jet airblast atomizer, is investigated in order to determine and understand the factors leading to its dispersion. To attain this goal, the problem is divided into the following tasks which involve: (1) developing planar imaging techniques that visualize fuel and air distributions in the spray, (2) characterizing the airblast spray without a crossflow, and (3) characterizing the airblast spray upon injection into a crossflow. Geometric and operating conditions are varied in order to affect the atomization, penetration, and dispersion of the spray into the crossflow. The airblast spray is first characterized, using imaging techniques, as it issues into a quiescent environment. The spray breakup modes are classified in a liquid Reynolds number versus airblast Weber number regime chart. This work focuses on sprays formed by the "prompt" atomization mode, which induces a well-atomized and well-dispersed spray, and which also produces a two-lobed liquid distribution corresponding to the atomizing air passageways in the injector. The characterization of the spray jet injected into the crossflow reveals the different processes that control its dispersion. Correlations that describe the inner and outer boundaries of the spray jet are developed, using the definition of a two-phase momentum-flux ratio. Cross-sections of the liquid spray depict elliptically-shaped distributions, with the exception of the finely-atomized sprays which show kidney-shaped distributions reminiscent of those obtained in gaseous jet in crossflow systems. A droplet trajectory analysis overpredicts the liquid mass penetration, and indicates a need for a more rigorous model to account for the three-dimensional mixing field induced by the jet-crossflow interaction. Nonetheless, the general procedures and criteria that are outlined can be used to efficiently assess and compare the quality of sprays formed under different conditions.				
14. SUBJECT TERMS Phase doppler; Planar laser induced fluorescence; Liquid jet fuel; Atomization combustor; Elevated pressure; Jet in crossflow; Air crossflow			15. NUMBER OF PAGES 387	
			16. PRICE CODE A17	
17. SECURITY CLASSIFICATION OF REPORT Unclassified	18. SECURITY CLASSIFICATION OF THIS PAGE Unclassified	19. SECURITY CLASSIFICATION OF ABSTRACT Unclassified	20. LIMITATION OF ABSTRACT	